Issue: 29
SCOPUS

pISSN : 1390-650X
eISSN : 1390-860X
january / june 2023

UNIVERSIDAD POLITÉCNICA SALESIANA ECUADOR

INGENIUS

Revista de Ciencia y Tecnología

Ingenius

Ingenius • Issue 29 • january/june 2023. Journal of Science and Tecnology of the Universidad Politécnica Salesiana of Ecuador. Publication dedicated to studies related to the Sciences of Mechanical Engineering, Electrical Engineering, Electronic Engineering, Mechatronic Engineering, Systems Engineering and Industrial Engineering.

Reviewers board

José Trinidad Holguín Momaca, MSc, Centro de Investigación en Materiales Avanzados, México.

Juan Manuel Alvarado Orozco, PhD, Centro de Ingeniería y Desarrollo Industrial, México.

Arnaldo Jélvez Caamaño, PhD, Universidad del BIOBIO, Chile.

Javier Murillo, PhD, Centro Internacional Franco Argentino de Ciencias de la Información y de Sistemas, Argentina.

Lucas Daniel Terissi, PhD, Universidad Nacional de Rosario, Argentina.

Rene Vinicio Sanchez Loja, MSc, Universidad Politécnica Salesiana, Ecuador.

Freddy Leonardo Bueno Palomeque, MSc, Universidad Politécnica Salesiana, Ecuador.

Diego Cabrera Mendieta, MSc, Universidad Politécnica Salesiana, Ecuador.

Edwuin Jesus Carrasquero, PhD, Universidad Técnica de Machala, Ecuador.

Carlos Mauricio Carrillo Rosero, MSc, Universidad Técnica de Ambato, Ecuador.

Diego Carrion Galarza, MSc, Universidad Politécnica Salesiana, Ecuador.

Carmen Celi Sanchez, MSc, Universidad Politécnica Salesiana, Ecuador.

Diego Chacon Troya, MSc, Universidad Politécnica Salesiana, Ecuador.

Paul Chasi, MSc, Universidad Politécnica Salesiana, Ecuador.

Juan Chica, MSc, Universidad Politécnica Salesiana, Ecuador.

Diego Marcelo Cordero Guzmán, MSc, Universidad Católica de Cuenca, Ecuador.

Luis Javier Cruz, PhD, Universidad Pontificia Bolivariana, Medellin, Colombia.

Fabricio Esteban Espinoza Molina, MSc, Universidad Politécnica Salesiana, Ecuador.

Jorge Fajardo Seminario, MSc, Universidad Politécnica Salesiana, Ecuador.

Patricia Fernandez Morales, PhD, Universidad Pontificia Bolivariana, Medellin, Colombia.

Marcelo Flores Vazquez, MSc, Universidad Politécnica Salesiana, Ecuador.

Carlos Flores Vázquez, MSc, Universidad Católica de Cuenca, Ecuador.

Carlos Franco Cardona, PhD, Universidad Nacional de Colombia, Colombia.

Cristian García García, MSc, Universidad Politécnica Salesiana, Ecuador.

Teonila García Zapata, PhD, Universidad Nacional Mayor de San Marcos, Perú.

Luis Garzón Mñoz, PhD, Universidad Politécnica Salesiana, Ecuador.

Natalia Gonzalez Alvarez, MSc, Universidad Politécnica Salesiana, Ecuador.

Ernesto Granado, PhD, Universidad Simón Bolívar, Venezuela.

Adriana del Pilar Guaman, MSc, Universidad Politécnica Salesiana, Ecuador.

Juan Inga Ortega, MSc, Universidad Politécnica Salesiana, Ecuador.

Esteban Inga Ortega, PhD, Universidad Politécnica Salesiana, Ecuador.

Paola Ingavélez, MSc, Universidad Politécnica Salesiana, Ecuador.

Cesar Isaza Roldan, PhD, Universidad Pontificia Bolivariana.

Nelson Jara Cobos, MSc, Universidad Politécnica Salesiana, Ecuador.

Ruben Jerves, MSc, Universidad Politécnica Salesiana, Ecuador.

Victor Ramon Leal, PhD, Investigador de PDVSA, Venezuela

Gabriel Leon, MSc, Universidad Politécnica Salesiana, Ecuador.

Edilberto Llanes, PhD, Universidad Internacional SEK, Ecuador.

Luis López, MSc, Universidad Politécnica Salesiana, Ecuador.

Carlos Mafla Yépez, MSc, Universidad Técnica del Norte, Ecuador.

Hader Martínez, PhD, Universidad Pontificia Bolivariana, Medellin, Colombia

Javier Martínez, PhD, Instituto Nacional de Eficiencia Energética y Energías Renovables, Ecuador.

Alex Mayorga, MSc, Universidad Técnica de Ambato, Ecuador.

Jimmy Molina, MSc, Universidad Técnica de Machala, Ecuador.

Andres Montero, PhD, Universidad de Cuenca, Ecuador.

Vicente Morales, MSc, Universidad Tecnica de Ambato, Ecuador.

Fabián Morales, MSc, Universidad Técnica de Ambato, Ecuador.

Diego Morales, MSc, Ministerio de Electricidad y Energías Renovables del Ecuador.

Yoandrys Morales Tamayo, PhD, Universidad Técnica de Cotopaxi, Cotopaxi

Olena Leonidivna Naidiuk, MSc, Universidad Politécnica Salesiana, Ecuador.

Oscar Naranjo, MSc, Universidad del Azuay, Ecuador.

Paul Narvaez, MSc, Universidad Politécnica Salesiana, Ecuador.

Hernán Navas Olmedo, MSc, Universidad Técnica de Cotopaxi, Ecuador.

Cesar Nieto, PhD, Universidad Pontificia Bolivariana, Medellin, Colombia

Fabio Obando, MSc, Universidad Politécnica Salesiana, Ecuador.

Luis Ortiz Fernandez, MSc, Universidade Federal de Rio Grande del Norte, Brasil

Pablo Parra, MSc, Universidad Politécnica Salesiana, Ecuador.

Paulo Peña Toro, PhD, Ministerio de Productividad, Ecuador.

Patsy Prieto Velez, MSc, Universidad Politécnica Salesiana, Ecuador.

Diego Quinde Falconi, MSc, Universidad Politécnica Salesiana, Ecuador.

Diana Quintana Espinoza, MSc, Universidad Politécnica Salesiana, Ecuador.

William Quitiaquez Sarzosa, MSc, Universidad Politécnica Salesiana, Ecuador.

Flavio Quizhpi Palomeque, MSc, Universidad Politécnica Salesiana, Ecuador.

Washington Ramirez Montalvan, MSc, Universidad Politécnica Salesiana, Ecuador.

Fran Reinoso Avecillas, MSc, Universidad Politécnica Salesiana, Ecuador.

Néstor Rivera Campoverde, MSc, Universidad Politécnica Salesiana, Ecuador.

Jorge Romero Contreras, MSc, Universidad de Carabobo, Venezuela

Fabian Saenz Enderica, MSc, Universidad de las Fuerzas Armadas, ESPE, Ecuador.

Luisa Salazar Gil, PhD, Universidad Simón Bolivar, Venezuela

Gustavo Salgado Enríquez, Msc, Universidad Central del Ecuador., Ecuador.

Juan Carlos Santillán Lima, MSc, Universidad Nacional de Chimborazo

Jonnathan Santos Benítez, MSc, Universidad Politécnica Salesiana, Ecuador.

Andrés Sarmiento Cajamarca, MSc, Universidad Federal de Santa Catarina, Brasil

Luis Serpa Andrade, MSc, Universidad Politécnica Salesiana, Ecuador.

Cristian Timbi Sisalima, MSc, Universidad Politécnica Salesiana, Ecuador.

Milton Tipan Simbaña, MSc, Universidad Politécnica Salesiana, Ecuador.

Paul Torres Jara, MSc, Universidad Politécnica Salesiana, Ecuador.

Rodrigo Tufiño Cárdenas, MSc, Universidad Politécnica Salesiana, Ecuador.

Fernando Urgiles Ortíz, MSc, Universidad Politécnica Salesiana, Ecuador.

Juan Valladolid Quitoisaca, MSc, Universidad Politécnica Salesiana, Ecuador.

Efrén Vázquez Silva, PhD, Universidad Politécnica Salesiana, Ecuador.

Julio Verdugo, MSc, Universidad Politécnica Salesiana, Ecuador.

Mary Vergara Paredes, PhD, Universidad de los Andes, Merida, Venezuela

Jennifer Yepez Alulema, MSc, Universidad Politécnica Salesiana, Ecuador.

Julio Zambrano Abad, MSc, Universidad Politécnica Salesiana, Ecuador.

Patricia Zapata Molina, MSc, Universidad Politécnica Salesiana, Ecuador.

Editorial

Editorial Abya Yala (Quito-Ecuador),
Av. 12 de octubre N422 y Wilson,
Bloque A, UPS Quito, Ecuador.
Casilla 17-12-719 Teléfonos: (593-2) 3962800 ext. 2638
email: editorial@abyayala.org

Printing: 800 copies

Typographic system used in the composition of this document LaTeX.

Ingenius

Revista de Ciencia y Tecnologia

Issue 29

january – june 2023

ISSN impreso 1390-650X / ISSN electrónico 1390-860X

The administration of the journal is done through the following parameters:

The journal uses the academic anti-plagiarism system

The articles have an identification code (Digital Object Identifier)

The editorial process is managed through the Open Journal System

The articles of the present edition can be consulted in
http://revistas.ups.edu.ec/index.php/ingenius

Universidad Politécnica Salesiana del Ecuador

Ingenius Journal, is indexed in the following Databases and scientific information systems:

SELECTIVE DATABASES

REVIEWS EVALUATION PLATFORMS

SELECTIVE DIRECTORIES

SELECTIVE SERIAL LIBRARY

SCIENTIFIC LITERATURE SEARCHERS OPEN ACCESS

OTHER BIBLIOGRAPHICAL DATABASES

CATALOG OF INTERNATIONAL UNIVERSITY LIBRARIES

Universität Passau – Fakultät für Informatik und Mathematik
BSB Bayerische StaatsBibliothek – Information in erster Linie
Deutsches Museum
Hochschule Rosenheim – University of Applied Sciences

Hochschule Landshut – Hochschule für angewandte Wissenschaften
Hochschule für angewandte Wissenschaften München
Hochschule Weihenstephan-Triesdorf – University of Applied Sciences
TUM – Technische Universität München

Universität der Bundeswehr München
LMU – Ludwig-Maximilians-Universität München
Technische Hochschule Ingolstadt
Hochschule Augsburg – University of Applied Sciences

Hochschule Kempten – University of Applied Sciences
HNU – Hochschule Neu-Ulm University of Applied Sciences
OTH – Ostbayerische Technische Hochschule Regensburg
Ostbayerische Technische Hochschule Amberg-Weiden

Staatliche Bibliothek Neuburg an der Donau
sbr – Staatliche Bibliothek Regensburg
Staats- und Stadtbibliothek Augsburg
Georg-Simon-Ohm Hochschule Nürnberg

UBA – Universitätsbibliothek Augsburg
Katholische Universität Eichstätt-Ingolstadt
UR – Universität Regensburg
Hochschule Ansbach

Coburg University of applied sciences and arts
hochschule hof – University of Applied Sciences
Hochschule Merseburg (FH) – University of Applied Sciences
ThULB – Thüringer Universitäts- und Landesbibliothek Jena

EZB – Elektronische Zeitschriftenbibliothek
Universität Bamberg
Universität Bayreuth

FAU – Friedrich-Alexander Universität Erlangen-Nürnberg
Bauhaus-Universität Weimar
UB WÜ
Freie Universität Berlin

FHE – Fachhochschule Erfurt University of Applied Sciences
h² – Hochschule Magdeburg • Stendal
htw – Hochschule für Technik und Wirtschaft Berlin – University of Applied Sciences

UB Braunschweig
Stiftung Tierärztliche Hochschule Hannover
Gottfried Wilhelm Leibniz Bibliothek – Niedersächsische Landesbibliothek

Editorial

Dear readers:

INGENIUS has been accepted into SCOPUS

In search of excellence, the journal Ingenius complying with all the editorial quality requirements demanded in the different instances, to date had indexations in selective databases such as ESCI (Emerging Source Citation Index), SCIELO (Scientific Electronic Library Online), EBSCO (Online Research Platform), Google scholar (search engine specialized in academic documents) and others, also in evaluation platforms of journals and selective newspaper libraries such as MIAR (Information matrix for the analysis of journals), REDIB (Ibero-American Network of Innovation and scientific knowledge), LATINDEX (Regional Online Information System for Scientific Journals of Latin America, the Caribbean, Spain and Portugal).

The strict process carried out in relation to the selection of the theme to be published executed by an editorial team of great experience, compliance with regulations for the structuring of the article, that is, compliance with the format, the IMRDC structure (introduction, materials and methods, results and discussion, and conclusions), the special attention paid to blind peer review with a large team of reviewers of different nationalities in all areas of interest of the journal, the layout process, the style review and the publication in Spanish and English have made the academic and scientific community at an international level read and cite the journal and consider it to publish their contributions. All of the above, worked synergistically, has allowed us to seek new challenges that position and publicize the contributions of many national and international researchers, who, trusting in the journal, have submitted their articles to the corresponding editorial process and have published them complying with the required quality standards; that is why after a rigorous, ethical and hard work the journal was postulated and we have received the pleasant news that it has been accepted in SCOPUS fulfilling all the required quality criteria.

All the journals that are in SCOPUS, which is one of the most prestigious databases worldwide, with a quality website and tools for monitoring, analysis and visualization of research, meet minimum criteria that were evaluated by a Content Advisory Committee, composed of a group of researchers and librarians of international and independent scope, covering the main scientific disciplines. The selection of the journal involves criteria grouped into 5 categories; the first considers the editorial policy that must be convincing, must perform peer review, and reviewers and authors must be diverse in geographical distribution; the second states that there must be an academic contribution in the field, the abstracts must be clear and have correspondence with the objectives of the journal and there must be readability in the articles; the third measures prestige based on citations of journal articles in Scopus and the prestige of the journal's editors; The fourth establishes that there must be online availability through a quality website and be available in English and the fifth establishes regularity, without considering any delay in the publication schedule.

This merit achieved is the result of an arduous work for which the Salesian Polytechnic University bets, since, among its institutional policies, the dissemination of knowledge in open access is paramount because it favors equality and the development of science in favor of society in general.

We reaffirm our commitment to continue in an ethical and responsible manner in the arduous editorial task and we hope that researchers will continue to send their contributions.

John Calle-Sigüencia, PhD

Editor in Chief

Table of Contents

Scientific Paper / Artículo Científico

UNIVERSIDAD POLITÉCNICA SALESIANA ECUADOR
INGENIUS
Revista de Ciencia y Tecnología
https://doi.org/10.17163/ings.n29.2023.01
pISSN: 1390-650X / eISSN: 1390-860X

Voltage stability and electronic compensation in electrical power systems using simulation models

Estabilidad de tensión y compensación electrónica en sistemas eléctricos de potencia usando herramientas de simulación

M. Campaña[1,*], P. Masache[1], E. Inga[1], D. Carrión[1]

Received: 21-04-2021, Received after review: 24-09-2021, Accepted: 08-11-2021, Published: 01-01-2023

Abstract

Increased demand in the different electrical power systems (EPS) has a negative impact in voltage stability, reliability and quality of the power supply. Voltage profile is reduced when generation units are not capable of supplying reactive power to the EPS at the times it is required. With the development of power electronics and complex control systems, flexible alternating current transmission system (FACTS) devices have been introduced. In this article, the impact of the introduction of a type of FACTS that allows reactive power compensation in the EPS is analyzed in detail. Furthermore, a methodology to decide the capacity of the Static Synchronous Compensator (STATCOM) and its optimal location with the execution of continuous power flows (CPF) will be analyzed. Finally, the positive impact of installing a Power System Stabilizer (PSS) control to ensure voltage stability in the EPS will be studied. This article is developed using the IEEE 14-bus base system under two mathematical models for power flow calculation developed in MATLAB software, which are: which are: i) through the power balance equations and ii) Newton Raphson with the toolbox PSAT.

Keywords: Load Factor, PSAT, contingency, Continuous Power Flow, PSS, STATCOM

Resumen

El aumento de la demanda en los distintos sistemas eléctricos de potencia (SEP) tiene un impacto negativo en la estabilidad de la tensión, la confiabilidad y la calidad del suministro eléctrico. El perfil de tensión disminuye cuando las unidades de generación no son capaces de suministrar potencia reactiva al sistema eléctrico en los momentos que se requiere. Con el desarrollo de la electrónica de potencia y los complejos sistemas de control, se han podido introducir dispositivos de sistemas flexibles de transmisión de corriente alterna (FACTS, del inglés *Flexible Alternating Current Transmission System*). En este artículo se analiza en detalle el impacto que genera la introducción de un tipo de FACTS que permite la compensación de potencia reactiva en el SEP. Además, se analizará una metodología para decidir la capacidad del compensador síncrono estático (STATCOM, del inglés *Static Synchronous Compensator*) y su ubicación óptima con la ejecución de flujos de potencia continuos (FPC). Finalmente, se estudiará el impacto positivo de la instalación de un control estabilizador de potencia (PSS, del inglés *Power System Stabilizer*) para asegurar la estabilidad de tensión en el SEP. Este artículo se desarrolla utilizando el sistema base IEEE de 14 barras bajo dos modelos matemáticos para el cálculo del flujo de potencia desarrollados en el software Matlab, que son: i) utilizando las ecuaciones de balance de potencia y ii) Newton Raphson con el *toolbox* de MATLAB (PSAT, del inglés *Power System Analysis Toolbox*).

Palabras clave: factor de carga, PSAT, contingencia, flujo de potencia continuo, PSS, STATCOM

[1,*]Grupo de Investigación de Redes eléctricas Inteligentes (GIREI), Universidad Politécnica Salesiana - Ecuador.
Corresponding author ✉: mcampana@ups.edu.ec.

Suggested citation: Campaña, M.; Masache, P.; Inga, E. and Carrión, D. "Voltage stability and electronic compensation in electrical power systems using simulation models," *Ingenius, Revista de Ciencia y Tecnología*, N.° 29, pp. 9-23, 2023, DOI: https://doi.org/10.17163/ings.n29.2023.01.

1. Introducción

Most interruptions in electric transmission networks (ETN) are due to voltage instability. Possible causes may be overloaded electric systems, occurrence of faults or lack of available reactive power in generation units. At present, it is possible to have a greater control of the voltage margin on each of the buses of the EPS [1–3]. The ETN are responsible for supplying electric power from the generation units to the loads, meeting safety and reliability criteria. The shortage of reactive power that a generation unit may supply to the system may be due to a load increase in the EPS, causing a possible degradation of the voltage stability in the electric system [4, 5], especially in buses that operate close to their limits. It is shown in [6] that the maximum capacity for transferring electric power through the ETN may be improved installing FACTS devices. Such devices may anticipate control of power flow and voltage profile, improve voltage stability and minimize losses. However, their high cost limits the installation of FACTS controllers in all lines of the EPS. It is assured in [7, 8] that the best FACTS devices are those based on converters such as: STATCOM and the Unified Power Flow Controller (UPFC). The present paper will pay special attention to the synchronous static compensator and its direct control on voltage stability.

Another detail addressed in this paper is the dynamic analysis in the presence of electromechanical oscillations in the EPS. These oscillations may be local (a single generator) or may involve a number of generators widely separated geographically (oscillations between areas). If they are not controlled, these oscillations may lead to a partial or total interruption of the power supply [9]. Electromechanical oscillations may be damped through the application of PSS. The objective of the PSS is to modulate the extinction voltage of a synchronous generator acting through the automatic voltage regulator (AVR) [10, 11], and are economically viable for improving voltage stability in the presence of small disturbances [12–14]. Therefore, PSS use auxiliary stabilizing signals, such as shaft speed, terminal frequency and power to vary the AVR input signal. The block diagram of the PSS used in this paper may be verified in [9], [15, 16]. Regarding this aspect, one of the main contributions of this paper is proving that the voltage instability produced by an $N-1$ contingency (opening of a line) may be eliminated adding a PSS in bus 1 of the proposed EPS (Figure 1).

The objective of this paper is to study voltage stability and the direct effects of installing synchronous static compensators in buses whose nominal voltage is critical, i.e., it is below or about to go below the lower voltage limit (0.95 pu). The IEEE 14-bus system is used as a base case to validate the proposed methodology. In addition, through the application of PSS and simulations in time-domain with the PSAT toolbox, it will be proven that power stabilizing systems may enable maintaining EPS stability or reducing the negative effect on it of an $N-1$ contingency. To achieve the objective of this paper, power flows will be simulated in static state under two iterative mathematical models based on power balance equations and Newton Raphson methodology. In addition, this analysis will enable evaluating the performance and error margins between each model. It is very important to mention that the Matlab software and the PSAT toolbox developed by Federico Milano will be used here.

The power flow analysis will help to verify the steady state magnitude of voltage, angle and active and reactive power of both load and generation. The different operating states will vary according to various initial parameters set on the EPS obtained from the IEEE 14-bus base case. These parameters will enable generating unstable conditions in the EPS, and further evaluating and being able to determine the best technical action to recover stability in the electric power system. The actions to which the system will be subject are: i) symmetrical increase of the load by a load factor λ that will directly multiply the active and reactive power of all loads and ii) opening of lines that simulate $N-1$ contingencies.

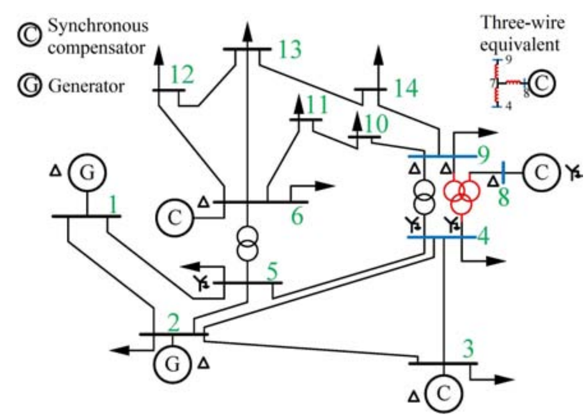

Figure 1. IEEE 14-bus system base case

Section II briefly analyzes the positive impact on the voltage profiles of an EPS when using synchronous static compensation in power transfer buses. Section III formulates the problem and explains the methodology applied in this paper. Section IV presents the results obtained in the simulations. At last, conclusions are presented in section V.

2. Materials y methods

The FACTS devices are not only capable of controlling the power transmitted and increasing the capacity of the lines, but also may suppress power fluctuations [4], [17, 18]. These devices are constructed with static elements and power electronics elements which, together, enable improving control and increasing the energy transfer capacity in alternating current (AC) systems. The operating principle of the synchronous compensator, which is a type of FACTS, considers three fundamental criteria i) a direct current (DC) capacitor after a transformer operates as a controllable voltage source, (ii) the voltage difference at the transformer reactance produces exchanges of active and reactive power between the STATCOM and the SEP and iii) the magnitude of the STATCOM output voltage may be controlled varying the voltage across the CC capacitor [19–21]. Figure 2 illustrates a basic structure that summarizes the STATCOM architecture.

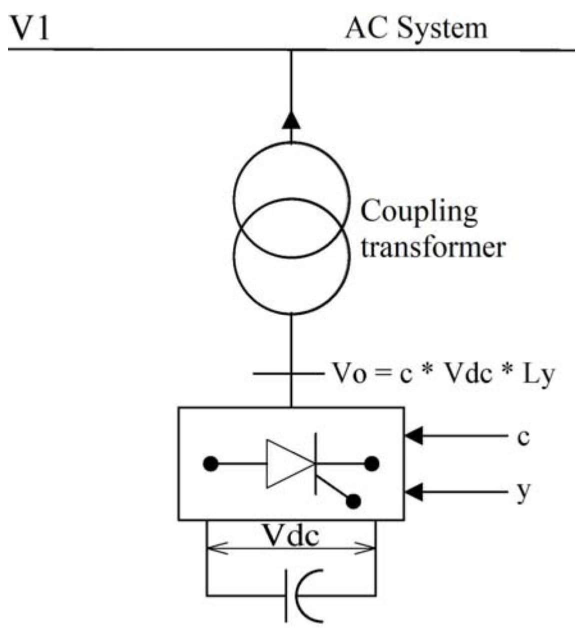

Figure 2. Basic structure of a type 2 STATCOM

There are two types of synchronous static compensators: the type 1 compensator is able to control active and reactive power in a transmission line, while type 2 can only control the angle ψ and the gain c remains fixed. ψ is the angular difference between V_1 (voltage at the STATCOM bus) and V_0 (Figure 2). In addition, the value of ψ should be kept very small to be able to control the system reactive power and desired voltage. For small values of ψ, the reactive power supplied by the STATCOM has a linear relationship [22,23]. Therefore, type 2 static synchronous compensators are not able to supply active power, because they spend active power to compensate transformer and commutation losses. Consequently, according to the voltage level of the system and the type of compensator, the STATCOM may operate as a capacitor or as an inductor. It is important to mention that the type 2 STATCOM will be used in this paper. The STATCOM may be modeled as a synchronous voltage source with maximum and minimum limits of voltage magnitude. In addition, the STATCOM obeys limits and according to the requirements is capable of generating or absorbing reactive power [24–26]. It is important to mention that in this paper the STATCOM will be modeled as a voltage source enabling a rigid voltage support mechanism.

The methodology implemented to analyze the problem considers the following statements: i) an analysis of the power flow in the system from differential equations comparing it with the Newton Raphson method and ii) stability analysis of angle and voltage. The EPS analyzed in this paper is illustrated in Figure 1. The system has 5 generation buses, 11 loads and 20 transmission lines. The base of the system is 100 MVA and bus 1 is defined as Slack or reference bus. The present paper will be analyzed at two moments i) power flow and arbitrary installation of a STATCOM at buses 13 and 14 and ii) it will be analyzed the voltage stability observing CPFs, which will enable to analyze the EPS behavior through the load factor increase. The power flow will be analyzed in two ways i) a mathematical model developed in Matlab considering the power balance equations and ii) the power flow using the PSAT toolbox. This will enable evidencing the error margins and performance of each model.

It is known that a load increase both in active and reactive powers will stress the system, and the reference values of voltage in each bus will be degraded. It the generation units are not capable of supplying the reactive power demanded by the system, these voltage values will decrease. This voltage reduction in the buses will compromise the EPS voltage stability. In the present paper the load factor λ will be increased 50%, i.e., λ will be equal to 1.5 pu. This will stress the system and through a static state power flow it will be possible to observe the voltage magnitudes updated with the load increase. Once the system has been stressed due to the load factor, buses 13 and 14 are chosen (Figure 1) as candidate sites for installing the STATCOM. The fundamental objective is to determine the type of STATCOM and the best location considering technical criteria at the lowest cost. The basic criteria for dimensioning and selecting the best location to install a STATCOM are defined in the literature considering three very important factors, namely: i) it should be chosen the STATCOM with minimum Mvar capacity that ii) guarantees that voltage remains within allowable limits (1.05-0.95 pu) verifying that iii) total reactive power losses in the EPS are minimum. At a second moment, it will be analyzed the stability of the electric system in the presence of $N-1$ contingencies in line 2-4 of Figure 1. Finally, it will be simulated the effect of the STATCOM on the EPS before and after its installation.

A modern electric system consists of a large mixture of renewable energy sources, variable and flexible loads, and is also experiencing a situation in which a significant number of conventional generators are being replaced by sources based on power electronics [27]. Consequently, the EPS stabilizers are controllers installed in synchronous generators whose main function is to dampen the oscillations of the electric system controlling the excitation, with the purpose of increasing the stability margin in the presence of low frequency oscillations in the EPS. The PSS controllers have two structures constituted by i) gain and phase compensation stages and ii) three bands corresponding to a specific frequency range (low, intermediate and high frequency) in which each band is constituted by two branches based on differential filters (with a gain, delay blocks and a hybrid block) [28]. Consequently, the design of power system stabilizers is a challenging task that requires long time, and thus an alternative for controller adjustment is the use of optimization methods [29]. An optimal design of a multimachine PSS is proposed in [30] for various simultaneous steady-state operating conditions.

2.1. Methodology for Power Flow Calculation

To know the behavior of the EPS at an operating point where the power flow is computed; the methodology and equations that model the power flow are detailed below:

- Initialize the unknown variables of the system. Voltage equal to 1 pu and angles equal to 0 rad.
- Admittance of the system (Ybus)

$$Y_{ii} = \sum_{k=1}(\frac{1}{Z_{ik}}) + \sum(Y_i) \tag{1}$$

$$Y_{ij} = -\frac{1}{Z_{ij}} \tag{2}$$

- Equations that govern the power flow

$$P_i = \sum_{k=1}(V_i * V_k * (G_{ik} * cos(\delta_i - \delta_k) + B_{ik} * sin(\delta_i - \delta_k))) \tag{3}$$

$$Q_i = \sum_{k=1}(V_i * V_k * (G_{ik} * sin(\delta_i - \delta_k) - B_{ik} * cos(\delta_i - \delta_k))) \tag{4}$$

- Balance of active and reactive power

$$\Delta P_i = P_{gen_i} - P_{d_i} - P_i \tag{5}$$

$$\Delta Q_i = Q_{gen_i} - Q_{d_i} - Q_i \tag{6}$$

- Jacobian matrix

$$\begin{bmatrix} \frac{d(\Delta P_i)}{d(\delta_i)} & \frac{d(\Delta P_i)}{d(V_i)} * |V_i| \\ \frac{d(\Delta Q_i)}{d(\delta_i)} & \frac{d(\Delta Q_i)}{d(V_i)} * |V_i| \end{bmatrix} = J \tag{7}$$

- Solution of equations

$$\begin{bmatrix} \Delta\delta_i \\ \Delta V_i \end{bmatrix} = J^{-1} * \begin{bmatrix} \Delta P_i \\ \Delta Q_i \end{bmatrix} \tag{8}$$

- New iteration values

$$\begin{bmatrix} \delta_{i+1} \\ V_{i+1} \end{bmatrix} = \begin{bmatrix} \Delta\delta_i \\ \Delta V_i \end{bmatrix} + \begin{bmatrix} \delta_i \\ V_i \end{bmatrix} \tag{9}$$

- Stopping criterion

$$\max\left(\begin{vmatrix} \Delta P_{i+1} \\ \Delta Q_{i+1} \end{vmatrix}\right) \leq 1e^{-5} \tag{10}$$

2.2. System transfer capacity

It enables knowing the maximum power transfer allowed in the electric system when an $N-1$ contingency occurs; the mathematical model given by equations **??**-**??** is used to calculate this index.

- Total transfer capacity

$$TTC = \sum(P_{Load} + \lambda_{max} * \sum(\Delta P_{Loss})) \tag{11}$$

- Real power transmitted

$$ETC = \sum(P_{Load}) \tag{12}$$

- Transmission margin before reaching instability

$$TRM = 0.05 * TTC \tag{13}$$

- Transfer capacity

$$ATC = TTC - ETC - TRM \tag{14}$$

2.3. Voltage stability

Voltage stability may be verified from CPF usage. The objective of CPF is periodically increasing λ to reach the maximum inflection point (λ_{max}) where the stability of the electric system operates at the limit; i.e., when it reaches its maximum value ($\lambda = P_{L_{max}}$), the voltage magnitudes at the different buses of the EPS will decrease until reaching a voltage collapse. The voltage stability analysis is carried out from the power *vs.* voltage curve (PV curves). The PV curve is simulated from the power flow using equations (1)-(10).

3. Results and discussion

This section presents a detailed description of the power flow and voltage stability analysis results. The magnitudes of voltage, angle, active and reactive power of both load and generation are obtained analyzing the EPS at an operating point under specific initial conditions. The EPS topology and its electric parameters (transmission lines and buses) are detailed in Tables 1 and 2 [31]. Table 1 describes the EPS topology and the line impedance parameters. Table 2 details the active and reactive powers of generation, load and base voltage, and also defines the type of line according to the following nomenclature i) 1 Slack bus ii) 2 PV bus and iii) 3 PQ bus.

Table 1. Data of lines in the IEEE 14-bus base case

Line	Line from	Line to	Line impedance [pu] Resistance	Reactance	Bsh/2
01	01	05	0.05403	0.22304	0.0219
02	01	02	0.01938	0.05917	0.0264
03	02	05	0.05695	0.17388	0.0170
04	02	04	0.05811	0.17632	0.0246
05	02	03	0.04699	0.19797	0.0187
06	03	04	0.06701	0.17103	0.0173
07	04	09	0.00000	0.55618	0.0000
08	05	04	0.01335	0.04211	0.0064
09	05	06	0.00000	0.25202	0.0000
10	06	12	0.12291	0.25581	0.0000
11	06	13	0.06615	0.13027	0.0000
12	06	11	0.09498	0.19890	0.0000
13	07	09	0.00000	0.11001	0.0000
14	07	04	0.00000	0.20912	0.0000
15	07	08	0.00000	0.17615	0.0000
16	09	14	0.12711	0.27038	0.0000
17	09	10	0.03181	0.08450	0.0000
18	10	11	0.08205	0.19207	0.0000
19	12	13	0.22092	0.19988	0.0000
20	14	13	0.17093	0.34802	0.0000

Table 2. Data for each Bus in the IEEE 14-bus base case

Bus N.°	Bus Type	P_g [pu]	Q_g [pu]	P_d [pu]	Q_d [pu]	V_m [pu]	Base [kV]
01	1	1.1417	-0.169	0.0000	0.0000	1.060	69.0
02	2	0.4000	0.0000	0.2170	0.1270	1.045	69.0
03	2	0.0000	0.0000	0.9420	0.1910	1.010	69.0
04	3	0.0000	0.0000	0.4780	0.0400	1.000	69.0
05	3	0.0000	0.0000	0.0760	0.0160	1.000	13.8
06	2	0.0000	0.0000	0.1120	0.0750	1.000	13.8
07	3	0.0000	0.0000	0.0000	0.0000	1.000	18.0
08	2	0.0000	0.0000	0.0000	0.0000	1.000	13.8
09	3	0.0000	0.0000	0.2950	0.1660	1.000	13.8
10	3	0.0000	0.0000	0.0900	0.0580	1.000	13.8
11	3	0.0000	0.0000	0.0350	0.0180	1.000	13.8
12	3	0.0000	0.0000	0.0610	0.0160	1.000	13.8
13	3	0.0000	0.0000	0.1380	0.0580	1.000	13.8
14	3	0.0000	0.0000	0.1490	0.0500	1.000	13.8

Once the initial parameters and the features of the ETN have been defined, it is verified the performance of two mathematical models developed in Matlab for power flows. The first model provides an iterative solution based on power balance equations (traditional method), whereas the second model uses the Newton Raphson algorithm with the PSAT toolbox.

3.1. Power flow using computational tools

Figure 3 enables to verify the voltage and angle variation ranges obtained from the simulation. Figure 3(a) shows the node voltage levels at each bus of the EPS for two computation models. The results of the mathematical model proposed in the PSAT toolbox are shown in orange, whereas the solution of the mathematical model proposed in Matlab using power balance equations is shown in blue. In buses 4, 5, 7, 9, 10, 11 and 14 the average error is 0.0037 p.u (Figure 3(a)); it can be seen that the error margin between the two models (Matlab – PSAT) is minimum, technically zero. Figure 3(b) represents the magnitude of the angles in each of the buses of the EPS; similarly, the average error margin in the angle results is 0.0042 radians. Therefore, the two models proposed for analyzing the power flow at steady state provide reliable solutions with minimum error margins. An additional detail that may be seen in Figure 3 is that the voltage magnitudes do not exceed the upper and lower limits of 1.05 pu and 0.95 pu, respectively, except for the Slack bus whose voltage is defined as 1.06 pu due to its nature.

The error margin in the active and reactive power is presented in Figure 4. The average error margin in the active power is 0.0019 pu, as it can be seen in Figure 4(a), whereas the average error margin in the reactive power is 0.0593 pu. A detail that should be taken into account is that both active and reactive power show similar trends, with error margins that approach zero. Therefore, considering only the comparative analysis of the results obtained for both models, presented in Figures 3 and 4, it may be concluded that both ways to obtain a solution to the power flow are reliable. However, Table 3 analyzes the performance of the methods proposed for power flow calculation.

It may be seen in Table 3 that the models execute the same number of iterations; however, the average margin of total active and reactive power losses is 0.0006 and 0.0485, respectively, and thus, it may be concluded that they are minimum and approach zero. It is important to mention that the same value of 1×10^{-5} for the error margin was considered for both methods. On the other hand, the CPU - Time achieved by the conventional method (power flow solved using power balance equations) is approximately 65 time larger (Table 3); hence, the PSAT toolbox is definitely a tool of very good performance, capable of providing reliable solutions in significantly small machine times.

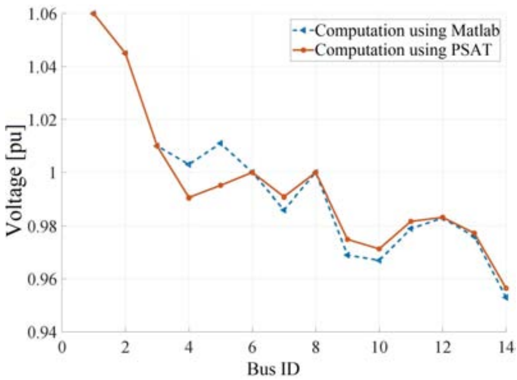

(a) Node voltage in pu

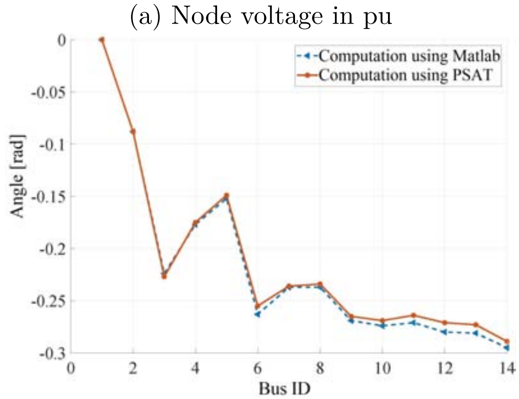

(b) Node angle in radians

Figure 3. Node Analysis of the IEEE 14-bus EPS

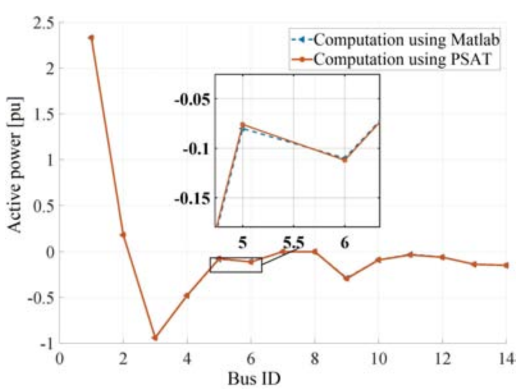

(a) Node active power in pu

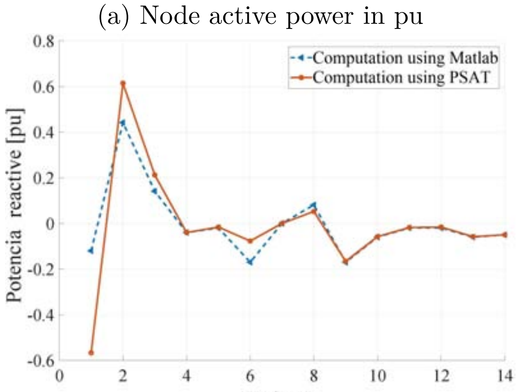

(b) Node reactive power in pu

Figure 4. Node Analysis of the IEEE 14-bus EPS

Table 3. Performance of the mathematical models proposed for computing the power flow

Parameter	Conventional method	Toolbox PSAT
CPU - Time [s]	19.641	0.3020
# of Iterations	4.0000	4.0000
Error margin of total P losses [pu]	0.1440	0.1434
Error margin of total Q losses [pu]	0.2740	0.3225

Table 4 presents the initial results obtained for the power flow, which will be referential magnitudes to start the study of voltage stability. It is very important to mention that the results achieved were extracted from the power flow solution provided by the PSAT Toolbox. As it can be seen, it is possible to monitor the magnitudes of voltage, angle, active and reactive power in each of the EPS buses; all the parameters presented in Table 4 were simulated without constraints in the maximum and minimum limits of active and reactive power.

Therefore, according to the initial values, the electric system operates at normal conditions, which indicates that it honors the voltage limits established by the regulation. In addition, Table 4 shows the total active and reactive power losses in the EPS.

Table 4. Low Newton-Raphson power flow solution in IEEE 14-bus base case

Bus N.°	Voltage [pu]	Angle [rad.]	Generación		Load	
			MW	Mvar	MW	Mvar
01	1.060	0.000	233.0	-5.70	0.000	0.000
02	1.045	-0.088	40.00	74.10	21.70	12.70
03	1.010	-0.227	0.000	40.30	94.20	19.10
04	0.991	-0.175	0.000	0.000	47.80	4.000
05	0.995	-0.149	0.000	0.000	7.600	1.600
06	1.000	-0.255	0.000	-0.200	11.20	7.500
07	0.991	-0.236	0.000	0.000	0.000	0.000
08	1.000	-0.234	0.000	5.200	0.000	0.000
09	0.975	-0.265	0.000	0.000	29.50	16.60
10	0.971	-0.269	0.000	0.000	9.000	5.800
11	0.982	-0.264	0.000	0.000	3.500	1.800
12	0.983	-0.271	0.000	0.000	6.100	1.600
13	0.977	-0.273	0.000	0.000	13.50	5.800
14	0.956	-0.289	0.000	0.000	14.90	5.000
Suma			273.6	113.8	259.3	81.50
Total power loss						
Active [MW]	14.34					
Reactive [Mvar]	32.25					

Table 55 presents the results for a load factor of 50% both in active and reactive power. In addition, the power flow is constrained to obey the power limits on the generation buses whose magnitudes oscillate between 0.5 p.u. for the active power and -0.06 p.u. for the reactive power. If the two cases presented in Tables 4 and 5 are compared, it may be seen the increase in active and reactive power, both generated and consumed. However, the voltage magnitudes in bus 14 fell below the lower limit of 0.95 pu (Table 5).

Table 5. Power flow solution for 50% load increase conditions with respect to the IEEE 14-bus base case

Bus N.°	Voltage [pu]	Angle [rad.]	Generation		Load	
			MW	Mvar	MW	Mvar
01	1.070	0.000	384.4	0.000	0.000	0.000
02	1.045	-0.145	40.00	114.2	32.60	19.10
03	1.010	-0.361	0.000	81.40	141.3	28.70
04	0.973	-0.281	0.000	0.000	71.70	6.000
05	0.980	-0.239	0.000	0.000	11.40	2.400
06	1.000	-0.405	0.000	26.90	16.80	11.30
07	0.973	-0.370	0.000	0.000	0.000	0.000
08	1.000	-0.370	0.000	15.20	0.000	0.000
09	0.948	-0.419	0.000	0.000	44.30	24.90
10	0.945	-0.425	0.000	0.000	13.50	8.700
11	0.966	-0.419	0.000	0.000	5.300	2.700
12	0.973	-0.431	0.000	0.000	9.200	2.400
13	0.963	-0.433	0.000	0.000	20.70	8.700
14	0.924	-0.457	0.000	0.000	22.40	7.500
Suma			424.4	237.0	389.0	122.3
		Total power loss				
Active [MW]		35.46				
Reactive [Mvar]		115.5				

The new power flow, considering active power limits with the implementation of STATCOM in buses 13 and 14, is illustrated in Table 6. It is very important to remember that the STATCOM is modeled as a voltage source. The initial parameters of the voltage source are fixed at 1 pu and 0 degrees, and thus, when a power flow is executed with the PSAT Toolbox it will be obtained the reactive power necessary to compensate and maintain the required voltage magnitude at 1 p.u. in the STATCOM installation bus. In other words, this magnitude of generated reactive power will be necessary to compensate the system for a load factor increase of $\lambda = 1.5$ pu of the demand. As it can be seen in Table 6, the generation reactive power to maintain the voltage in buses 13 and 14 at 1 pu at different instants, reaches magnitudes of 40.5 and 34.8 Mvar respectively. In addition, it should be noted that when the STATCOM is placed at bus 13 the voltage profiles do not reach the admissible minimum values, whereas when it is placed at bus 14 the bus voltages have appropriate values. An additional detail is that the EPS at normal and stress conditions ($\lambda = 1.5$ pu) records minimum magnitudes of 0.956 and 0.924, respectively, in bus 14, which implies this is a candidate bus to install the STATCOM because it exhibits lower voltage magnitudes in pu; therefore, it requires to be compensated with reactive power to raise the voltage magnitude to appropriate ranges.

On the other hand, Table 6 presents total active and reactive power losses. It may be seen that the active power loss is of equal magnitude, regardless of the bus where the STATCOM is installed. However, there is a slight difference in terms of the total reactive power loss if the STATCOM is installed in buses 13 or 14 (Table 6), with the smaller magnitude corresponding to the case when the STATCOM is installed in bus 14. Therefore, when minimizing total losses of reactive power, the optimal location of the STATCOM is determined by the requirement of maintaining the voltage profiles in moderate ranges and being the one with the lowest class. Class refers to the magnitude of Mvar required for the STATCOM. Finally, when the load factor is increased in 50% in all PQ buses (load buses), it is required to install a STATCOM of class 34.80 Mvar in bus 14 with the purpose of maintaining the voltage levels at allowable magnitudes, thus guaranteeing voltage stability using synchronous static compensation to minimize losses. When losses are minimized, the power flow transfer capacity is maximized in the EPS, as specified in the literature.

Table 6. Power flow solution applying STATCOM to the IEEE 14-bus base case

Bus N.°	STATCOM Barra 13						STATCOM Barra 14					
	Voltage	Angle	Generation		Load		Voltage	Angle	Generation		Load	
	[pu]	[rad.]	MW	Mvar	MW	Mvar	[pu]	[rad.]	MW	Mvar	MW	Mvar
01	1.070	0.000	384.5	0.000	0.000	0.000	1.071	0.000	384.3	0.000	0.000	0.000
02	1.045	-0.145	40.00	113.0	32.60	19.10	1.045	-0.145	40.00	109.3	32.60	19.10
03	1.010	-0.361	0.000	80.80	141.3	28.70	1.010	-0.361	0.000	79.10	141.3	28.70
04	0.974	-0.281	0.000	0.000	71.70	6.000	0.977	-0.282	0.000	0.000	71.70	6.000
05	0.980	-0.239	0.000	0.000	11.40	2.400	0.982	-0.240	0.000	0.000	11.40	2.400
06	1.000	-0.404	0.000	-10.20	16.80	11.30	1.000	-0.400	0.000	4.600	16.80	11.30
07	0.977	-0.370	0.000	0.000	0.000	0.000	0.986	-0.372	0.000	0.000	0.000	0.000
08	1.000	-0.370	0.000	13.30	0.000	0.000	1.000	-0.372	0.000	8.200	0.000	0.000
09	0.955	-0.419	0.000	0.000	44.30	24.90	0.973	-0.420	0.000	0.000	44.30	24.90
10	0.951	-0.426	0.000	0.000	13.50	8.700	0.966	-0.426	0.000	0.000	13.50	8.700
11	0.969	-0.418	0.000	0.000	5.300	2.700	0.977	-0.417	0.000	0.000	5.300	2.700
12	0.993	-0.436	0.000	0.000	9.200	2.400	0.983	-0.428	0.000	0.000	9.200	2.400
13	1.000	-0.451	0.000	40.50	20.70	8.700	0.980	-0.436	0.000	0.000	20.70	8.700
14	0.945	-0.464	0.000	0.000	22.40	7.500	1.000	-0.482	0.000	34.80	22.40	7.500
Suma			424.5	237.3	390.0	122.3			424.3	235.8	389.0	122.3
Total power loss												
Active [MW]	35.532						Actiea [MW]	35.343				
Reactive [Mvar]	115.07						Reactive [Mvar]	113.59				

3.2. Continuous power flow in voltage stability analysis

This section presents the voltage stability analysis before and after a contingency. In addition, it is analyzed the response of the system after installing the synchronous static compensation.

Figure 5 presents the voltage stability analysis in bus 11 of the EPS. It may be seen the behavior of the bus in three scenarios: i) normal operation (yellow curve), ii) disconnection of lines L2 and L4 (blue curve) and iii) voltage stability analysis when reactive compensation is incorporated through a STATCOM (red curve). Figure 5 presents the behavior of bus 11 in normal operating conditions with $\lambda_{max} = 3.7$ (approximately). When the load increase occurs with $\lambda_{max} = 3.2$, the stability margin is reduced. This occurs because the EPS is stressed and its maximum power transfer capacity is reduced, as shown in points 2-4 of Figure 5. The yellow and blue metrics represent the PV curve in conditions before and after the contingency without synchronous static compensation. An additional detail shown by Figure 5 is that the capacity of keeping the system stable decreases when the contingency occurs. When STATCOM is used, the voltage level increases and it is able to transmit slightly more power, as can be seen in points 4-6 of Figure 5. Therefore, the load factor level does not vary significantly when synchronous compensation is used, however, the profile improves. Points 1, 3, 5 of Figure 5 represent the optimal operating levels of the system where it can be seen more clearly that the power transmission capacity increases if the system has STATCOM to provide reactive power in specific operating conditions.

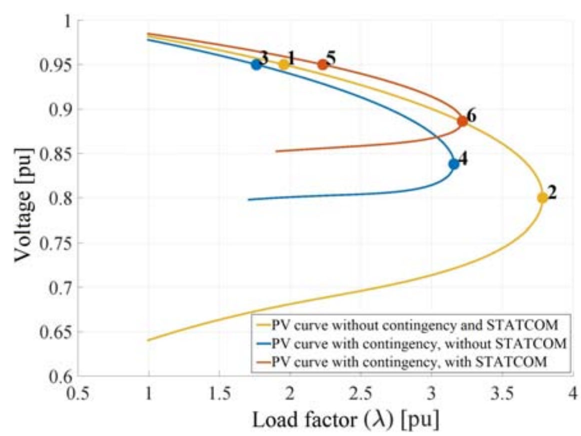

Figure 5. Voltage level as a function of the normal operating parameter, N – 1 contingency using reactive compensation

The Available Transmission Capacity (ATC) is calculated in Table 7. This analysis is carried out considering the worst contingency that may occur in the system; for this case, the worst contingency is when the line 2–4 is disconnected, TPlo represents the power demanded, i.e., the power required by the system for its normal operation. Pl are the losses present in the entire EPS, TTC is the maximum power value that may be present in the system, ETC represents the actual power in the EPS and TMR is the available power margin in which the electric system should remain before a voltage collapse occurs. Finally, it is proven that the STATCOM is capable of adjusting the voltage magnitudes in the buses of the EPS. A particular detail is that the STATCOM does not modify the active power values of the electric system. Based on the above, it may be inferred that the STATCOM adjusts the voltage levels injecting reactive power in the buses and maintains stable the voltage parameters under normal operating conditions, and increases the voltage in case of a fault so that the system remains stable.

Table 7. Available transfer capacity in the $N-1$ contingency

Bus N.°	Units	W/O STATCOM	With STATCOM
λ maximum	p.u	3.15760	3.21820
TPlo	MW	259.300	259.300
Pl	MW	15.2020	15.1810
TTC	MW	307.302	308.156
ETC	MW	259.300	259.300
TMR	MW	15.3651	15.4078
ATC	MW	32.6367	33.4477

The voltage stability analysis is performed with the metrics of Figure 6 considering different scenarios. The continuous power flow in initial conditions is computed with Figures 6(a, b and c), i.e., without contingencies and without the installation of synchronous static compensators. The voltage stability when a contingency is applied in lines L2 - L4 is analyzed in Figures 6(d, e and f). For the analysis mentioned it is proven the behavior of the PV curve for different values of λ. The PV curves shown in Figure 6 illustrate the magnitudes of the variables in the PQ buses. In the reference and generation buses, the voltage level is constant. From Figures 6(a-b) and 6(d-f) it may be inferred that as λ increases, the transmission capacity (resulting λ) decreases, and this occurs because the capacity of the electric transmission system operates inversely to the load, i.e., as the load increases the maximum electric power transfer capacity decreases. When a fault occurs (Figures 6(d-f) and the load factor increases, the voltage levels drop drastically putting the system in critical operating conditions, potentially leading it to experience a voltage collapse. An additional detail is that through the voltage stability analysis it is verified that, when a disconnection or fault occurs in the system, the voltage in all its PQ buses is reduced, mainly because they are load buses, but voltage drops are not significant in the generation buses.

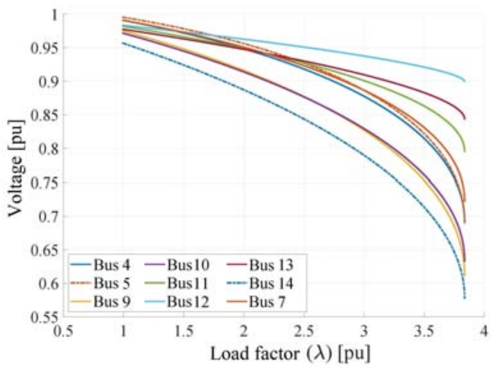

(a) Voltage with load factor ($\lambda = 1$)

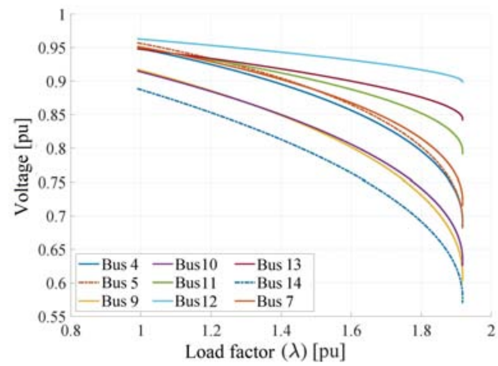

(b) Voltage with load factor ($\lambda = 2$)

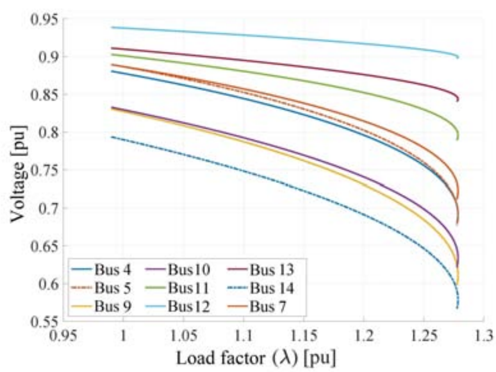

(c) Voltage with load factor ($\lambda = 3$)

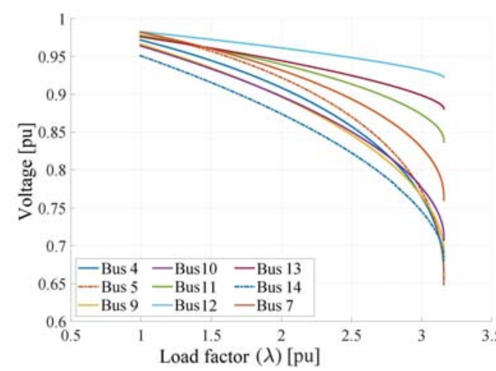

(d) Voltage with load factor ($\lambda = 1$)

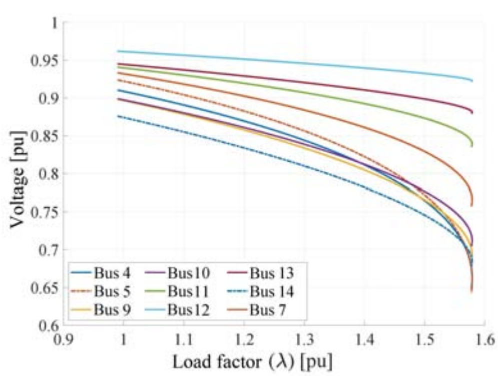

(e) Voltage with load factor ($\lambda = 2$)

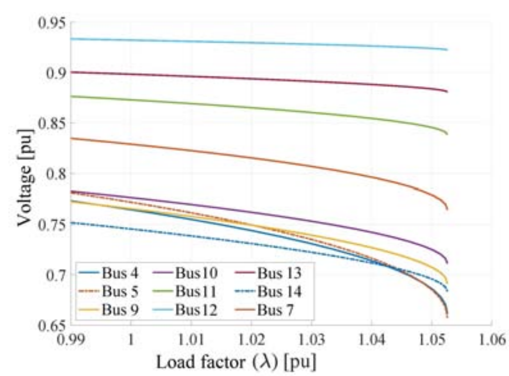

(f) Voltage with load factor ($\lambda = 3$)

Figure 6. PV curves with Continuous Power Flow (CPF) analysis. Figures a, b and c correspond to a CPF without STATCOM and without contingencies, and Figures d, e and f include a CPF without STSTCOM and a contingency produced by the opening of the 2-4 line

Figures 7 and 8 and Table 8 display the metrics for analyzing voltage stability and angular behavior in the buses considered; the voltage variable is analyzed with Figure 7; the angular variation analysis corresponds to Figure 8 together with Table 8. The PV curve that enables analyzing the voltage stability when line L2-L4 is disconnected is identified in Figure 7; this is considered the worst contingency of the electric system. In addition, it is seen the load factor variation reducing the stable operation margin of the electric system in the PQ buses when the load factor increases to $\lambda = 1.3$ pu. The voltage drop is seen in Figure 8. When a fault occurs, the voltage stability margin decreases, and this may be seen in Figure 7(b).

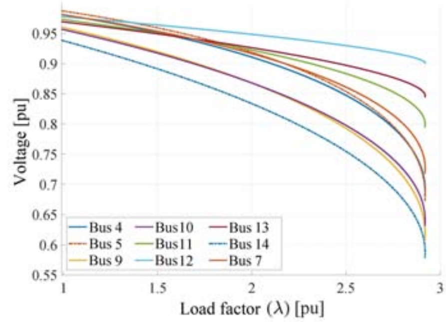

(a) Curva PV en condiciones normales

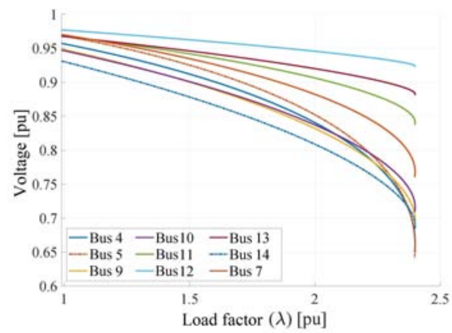

(b) Curva PV en contingencia $N-1$

Figure 7. PV curves in normal conditions and temporary opening of line 2-4, $\lambda = 1.3$, $t = 1$ s, $t = 1$ s

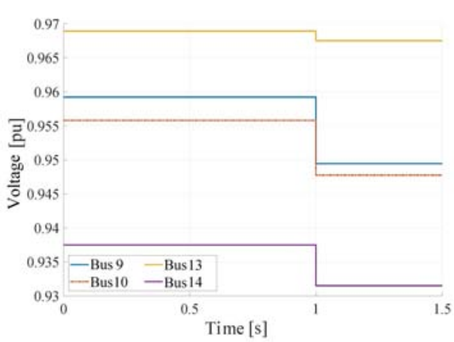

(a) Voltage profile

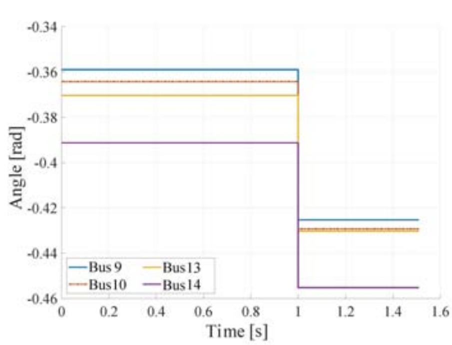

(b) Angle profile

Figure 8. Time domain curve in $N-1$ contingency in line 2-4

Table 8. Magnitudes of voltage and angle

Bus N.°	Normal conditions		Opening of line 2-4	
	Voltage	Angle	Voltage	Angle
01	1.060	0.000	1.060	0.000
02	1.045	-0.124	1.045	-0.115
03	1.010	-0.309	1.010	-0.346
04	0.980	-0.240	0.958	-0.310
05	0.985	-0.204	0.969	-0.252
06	1.000	-0.346	1.000	-0.405
07	0.981	-0.316	0.970	0.385
08	1.000	-0.317	1.000	-0.385
09	0.959	-0.358	0.949	-0.425
10	0.956	-0.364	0.948	-0.429
11	0.973	-0.358	0.969	-0.420
12	0.977	-0.368	0.977	-0.428
13	0.969	-0.370	0.968	-0.430
14	0.938	-0.391	0.932	-0.455

Figure 8(a) enables performing a wide analysis, because it shows an evaluation of the behavior of the buses in time domain when there is a 30% increment in the load, and the disconnection occurs in 1 second; the behavior of all buses is similar, therefore, Figure 8(a) will only present the buses in which there are significant variations due to the contingency generated. Therefore, when there is an unscheduled opening of any element of the electric system, mainly lines, this contingency affects all PQ buses since the supply of reactive power from the generation nodes to the loads is cut.

Figure 8(b) presents the behavior of the angle in time domain. The angular level varies according to the power flow and the initial conditions considered for the calculation; Figure 8(a) represents the angular variation in the PQ buses where there is a larger angular variability; it may be observed that the larger angular variation occurs in buses 9, 10, 13 and 14, where there is a drastic change in the voltage levels, as may be seen in Table 8. Consequently, it is concluded that the disconnection of an element of the system or a fault modify the system operating parameters and affect the maximum and minimum voltage operating limits.

Another very important aspect revealed by Table 8 is a summary of the voltage level variations and angular variation in each of the buses in time domain. Table 8 shows the voltage variations in all the buses; no changes are observed in the PV buses, but in the PQ buses the voltage varies due to the line disconnection. This occurs because the system power flow changes, due to the drastic topology change and the redirection of the power flow due to the opening of line $2-4$; an important point is that under operating conditions of 30% overload in the EPS, the voltage level in bus 14 is below 0.95 p.u.; a critical point of analysis is when the line is disconnected at bus 14 and its voltage magnitude is below 0.93 p.u.; i.e., the disconnection or fault in the system is affected by the connection to bus 14; a way to stabilize the parameters at such bus is through synchronous static compensation, which demonstrates that a candidate location to place the STATCOM is bus 14.

Table 8 enables analyzing the behavior of all system buses. The angular variation is different in all PQ buses and, unlike the voltage level, when an angular analysis is performed there is a variation in the PV buses; the only bus that remains under the same operating levels, both in voltage and angle, is the Slack bus, because when the power flow varies, the angle also varies. Consequently, Figure 8 shows the angular variation and Table 8 the voltage and angular variation in all system buses.

Figure 9 illustrates the voltage stability when a type II PSS controller is used, which implies that the possibility of analysis varies according to the PSS input signal (angular speed, voltage and power); when a speed controller is used, it is fundamental to assign various parameters for its full operation, namely, maximum and minimum voltage, stability gain. Figure 9 has a gain of 100 and it is seen that the generator controller starts to operate after line 2-4 is disconnected to maintain system stability. This type of control is known as primary voltage control, where the important issue is to stabilize voltage levels after the EPS experiences any contingency.

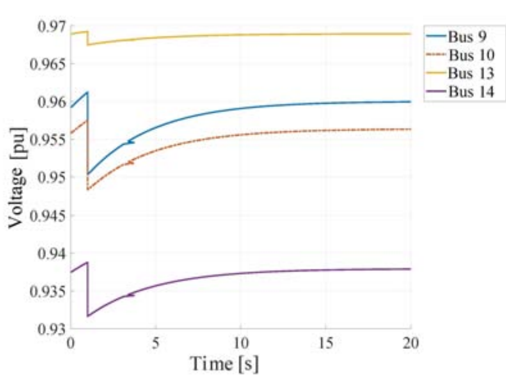

Figure 9. Voltage as a function of time in $N-1$ Contingency with the opening of line 2-4 with PSS voltage regulation

4. Conclusions

It has been possible to verify the reliability of the data obtained from the PSAT Toolbox and the performance, to provide results of voltage stability analysis and angular variation. Consequently, it is a reliable tool to perform detailed voltage stability analyses, considering the installation of STATCOM and PSS. The use of STATCOM FACTS devices has demonstrated to be an effective method to reduce the stress of the electric transmission network, and thus be able to maximize the power flow exchange from generation units to the different consumption points. In addition, the present research evidences that there are alternatives such as the PSS controllers to adjust the voltage in buses before deciding to install STATCOM, which has a higher cost.

On the other hand, the main contribution of this paper is considering a load factor that leads the EPS to operate in congestion conditions. Such congestion produces marginal operating costs, which raise the electric power transportation costs. In addition, contingencies are considered to be able to evaluate and select the most critical node (lowest voltage level), and thus be able to determine the location of reactive compensation. Therefore, this paper guarantees the optimal dimensioning of the STATCOM, to minimize power losses.

There is a big difference between the use of a FACTS compensator and the use of a PSS controller in the generator. FACTS is a device that improves stability of the voltage at the bus where it is located, and modifies voltage levels in most of the buses of the EPS seeking to maintain them at 1 pu. On the other hand, a PSS voltage control enables stabilizing the voltage levels in the generation buses through a control additional to the AVR. The gain is one of the fundamental variables to model PSS in the PSAT. The PSS gain is directly proportional to the voltage magnitude increase in the desired bus.

Therefore, PSS only actuates when there is a voltage drop in the buses of the generation units, thus maintaining a stable voltage in adjacent buses through electromechanical control of generation units. In addition, the paper proposes a methodology to guarantee voltage stability in the buses of the EPS using a STATCOM and a PSS controller, considering scenarios of $N-1$ contingency and load increase in the system. Finally, continuous power flows have been a fundamental tool to foresee the maximum voltage stability margin in an EPS.

References

[1] V. S. Rao and R. S. Rao, "Optimal Placement of STATCOM using Two Stage Algorithm for Enhancing Power System Static Security," *Energy Procedia*, vol. 117, pp. 575–582, 2017. [Online]. Available: http://dx.doi.org/10.1016/j.egypro.2017.05.151

[2] O. Samuelsson, S. Lindahl, P. Kundur, J. Paserba, V. Vittal, and T. T. Force, "Definition and Classification of Power System Stability," *Ieee Transactions on Power Delivery*, vol. 21, no. 1, pp. 446–447, 2006. [Online]. Available: https://doi.org/10.1109/TPWRS.2005.861952

[3] R. K. Varma and R. Salehi, "SSR Mitigation with a New Control of PV Solar Farm as STATCOM (PV-STATCOM)," *IEEE Transactions on Sustainable Energy*, vol. 8, no. 4, pp. 1473–1483, 2017. [Online]. Available: https://doi.org/10.1109/TSTE.2017.2691279

[4] A. K. Dwivedi and S. Vadhera, "Reactive Power Sustainability and Voltage Stability with Different FACTS Devices Using PSAT," in *2019 6th International Conference on Signal Processing and Integrated Networks, SPIN 2019*. IEEE, 2019, pp. 248–253. [Online]. Available: https://doi.org/10.1109/SPIN.2019.8711587

[5] B. Hernández, C. A. Cañizares, J. M. Ramírez, B. Hu, and M. Liu, "Secondary and tertiary voltage regulation controls based on regional optimal power flows," *20th Power Systems Computation Conference, PSCC 2018*, pp. 1–7, 2018. [Online]. Available: https://doi.org/10.23919/PSCC.2018.8442443

[6] J. Kumar and N. Kumar, "Determination and allocation of optimal size of TCSC and STATCOM for obstruction alleviation in power system," in *2018 2nd IEEE International Conference on Power Electronics, Intelligent Control and Energy Systems (ICPEICES)*, 2018, pp. 65–72. [Online]. Available: https://doi.org/10.1109/ICPEICES.2018.8897336

[7] L. Chun, J. Qirong, X. Xiaorong, and W. Zhonghong, "Rule-based control for statcom to increase power system stability," in *POWERCON '98. 1998 International Conference on Power System Technology. Proceedings (Cat. No.98EX151)*, vol. 1, 1998, pp. 372–376 vol.1. [Online]. Available: https://doi.org/10.1109/ICPST.1998.728989

[8] P. M. Chavan and G. P. Chavan, "Interfacing of hybrid power system to grid using STATCOM amp; power quality improvement," in *2017 International Conference on Information, Communication, Instrumentation and Control (ICICIC)*, 2017, pp. 1–5. [Online]. Available: https://doi.org/10.1109/ICOMICON.2017.8279079

[9] N. Mithulananthan, C. A. Cañizares, J. Reeve, and G. J. Rogers, "Comparison of PSS, SVC, and STATCOM controllers for damping power system oscillations," *IEEE Transactions on Power Systems*, vol. 18, no. 2, pp. 786–792, 2003. [Online]. Available: https://doi.org/10.1109/TPWRS.2003.811181

[10] C. Cañizares, T. Fernandes, E. Geraldi, L. Gerin-Lajoie, M. Gibbard, I. Hiskens Tf Past Chair, J. Kersulis, R. Kuiava, L. Lima, F. Demarco, N. Martins, B. C. Pal, A. Piardi, R. Ramos Tf Chair, J. Dos Santos, D. Silva, A. K. Singh, B. Tamimi, and D. Vowles, "Benchmark Models for the Analysis and Control of Small-Signal Oscillatory Dynamics in Power Systems," *IEEE Transactions on Power Systems*, vol. 32, no. 1, pp. 715–722, 2017. [Online]. Available: https://doi.org/10.1109/TPWRS.2016.2561263

[11] R. K. Varma and H. Maleki, "PV Solar System Control as STATCOM (PV-STATCOM) for Power Oscillation Damping," *IEEE Transactions on Sustainable Energy*, vol. 10, no. 4, pp. 1793–1803, 2019. [Online]. Available: https://doi.org/10.1109/TSTE.2018.2871074

[12] C. C. A. Gomes-Exposito, A. Conejo, "Electric Energy Systems Analysis and Operation," *Engineering - Technology*, p. 748, 2018. [Online]. Available: https://doi.org/10.1201/9781315192246

[13] M. Ahmadinia and R. Ghazi, "Coordinated Control of STATCOM and ULTC to Reduce Capacity of STATCOM," *26th Iranian Conference on Electrical Engineering, ICEE 2018*, pp. 1062–1066, 2018. [Online]. Available: https://doi.org/10.1109/ICEE.2018.8472712

[14] Y. T. Jeon, G. Farivar, C. D. Townsend, J. H. Park, and J. Pou, "Capacitor Voltage Shaper for Cascaded H-Bridge StatCom," *2018 IEEE 4th Southern Power Electronics Conference, SPEC 2018*, 2019. [Online]. Available: https://doi.org/10.1109/SPEC.2018.8635915

[15] A. S. Tamboli and H. T. Jadhav, "Hybrid STATCOM for Reactive Power Compensation," *Proceedings of the 2018 International Conference on Current Trends towards Converging Technologies, ICCTCT 2018*, pp. 1–5, 2018. [Online]. Available: https://doi.org/10.1109/ICCTCT.2018.8550889

[16] C. Xing, X. Xi, S. Li, and X. He, "Analysis on the Control Strategy and Response Characteristics of Large Capacity STATCOM Device in DC Converter Station," *2018 International Conference on Power System Technology, POWERCON 2018 - Proceedings*, no. 201804270001168, pp. 2873–2879, 2019. [Online]. Available: https://doi.org/10.1109/POWERCON.2018.8602013

[17] M. R. Wara and A. H. Rahim, "Supercapacitor E-STATCOM for power system performance enhancement," *1st International Conference on Robotics, Electrical and Signal Processing Techniques, ICREST 2019*, pp. 69–73, 2019. [Online]. Available: https://doi.org/10.1109/ICREST.2019.8644388

[18] J. Chen, P. Wang, Y. Hu, H. Shao, G. Li, X. Wang, and J. Qin, "Analysis of negative influence of harmonic circulation between parallel STATCOMs and suppression method," *PEDG 2019 - 2019 IEEE 10th International Symposium on Power Electronics for Distributed Generation Systems*, pp. 751–755, 2019. [Online]. Available: https://doi.org/10.1109/PEDG.2019.8807514

[19] H. A. Hassan, Z. H. Osman, and A. E.-A. Lasheen, "Sizing of STATCOM to Enhance Voltage Stability of Power Systems for Normal and Contingency Cases," *Smart Grid and Renewable Energy*, vol. 05, no. 01, pp. 8–18, 2014. [Online]. Available: https://doi.org/10.4236/sgre.2014.51002

[20] S. Isik, H. Nath, M. Alharbi, and S. Bhattacharya, "Negative Sequence Component Elimination with M-STATCOM for Versatile FACTS," *IECON Proceedings (Industrial Electronics Conference)*, vol. 2019-October, pp. 7069–7073, 2019. [Online]. Available: https://doi.org/10.1109/IECON.2019.8927805

[21] A. Raju, E. P. Cheriyan, and R. Ramchand, "Nearly Constant Switching Frequency Hysteresis Current Controller for Multilevel Inverter based STATCOM," *IEEE Region 10 Annual International Conference, Proceedings/TENCON*, vol. 2019-October, pp. 176–180, 2019. [Online]. Available: https://doi.org/10.1109/TENCON.2019.8929458

[22] V. Jain and N. Kumar, "Designing of Supplementary Controller for STATCOM for Damping of Oscillations in Power System," *Journal of The Institution of Engineers (India): Series B*, vol. 99, no. 5, pp. 419–429, 2018. [Online]. Available: https://doi.org/10.1007/s40031-018-0330-z

[23] G. G. Farivar, H. Dehghani Tafti, C. D. Townsend, and J. Pou, "Low Capacitance StatCom Capacitor Lifetime and Current Stress Analysis," *2019 9th International Conference on Power and Energy Systems, ICPES 2019*, no. 5, pp. 0–4, 2019. [Online]. Available: https://doi.org/10.1109/ICPES47639.2019.9105361

[24] A. M. Vural and K. C. Bayindir, "Optimization of parameter set for STATCOM control system," *2010 IEEE PES Transmission and Distribution Conference and Exposition: Smart Solutions for a Changing World*, pp. 1–6, 2010. [Online]. Available: https://doi.org/10.1109/TDC.2010.5484230

[25] A. B. Nassif and D. Fedaku, "A reactive power compensation scheme using distribution STATCOMs to manage voltage in rural distribution systems," *2020 IEEE Electric Power and Energy Conference, EPEC 2020*, vol. 3, pp. 1–5, 2020. [Online]. Available: https://doi.org/10.1109/EPEC48502.2020.9320005

[26] L. Sun, H. Zhang, Y. Cao, C. Li, Q. Guo, and Y. Zhu, "Design of micro dynamic simulation system for power system with wind power and VSC-HVDC," *2020 IEEE 4th Conference on Energy Internet and Energy System Integration: Connecting the Grids Towards a Low-Carbon High-Efficiency Energy System, EI2 2020*, no. 51627811, pp. 1355–1360, 2020. [Online]. Available: https://doi.org/10.1109/EI250167.2020.9347174

[27] S. Gurung, F. Jurado, S. Naetiladdanon, and A. Sangswang, "Comparative analysis of probabilistic and deterministic approach to tune the power system stabilizers using the directional bat algorithm to improve system small-signal stability," *Electric Power Systems Research*, vol. 181, no. June 2019, p. 106176, 2020. [Online]. Available: https://doi.org/10.1016/j.epsr.2019.106176

[28] W. Peres, I. C. Silva Júnior, and J. A. Passos Filho, "Gradient based hybrid metaheuristics for robust tuning of power system stabilizers," *International Journal of Electrical Power and Energy Systems*, vol. 95, pp. 47–72, 2018. [Online]. Available: http://dx.doi.org/10.1016/j.ijepes.2017.08.014

[29] H. Verdejo, V. Pino, W. Kliemann, C. Becker, and J. Delpiano, "Implementation of particle swarm optimization (PSO) algorithm for tuning of power system stabilizers in multimachine electric power systems," *Energies*, vol. 13, no. 8, 2020. [Online]. Available: https://doi.org/10.3390/en13082093

[30] T. Guesmi, A. Farah, H. H. Abdallah, and A. Ouali, "Robust design of multimachine power system stabilizers based on improved non-dominated sorting genetic algorithms," *Electrical Engineering*, vol. 100, no. 3, pp. 1351–1363, 2018. [Online]. Available: https://doi.org/10.1007/s00202-017-0589-0

[31] S. Orlando, "A Study of STATCOM on Stability and Efficiency in IEEE 14-bus," Master's thesis, 2016. [Online]. Available: https://bit.ly/3qT2McR

Scientific Paper / Artículo Científico

UNIVERSIDAD POLITÉCNICA SALESIANA ECUADOR
INGENIUS
Revista de Ciencia y Tecnología
https://doi.org/10.17163/ings.n29.2023.02
pISSN: 1390-650X / eISSN: 1390-860X

Analysis of regenerative braking efficiency in an electric vehicle through experimental tests

Análisis de la eficiencia del freno regenerativo en un vehículo eléctrico mediante pruebas experimentales

Juan Valladolid[1,2], Mauricio Calle[1], Angel Guiracocha[1,*]

Received: 14-04-2021, Received after review: 13-12-2021, Accepted: 24-01-2022, Published: 01-01-2023

Abstract

This paper presents a regenerative braking analysis of efficiency in real driving conditions and different road geographies. Factors affecting or benefiting energy recovery were identified, these are: the weight of the vehicle, torque, speed, inclination of road, and braking time; however, the sport and Eco driving modes were not considered because the same driving pace was chosen for the different routes. These results are intended to collaborate with real energy regeneration data and help investigators, academics, and automotive engineering, improving this system's efficiency. In the driving process, the state of charge (SOC), speed, torques, and road geography effect the efficiency of regenerative braking, as driving a vehicle on a road with irregular geography exposes it to aggressive physical factors, which considerably reduces its energy autonomy. The main aspects of recovery and regenerative braking efficiency were determined through quantitative data analysis, resulting in experimental surfaces and curves, which present the performance of current and deceleration during vehicle braking. Thus, it is shown that the energy recovery during braking is 78% considering the low autonomy of the electric vehicle.

Keywords: Brake pedal, electric vehicle, energy recovery, regenerative braking

Resumen

Este artículo presenta un análisis de la eficiencia del frenado regenerativo en condiciones reales de conducción y en diferentes geografías de carretera. Se identificaron los factores que afectan o benefician a la recuperación de energía, estos son: el peso del vehículo, el par, la velocidad, la inclinación de la calzada y el tiempo de frenado; no obstante, no se consideraron los modos de conducción deportivo y Eco debido a que se optó por un mismo ritmo de conducción en las diferentes rutas. Estos resultados pretenden colaborar con datos reales de regeneración de energía y ayudar a los investigadores, académicos e ingenieros de automoción, a mejorar la eficiencia de este sistema. En el proceso de conducción, el estado de carga (SOC), la velocidad, torques y la geografía de la carretera afectan a la eficiencia del frenado regenerativo, ya que conducir un vehículo por una carretera con una geografía irregular lo expone a factores físicos agresivos, lo que reduce considerablemente su autonomía energética. Se determinaron los principales aspectos de la recuperación y la eficiencia del frenado regenerativo mediante análisis de datos cuantitativos, dando como resultado superficies y curvas experimentales, que presentan el rendimiento de la corriente y la desaceleración durante el frenado del vehículo. Así, se demuestra que la eficiencia de recuperación de energía durante el frenado es de un 78 % considerando la baja autonomía del vehículo eléctrico.

Palabras clave: pedal de freno, vehículo eléctrico, recuperación de energía, freno regenerativo

[1,*]Grupo de Investigación de Ingeniería del Transporte (GIIT), Carrera de Ingeniería Mecánica Automotriz, Universidad Politécnica Salesiana, Cuenca, Ecuador.
[2]Grupo De Investigación En Control, Electrónica De Potencia y Gestión De La Innovación Tecnológica (CEPIT) Departamento de Ingeniería Electrónica, Pontificia Universidad Javeriana, Bogotá, Colombia.
Corresponding author ✉: aguiracochac@est.ups.edu.ec

Suggested citation: Valladolid, J.; Calle, M. and Guiracocha, A. "Analysis of regenerative braking efficiency in an electric vehicle through experimental tests," *Ingenius, Revista de Ciencia y Tecnología*, N.° 29, pp. 24-31, 2023, doi: https://doi.org/10.17163/ings.n29.2023.02.

1. Introduction

Electric vehicles (EV) are very attractive and have generated interest in science, academia, and public and private transportation systems at a global scale [1–3]. In this type of vehicle, the search to improve the system efficiency is essential; since it presents an important alternative of transport compared to conventional vehicles with internal combustion engines. Nevertheless, these vehicles have a limited driving autonomy, and this factor continues to be the main obstacle for the mass acceptance and use of EVs [1], [2], [4], [5].

As opposed to conventional vehicles and in addition to reducing air contamination, EVs can recover part of the energy lost in the braking process thanks to the regenerative braking system, thus improving the driving autonomy of electric vehicles [6].

Irregular road geography exposes vehicles to factors at an altitude on the mountain road. In relation to energy consumption, these factors require more performance of batteries in electric vehicles, especially on mountain routes. In this sense, the slope of the road is a factor that cannot be neglected in the design of strategies for optimizing regenerative braking [7, 8].

In a regenerative braking system, energy is transferred to generators under a strategy of integrated control, which consists of generating an estimate for the deceleration by the driver and distributing the needed braking force between the regenerative system and mechanical braking [9].

In literature, the authors consider that the deceleration rate and the mass of the vehicle have significant effects in the regenerative braking threshold at low speeds, as it is considered that a regenerative brake at low speed is effective in the city, because more action is needed in the braking system for the heavy traffic, thus increasing the power and autonomy of the vehicle [4], [10]. Strategies of regenerative braking that take into account the slope of the road, are considered by other authors to be more efficient. A noticeable improvement can be seen in the recovery of energy [8].

In other literature they show through simulations that the lowest energy consumption happens with a complete braking system in series, due to better use of the braking torque and therefore less energy is consumed [11]. The potential energy consumption is lower in road travel than in a driving in the urban area, where there is little brake actuation affecting the energy recovery in the EV vehicle [12].

In the present work, experiments are carried out on the EV on established routes to determine the efficiency of the regenerative brake, its performance and its influence on the autonomy of the EV. Behavior maps were used to analyze the influence of factors such as braking time, initial braking speed, and road grade on energy recovery. The maximum and minimum recovery energy percent per range will be estimated numerically.

The paper is organized as follows: In Section 2, the mathematic support of regenerative braking is presented, describing with detail subsystems such as the dynamical model; in Section 3, the energy efficiency and performance on regenerative braking are presented. Finally, the conclusions of this study are presented in Section 4.

2. Materials and methods

2.1. Traditional SOC estimation

This method mainly uses the battery discharge current as input and integrates the current discharge over a period to calculate the SOC state [13], the equation (1) is as follows.

$$SOC = SOC_o - \frac{1}{C_n}\int_{t_0}^{t} i(t)dt \tag{1}$$

Where C_n corresponds to the nominal capacity of the battery, $i(t)$ corresponds to the current flowing in and out the battery and t is the time. On the other hand, this other calculation method requires a variation to Equation (11), multiplying a coulombic efficiency factor (μi) to the integral, which is represented between the discharge capacity and load capacity, represented in the equation (2).

$$SOC = SOC_o - \frac{\mu i}{C_n}\int_{t_0}^{t} i(t)dt \tag{2}$$

2.2. SOC status

The charge is expressed in the equation (3).

$$Chatge = (Current) \times (time)\ [Ah] \tag{3}$$

The SOC is the charge level of a battery expressed as a percentage, the equation (4) is.

$$SOC(\%) = \frac{Charge\ [Ah]\ (100\%)}{Total\ battery\ capacity\ [Ah]} \tag{4}$$

2.3. Evaluation of the recovery of the energy

Evaluating energy recovery in regenerative braking mainly includes the energy recovery capacity during braking and the energy recovery rate during braking [14]. Where, E_m is the energy recovery presented in Equation (5).

$$E_m = \int_{t_0}^{t} U_b(t) i_b(t) dt \tag{5}$$

Where, $U_b(t)$ is the voltage at the motor controller while recovering braking energy, $i_b(t)$ is the motor controller current present in the braking action, and t time of braking of the motor.

2.4. Measure of energy recuperation of braking

Braking energy recovery measurement, n_b is the relation between energy E_m and the total consumed energy. E_b is the energy lost calculated as a function of the velocity of the start and end of braking, as shown in the equation (6).

$$E_b = \frac{1}{2} m \left(V_f^2 + V_0^2 \right) \tag{6}$$

Where, m is the mass of the vehicle, V_0 is the initial velocity of braking, V_f is the final velocity of braking, and n_b is the efficiency shown in the equation (7).

$$\frac{E_m}{E_b} = \frac{\int_{t_0}^{t} U_b(t) i_b(t) dt}{\frac{1}{2} m \left(V_f^2 + V_0^2 \right)} (100\ \%) \tag{7}$$

Equation (7) allows to determine efficiency values of regenerative braking mainly using the initial velocity used by the vehicle to start the braking process.

3. Results and discussion

The results in real driving experimental tests are represented in this section with the use of Matlab and Electric Mobility Laboratory (Emolab) software to determine the parameters that affect the efficiency of regenerative braking [15].

3.1. Variables involved in energy recovery process

Emolab was used in order to obtain the variables of the vehicle. Emolab registers in real time are: the battery current, the vehicle speed, the motor torque, and the SOC [14]. Matlab was used to model this data in the braking process in real driving. Performance surfaces were generated, where the relationship between torque and speed is observed. In this manner, when values for torque and speed are changed, the system outputs a new value of energy recuperation charge, which influences the autonomy of the vehicle.

The geography of route one presents a higher slope which translates into a higher power demand of the vehicle in order to overcome pronounced inclinations. The principal variable of route two was a high degree of traffic which caused braking more often. Meanwhile, route three presented a combination of these two factors, considerable slopes and traffic of the routes one and two.

Figures 1, 2 and 3 show that variables such as velocity and motor torque play key roles in energy recovery during the braking process; since during the braking action the system generates current by means of an AC motor, which is represented with negative values. In this case, energy regeneration in the vehicle is affected by the speed, and therefore the braking torque applied to the vehicle.

Figure 1 indicates a greater recovery of energy, because the geography of route one has different types of roads and inclinations. These characteristics also allow higher vehicle speeds, and consequently, longer times of brake application, resulting in greater motor torques and greater currents.

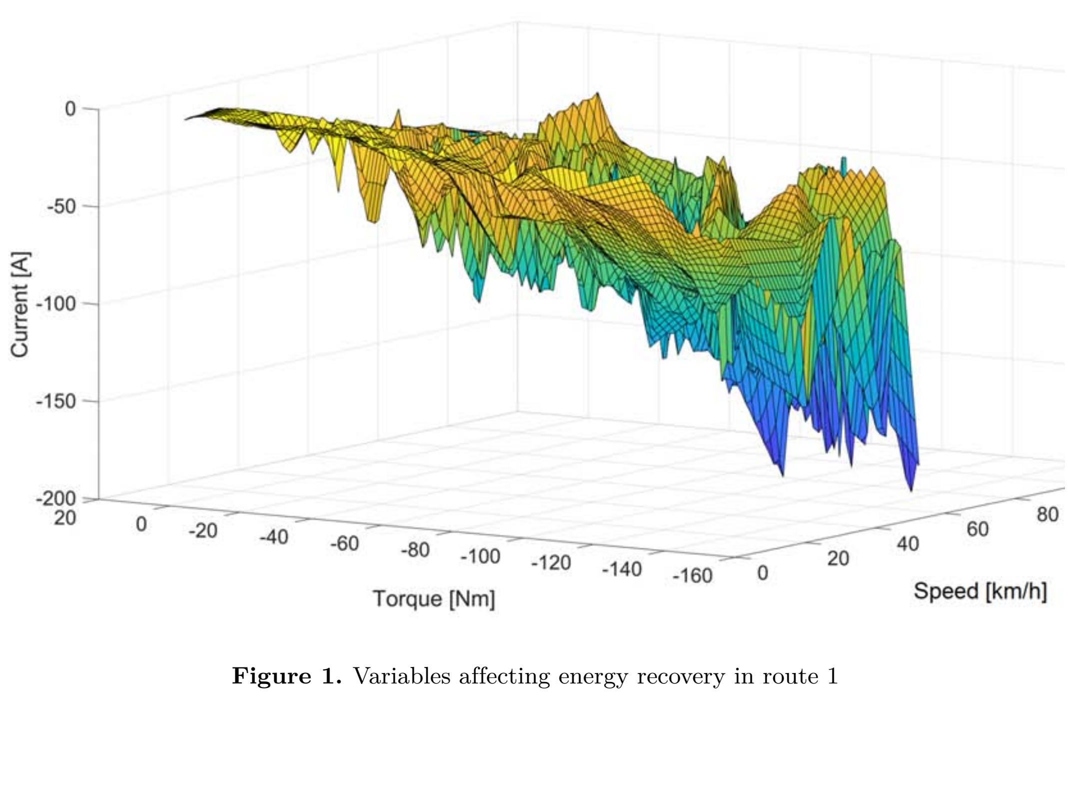

Figure 1. Variables affecting energy recovery in route 1

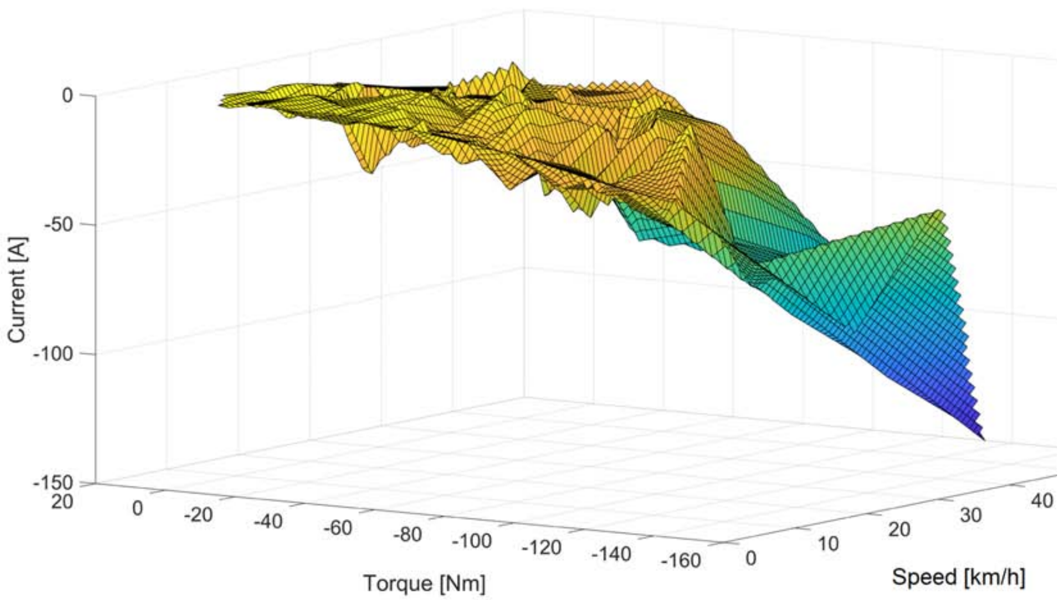

Figure 2. Variables affecting energy recovery in route 2

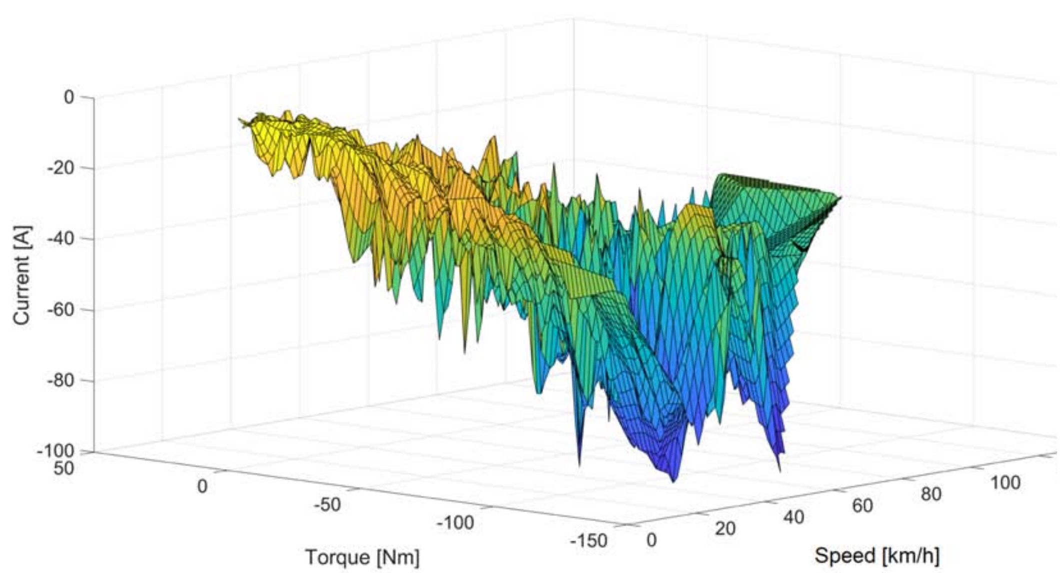

Figure 3. Variables affecting energy recovery in route 3

3.2. SOC behavior

This section presents the SOC performance of the three types of routes, taking into account the type of road and the elapsed driving time during each route.

In Figure 4, the different SOC performances can be seen for each route and different length. Route one has a greater inclination across all its trajectory, and it tends to discharge at a rate of 47%. The battery of the vehicle was discharged aggressively because of the high-power demand it endures in overcoming the considerable route geography. After a certain point, the geography of this route changes to an only downward slope. While descending, the vehicle recovers 9% of its charge because of the longer brake times and high speeds up to 70km/h, as can be seen in Figure 1 and the resulting elevated motor torques. Route two only has a discharge process. Figure 2 shows low velocities in the range of 30 - 60 km/h. The added amount of traffic results in a more extended brake usage. The battery discharge tendency is almost lineal during its entire trajectory since there is a variation of 5% of the charge from its initial value. Route three presents a more abrupt discharge process compared to route two. The road type is rural; it has more pronounced slopes, a moderate power demand on the vehicle, less traffic and speeds in the range of 50 - 100 km/h as shown in Figure 3. In this route, there is low brake usage. Figure 4 shows certain points along this route where the discharge is significant, reaching a 32% level until its end point.

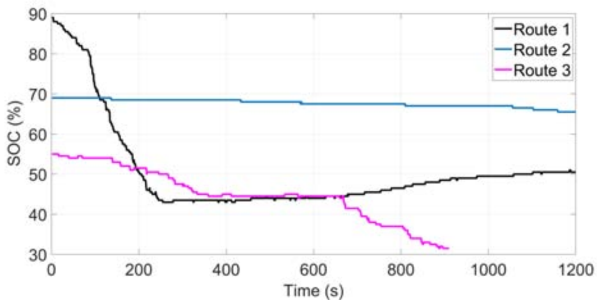

Figure 4. Behavior of SOC with respect to recovered energy

3.3. Deceleration Performance

In this section, the deceleration comportment during braking is explained.

Figure 5 presents a 1600 seconds sample of deceleration values during the regenerative braking process, rendered with MATLAB. Results tend to vary with factors such as inclination, driving style, and the road geography, provoking a heterogeneous deceleration. The deceleration values observed favor energy recuperation, because the state of the charge increases when the brake is used, thus the vehicle recovers energy to continue moving forward.

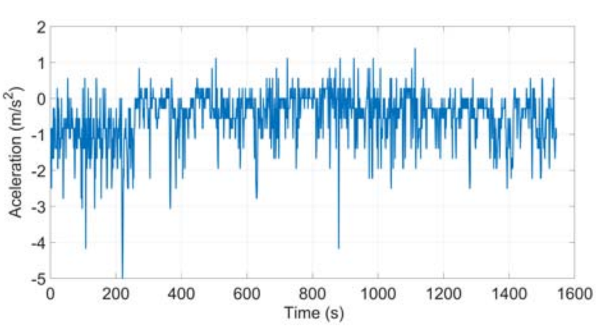

Figure 5. Deceleration regarding regenerative system application

3.4. Efficiency of regenerative braking

The efficiency of regenerative braking was calculated using Eq (7). The most significant values are the initial and final braking velocities, the recovered charge, and the weight of the vehicle.

Figure 6 shows the relationship between the initial braking velocity and the efficiency for each route. These values are sampled at specific points to better observe the behavior of the efficiency. In routes 1, 2 and 3 in the driving process the different types of road geography, slopes, and initial braking speeds have an impact on the variability of the obtained efficiencies as shown in Figure 6. In route 1, the result of the average efficiency in the specific sample is 23%, and due to the type of geography of the road it is necessary the use of more power by the vehicle, so the brake pedal is not used with high frequency The brake efficiency at its peak reaches up to 76%, this is due to a longer braking time and the final speed reached.

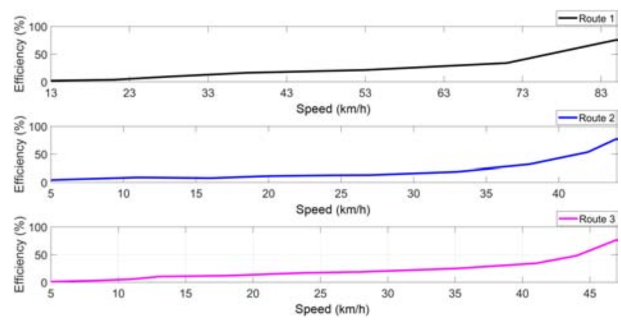

Figure 6. Efficiency of regenerative braking at specific speeds

According to Figure 6, values vary in route 2 because it presented a high vehicular flow, low driving speeds and high use of the brake pedal, hence there is greater efficiency of the regenerative system. In turn, this efficiency tends to stabilize, resulting in greater energy recovery, since it has optimal load values reaching an average of 24% and its highest efficiency reaching a value of 78%.

The efficiency of route three shows values that vary with the road geography, average braking velocities, and the amount of traffic. The average efficiency was of 22% with a max value of 77%. In routes 1 and 3, the efficiency decreases significantly and does not stabilize, resulting in low values close to zero.

The regenerative braking efficiency of each route is shown to be dependent on the loss and recovered energy of the vehicle. The road geographies, the initial braking velocity, and the time of brake application, summarized in Table 1, are the main variables that affect the values of loss and recovered energy. The values presented in Table 2 are greatly improved by the extended use of the brake pedal even though its velocity values are lower due to high traffic. There is lower consumption of energy because there is no need for a high-power demand. Energy recovery and high efficiencies are favored by a lack of aggressive changes in the route. Table 3 shows that the vehicle has high energy loss compared to Table 2, due to the geography of the road, high power when overcoming slopes and moderate use of the brake pedal, resulting in lower energy recovery compared to Table 2.

Table 1. Minimum, average and maximum efficiency of the regenerative braking system in route 1

Speed (km/h)	**Recovery braking energy** E_m **(J)**	**Braking energy loss** E_b **(J)**	**Efficiency (%)**
9	3053,4	409 842,90	0,07
44	6930,63	19 275,92	36
74	44472	55 819,86	79

Table 2. Minimum, average and maximum efficiency of the regenerative braking system in route 2

Speed (km/h)	**Recovery braking energy** E_m **(J)**	**Braking energy loss** E_b **(J)**	**Efficiency (%)**
9	111,72	8261,11	1,35
22	6346,1	17210,64	37
44	8030,25	10 326,39	78

Table 3. Minimum, average and maximum efficiency of the regenerative braking system on route 2

Speed (km/h)	**Recovery braking energy** E_m **(J)**	**Braking energy loss** E_b **(J)**	**Efficiency (%)**
9	346,96	56 9041,39	0,06
22	1748,81	4818,98	36
52	34224	44 059,25	77

4. Conclusions

In this paper, an analysis of the regenerative braking system was carried out through real driving experiments, where variables such as: current, torque and speed influence with respect to the vehicle's energy recovery were considered in order to determine the efficiency and performance of the regenerative braking system . The difference between the routes is the type of road geography, the vehicle driving time and brake pedal actuation, so in route 1 it was possible to observe a greater energy recovery due to the factors mentioned.

With respect to the state of charge (SOC) of the vehicle, it was observed that the different powers used for each route and the type of geography are significant variables for a greater energy loss. The results obtained indicate that the use of the vehicle in route 2 has a progressive energy loss, which at a certain time tends to stabilize because of the greater use of the brake due to the high vehicular flow; while in route 1 a small energy recovery was achieved due to the use of the brake due to the descent of steep slopes.

In the efficiency of the regenerative braking system, the results demonstrate that the type of road geography, initial braking speeds, brake usage, and vehicle mass are variables that greatly influence the efficiency of this system. Additionally, driving in route 2 is more efficient than in routes 1 and 3, as it has lower energy loss values and high energy recovery values.

References

[1] P. Spichartz and C. Sourkounis, "Influence of the braking system and the type of regenerative braking request on the energy consumption of electric vehicles," in *2020 Fifteenth International Conference on Ecological Vehicles and Renewable Energies (EVER)*, 2020, pp. 1–7. [Online]. Available: https://doi.org/10.1109/EVER48776.2020.9242939

[2] J. D. Valladolid, D. Patiño, G. Gruosso, C. A. Correa-Flórez, J. Vuelvas, and F. Espinoza, "A novel energy-efficiency optimization approach based on driving patterns styles and experimental tests for electric vehicles," *Electronics*, vol. 10, no. 10, 2021. [Online]. Available: https://doi.org/10.3390/electronics10101199

[3] T. A. Skouras, P. K. Gkonis, C. N. Ilias, P. T. Trakadas, E. G. Tsampasis, and T. V. Zahariadis, "Electrical vehicles: Current state of the art, future challenges, and perspectives," *Clean Technologies*, vol. 2, no. 1, pp. 1–16, 2020. [Online]. Available: https://doi.org/10.3390/cleantechnol2010001

[4] S. Heydari, P. Fajri, N. Lotfi, and B. Falahati, "Influencing factors in low speed regenerative braking performance of electric vehicles," in *2018 IEEE Transportation Electrification Conference and Expo (ITEC)*, 2018, pp. 494–499. [Online]. Available: https://doi.org/10.1109/ITEC.2018.8450260

[5] V. Totev and V. Gueorgiev, "Efficiency of regenerative braking in electric vehicles," in *2020 21st International Symposium on Electrical Apparatus & Technologies (SIELA)*, 2020, pp. 1–4. [Online]. Available: https://doi.org/10.1109/SIELA49118.2020.9167153

[6] Y. Wang and Y. Su, "A research for brake strategy based on fuzzy control in pure electric vehicles,"

in *2015 4th International Conference on Computer Science and Network Technology (ICCSNT)*, vol. 01, 2015, pp. 689–693. [Online]. Available: https://doi.org/10.1109/ICCSNT.2015.7490838

[7] M. Gupta, "Evaluation of regenerative braking and its functionality in electric vehicles," in *2020 International Conference for Emerging Technology (INCET)*, 2020, pp. 1–6. [Online]. Available: https://doi.org/10.1109/INCET49848.2020.9154047

[8] J. Bian and B. Qiu, "Effect of road gradient on regenerative braking energy in a pure electric vehicle," *Proceedings of the Institution of Mechanical Engineers, Part D: Journal of Automobile Engineering*, vol. 232, no. 13, pp. 1736–1746, 2018. [Online]. Available: https://doi.org/10.1177/0954407017735020

[9] J. Zhang, X. Lu, J. Xue, and B. Li, "Regenerative braking system for series hybrid electric city bus," *World Electric Vehicle Journal*, vol. 2, no. 4, pp. 363–369, 2008. [Online]. Available: https://doi.org/10.3390/wevj2040363

[10] T. T. Duong, D. V. Do, and T. T. Nguyen, "Research on braking force distribution in regenerative braking system apply to conventional vehicle," in *2018 4th International Conference on Green Technology and Sustainable Development (GTSD)*, 2018, pp. 48–52. [Online]. Available: https://doi.org/10.1109/GTSD.2018.8595456

[11] Y. Zhang, C. Zhao, and Z. Li, "Electric vehicle regenerative braking system simulation based on Kalman filter," in *2020 Chinese Automation Congress (CAC)*, 2020, pp. 2936–2941. [Online]. Available: https://doi.org/10.1109/CAC51589.2020.9327759

[12] P. Spichartz and C. Sourkounis, "Influence of the braking system and the type of regenerative braking request on the energy consumption of electric vehicles," in *2020 Fifteenth International Conference on Ecological Vehicles and Renewable Energies (EVER)*, 2020, pp. 1–7. [Online]. Available: https://doi.org/10.1109/EVER48776.2020.9242939

[13] N. Watrin, B. Blunier, and A. Miraoui, "Review of adaptive systems for lithium batteries state-of-charge and state-of-health estimation," in *2012 IEEE Transportation Electrification Conference and Expo (ITEC)*, 2012, pp. 1–6. [Online]. Available: https://doi.org/10.1109/ITEC.2012.6243437

[14] Y. Sun, Y. Wang, R. Zhu, R. Geng, J. Zhang, D. Fan, and H. Wang, "Study on the control strategy of regenerative braking for the hybrid electric vehicle under typical braking condition," *IOP Conference Series: Materials Science and Engineering*, vol. 452, p. 032092, 2018. [Online]. Available: https://doi.org/10.1088/1757-899x/452/3/032092

[15] EmoLab. (2022) Grupo de Investigación en Ingeniería de Transporte. Universidad Politécnica Salesiana. [Online]. Available: https://bit.ly/3Sju2gP

Scientific Paper / Artículo Científico

UNIVERSIDAD POLITÉCNICA SALESIANA ECUADOR
INGENIUS
Revista de Ciencia y Tecnología
https://doi.org/10.17163/ings.n29.2023.03
pISSN: 1390-650X / eISSN: 1390-860X

Calculation of abrasive wear speed in straight and helical gears with evolving profile, using a Matlab GUI

Cálculo de la velocidad de desgaste abrasivo en engranajes de dientes rectos y helicoidales con perfil evolvente, utilizando una GUI de Matlab

José Miguel Mena Chavarrea[1,*], José Antonio Granizo[2], Eduardo Segundo Hernández Dávila[2], Mario Efraín Audelo Guevara[3]

Received: 11-02-2022, Received after review: 20-10-2022, Accepted: 09-11-2022, Published: 01-01-2023

Abstract

The present investigation originated under the objective of designing a software with Matlab that allows calculating the abrasive wear rate of spur and helical gears with involute profile. Where, the unstudied generalities about the design of gears have generated negative consequences in functionality and have generated catastrophic failures that have produced unexpected stoppages of mechanical processes, for which understanding their causes becomes essential. Considering, for the calculation of the abrasive wear of the tribological pairs in heavy machinery, it will depend on the degree of grinding or size of the abrasive particles, the hardness, the material of the base gear, the lubrication regime and the geometric conditions that determine the nature of tribological contact, as well as the time and speed of use of heavy machinery. Initially, the theoretical environment that makes up the study based on the main components such as: gears, lubrication, steel, heat treatments and finally Matlab is established.

Resumen

La presente investigación se originó con el objetivo de diseñar un *software* con Matlab que permita calcular la velocidad de desgaste abrasivo de engranajes rectos y helicoidales de perfil evolvente. Donde, las generalidades no estudiadas sobre el diseño de engranajes han generado consecuencias negativas en la funcionalidad y fallas catastróficas que han producido paras imprevistas de procesos mecánicos, por lo cual entender las causas de los mismos se vuelve fundamental. El cálculo del desgaste abrasivo de los pares tribológicos en maquinaria pesada dependerá del grado de trituración o tamaño de las partículas abrasivas, la dureza, el material del engrane base, el régimen de lubricación y las condiciones geométricas que determinen la naturaleza del contacto tribológico, así como el tiempo y velocidad de uso de la maquinaria pesada. Inicialmente, se establece el entorno teórico que compone el estudio basado en los principales componentes como engranajes, lubricación, el acero, los tratamientos térmicos y, al final, Matlab.

[1,*]Tecnología Superior en Electromecánica, Instituto Superior Tecnológico Cotopaxi, Ecuador.
Corresponding author ✉: jmmenac@istx.edu.ec
[2]Grupo de investigación Ciencia del Mantenimiento, Escuela Superior Politécnica de Chimborazo, Ecuador.
[3]Ingeniería Automotriz, Facultad de Mecánica, Escuela Superior Politécnica de Chimborazo, Ecuador.

Suggested citation: Mena Chavarrea, J. M.; Granizo, J. A.; Hernández Dávila, E. S. and Audelo Guevara, M.E. "Calculation of abrasive wear speed in straight and helical gears with evolving profile, using a Matlab GUI," *Ingenius, Revista de Ciencia y Tecnología*, N.° 29, pp. 32-45, 2023, doi: https://doi.org/10.17163/ings.n29.2023.03.

Next, the mathematical models of Archard and Kraglesky were established, which were adapted to the circumstances of the problem and based on this information, a software capable of calculating the rate of abrasive wear was formulated using a graphical Matlab user tool; We proceed to execute the manual calculation with the determined variables taking experimental data obtained from previous investigations and that comply with the variables determined for the execution of the mathematical process, given that the results generated through the software can be tabulated, graphed in Excel and verified. with manual mathematical development. Looking for the comparison, differentiation and trend of the behavior of the wear rate, varying the parameters involved in the process using the two mathematical models proposed.

Keywords: Gears, Abrasive, Wear, GUI, Matlab, Wear rate

Seguidamente, se establecieron los modelos matemáticos de Archard y Kraglesky que fueron adaptadas a las circunstancias del problema y en función de esta información formular un *software* capaz de calcular la velocidad de desgaste abrasivo mediante una herramienta gráfica de usuario de Matlab. Se procede a ejecutar el cálculo manual con las variables determinadas, tomando datos experimentales obtenidos de investigaciones previas y que cumplan con las variables determinadas para la ejecución del proceso matemático, dado que los resultados generados a través del software puedan ser tabulados, graficados en Excel y comprobados con el desarrollo matemático manual. Buscando la comparación, diferenciación y tendencia del comportamiento de la velocidad de desgaste, variando los parámetros involucrados en el proceso utilizando los dos modelos matemáticos planteados.

Palabras clave: engranajes, desgaste, abrasión, GUI, Matlab, velocidad de desgaste

1. Introduction

At present, gears have a great importance as transmission elements in mechanical systems, since they are mechanical pieces found in any industry as main machine elements that generate force and movement. The degree of wear of the gears depends on the work carried out by the equipment, the grain size and composition of the abrasive, the working power, the design load, and the efficiency and reliability of the process. These are major factors that should be considered to determine the costs of executing corrective and preventive maintenance.

Detecting failures in a timely and efficient manner constitutes one of the most important challenges associated to predictive maintenance. Unexpected failures may affect the integrity and reliability of equipment through unscheduled stops, reduction of useful life, high costs of corrective maintenance and low quality of products [1].

Studying the wear process of gears is increasingly important, because they are the mechanical transmission elements mostly used in different fields and under different working conditions, from tiny gears used in watches or as part of any machine independent of its size.

In industry, wear is one of the most frequent problems that appear in systems that contain gears, regardless of the work they perform. The abrasives are elements that are found in the environment and are typical of heavy machinery elements, such as walking equipment, agricultural machinery, construction machinery, mining industry machinery, etc. The abrasive particles are a determining factor to significantly reduce the useful life of the gear.

The most important aspects to be considered in the design of the gear teeth profile, are related to the load capacity, transmission error, pressure angle, wear and failure analysis [2].

The lack of information and review of the analysis criteria for designers and for people responsible for machinery maintenance, whose main object of design are spur and helical gears with involute profile which are continuously subject to abrasive elements, has generated that mechanisms get damaged with the consequent unnecessary stops, and even the no implementation of laboratory research processes that are extremely delayed and costly. The abrasive found in the environment directly affects the performance of mechanical systems, since it generates catastrophic failures that produce losses to the industrial processes of companies. The parameters that have influence are grain size, abrasive hardness, quantity of abrasive and work carried out, which reduce the performance of industrial processes and the production.

Hence, it is necessary to study them to try to address the problems that may appear in gears. Thus, the wear, the abrasive and the failures are related aspects that will be the case study here, to determine the wear rate depending on the abrasive and on the gear material. The substitution of 90% of the gearwheels is due to an efficiency loss as a consequence of the wear of the teeth; in general, the following mechanisms are used to tackle this phenomenon:

- Optimization of geometrical parameters according to the design.
- Improvement of the quality of the teeth surface and of the assembly of the parts
- Appropriate selection of the material and of the parameters of the thermal treatment.
- Appropriate selection of the lubricant and optimization of the lubrication process [3].

Hence, it follows that there will be a greater chance that a hydrodynamic film is formed in the zone of the gear pole, and if lubricant is present in the tribological process, this zone will have less wear in the toothed transmissions.

The present work proposes the usage of a graphical user interface to carry out the theoretical calculation of the wear rate in gears with involute profiles, to provide the designer with tools that enable to predict the behavior of the tribological system, evaluate the validity of its design theories and generate timely maintenance plans.

Taking into account the approximations made, it is considered the process based on a scheme that uses vibrations to update a wear prediction model. First, it is developed a dynamic model of a system of spur gears to generate realistic vibrations, which enables a quantitative study of the effects of wear on the surface of the gear teeth. The sliding speed and the contact forces of the model are used in combination with the known Archard wear model, to calculate the wear depth at each contact point in the mesh. Since the wear coefficient in the model is not constant during the wear process (and in any case it is difficult to estimate initially), the vibrations measured are compared with the vibrations generated by the model, to update the coefficient when it is detected a deviation in the predictions [4].

1.1. Tribology

The term tribology comes from the Greek terms «tribos» and «logos», which mean friction and study, respectively. Hence, this term is used to designate the science that studies the surfaces with relative movements between each other.

For this reason, terminologies such as friction, wear of the different surfaces and the presence or absence of lubricant between the parts in contact, are essential to obtain machines and processes with less energy loss, avoid long stop times that limit the efficiency of the production activity, improve the life cycle of machines and, above all, have available a reliable tool to generate good repair and maintenance practices [5].

1.2. Mechanical contact

Figure 1 shows the apparent area corresponding to the entire surface of the parts in contact, and the real area, which considers that all surfaces have rough points that cause that the contact occurs only at the points of coincidence of the corresponding crests of each of the surfaces involved in the movement [6].

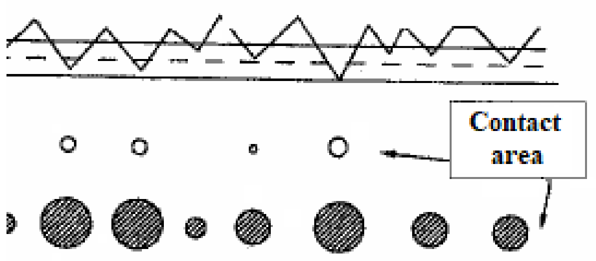

Figure 1. Apparent contact area [6]

1.3. Wear

Is the process of destruction and detachment of material that occurs between the surfaces of the bodies, revealed as accumulation of deformations and variation of the initial dimensions of the corresponding object [7].

1.3.1. Abrasive wear

This wear mechanism is characterized by the presence of hard particles that interact with surfaces that slip against each other. As it is determined in Figure 2, under this system it is important to characterize that this type of wear causes imperfections and microbreaks, due to the action of extremely hard and small particles, compared to the base surface [8].

Figure 2. Wear due to abrasion [8]

Figure 3 indicates that, according to its nature, abrasive wear may be classified in two types, namely, of two or three bodies. The abrasive wear of two bodies is generally used as a machining mechanism, to obtain specific results in a particular surface, whereas the abrasive wear of three bodies is due to the contamination of the interface between two surfaces.

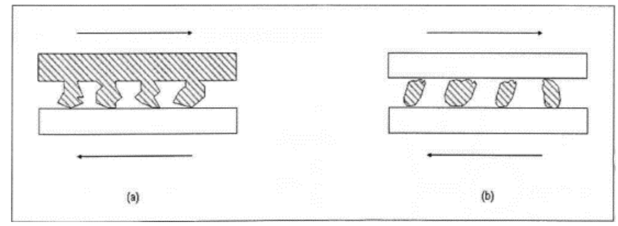

Figure 3. Abrasive wear a) 2 bodies y b) 3 bodies [9]

1.4. Failure analysis in gears

The American Society for Metals has created four subgroups to classify failure modes, namely, wear, surface fatigue, deformations and crack. Table 1 shows the percentages of the common failures, which take into account the parameters that are established due to the abrasive wear of gears, analyzing each failure mode and consequence.

1.5. Matlab

Matlab is a very powerful and adaptable tool for mathematical calculation, with graphical capabilities that improve the data presentation experience. As a consequence of these features, it has become popular as an option for making calculations in science and research [10].

Table 1. Causes of failures in gears [11]

Cause of failure	Percentage %
Related to the service (Total)	74,7
Inappropriate assembly	21,2
Inadequate lubrication	11
Continuous overloads	25
Impact loads	13,9
Bearing failures	0,7
Foreign material	1,4
Equipment operation errors	0,3
Abusive operation	1,2
Related to Thermal Treatment (Total)	16,2
Excessive hardness of the gear body	0,5
Insufficient hardness of the gear body	2
Excessive depth of the coating	1,8
Insufficient depth of the coating	4,8
Inappropriate hardening	5,9
Inappropriate tempering	1
Related to The Design (Total)	6,9
Inappropriate design	2,8
Inappropriate material selection	1,6
Inappropriate treatment specification	2,5
Related to Manufacturing (Total)	1,4
Burns due to grinding	0,7
Marks of tools Marks or notches	0,7
Related to the Material (Total)	0,8
Forging defects	0,1
Steel defects	0,5
Steel mixture or composition errors	0,2

One of the most important Matlab features in the interactive user interface, which enables a fast numerical calculation and an efficient data processing. In addition, it has various functionalities, such as the presentation of graphical tools that enable that user's experience is simpler, pleasant and efficient enough to fulfill all needs, without requiring many software [12].

1.5.1. GUI Tool

A Graphical User Interface (GUI) is a software package within Matlab, that uses a set of preprogrammed images and action boxes to synthetize the need of the user for managing data and tasks.

Figure 4 determines the main functionality of this tool, which is to facilitate the communication between the user and the software, so that it is not necessary to consider programming processes and the language required to modify and create the graphical interface [13].

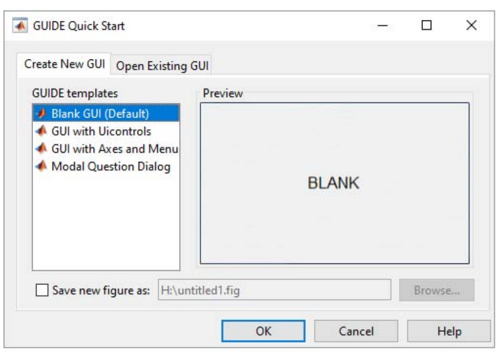

Figure 4. Interface "GuideMatlab"

2. Materials and methods

The aim is to obtain the necessary theoretical-conceptual tools, evaluate the formulas presented in the selected bibliography and adapt them to the circumstances of the problem, and appropriately arrange, interpret and use the data obtained.

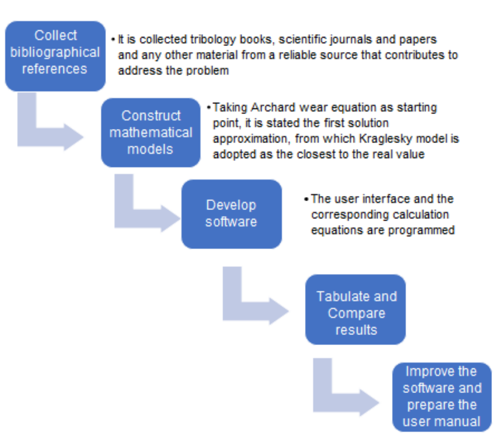

Figure 5. Flow diagram of the methodology [14]

For this purpose, dependent and independent variables are defined and, based on this information, it is formulated a software capable of calculating the abrasive wear rate of gearwheels through a Matlab graphical user tool. The flow diagram of the methodology is illustrated in Figure 5.

2.1. Techniques for collecting information

The techniques used during this research work will focus on two main aspects, as described below.

2.1.1. Documentary-Bibliographic

It has been collected books, certified journals, scientific papers and user manuals about the abrasive wear of gearwheels and the use of Matlab. This information will be the base to discretize and adapt the calculation equations and the mathematical models to the problem stated, and will guide the process of constructing the Matlab graphical tool.

2.1.2. Theoretical and experimental

Once the software has been developed, the validity of equations will be evaluated based on the results obtained, the similarity between the mathematical models and the trends of the wear rate. A value of error will be obtained when the parameters of the equations are varied, and it will be intended to adjust the constants of the equations to get an appropriate fit to real values, that enable to obtain the initial approximations of the design. The data obtained in the real approximations carried out in the operation tests is taken into account [4].

2.2. Fundamentals of gears

Since gears are key for this work, it should be remarked the importance of the fundamental tools and knowledge to determine the geometry, type, materials and manufacturing processes of the most common gears, to correctly do the calculation and dimensioning process.

2.2.1. Terminology

To introduce the analysis and study of gears, it is necessary to define the terminology shown in Figure 6. The INEN 1143 standard about gears states that:

- **Teeth of a gear** Elements that carry out the thrust work, transmit power and have a characteristic profile according to their arrangement.
- **Outer circumference.** Part of the circumference of the gear shape that limits it on its outmost part.
- **Inner circumference.** Part that limits the base of the teeth, also known as root.

- **Primitive circumference.** Circumference formed due to the rotation of the contact points of the gear teeth involved in the process.
- **Addendum.** Perpendicular distance between the pitch circle or primitive circumference and the highest point of the teeth.
- **Helix angle.** Angle formed by the base of the cylinder and the teeth of a helical or screw gear with involute profile.
- **Gear or crown.** It refers to the largest gear in an arrangement of gears.
- **Pinion.** Smallest gear, typically in charge of transmitting movement.
- **Eccentricity.** Is the offset between the common centers of two circumferences.
- **Face width.** Length of the tooth at the plane located at 90 degrees of the gear formation plane.
- **Gear ratio.** Ratio between the greatest and the smallest number of teeth in meshed gears.
- **Module.** Ratio between the pitch circle diameter (in millimeters) and the number of teeth.
- **Pitch.** Distance between a point of a tooth and the same point in the adjacent tooth. It is an indication of the tooth size.
- **Reference line.** Imaginary flat surface tangent to the pitch surfaces of two gears; it is basically the plane that limits the contact points between the gears.
- **Pressure angle.** Angle between the pressure line of the tooth and the flat tangent to the pitch surface. It is basically the direction normal to a gear tooth [15].

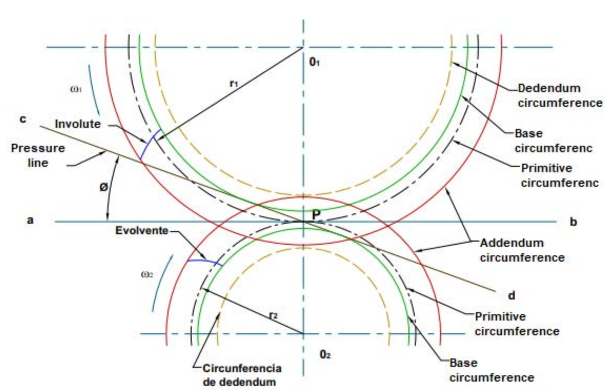

Figure 6. Elements that constitute a gear [16]

2.3. Spur gear

Consider that the total force in a gear is given by Equation (1).

$$F = 19100 \times \frac{power}{Do \times n} \tag{1}$$

Where: F is the total contact force in gears, P is the power of the machine given in KW, Do is the outer diameter and n is the angular speed. The outer diameter is given by Equation (2).

$$Do = z \times m + 2mcos(tan^{-1}(z)) \tag{2}$$

Where z is the number of teeth and m is the gear module.

For the spur gear, the normal force applied in the process is given by Equation (3).

$$Pnormal = Fsen\theta \tag{3}$$

With θ equal to the pressure angle of the gear [17].

2.4. Helical gear

The normal force applied for helical gears is given by Equation (4).

$$Pnormal = F \times sen\phi t \times cos\psi \tag{4}$$

Where: ψ is the helix angle and ϕt is the angle of transverse pressure.

To incorporate time as a variable in the base Archard formula of Equation (5), it is necessary to relate the distance traveled in the abrasion process with the linear displacement of the gear surface when the machine is in operation.

$$L = \frac{Dp \times n \times t}{2} \tag{5}$$

Where n is the angular speed, t is the time variable, and Dp the primitive diameter of the gear, given by Equation (6):

$$Dp = z \times m \tag{6}$$

Where Do is the outer diameter, and z is the number of teeth in the gear.

2.5. Calculation of abrasive wear

According to Equation (7), the volume loss (W) in a piece is directly proportional to the probability (z) that an abrasive particle removes material when it finds a crest of the surface in its trajectory, and to the normal force (N) that acts between the sliding surfaces and the abrasive particles, and is inversely proportional to their hardness measured in the Brinell scale (HB) [18], i.e.

$$W = z \times \frac{N}{HB} \tag{7}$$

Equation (8) shows the abrasive particle that has semispherical shapes with a radius given by the radius of the contact point between the surfaces.

$$W = \frac{k}{3} \times \frac{N}{HB} \tag{8}$$

Where k is the probability of finding an abrasive particle of the contact point between the surfaces, and varies between 10^{-2} and 10^{-7} [19].

The methods of Equation (9) to calculate the wear due to abrasion in various machines elements were tested experimentally and widely by the scientific community, recognizing the nature of wear due to fatigue, and finally, Kraglesky equation will be taken as reference.

$$V = \frac{A \times K}{M} \tag{9}$$

Where (V) is the wear rate measured in [um/h], (A) is the parameter that characterizes the abrasive material, (K) is the characterization of the geometrical conditions of the contact point of the sliding surfaces and (M) depends on the properties of the material of the surface [3].

The base equation to measure the wear rate in spur and helical gears is obtained from these considerations.

- Archard Equation: Wear rate in a spur gear [3] (10).

$$V = K_{process} \frac{\frac{19100 \times power}{Do} \times sen\theta \times \frac{Dp \times n}{2}}{H} \tag{10}$$

- Archard Equation: Wear rate in a helical gear [3] (11).

$$V = K_{process} \frac{\frac{19100 \times power}{Do} \times sen\theta t \times cos\psi \times \frac{Dp \times n}{2}}{H} \tag{11}$$

- Kraglesky abrasive wear rate (12).

$$V = \frac{A \times K}{M} \tag{12}$$

The variables necessary to characterize Kraglesky equation (Equation (12)) are divided in three parameters, the term corresponding to the abrasive particle, where the mechanical properties, size and composition of the abrasive material modify its characteristics according to Equation (13) [20].

- Properties of Kragelsky abrasive particle.

$$A = \epsilon^{2/3} r^{0.5} \vartheta^{2.5} \tag{13}$$

In this same context, factor (M) of Equation (14) is related to the mechanical properties of the base material, and is directly proportional to the hardness and the stretching percentage of the material under analysis, taking the abrasive data from the values in Table 2 [20].

Table 2. Size of the types of abrasive particles

Granulometry of the soil	Particle size range (mm)
Brick	600 >
Stone	250 - 600
Gravel	75 - 250
Coarse-grained sand	0,5 - 1
Medium-grained sand	0,25 - 0,5
Fine-grained sand	0,05 - 0,25
Clay	< 0,002

- Kragelsky parameter of mechanical properties of the material (14).

$$M = \epsilon_0^t HB_1^{1.5} HB_2 \tag{14}$$

Where ϵ_0^t corresponds to the stretching percentage of the material before the crack, t is a nondimensional parameter associated to the contact between bodies, and HB represents the hardness of the materials that constitute the tribological pair of the process, measured in Brinell scale. Finally, factor (K) involves all the geometrical conditions that impact the variation of the contact between the surfaces, such as the type and size of pieces, lubrication conditions and distribution of the contact forces between the elements of the tribological pair. For this reason, Equations (15) and (16) are established for spur and helical gears, respectively [20].

- Spur gear

$$K = (m \times (z1 + z2) sin\vartheta)^{0.5} \times 0.106 \times n \tag{15}$$

- Helical gear

$$K = \left(\frac{m \times (z1 + z2) sin\vartheta}{cos\psi(1 - cos\vartheta^2 \times sin\psi^2)} \right)^{0.5} \times 0.106 \times n \quad (16)$$

Therefore, according to Kraglesky, the calculation of abrasive wear rate is summarized as follows (17) and (18).

- Kraglesky Equation: Wear rate spur gear

$$V = 576 \frac{\left(\epsilon^{2/3} r^{0.5} \vartheta^{2.5}\right)}{\varepsilon_0^t HB_1^{1.5} HB_2} (m \times (z1 + z2) sin\psi)^{0.5} \times 0.106n \quad (17)$$

- Kraglesky Equation: Wear rate helical gear

$$V = 576 \frac{\left(\epsilon^{2/3} r^{0.5} \vartheta^{2.5}\right)}{\varepsilon_0^t HB_1^{1.5} HB_2} \left(\frac{(m \times (z1 + z2) sin\psi)^{0.5}}{cos\psi(1 - cos\vartheta^2 \times sin\psi^2)} \right)^{0.5} \times 0.106n \quad (18)$$

2.6. Designation of variables for calculating the abrasive wear rate

Archard equation was used as a first approximation for calculating the abrasive wear rate in gearwheels. On the other hand, the mathematical model formulated by Kragelsky, given by Equation 3, was used to determine the result closest to the real value. Afterwards, both methods were programmed in a beta version of the software designed with the Matlab graphical tool. Then, results were generated to test the calculation application, aspect issues were improved and the software mas made as friendly as possible for the user.

At last, the final version of the application was developed and compiled to make it independent of Matlab. Then, the variables and the parameters of the equations are changed, and the data obtained is used to make plots in Excel. The final step involved preparing a user manual and presenting the results.

2.7. Declaration of variables

Based on the data required by the equations and to clearly state the names of the variables used in the programming process, this section presents.

ϑ (theta) = pressure angle
ψ (psi) = helix angle
$z1$ = number of teeth of gear 1
$z2$ = number of teeth of gear 2
m = module of the gears
P = power of the machine
$H1$ = hardness of material 1 (Brinell)
$H2$ = hardness of material 2 (Brinell)
$Karch$ = process constant, Archard equation
n = angular speed
rg = average grain size of the abrasive particle
cv = concentration in volume of the abrasive particle
$Eo1$ = stretching percentage of the material of gear
$Eo2$ = stretching percentage of the material of gear

3. Results and discussion

3.1. Results

3.1.1. App version

When entering the app (see Figure 7), it should be selected the gear type and the known parameters. The interface enables a clear view of the requirements, such as number of teeth of the gear, gear diameter, pressure angle, helix angle, gear type, power required, angular speed, among the most important factors for recording the data necessary for the calculation.

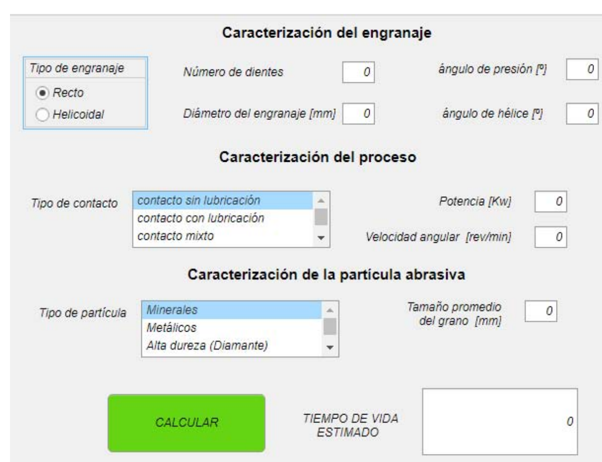

Figure 7. App for calculating the wear rate

Afterwards, the necessary inputs and outputs of the system are evaluated for each equation, as shown in Figure 8. Then, a second test version of the model was generated taking into account details that improve user's experience, such as a help button, a table for unit conversion, as well as other factors to avoid unnecessary formulation errors. In other words, it is sought to avoid repetitive data, or to minimize the data that should be entered when the values necessary can be calculated from the ones already obtained.

Figure 8. Version 2 of the App for calculating the wear rate

Based on the necessary variables and on the requirements for the correct operation of the software for calculating the abrasive wear rate of gearwheels, using the Archard and Kraglesky methods, Figure 9 shows the final interface developed so that it is user friendly and has a pleasant look.

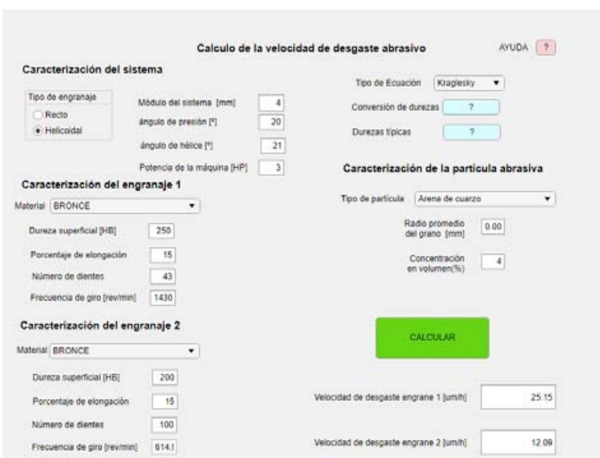

Figure 9. Versión final APP

3.1.2. Collection of final data

At this point, it is sought a comparison of the mathematical models to point out their differences, and compare the results for the cases of plots with spur and helical gears. In this manner, it is possible to see a trend in the models to assure that there are no data with significant errors, and verify the validity of the model in each case. Hence, isolated cases are limited, and it is understood when and under which conditions it is relevant to use each of the models stated.

For this purpose, two simple analyses are performed. In the first one, which is shown in Table 3, the number of teeth of one of the gears is changed, and it is intended to calculate the wear for both spur and helical gears, for each of the gearwheels involved in the process.

The hardness and the stretching percent of the base material of both wheels are kept constant at 250 HB and 18%, respectively; it is also kept constant at 1430 rpm the frequency of gearwheel one. The module of the system is set at 4, and the pressure angles at 20 and 21 degrees, respectively.

The average power of the machine to be evaluated was set at 200 HP for Archard equation. Regarding the particle characterization for Kraglesky equation, it was used quartz sand with an average grain size of 0.05 mm and 4% of concentration in volume in the surrounding medium [20].

Table 3. Wear rate with variable number of teeth [14]

Number of teeth		Spur gear				Helical gear			
		Wear speed 1		Wear speed 2		Wear speed 1		Wear speed 2	
z1	z2	Archard	Kraglesky	Archard	Kraglesky	Archard	Kraglesky	Archard	Kraglesky
43	10	17,42	15,03	73,54	64,63	18,66	16,52	78,77	71,03
43	12	17,42	15,31	61,65	54,86	18,66	16,83	66,03	60,3
43	15	17,42	15,72	49,56	45,07	18,66	17,28	53,09	49,54
43	20	17,42	16,39	37,31	35,23	18,66	18,01	39,97	38,72
43	25	17,42	17,02	29,91	29,28	18,66	18,71	32,03	32,18
43	43	17,42	19,14	18,66	19,14	18,66	21,04	18,66	21,04
43	50	17,42	19,91	14,99	17,12	18,66	21,88	16,05	18,82
43	60	17,42	20,95	12,49	15,02	18,66	23,03	13,38	16,5

The wear values for spur gears under the aforementioned variable specifications are determined in Figures 10 and 11; these values are changed to obtain the data plotted in Excel, to be able to appropriately manage the parameters of the approximations, taking into account that Kraglesky mathematical equation is the appropriate one for analyzing the closeness to the values under data variability.

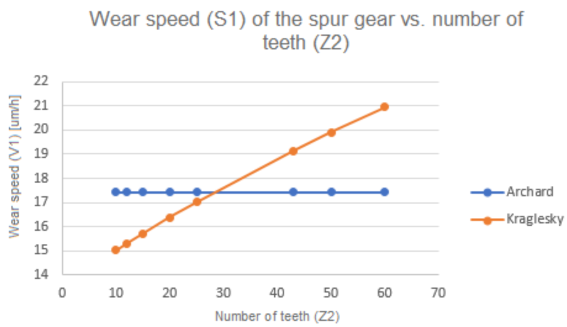

Figure 10. Wear rate 1 of spur gears with Z2

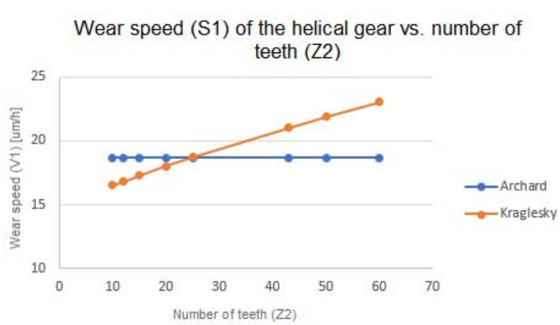

Figure 11. Wear rate 1 of helical gears with Z2

The results of both Archard and Kraglesky models are plotted in an Excel sheet for spur gears (Figure 12) and helical gears (Figure 13).

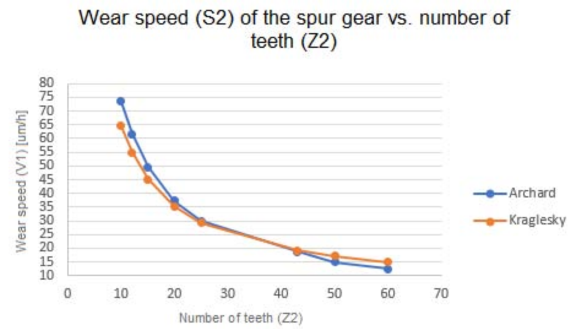

Figure 12. Wear rate 2 of spur gears with Z2

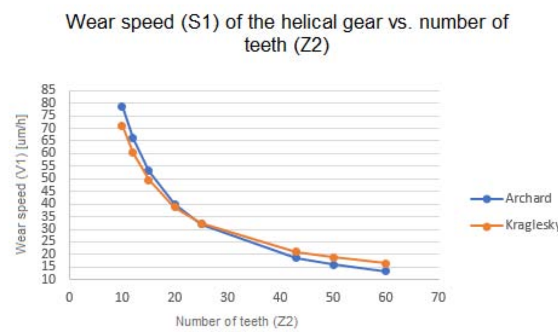

Figure 13. Wear rate 2 of helical gears with Z2

The previously stated data will be considered for the second case of analysis, with the difference that the number of teeth of the gears involved will be kept constant at 43, and the surface hardness of the second gear will be varied. Similarly, it will be calculated the wear rate for each gear, either spur or helical. In this manner, the data given by the final version of the App will be presented in detail, where another comparison is made according to the resistance HB2 (Table 4).

Table 4. Velocidad de desgaste con dientes variables [14]

Material hardness		Spur gear				Helical gear			
		Wear speed 1		Wear speed 2		Wear speed 1		Wear speed 2	
HB1	HB2	Archa	Kragle	Archa	Kragle	Archa	Kragle	Archa	Kragle
250	150	17,42	31,91	29,04	41,91	18,66	35,07	31,11	45,28
250	170	17,42	28,15	26,62	34,14	18,66	30,95	27,45	37,53
250	190	17,42	25,19	22,93	28,9	18,66	27,69	24,56	31,76
250	220	17,42	21,76	19,8	23,19	18,66	23,91	21,21	25,49
250	250	17,42	19,14	17,42	19,14	18,66	21,04	18,66	21,04
250	280	17,42	17,09	15,56	16,15	18,66	18,79	16,66	17,75
250	300	17,42	15,95	14,52	14,56	18,66	17,54	15,55	16,01
250	350	17,42	13,67	12,45	11,56	18,66	15,03	13,33	12,7

3.2. Discussion

Considering the real approximations performed, it is taken into account the scheme based on vibrations proposed in [4] for updating a wear prediction model. First, it is developed a dynamic model of a system of spur gears to generate realistic vibrations, which enables performing a quantitative study of the effects of wear on the surface of the gear teeth.

The sliding speed and the contact forces are used in combination with Archard wear model, to calculate the depth at each contact point of the mesh. The profile of the teeth of the worn-out gear is fed back in the dynamic model as a new geometrical transmission error, which represents the offset of the profile from an ideal involute curve; hence, it is zero for perfect gears.

Since the wear coefficient of the model is not constant during the wear process (and difficult to estimate initially in any case), the vibrations measured are compared with the ones generated by the model, to update the coefficient when offsets in the predictions are detected.

3.2.1. Data for the calculation

The following data obtained from a study are considered to determine the evaluation process:

Acero dulce AISI 1045

Module: 4

Pressure angle: 20

Power: 4 kW (5,3641 HP)

Hardness: 163 HB

Stretching percentage: 16

Number of teeth: pinion 19 gear 52

Frequency: 6000 rpm

Grain average: 0.05

Concentration of the volume: 1.85 [4]

Figure 14 shows the values determined in the paper under analysis, which specifies the values of the experimental model and Archard model, calculated by the authors; the data obtained from this paper is used for the comparative analysis between the experimental process and the calculations carried out by the Matlab App developed in this work.

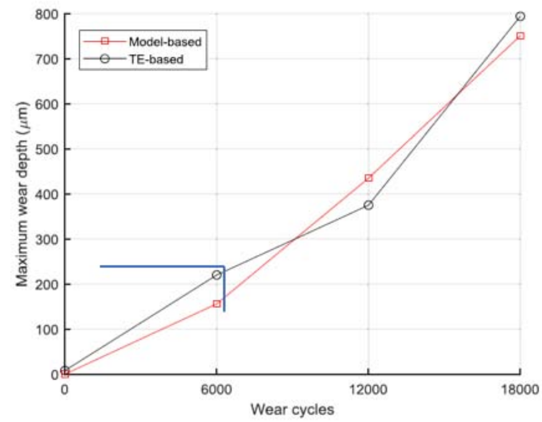

Figure 14. Results for the comparison of the maximum wear depth: experiment and model [4]

3.2.2. Evaluation of the experimental model from the paper and Kraglesky model in the Matlab App.

The error percentage is calculated in this subsection, to verify the coincidence between the data of the application from Kragelsky equation and the data of the experimental model, to plot the analysis model of the abrasive wear prediction with the use of vibrations.

A primary analysis is performed between the mathematical model (blue line) and the experimental model (orange dots). Figure 15 shows the data obtained from the calculation with Kragelsky mathematical model (gray line), used in this research work, and Archard equation (yellow line).

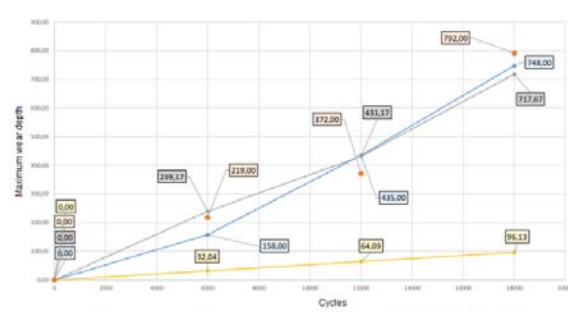

Figure 15. Calculation of proximities between the values given by the App and the experimental paper [14]

Based on the above, it will be verified if the data calculated through the Matlab application are within the permissible ranges to consider them as appropriate for comparing the two situations, namely, Kraglesky equation and the data obtained from the experiment.

The mean quadratic error is considered for the statistical calculation, since it enables to compare the difference between the estimator and what is being estimated. This function is a risk evaluator corresponding to the expected value of the quadratic loss. The difference is due to the randomness or because the estimator does not take into account the information that could produce a more precise estimation (ecuation (19)).

$$ECM = \frac{1}{n}\sum_{t=1}^{n}(Ye - Yc)^2 \tag{19}$$

The mean square error (MSE) given by Equation (19) is used to calculate the difference of the randomness process to produce a more precise estimation. The data chosen corresponds to the data that will be used to determine the expected loss.

Table 5 shows the values calculated, which reflect the effectiveness of the proximity with the data of the experiment. In particular, Krageslsky mathematical model is effective for predicting the wear index, with a 48.56 %, which indicates that the data calculated are within the range of the experimental values of wear. It is convenient to specify that the mathematical model of the paper yields an approximation of 49.06 % with respect to the experimental values.

Table 5. Data of the mean square error [14]

	Experiment vs Kragelsky (APP)	**Experiment vs model in paper**
	0,00	0,00
	406,69	3721,00
	3500,69	3969,00
	5525,44	1936,00
Total sum	9432,83	9626,00
1/n	2358,21	2406,50
Calculated value	48,56%	49,06

On the other hand, Archard equation is analyzed for the identification of the values calculated; Figure 15 depicts that the data show a significant offset, with an error close to 90 %.

It is important to remark that the analysis shows that Kragelsky equation is more effective than Archard equation, since it has data that encompasses the abrasive size and percentage; for this reason, it is feasible for determining the wear index in mechanical elements.

4. Conclusions

Archard and Kraglesky mathematical models have been selected, and it has been correctly identified the necessary variables and the usage of each of these models for calculating the abrasive wear rate. Based on the analysis with the paper under study and the analysis of the quadratic error between the experimental values and the values obtained with the equations, it was determined that Kragelsky model shows a better performance, since it yields a quadratic error of 48.56 % with respect to the experimental data, compared to a quadratic error of 49.06 % given by the mathematical model of the paper. The limitations of this research work are that the data necessary for the calculations should be obtained after the element has been designed and it is also known the construction material.

Regarding the graphical tool created using the Matlab user graphical application (GUIDE), it fulfilled the requirements to calculate the abrasive wear rate in gearwheels, needing prior knowledge of the variables that the user should enter as well as the data of the type of abrasive to be analyzed. The programming was made according to the mathematical model under study, avoiding unintentional errors, and providing options to help the user to determine the unknown variables.

The results obtained with the software were tabulated and plotted in Excel to compare their trends, as shown in the results section, concluding that the best decision for the design of a gear with specific features can be made after the data has been varied; in addition, the designer has available data that may improve the functionality of the mechanical element designed, taking into account the abrasive found in the environment.

Based on the verification of the data obtained from the app and the experiment, besides the explanation provided, it is concluded that the software developed in this research work enables to calculate the abrasive wear rate on spur and helical gearwheels with involute profile. It also establishes prediction data for decision making regarding the execution of maintenance programs, and the prevention of catastrophic failures that may harm the working area and the personnel in charge of the machinery. The contribution of the software is to become a tool to determine values that enable the mechanical designer to perform a quick evaluation of the construction of a mechanical element, based on variables that may be found in the gear construction process.

Future works

The perfect companion for the software developed is a short-term database that contains experiments with gears and different abrasives, to verify the data and similarly calibrate the constants of the processes for different working conditions under lubrication regime and controlled operation. In addition, to assess the data with statistical tools for improving the error percentage, and that the data calculated with the Matlab app are as close as possible to the data obtained when executing an experimental process.

References

[1] J. C. Vesga Ferreira, G. Granados Acuña, and J. E. Sierra Carrillo, “Optimización de una red

multiservicio sobre un canal PLC bajo MmQoS," *Ingeniería y Desarrollo. Universidad del Norte*, vol. 33, no. 2, pp. 260–280, 2015. [Online]. Available: http://dx.doi.org/10.14482/inde.33.2.6368

[2] P. N. Martínez Henao and N. A. de la Peña, "Estado del arte sobre perfiles de dientes para engranajes," *Prospectiva*, vol. 12, no. 2, pp. 29–40, 2014.

[3] A. Fernández del Rincón and P. García Fernández. (2019) Máquinas y mecanismos. [Online]. Available: https://bit.ly/3UG1X4K

[4] K. Feng, P. Borghesani, W. A. Smith, R. B. Randall, Z. Y. Chin, J. Ren, and Z. Peng, "Vibration-based updating of wear prediction for spur gears," *Wear*, vol. 426-427, pp. 1410–1415, 2019, 22nd International Conference on Wear of Materials. [Online]. Available: https://doi.org/10.1016/j.wear.2019.01.017

[5] I. D. Marinescu, W. B. Rowe, B. Dimitrov, and H. Ohmori, *Tribology of Abrasive Machining Processes*. Elsevier Inc., 2013. [Online]. Available: https://doi.org/10.1016/C2010-0-67070-2

[6] G. W. Stachowiak, *Wear - Materials, Mechanisms and Practice*. John Wiley & Sons, Ltd., 2005.

[7] Robles, *Desgaste*. Universidad Autónoma de Nuevo León, 2012. [Online]. Available: https://bit.ly/3X2BkbV

[8] L. Marciano Vázquez, "Diseño de engranajes rectos y helicoidales asistido por computadoras," Master's thesis, 2000. [Online]. Available: https://bit.ly/3X2OWno

[9] Motorex. (2019) Qué es un engranaje recto. [Online]. Available: https://bit.ly/3EbMX7S

[10] D. O. Barragán Guerrero, *Manual de interfaz gráfica de usuario en Matlab*. Escuela Superior Politécnica del Litoral, 2013. [Online]. Available: https://bit.ly/2UUgwD2

[11] D. S. Romero Lozano and J. A. Giraldo Ramos, *Análisis de falla de un engranaje de la caja de cambios de una motocicleta*. Fundación Universitaria Los Libertadores, 2018. [Online]. Available: https://bit.ly/3E9NtDk

[12] Hardwaresfera. (2020) Definición de software de sistema, de programa y de aplicación, además de la definición de software libre y software propietario. [Online]. Available: https://bit.ly/2UVU644

[13] G. Cid Espinoza, "Programación de interfaz gráfica en app designer MATLAB," 2018. [Online]. Available: https://bit.ly/3O6EXcK

[14] J. M. Mena Chavarrea, "Cálculo de la velocidad de desgaste abrasivo en engranajes de dientes rectos y helicoidales con perfil evolvente, utilizando una GUI de Matlab," 2021.

[15] INEN, "Engranajes. terminología para negranajes helicoidales cruzados 90°," 1983. [Online]. Available: https://bit.ly/3g3TeKT

[16] J. L. M. Rodríguez and J. A. Velázquez Pérez, "Cálculo de engranajes plásticos," *Ingeniería Mecánica*, vol. 10, no. 3, pp. 25–32, 2007. [Online]. Available: https://bit.ly/3UCqO9v

[17] H. W. Gamboa Mariño and D. R. Vistin Guilcapi, "Análisis tensional en transmisiones de engranajes rectos mediante el método de los elementos finitos," 2006. [Online]. Available: https://bit.ly/3UDsVtV

[18] Masterhacks. (2017) Fundamentos de engranajes. [Online]. Available: https://bit.ly/3UJtpyD

[19] Engranabreider. (2016) Engranajes. [Online]. Available: https://bit.ly/3X7SCEr

[20] I. V. Kragelsky, M. N. Dobychin, and V. S. Kombalov, *Friction and WearCalculation Methods*. Elsevier Ltd., 1982. [Online]. Available: https://doi.org/10.1016/C2013-0-03333-6

Scientific Paper / Artículo Científico

UNIVERSIDAD POLITÉCNICA SALESIANA ECUADOR
INGENIUS
Revista de Ciencia y Tecnología
https://doi.org/10.17163/ings.n29.2023.04
pISSN: 1390-650X / eISSN: 1390-860X

Study of the Energy Efficiency of an Urban E-Bike Charged with a Standalone Photovoltaic Solar Charging Station and its Compliance with the Ecuadorian Grid Code No. Arcernnr – 002/20

Estudio de Eficiencia Energética de una Bicicleta Eléctrica Urbana Cargada con una Estación de Carga Solar Fotovoltáica Autónoma y su Cumplimiento con la Regulación Ecuatoriana No. Arcernnr – 002/20

Vinicio Iñiguez-Morán[1,*], Edisson Villa-Ávila[1],
Danny Ochoa-Correa[2], Ciro Larco-Barros[2], Rodrigo Sempertegui-Álvarez[1]

Received: 02-08-2022, Received after review: 20-10-2022, Accepted: 10-11-2022, Published: 01-01-2023

Abstract

E-bikes are an emerging sustainable means of transportation, if adopted massively, they can help face the challenges of human mobility in urban centers worldwide. In Cuenca, Ecuador, the local government built cycle routes (13.47 km) connecting strategic points to facilitate and encourage sustainable mobility. However, the effective implementation of the electromobility strategies at a large scale entails impacts on the power grid, like the increase in the energy demand and the possible decrease of the energy quality due to the harmonic distortion that characterizes the battery's charging current. This research aims to obtain a primary input to evaluate such impacts through an energy efficiency study of an urban e-bike charged by a standalone solar photovoltaic charging station implemented in the Microgrid Laboratory of Universidad de Cuenca.

Resumen

Las bicicletas eléctricas (*e-bikes*) son un medio de transporte sostenible emergente. Si se adoptan masivamente, ayudarían a enfrentar los desafíos de movilidad humana en las ciudades del mundo. En Cuenca, Ecuador, el gobierno local construyó ciclovías (13,47 km) que conectan puntos estratégicos, para facilitar y fomentar la movilidad sostenible. Sin embargo, la implementación efectiva de las estrategias de electromovilidad a gran escala conlleva impactos en la red eléctrica, como el aumento de la demanda de energía y la posible disminución de su calidad debido a la distorsión armónica de la corriente de carga de la batería. El propósito de esta investigación es hacer una evaluación preliminar de dichos impactos, mediante el estudio de eficiencia energética de una *e-bike* urbana cargada con una estación solar fotovoltaica aislada, implementada en el Laboratorio de Micro-Red de la Universidad de Cuenca.

[1,*] Laboratorio de Micro-Red, Universidad de Cuenca, Ecuador.
Corresponding author ✉: vinicio.iniguezm@ucuenca.edu.ec
[2]Facultad de Ingeniería, Universidad de Cuenca, Ecuador.

Suggested citation: Íñiguez-Morán, V.; Villa-Ávila, E.; Ochoa-Correa, D.; Larco-Barros, C. and Sempértegui-Álvarez, R. "Study of the Energy Efficiency of an Urban E-Bike Charged with a Standalone Photovoltaic Solar Charging Station and its Compliance with the Ecuadorian Grid Code No. Arcernnr – 002/20". *Ingenius, Revista de Ciencia y Tecnología*. N.° 29, (january-june). pp. 46-57. 2023. DOI: https://doi.org/10.17163/ings.n29.2023.04.

The methodology includes the experimental characterization of the battery's charging regime, the vehicle's energy efficiency calculation, and the evaluation of its compliance with Ecuadorian grid code No. ARCERNNR – 002/20. Results show that the battery's charger performs a charging regime standardized by German regulations, delivering 92% of charge in 4.82 hours. The e-bike's calculated average energy efficiency is 2.18 kWh/100 miles or 73.77 m/Wh, and a fuel economy of 1545.1 MPGe. Finally, the magnitude of the first four odd harmonic components and the total harmonic distortion of the charging current exceeds the limits established by the grid code in force.

Keywords: e-Bike, Electromobility, Power Quality, Lithium-Ion Batteries, Grid code No. ARCERNNR 002/20, Std. DIN 41772

La metodología incluye la caracterización experimental del régimen de carga de la batería, el cálculo de la eficiencia energética del vehículo y la evaluación del cumplimiento de la normativa ecuatoriana No. ARCERNNR–002/20. Los resultados muestran que el cargador de la batería implementa un régimen de carga estandarizado por normas alemanas, entregando 92% de carga en 4,82 horas. La eficiencia energética promedio de la *e-bike* es 2,18 kWh/100 millas o 73,77 m/Wh, y una economía de combustible de 1545,1 MPGe. Finalmente, la magnitud de las primeras cuatro componentes armónicas impares y la distorsión armónica total de la corriente de carga supera los límites establecidos por la normativa.

Palabras clave: bicicleta eléctrica, electromovilidad, calidad de energía, batería de iones de litio, resolución N.° ARCERNNR 002/20, Est. DIN 41772

1. Introduction

Nowadays, many urban population centers worldwide are experiencing serious problems related to vehicular congestion, negatively impacting people's quality of life. Its main manifestation is the progressive reduction in traffic speeds, observed in increases in travel times, consumption of fossil fuels, other operating costs, and atmospheric pollution, concerning a traffic flow free of traffic jams [1].

Therefore, the authorities, the different social actors and citizens have used some strategies aimed at mitigating these impacts. These strategies follow various paths, such as improving the mass public transport offer (in terms of fares and routes), restricting the access of private transport in urban centers, promoting fleets of energy-efficient vehicles, and promoting modes of transportation of low environmental impact [2]. Among the initiatives that are part of this last strategy, micromobility has been gaining relevance as an increasingly widespread transport solution [3].

Micromobility refers to using a wide variety of private or shared light vehicles that operate at low speeds and for short trips; it includes electric bicycles (e-bikes), electric scooters (e-scooters) and electric mopeds. The way people travel in urban areas is rapidly changing as this concept is quickly adopted and promoted to achieve a more sustainable transportation system [4]. The growing popularity of electric micromobility means has gained the interest of scientists around the world, a fact reflected in a considerable number of research works. In the literature, many papers address legislative issues related to micromobility, perhaps motivated mainly by the report "Global EV Outlook 2020 - Entering the decade of electric drive?" published by the International Energy Agency (IEA) in 2020 [5].

For example, the authors in [6] showed that European Union (EU) countries and the United Kingdom (UK) have different approaches to electromobility means in legal terms, considering them as a means of micro transportation or personal transport. In addition, this work shows that in some countries, electromobility means such as e-scooters are not defined in regulations, but other rules apply (e.g., regulations for bicycles). The fact that such regulations consider users of micromobility means as pedestrians or cyclists massifies them in urban environments, generating the need to develop detailed legislation to condition the safe movement of its users and manage them properly in cities to avoid chaos, as mentioned by researchers in [7].

In this sense, [8] presents a comparative study conducted in thirty European cities aimed at assessing the management problems of e-scooters in urban spaces. The results show that the shared use of micromobility means is becoming more and more attractive, forcing public electric energy service providers to assume significant increases in the loadability of their networks.

In the United States of America (USA) context, researchers in [9] show that people often prefer electric micromobility modes to cars, especially in many USA cities. Moreover, in the same work, the authors claim that electric micromobility modes could complement public transport, emphasizing the modal integration and social benefits of introducing a shared-use model. On the other hand, researchers in [10] studied the impact of time variables, such as weather data and time-invariant variables on the expected demand for micromobility means (taking e-scooters as a case) in Chicago (USA). The authors focused on determining the location of e-scooter charging stations and found that economic factors were decisive in this task. Similarly, authors in [11] considered a multi-objective stochastic location assignment model for e-scooter battery swapping stations. In [12], the study focused on finding an optimization model to define the location of multiple charging stations of different technical characteristics for electric micromobility vehicles.

Then, in the Latin American context, interesting works in [13, 14] report electromobility experiences in countries such as Brazil and Uruguay, respectively, while in [15], the Inter-American Development Bank (IDB) presents a more general Latin American perspective on this matter.

In the Ecuadorian context, since 2020, the most populated cities have experienced a significant increase in the demand and use of electric vehicles to meet their mobility needs [16]. According to [17, 18], the COVID-19 pandemic boosted this growth in electromobility, which affected conventional urban transport (buses and taxis) both in terms of availability and increased risk of contagion in these mass media of human mobility. A reality perceived on a global scale as well.

Although government authorities substantially eased the health restrictions established during the pandemic and reactivated public and private transport services, statistics show that the preference for using electric bicycles and scooters has remained in the main cities. This fact points to an imminent paradigm shift in mobility that neither local governments, companies, nor businesses specialized in mobility have ignored. In the city of Cuenca, the third most populated in Ecuador, the Decentralized Autonomous Government (GAD-Cuenca) has undertaken actions to facilitate and encourage sustainable mobility through a Mobility Plan [19], three of which are worth mentioning. The construction of 13.47 km of cycle routes connecting the most strategic points of the city [20]; the operation of "Tranvía de Cuenca", the mass electric transport service with 21.4 km of tracks [21]; and the implementation of charging stations in one of the city's emblematic parks [22].

Universidad de Cuenca, a public institution of higher education based in the city, launched its institutional program named MoverU, whose purpose is to develop a sustainable mobility system based on scientific evidence that contributes to proposals and actions to solve urban transportation problems, aiming to improve people's quality of life. Within the program's initiatives, it is possible to identify micromobility projects build around using light means of transport with electric assistance. In addition, the Centro Científico Tecnológico y de Investigación Balzay (CCTI-B) of Universidad de Cuenca has the electrical Micro-grid Laboratory that constitutes a test bench for carrying out studies on using and managing renewable energy sources to meet human energy necessities cleanly and sustainably. This laboratory has different electrical generation systems: solar photovoltaic, wind, hydraulic, fuel cells, etcetera; energy storage systems: electrochemical batteries, vanadium flow batteries, hydrogen production by electrolysis, among others; and different final uses of the energy produced/stored: the electrical installations of the building that houses the laboratory, programmable electrical loads (for the emulation of consumption profiles), and electric vehicle charging stations [23].

All the characteristics listed previously make the CCTI-B's electrical Micro-grid Laboratory an energy self-sustaining entity with a wide range of opportunities for research, technological development and innovation. According to the conclusions reported in [24], the laboratory is a Latino-American benchmark since it is the most well-equipped in the region. Among the technical equipment available stands out three electric vehicles (a car and two vans), five urban electric bicycles, one electric mountain bicycle, and two electric mopeds that have motivated a line of research focused on electromobility, the object of this research work.

From a technical point of view, the effective implementation of the electromobility strategies mentioned entails a series of impacts on the electrical network. The most evident is the increase in the demand for electrical energy caused by the massive connection of vehicles at different points of the network to charge their batteries, which is a problem for electricity distribution companies. Particularly in the case of electric micromobility users scattered throughout the electric coverage area of a city, it is essential to characterize their short-term power consumption profile. This information enables assessing the possible effects on the energy quality presented by battery charging systems, especially when there are a lot of users. A characterization of this energy consumption will provide the distribution company with invaluable input for planning and carrying out studies of the impact on the network of residential consumers with loads intended for electromobility.

This work presents a detailed study to calculate the energy efficiency of a commercial model of an urban e-bike charged with an isolated charging station based on a photovoltaic solar source, implemented with equipment from the inventory of the electrical Micro-grid Laboratory of the CCTI-B. The electric autonomy tests of this electric means of transportation are carried out through actual trips in the city of Cuenca, taking care of using the existing cycle routes in most cases.

Besides presenting the methodology used to estimate the autonomy of the electric bicycle, the paper describes a procedure leading to the characterization of the electrical profile of energy consumption during the charging hours of its battery. Also, it contains an evaluation of the affectation on the quality of energy supplied by the grid assessed under the Ecuadorian grid code ARCERNNR 002/20. The study aims to obtain a primary input to evaluate the impact that the massification of these new actors would have on the electricity distribution network and to face this new paradigm of urban mobility.

2. Materials and Methods

2.1. E-bike under study

The electric vehicle under study is an e-bike of the brand ECOMOVE, model TIV, shown in Figure 1. It belongs to the Microgrid Laboratory, a part of the CCTI-B, Universidad de Cuenca. The electrical tests performed on the e-bike, which are described below, were non-invasive. In other words, the vehicle's internal components were never accessed or tampered with.

This urban e-bike weighs 25 kg and is made of 6061 aluminum alloy. It has a 36 V/10 Ah Lithium-Ion (Li-ion) battery and a 36 V/250 W Brushless Gearless Hub Motor in the back or rear wheel. It has a maximum speed of 28 km/h and an autonomy of 30 km when driven in electric assist mode.

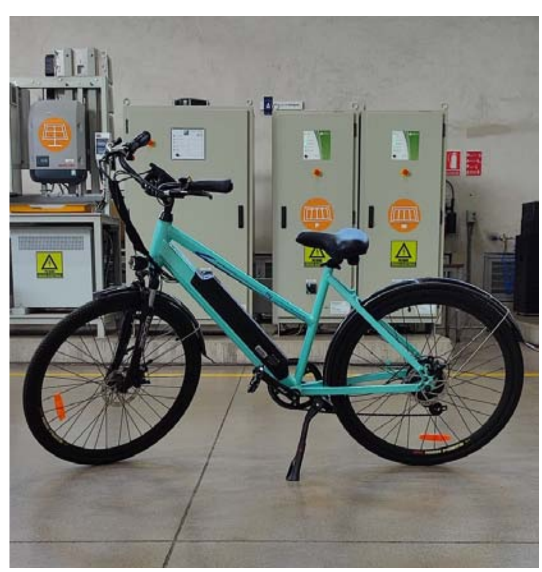

Figure 1. E-bike ECOMOVE model TIV under study

The battery's nominal electrical energy storage capacity does not appear in the manufacturer's datasheet. However, using the charging capacity (10 Ah) and average battery voltage (36 V_{DC}) for calculation resulted in 0.360 kWh.

The battery charger is the model KYLC084V42J – Class II, manufactured by WuXi KeYu Electronic Technology Co., Ltd., and designed for 42V lithium-ion rechargeable batteries. The device's AC input supports a nominal voltage of 100 to 240 V_{AC}, at a frequency of 50 to 60 Hz, and a maximum RMS current of 1.8 A. The DC output offers 42 V_{DC} and a maximum average current of 2 A (with protection fuse T/3.15 A/250 V, slow action).

2.2. Route planned to discharge the e-bike's battery

A 34 km route (approx.) was planned, allowing the use of the cycle routes in Cuenca. The Microgrid Laboratory, located in Campus Balzay, is the point of departure and arrival. A GPS watch is used to calculate the actual distance traveled. This device records geolocation data and other parameters of interest to the user, such as the linear speed of movement (km/h) and heart rate (bpm). Figure 2 shows the entire route, with five reference points identified.

Figure 2. Route traveled with the e-bike. White bubbles with numbers identify each kilometer traveled. The geolocation data was recorded with the GPS device

The departure where the entire battery's state of charge (SOC) is available (SOC = 100%); the arrival where the battery has been fully discharged (SOC = 0%); it is no longer possible to use the electric assist mode of the e-bike; and three additional reference points so the reader can easily recognize the route traveled.

2.3. Standalone solar photovoltaic charging station

A solar photovoltaic charging station isolated from the power grid is implemented in the Microgrid Laboratory to recharge the e-bike's battery, using an Ampere Square Pro (ASP) energy storage and management system based on lithium batteries.

The ASP has five main components starting with a 6-kWh lithium-ion battery (BT). A 3-kW hybrid bidirectional inverter (INV) to carry out the DC-AC and AC-DC power conversions. An energy management system (EMS) manages the energy to regulate the charge/discharge cycles of the device. It has a bidirectional energy meter to register generation and consumption; and electrical protections (B1, B2, . . . , and B5) to look after the main components and to perform command actions.

Also, five polycrystalline solar panels of 38 V at a maximum power of 335 W, series-connected, supply energy to the ASP. The panels are installed on the roof of the laboratory building, as can be seen in Figure 3.

1, 2, 3, 4, and 5: polycrystalline solar panels model A-335P GS manufactured by ATERSA

Figure 3. Solar panels installed on the terrace of the Microgrid Laboratory. The five series-connected panels indicated and numbered in the picture are series-connected to the PV String 1 input of the Ampere Square Pro energy storage system

Figure 4 shows the complete standalone solar photovoltaic charging station, pointing out its main components. The photograph shows the measurement equipment installed at the outlet of the charging station.

1. E-bike.
2. Battery charger.
3. Outlet at 127 VAC/60Hz.
4. Thermomagnetic protection.
5. Power Quality and Energy Analyzer Fluke 435 Series II.
6. AMPERE Square PRO's output at 127 VAC/60Hz.
7. AMPERE Square PRO's input (PV string 1), 190 V_{DC} at maximum power, 1675W, from the 5 series-connected solar panels.
8. AMPERE Square PRO.

Figure 4. Standalone solar photovoltaic charging station for e-bikes implemented in the Microgrid Laboratory. The e-bike under study is being recharged

Figure 5 shows the electrical diagram of the standalone charging station. An energy & power quality analyzer that fulfills the international standards IEC 61000-4-7, IEC 61000-4-30, and IEEE Std 519-2014 measures the energy consumption of the e-bike and records the variables of interest.

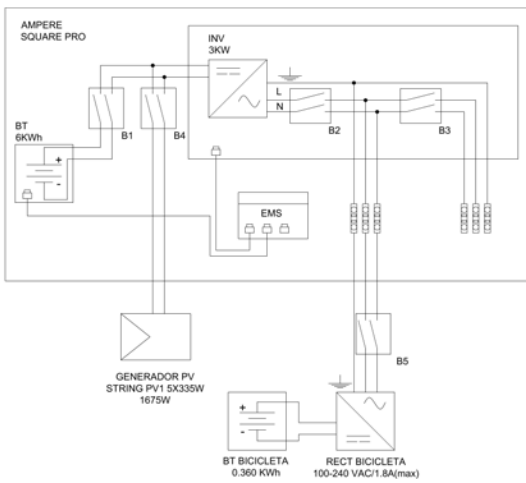

Figure 5. Electrical diagram of the standalone solar photovoltaic charging station implemented in the Microgrid Laboratory. Source: Own elaboration based on the diagrams available in [25]

The only connected load is the e-bike under study. The analyzer works in logger mode to take measurements from an AC single-phase system with line and neutral 127 V_{RMS} nominal, using two voltage terminals and two current probes (one for neutral) with a recording interval of one second. The electrical variables recorded are in line to neutral (L-N) voltage, phase current, frequency, distortion power factor, displacement power factor, current and voltage total harmonic distortion, current and voltage harmonic components (H2, H3, . . . , H11), crest factor of current and voltage, flicker, active power, apparent power, and active energy consumed (Wh).

2.4. Ecuadorian grid code ARCERNNR 002/20

The Ecuadorian grid code ARCERNNR 002/20 entitled Quality of the Electricity Distribution and Commercialization Service has the purpose of: "Establishing the indicators, indices, and limits of quality of the service of distribution and commercialization of electrical energy; and defining the measurement, registration and evaluation procedures to be fulfilled by the electricity distribution companies and consumers, as appropriate" [26, p. 4].

For this research, the quality attribute of interest is at the consumer's side, stated in section 5.2 of [26] as Consumer Quality Aspect and evaluated through the current harmonic distortion. According to section 29 of [26], the indexes to evaluate the current's individual harmonic distortion and its total demand distortion (also known as the current's total harmonic distortion, THD) are calculated as follows:

$$I_{h,k} = \sqrt{\frac{1}{200} \cdot \sum_{i=0}^{200} (I_{h,i})^2} \quad (1)$$

$$DI_{h,k} = \frac{I_{h,k}}{I_{h,1}} \cdot 100\ [\%] \quad (2)$$

$$THD_k = \left[\frac{1}{I_{h,1}} \cdot \sqrt{\sum_{h=2}^{50} (I_{h,k})^2} \right] \cdot 100\ [\%] \quad (3)$$

Where: $I_{h,k}$ is the h^{th} current's harmonic in the k^{th} 10-minute range as required by the standard IEEE Std 519-2014; $I_{h,i}$ is the effective value (RMS) of the h^{th} current's harmonic (for h = 2, 3,. . . , 50) measured every three seconds (for i = 1, 2, 3,. . . , 200); $DI_{h,k}$ is the individual distortion factor of the h^{th} current's harmonic (for h = 2, 3, . . . , 50) in the k^{th} 10-minute range; THD_k is the current's total harmonic distortion in the k^{th} 10-minute range; and $I_{h,1}$ is the effective value (RMS) of the fundamental component of the current (60 Hz).

Table 1 shows the maximum levels for the current's individual and total harmonic distortion, taken from section 29.2 of [26], only up to the 17th harmonic component for this study.

Table 1. Maximum levels for the current's odd harmonic components [a] as a percentage of the maximum demand current at fundamental frequency (60Hz) [26]

ICC/IL	$3 \leq h < 11$	$11 \leq h < 17$	TDD (THD-A)
< 20 [b]	4.0	2.0	5.0
20 < 50	7.0	3.5	8.0
50 < 100	10.0	4.5	12.0
100 < 1000	12.0	5.5	15.0
> 1000	15.0	7.0	20.0

a The limits for even harmonics are the 25% of the limits shown in this table.
b All the equipment is limited to these values of current distortion, where: I_{CC} = maximum current of short circuit at the point of common coupling (PCC): and, I_L = maximum load current at fundamental frequency (60Hz)

Section 29.4 of the grid code establishes that consumers fulfill at the measurement point the current's individual harmonic distortion factor $DI_{h,k}$ and the current's total harmonic distortion factor THD_k, both calculated using equations (1), (2), and (3) when 95% or more of the data registered during an evaluation period of at least seven days are between the limits listed in Table 1.

This research uses the indexes and limits specified by the Ecuadorian grid code [26] to analyze the impacts on the power grid of charging the e-bike by processing the data of the lithium-ion battery's charging entire regime, which takes a few hours to complete.

3. Results and discussion

One of the technicians of the Microgrid Laboratory (male, 36 years old, 73 kg of weight and 1.73 m of height) used the e-bike under study to ride through the previously planned route, only using the electric assist mode of the vehicle. All the electrical energy stored in the battery drained over 30.91 km of distance in two hours, ten minutes and thirty-five seconds (02:10:35), with an average linear speed of 14.2 km/h. So, the experiment achieved a full discharge in ordinary battery operation.

The battery charging process started in the Microgrid Laboratory, connecting the charger to the standalone solar photovoltaic charging station as its only load. It is necessary to mention that the charger stayed connected even after it turned on the light signal of fully charged to register data of the last charging stage of the battery, known as the float charge state. The following is an analysis of the data, acquired by the energy & power quality analyzer.

3.1. Energy quality analysis

The lithium-ion battery's charging process was 6.77 hours long (06:46:06), and the analyzer took 24366 measurements of the electrical variables of interest. The average measured values of the AC RMS phase to neutral voltage ($V_{F\text{-}N}$) connected to the input of the battery charger are 127.24 V at a frequency (f) of 59.95 Hz. The equipment registered an average crest factor (CF-V) of 1.42, with a maximum value of 1.43 over the entire measurement range.

Regarding the AC RMS phase current (I_F) the analysis of the average measurements registered shows that the charger performs a charging regime named IUoI specified by the German standards DIN 41772 [27], Supplement 1 to DIN 41772 [28], and DIN 41773-1 [29]. The goal of this standardized regime is to charge the battery in a relatively short time without affecting its useful life, and to keep the charge in the battery while the charger remains connected.

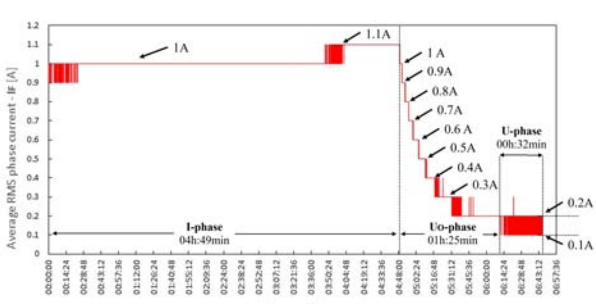

Figure 6. The average RMS phase current (I_F) data registered throughout the charging period show the three stages of the charging regime IUoI

Data shows that the charging regime carried out by the charger of the e-bike under study consists of 3 well-defined stages (refer to Figure 6). The following is a brief description of these stages.

I-phase. Also called the bulk charge stage. The charger provides a constant charging current to the battery when there is a deep discharge. The voltage increases without exceeding Umax (which can be a fixed value or dependent on temperature), and the battery absorbs the charge. When the battery terminals reach Umax, the charger goes to phase Uo.

The charger operated in the I-phase stage for 4 hours and 49 minutes; the average RMS phase current I_F applied was 1 A; the average active power delivered was 81.30 W; and the charging station supplied 385 Wh of active energy to the e-bike's charger.

Uo-phase. Known as the constant-voltage boost stage or absorption stage. Here the charger maintains a constant overvoltage at the battery terminals while the charging current decreases. This voltage value is not safe for an indefinite application, but it allows charging the battery in less time. According to [29] , the maximum voltage should be between 2.33 V and 2.40 V per cell, depending on the battery's design and operating conditions. This phase ends when the charging current reaches a minimum threshold I_{min}, and the charger passes to phase U.

In this stage, the average RMS phase current I_F applied decreases from 1.1 A to 0.2 A (I_{min}) in 1 hour and 25 minutes. Figure 6 shows that the decrease of the charging current occurs in 0.1 A steps. Throughout the Uo-phase, only 34 Wh were supplied to charge the e-bike's battery. As a result, at the end of the stage, the total active energy provided by the charging station to the charger is 419 Wh in 6 hours and 14 minutes. At this point, the battery is fully charged (SOC = 100%).

U-phase. This last stage is called the float charge stage. The charger applies a voltage safe to maintain for longer periods without significantly affecting battery's life. In this stage, the current decreases to a residual value, making it possible to compensate for the battery's self-discharge.

Since the charger remained connected even after it turned the light signal of fully charged on to register data of the U-phase stage, it was possible to determine that the residual value of the charging current is 0.1 A. Figure 6 shows that in this stage, the charging current stays at 0.1 A and commutes to 0.2 A for a few seconds to compensate the battery's self-discharge. This behavior keeps happening while the charger is connected to the station. In 32 minutes, the station supplied only 3 Wh to the charger, for the compensation.

A well-known fact about lithium-ion batteries is that they do not need charging up to 100% to prolong the battery's life by avoiding the overvoltage of the second stage of the charging regime shown in Figure 6. Because measurements prove that 91.89% of the total electrical energy supplied by the charging station to the charger (385 Wh out of 419 Wh, see Figure 7) occurred in the I-phase, the forthcoming analysis focuses on the electrical parameters of interest registered during the I-phase.

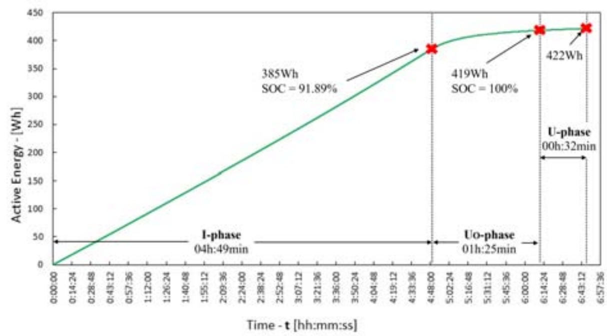

Figure 7. Active energy measured in Wh delivered to the charger during the charging process

Regarding total harmonic distortion, THD-V for the voltage $V_{F\text{-}N}$ and THD-A for the charging current I_F, the measured values were 4.71% and 106.01%, respectively. The total power factor of the charger is 0.62, calculated by multiplying the average registered values of displacement power factor (PF) and distortion power factor (DPF), 0.63 and 0.99, respectively, since the charger is a non-linear load.

The odd harmonic components of the phase current I_F are responsible for the high values of THD-A and the low total power factor, especially the components H3, H5 and H7, whose average magnitudes are 80.71%, 57.14% and 32.41% of the fundamental, respectively. Figure 8 shows the behavior of the first five odd harmonic components of I_F for the entire charging regime.

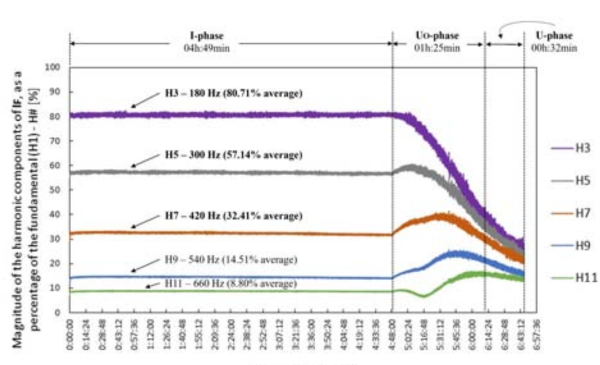

Figure 8. Measured average values of the odd harmonic components (H3, H5, H7, H9 and H11) of the charging current I_F. The measuring equipment calculates these and other data in a time window of 200 ms according to the IEC 61000-4-7 standard for FTT fast Fourier transform algorithms

At 3 hours and 51 minutes of charging during the I-phase, the waveform of the charging current I_F shown in Figure 9 results from the effect of its odd harmonic components. The high value of THD-A makes sense by only looking at the waveform. Regarding the waveform AC RMS phase to neutral voltage $V_{F\text{-}N}$, also presented in Figure 9, it is possible to notice its closeness to a perfect sinusoidal. However, the absolute instant values of $V_{F\text{-}N}$ slightly decrease when I_F goes up to its maximum positive value and negative minimum (highlighted in blue circles in figure 8), which justifies the 4.71% of the measured THD-V.

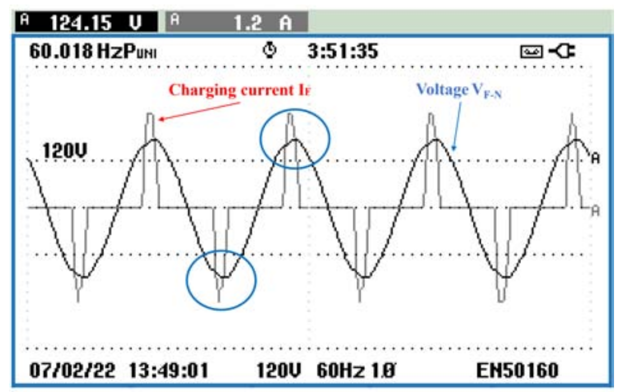

Figure 9. Waveforms of the charging current I_F and phase to neutral voltage $V_{F\text{-}N}$ taken by the oscilloscope of the energy & power quality analyzer at 3 hours and 51 minutes of charging during the I-phase

Concerning the Ecuadorian grid code ARCERNNR 002/20, the limits for the magnitude of the individual charging current's odd harmonic components as a percentage of the fundamental and its total harmonic distortion differ in different ranges of the relationship between the maximum short circuit current at the point of common coupling and the maximum load current of fundamental frequency (H1), named I_{CC}/I_L (refer to Table 1). The grid code mandates that the magnitude of the first four odd harmonics cannot exceed 15% in all the ranges. Likewise, the current's total harmonic distortion (THD-A) should never exceed 20%.

In this context, the measurements of the parameters above-mentioned (H3 = 80.71%, H5 = 57.14%, H7 = 32.41%, H9 = 14.51%, and THD-A = 106.01%) exceed the limits established by the grid code regarding the consumer quality aspect, which has to be accounted to evaluate the impact of a future large-scale utilization of e-bikes (brand and model under study, and others) in Ecuador.

3.2. Energy efficiency analysis

According to [30], the user's habits determine an e-bike's energy efficiency. It also mentions that no unique metric exists to study this critical parameter. However, it suggests that manufacturers often use the number of kWh per 100 miles to inform their products' energy efficiency ranges. Thus, the charger's 419 Wh (0.419 kWh) absorbed in 6 hours and 14 minutes at the end of the Uo-phase is the battery's actual electrical energy storage capacity (SOC = 100%), assuming the losses in the charger are neglectable. Since this amount of electrical energy drained over the 30.91 km ride (19.21 miles) during the experiment, then the average energy efficiency of the e-bike under study is:

$$\eta_{E(kWh-100miles)} = \frac{E}{d} \cdot 100 \tag{4}$$

Where η_E is the average energy efficiency measured in kWh/100miles, d is the distance in miles, and E is the battery's electrical energy stored at SOC = 100% in kWh. The result of substituting terms in (4) is 2.18 kWh/100miles. With the Ecuadorian national average rate of 0.092 USD per kWh, the cost of riding 100 miles with the e-bike under study is 0.2 USD (20 cents).

The number of meters the e-bike can go per watt-hour of electrical energy stored in its battery is also helpful in evaluating energy efficiency, which is calculated as follows:

$$\eta_{E(m/Wh)} = \frac{E}{d} \tag{5}$$

With $d = 30910$ m and $E = 419$ Wh, the calculation results in 73.77 m/Wh for the vehicle under study.

The USA's Environmental Protection Agency (EPA) defines the term miles per gallon equivalent or MPGe to rate the efficiency or fuel economy of electric vehicles (EVs). It compares the amount of electric energy required to charge EVs to the energy provided by a gallon of gas. According to EPA estimations, the energy provided by one gallon of gas is 33.7 kWh. So, the 0.419 kWh required to charge the e-bike entirely is equivalent to 0.0124 gallons of gas. Since the e-bike covered 19.21 miles with that amount of energy, its MPGe is calculated as follows:

$$MPGe = \frac{d}{G} \tag{6}$$

Where d is the distance covered by the e-bike measured in miles, and G is the gallons of gas equivalent previously calculated. The substitution of terms results in 1545.1 MPGe, which is 12 times fold the fuel economy of a 2022 Tesla Model 3 RWD (132 MPGe), the highest-ranked EV in the Fuel Economy Guide Model Year 2022 of the US Department of Energy [31]. The last statement exemplifies the potential benefits of micromobility vehicle usage.

4. Conclusions

The research carried out in the Microgrid Laboratory of Universidad de Cuenca analyzes the energy behavior of an urban e-bike of the brand ECOMOVE, model TIV, on a route of 30.91 km in the urban area of Cuenca, in electric assistance mode only. A solar photovoltaic charging station isolated from the power grid was implemented in the laboratory. The station has five polycrystalline solar panels of 335 W each, series-connected; an energy storage and management system; and electrical protections. To estimate the energy consumption of the e-bike and record the variables of interest, a power quality and energy analyzer was used.

The average AC RMS phase current data analysis shows that the e-bike's battery charger applies an IUoI charging regime standardized by the German regulations DIN41772, Supplement 1 to DIN 41772, and DIN 41773-1, with three well-defined stages. First, the bulk charge stage (I-phase), in which the charger receives a constant current of 1 A for about 4.82 hours, delivers 91.89% of the charge to the battery, and raises the voltage at its terminals. Then, the constant-voltage boost stage (Uo-phase), where the charging current decreases in discrete steps of 0.1 A, from 1.1 A to a minimum value of 0.2 A in about 1.42 hours, and only delivers the 8.11% of charge remaining. Finally, the charger reaches the float charge stage (U-phase) to solely compensate battery's self-discharge by applying 0.2 A for short periods, when required. At this point, the reader has a characteristic model of the load profile of a micromobility transport, which will allow carrying out electrical network studies related to massifying this type of consumer.

Moreover, measurements show that the battery's actual electrical energy storage capacity is 419 Wh, approximately. This capacity provides an autonomy of 30.91 km, measured through a previously planned urban route and only using the electric assist mode of the vehicle. Therefore, the estimated average energy efficiency of the e-bike under study is 2.18 kWh/100miles or 73.77 m/Wh, and a fuel economy of 1545.1 MPGe. Hence, the cost of riding 100 miles is 0.2 USD (20 cents).

About 92% of the total electrical energy supplied by the charging station to the charger, 385 Wh out of 419Wh, occurred in the first stage of the charging regime (I-phase). The charging current is constant and presents its highest average value, 1 A. Hence, the I-phase data are the most relevant for energy quality analysis.

Data analysis proves that the total power factor of the charger is 0.62, and the total harmonic distortion of the charging current (THD-A) is 106.01%, primarily due to its first three odd harmonic components, H3, H5, and H7, whose average magnitudes are 80.71%, 57.14% and 32.41% of the fundamental, respectively. The voltage waveform is close to a perfect sinusoidal, which is proven by a total harmonic distortion (THD-V) of 4.71%.

According to the technical specifications for assessing the consumer quality aspect of the Ecuadorian grid code ARCERNNR 002/20, the magnitudes of the individual charging current's odd harmonic components as a percentage of the fundamental (H3 = 80.71%, H5 = 57.14%, H7 = 32.41%, and H9 = 14.51%, and the charging current's total harmonic distortion (THD-A= 106.01%) are well above the limits established by the grid code. For a future large-scale use of e-bikes as a means of transportation in the urban centers of Ecuador, the vehicles' charger's fulfillment of the law in force must be checked beforehand.

Acknowledgments

The work documented in this manuscript is part of the activities carried out in the project entitled: "Movilidad Eléctrica: retos, limitaciones y plan de implementación en el régimen especial de la Provincia de Galápagos enfocada en el desarrollo sostenible y su factibilidad en la Ciudad de Cuenca", II Concurso de Proyectos de Investigación – Vinculación, Vicerrectorado de Investigación y la Dirección de Vinculación con la Sociedad de la Universidad de Cuenca. The authors thank Universidad de Cuenca for easing access to the facilities of the Microgrid Laboratory of the Centro Científico Tecnológico y de Investigación Balzay (CCTI-B), for allowing the use of its equipment, and for authorizing its staff the provision of technical support necessary to carry out the experiments described in this article.

References

[1] A. Bull, *Congestión de tránsito: el problema y cómo enfrentarlo*. Comisión Económica para América Latina y el Caribe (CEPAL), Naciones Unidas, 2003. [Online]. Available: https://bit.ly/3TW587t

[2] I. Thomson and A. Bull, *La congestión del tránsito urbano: causas y consecuencias económicas y sociales*. Comisión Económica para América Latina y el Caribe (CEPAL), División de Recursos Naturales e Infraestructura, Unidad de Transporte, Naciones Unidas, 2001. [Online]. Available: https://bit.ly/3TW587t

[3] P. Felipe-Falgas, C. Madrid-Lopez, and O. Marquet, "Assessing environmental performance of micromobility using lca and self-reported modal change: The case of shared e-bikes, e-scooters, and e-mopeds in barcelona," *Sustainability*, vol. 14, no. 7, p. 4139, 2022. [Online]. Available: https://doi.org/10.3390/SU14074139

[4] M. Elhenawy, H. A. Rakha, Y. Bichiou, M. Masoud, S. Glaser, J. Pinnow, and A. Stohy, "A feasible solution for rebalancing large-scale bike sharing systems," *Sustainability*, vol. 13, no. 23, p. 13433, 2021. [Online]. Available: https://doi.org/10.3390/su132313433

[5] IEA, *Global EV Outlook 2020*. IEA. Paris, 2020. [Online]. Available: https://bit.ly/3gne4EW

[6] M. M. Sokolowski, "Laws and policies on electric scooters in the european union: A ride to the micromobility directive?" *European Energy and Environmental Law Review*, vol. 29, pp. 127–140, 2020, place: Alphen aan den Rijn, The Netherlands Publisher: Kluwer Law International. [Online]. Available: https://doi.org/10.54648/EELR2020036

[7] K. Turoń and P. Czech, "The concept of rules and recommendations for riding shared and private e-scooters in the road network in the light of global problems," in *Modern Traffic Engineering in the System Approach to the Development of Traffic Networks*, E. Macioszek and G. Sierpiński, Eds. Springer International Publishing, 2020, pp. 275–284. [Online]. Available: https://doi.org/10.1007/978-3-030-34069-8_21

[8] A. Li, P. Zhao, X. Liu, A. Mansourian, K. W. Axhausen, and X. Qu, "Comprehensive comparison of e-scooter sharing mobility: Evidence from 30 european cities," *2022*, vol. 105, p. 103229, Transportation Research Part D: Transport and Environment. [Online]. Available: https://doi.org/10.1016/j.trd.2022.103229

[9] K. Wang, X. Qian, D. T. Fitch, Y. Lee, J. Malik, and G. Circella, "What travel modes do shared e-scooters displace? a review of recent research findings," *Transport Reviews*, pp. 1–27, 2022. [Online]. Available: https://doi.org/10.1080/01441647.2021.2015639

[10] E. Ayyildiz, "A novel pythagorean fuzzy multi-criteria decision-making methodology for e-scooter charging station location-selection," *Transportation Research Part D: Transport and Environment*, vol. 111, p. 103459, 2022. [Online]. Available: https://doi.org/10.1016/j.trd.2022.103459

[11] M.-D. Lin, P.-Y. Liu, J.-H. Kuo, and Y.-H. Lin, "A multiobjective stochastic location-allocation model for scooter battery swapping stations," *Sustainable Energy Technologies and Assessments*, vol. 52, p. 102079, 2022. [Online]. Available: https://doi.org/10.1016/j.seta.2022.102079

[12] Y.-W. Chen, C.-Y. Cheng, S.-F. Li, and C.-H. Yu, "Location optimization for multiple types of charging stations for electric scooters," *Applied Soft Computing*,

vol. 67, pp. 519–528, 2018. [Online]. Available: https://doi.org/10.1016/j.asoc.2018.02.038

[13] J. G. Schmidt, F. J. De Faveri, J. C. De Bona, E. A. Rosa, L. S. Dos Santos, C. Q. Pica, L. B. R. Morinico, and I. França, "Forecasts and impact on the electrical grid with the expansion of electric vehicles in northeast of brazil," in *2022 IEEE/PES Transmission and Distribution Conference and Exposition (T&D)*, 2022, pp. 1–5. [Online]. Available: https://doi.org/10.1109/TD43745.2022.9816978

[14] L. Di Chiara, F. Ferres, and F. Bastarrica, "Impact of electromobility deployment scenarios in the power system of uruguay by 2028," in *2021 IEEE URUCON*, 2021, pp. 360–363. [Online]. Available: https://doi.org/10.1109/URUCON53396.2021.9647426

[15] D. P. Jaramillo, M. C. Gutiérrez, and R. Mix, *Electromovilidad: Panorama actual en América Latina y el Caribe: Versión infográfica.* Banco Interamericano de Desarrollo, 2019. [Online]. Available: http://dx.doi.org/10.18235/0001654

[16] Primicias. (2020) Las ventas de vehículos híbridos y eléctricos crecen casi 300 %. [Online]. Available: https://bit.ly/3EM9mZR

[17] J. Figura and T. Gadek-Hawlena, "The Impact of the COVID-19 Pandemic on the Development of Electromobility in Poland. The Perspective of Companies in the Transport-Shipping-Logistics Sector: A Case Study," *Energies*, vol. 15, no. 4, pp. 1–18, 2022. [Online]. Available: https://bit.ly/3XkWfaj

[18] T. Rokicki, P. Bórawski, A. Beldycka-Bórawska, A. Zak, and G. Koszela, "Development of electromobility in european union countries under covid-19 conditions," *Energies*, vol. 15, no. 1, 2022. [Online]. Available: https://doi.org/10.3390/en15010009

[19] GAD Cuenca. (2022) Plan de movilidad. [Online]. Available: https://bit.ly/3EPQlqh

[20] P. Ochoa, *Ciclovía de los Ríos de Cuenca.* GAD Municipal de Cuenca, 2018. [Online]. Available: https://bit.ly/3ETFQCw

[21] C. A. Cruz Leal and M. Virviescas Arias, "Evaluación de la operación del tranvía de cuenca ecuador y del tranvía de medellín colombia," 2018.

[22] Redacción El Mercurio. (2021) Nueva electrolinera en Cuenca. [Online]. Available: https://bit.ly/3vnx7CY

[23] J. L. Espinoza, L. G. González, and R. Sempértegui, "Micro grid laboratory as a tool for research on non-conventional energy sources in ecuador," in *2017 IEEE International Autumn Meeting on Power, Electronics and Computing (ROPEC)*, 2017, pp. 1–7. [Online]. Available: https://doi.org/10.1109/ROPEC.2017.8261615

[24] J. M. Rey, G. A. Vera, P. Acevedo-Rueda, J. Solano, M. A. Mantilla, J. Llanos, and D. Sáez, "A review of microgrids in latin america: Laboratories and test systems," *IEEE Latin America Transactions*, vol. 20, no. 6, pp. 1000–1011, 2022. [Online]. Available: https://doi.org/10.1109/TLA.2022.9757743

[25] AMPERE ENERGY, *AMPERE square PRO Manual del instalador.* AMPERE POWER ENERGY S.L., 2021. [Online]. Available: https://bit.ly/3ABgxm4

[26] ARCERNNR, *Calidad del servicio de distribución y comercialización de energía eléctrica.* Agencia de Regulación y Control de Energía y Recursos Naturales no Renovables, 2020. [Online]. Available: https://bit.ly/3tRydGr

[27] DIN, *DIN 41772 Static power convertors; semiconductor rectifier equipment, shapes and letter symbols of characteristic curves.* German Institute for Standardisation (Deutsches Institut für Normung), 1979. [Online]. Available: https://bit.ly/3GCFD8b

[28] ——, *DIN 41772 Supplement 1 Static power convertors; semiconductor rectifier equipment, examples of characteristic curves for battery chargers.* German Institute for Standardisation (Deutsches Institut für Normung). [Online]. Available: https://bit.ly/3GCJTEp

[29] ——, *DIN 41773-1 Static power convertors; semiconductor rectifier equipment with IU-characteristics for charging of lead-acid batteries, guidelines.* German Institute for Standardisation (Deutsches Institut für Normung). [Online]. Available: https://bit.ly/3hSi28X

[30] T. McCarran and N. Carpenter, "Electric bikes: Survey and energy efficiency analysis," *Efficiency Vermont*, 2018. [Online]. Available: https://bit.ly/3ACmgYP

[31] Department of Energy. (2022) Fueleconomy.gov Top Ten. [Online]. Available: https://bit.ly/3VdjKjy

Scientific Paper / Artículo Científico

UNIVERSIDAD POLITÉCNICA SALESIANA ECUADOR
INGENIUS
Revista de Ciencia y Tecnología
https://doi.org/10.17163/ings.n29.2023.05
pISSN: 1390-650X / eISSN: 1390-860X

Characterization of the RSU thermal potential, for the generation of Electric Energy, using Hydrothermal carbonization

Caracterización del potencial térmico RSU, para la generación de energía eléctrica, utilizando carbonización hidrotérmica

Aníbal Salazar[1,*]

Received: 10-08-2022, Received after review: 15-11-2022, Accepted: 28-11-2022, Published: 01-01-2023

Abstract

The zenith of oil and the greenhouse effect are the main reasons why it is necessary to use nonconventional renewable energy (NCRE) sources. Solid urban waste is one of these sources, and the main objective of this research is to determine its main features, including calorific value, as well as the use of modern hydrothermal carbonization (HTC) and hydrothermal liquefaction (HTL) procedures for the generation of energy and electrical power. For this purpose, it was used the sampling data of urban solid waste from the metropolitan Chiclayo area. A calorimetric bomb was employed for measuring its calorific value and the electrical generation potential was simulated. In addition, the main objective was fulfilled, and it was also possible to steadily generate energy and power. This will help to avoid greenhouse gas emissions, and thus contribute to meet the commitments signed by Peru to reduce greenhouse gases, and follow the path to a new sustainable energy matrix, while simultaneously providing a potential solution to the problem of managing solid urban waste, which is the main environmental problem of the city of Chiclayo Peru.

Keywords: Solid, Waste, calorific value, carbonization, liquefaction, generation

Resumen

El cenit del petróleo y el efecto invernadero son las razones que justifican la necesidad de utilizar energías renovables no convencionales (ERNC). Los residuos sólidos urbanos constituyen una de esas fuentes, por lo que la determinación de las principales características, incluido el poder calorífico, fue el primer objetivo de la presente investigación, así como la utilización de los modernos procedimientos de carbonización hidrotermal (CHT) y licuefacción hidrotermal (LHT), para la generación de energía y potencia eléctrica. Se trabajó con los datos de muestreo de los residuos sólidos urbanos del área de Chiclayo metropolitano. Se empleó una bomba calorimétrica para la medición del poder calorífico y la simulación numérica del potencial de generación eléctrica. Además, se obtuvo como resultado el cumplimiento del objetivo principal, y el hecho de que es posible obtener energía y potencia firme, que ayude a evitar las emisiones de gases efecto invernadero, contribuyendo a los compromisos firmados con tal efecto y a seguir el camino a una nueva matriz energética sostenible; a la vez se da una posible solución al problema del manejo de residuos sólidos urbanos, principal problema ambiental de la ciudad de Chiclayo, Perú.

Palabras clave: residuos, sólidos, poder calorífico, carbonización, licuefacción, generación

[1,*] Facultad de Ingeniería Mecánica Electrica, Universidad Nacional Pedro Ruiz Gallo, Lampayeque, Perú.
Corresponding author ✉: asalazar@unprg.edu.pe

Suggested citation: Salazar, A. "Characterization of the RSU thermal potential, for the generation of Electric Energy, using Hydrothermal carbonization". *Ingenius, Revista de Ciencia y Tecnología*. N.° 29, (january-june). pp. 58-65. 2023. DOI: https://doi.org/10.17163/ings.n29.2023.05.

1. Introduction

At present, in front of the oil crisis or zenith effect that predicts that planet Earth has reached its oil production limit, humanity is increasingly using biofuels in both traditional combustion processes and in thermochemical processes; hydrothermal carbonization (HTC) and hydrothermal liquefaction (HTL) stand out in the latter [1]. Moreover, the increase in urban solid wastes (USW) in Peru and worldwide can be observed in Figure1.

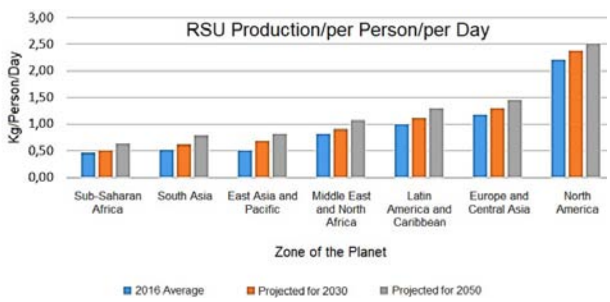

Figure 1. Projected increase in the worldwide generation of urban solid wastes [2]

It should be also highlighted that biofuels are projected as one of the main resources for "green" hydrogen production in the northern region of Peru, because its production is seasonal. Therefore, it is necessary to accumulate it in gaseous state for its further distribution through gas pipeline networks, to assure the energy horizon of northern Peru for the entire 21st century.

These solid wastes (urban solid wastes, rice husks, sugar cane bagasse, stubbles of the mechanized harvesting of sugar cane, coffee draff, among other main types of biomasses) have an energy use, through various procedures that may be classified as: biochemical processes, among which fermentation and digestion (aerobic and anaerobic in controlled reaction tanks) stand out; dry thermochemical processes, which include simple combustion, complex combustion, gasification, roasting and pyrolysis; and wet thermochemical processes, that are part of this study and include gasification, liquefaction and hydrothermal carbonization [3]. This determines that the energy coming from urban solid wastes is increasing worldwide, as well as locally in the north of Peru, as it is shown in Figure 2.

Most of this thermal energy is used for generation of energy and electric power, and to be sold to interconnected or isolated systems (this constitutes one of the main ways through which the use of distributed energy is extending). It is also used for the production of industrial heat, heating and air conditioning. In the 19th century, solid fuels were used for machinery and manufacturing processes [4], whereas liquid fuels were preferred in the 20th century due to their easy logistic distribution and high energy concentration; this enabled movement autonomy. However, at the end of the past century started to become evident what was predicted by engineer Hubbert and his logistic models of depletion of oil worldwide reserves.

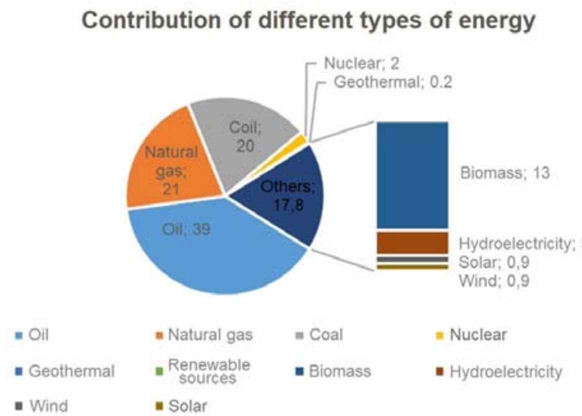

Figure 2. Global contribution of biomass in energy production [5]

Consequently, the 21st century has been devised as the era of gaseous fuels, and it is expected that the second half of this century will shift to the hydrogen as energy carrier, especially "green" hydrogen, which will not be combusted, but transformed into electricity through hydrolysis machines and fuel cells, thus avoiding the emission of greenhouse gases and their concentration in the atmosphere, which constitute the main causes of the atmospheric disturbances known as greenhouse effecto [6].

Likewise, this energy generation is classified as renewable, according to the information depicted in Figure 3, which shows its importance in the global energy matrix. It is also appreciated a decrease in the importance of fossil hydrocarbons, which are in a zenith since the discovery of new oil reserves as well as their production are slowing down, and also the places where such hydrocarbons are being produced are becoming more remote, such as the deep seas and the virgin forests, where the environmental impacts are increasingly larger and thus more difficult to remedy or mitigate. This has caused an inflationary processes in all countries of the world, especially in those that are highly dependent on hydrocarbon fuels, and thus it is important to increase the use of nonconventional renewable energy sources, such as onshore and offshore wind energy, photovoltaic energy in desert areas and in urban buildings for distributed generation, thermal solar with thermal salts, but also urban biomass and rural agricultural biomass, adding value to the products and generating employment opportunities and wealth in the rural sector [7].

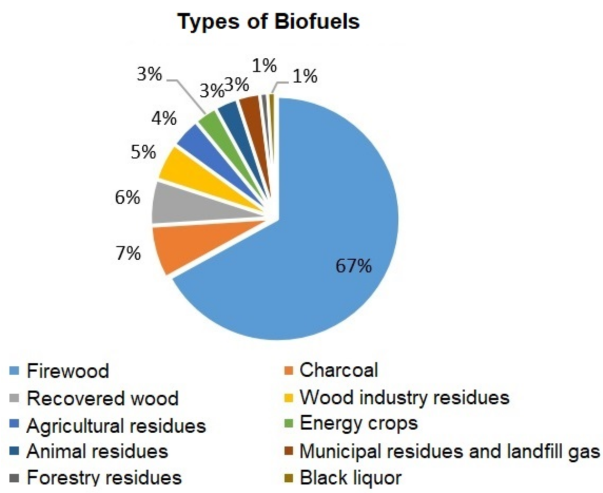

Figure 3. Breakdown of the energy produced by type of biofuel [8]

Figure 3 shows traditional biomass fuels with large environmental impact, such as wood, whose production implies the deforestation of dry woods in northern Peru.

Moreover, it systematically outlines all the possibilities for leveraging existing solid urban waste biomasses; Figure 4 shows the position occupied by hydrothermal processes.

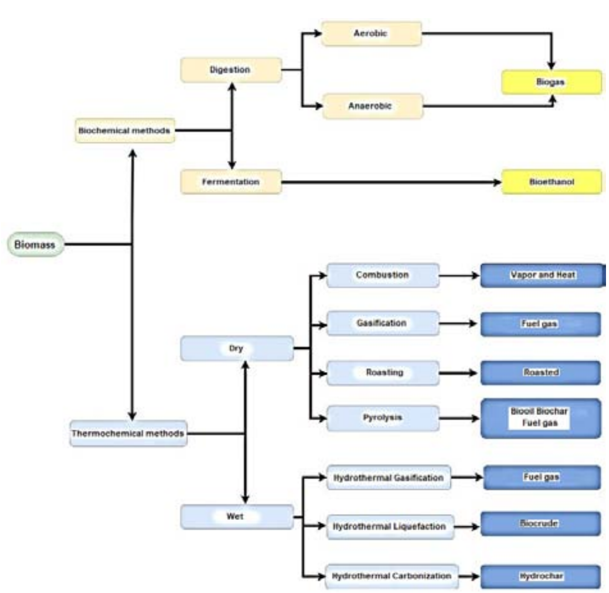

Figure 4. Different methods for leveraging biofuels

In other words, the northern region of Peru has a long history of biomass usage (especially sugar cane bagasse) in combustion processes in bagasse cauldron furnaces in sugar agricultural companies, gasification of rice husk in over a hundred of big rice mills existing in the region, as well as in anaerobic pyrolysis prototype processes for generating electric power and heat in industrial processes. This enables achieving costs savings in production and mitigation of the environmental impacts on the air quality in the concentration at the receiving body as well as at the emitting points (chimneys and others), and in turn end up with the problem of disposing the rice husk excess, which are discharged in dumps that pollute air, the water of lake ecosystems and the soil itself, which losses its superior agricultural properties [9].

In addition, it should be taken into account that hydrothermal carbonization (HTC) is a process that occurs in the temperature range from 200 a 300 ºC, at the corresponding vapor pressure, with reaction times that go from two to several hours. The main objective of hydrothermal carbonization (HTC) is to produce a carbon-rich solid known as hydrochar [10].

In general, during this process, carbohydrates are hydrolyzed and completely dissolved in the liquid phase and then repolymerized, giving rise to hydrochar and some subproducts such as organic acids and water [11].

All these works were conducted under the control and supervision of the environmental entities responsible for processing organic solid wastes in the city of Chiclayo, with the perspective of using the residues from agricultural activities, such as sugar cane bagasse, which has had an energy use in the zone for more than 140 years due to the industrial sugarcane activity.

2. Materials and methods

The lower heating value of the USWs was determined. The equipment and instruments used to determine the calorific value of the solid wastes sampled are described below.

Constant volume calorimetric bomb. It consists of a stainless-steel cylinder which is put in an isothermal bucket with a capacity of more than two liters of water. It also has a mixer, driven by a squirrel cage electric motor, that evens the temperatures [12], to prevent heat from leaking to the exterior by conduction, convection or radiation. Errors when adjusting the jacket temperature should be avoided during the tests, to maintain a high precision in the measurements. The bomb is sealed by a precision machined screw cap that is closed manually and seals automatically, to enable the pressure increase [13].

Regarding the assembly, it will be carried out in stages in the following sequence:

The bucket should have a minimum volume of two liters, and it should be verified that the initial temperature is 25 ºC, according to the ASTM D240 – 09 standard. In the case of the city of metropolitan Chiclayo it is not necessary a preliminary heating, because that is the annual average temperature. Afterwards, the USW pellet is prepared through a pressure compacting process in special machines manufactured by the university; then, the calorific value is calculated and the thermal wire that will be connected to the electrical electrodes is installed. Once the bomb is closed, it is filled with oxygen at 99% under the appropriate supervision, due to the risks associated to the transfer; then, it is connected to the electric source, causing the complete combustion of the test material.

A precision thermometer, with a resolution of 0.01 ºC, and an OHAUS electronic precision scale, with a resolution of 0.00001 grams, were also used.

The fuel mass is between 0.9 grams and 1.1 grams, at an operating pressure of 380 psi that is obtained pumping oxygen.

The data should be collected every five minutes, and after the fuel is ignited it should be collected at 15, 30, 45, 60, 75, 90 and 115 seconds.

All pertinent safety measures should be taken, as expressed in the corresponding IPERC matrices; such measures include the presence of fire extinguishers, ventilation systems to prevent the concentration of explosive gases and control of biological risks.

As a method to characterize the calorific value of the organic solid wastes of metropolitan Chiclayo during the 2016-2020 period, it was made a sampling to obtain 100 kg of solid wastes in the proportion shown in Table 1, which coincides with what was determined by Rodríguez [14].

Table 1. Percentage production of solid wastes

Item	City	Percentage
1	Chiclayo	52,85%
2	José Leonardo Ortiz	22,93%
3	La Victoria	9,27%
4	Pimentel	2,93%
5	Reque	1,71%
6	Pomalca	3,46%
7	Monsefú y Eten	6,85%
	Total	100,00%

The second objective of this research work was to demonstrate the technical feasibility to experimentally carbonize moist biomass, and make combustion with mineral coal to produce energy. It should be taken into account that hydrothermal carbonization is the process through which a material is subject to high temperatures, immersed in a moist environment, without allowing that boiling occurs. It has been detected that this type of reaction enables carbonizing solid lignocellulosic materials, but also polysaccharides dissolved in water, obtaining as products nanostructured carbonaceous materials [15].

The particular requirement of an aqueous medium is very useful for the application of this method to residues that, precisely, have a high content of water. In fact, without this method such residues would require various drying steps to be able to carbonize them in dry conditions and directly.

Similarly, it should be pointed out that the development of the hydrothermal carbonization (HTC) technology and its application at an industrial level, was initially possible thanks to the scientific work conducted by Friedrich Bergius approximately one hundred years ago, which was complemented by subsequent developments conducted by Max Planck [16], among others; it should be indicated that it is also an objective the design and construction of a biomass hydrothermal carbonization plant at an industrial scale, as part of the R + D activities of the process.

The great strength and opportunity posed by the HTC process is that it occurs in an aqueous medium, and thus the moist of the source biomass is not a problem. Therefore, it is possible to add the calorific value of the source biomass in a biofuel solid and, conversely, be able to generate fertilized water that may be reused in watering activities [17].

For the ideal case of biochar production, it will be followed the procedures carried out with various alternatives of solid wastes processed in the city of Chiclayo, which will be plotted and used to measure the efficiency of the hydrochar production process. The moist biomass was weighted at the inlet of the process, after the autoclave and runoff process, and finally after it is passed through the furnace.

The precision scale that will be used for weighting the biomass was cleaned; the calorific value of such biomass will be further measured.

A biomass pellet with urban solid wastes was obtained through compaction, based on the samples collected.

The calorimetric bomb was purged with oxygen, its electrodes were cleaned and the calibrated ignition wire was installed.

The biomass pellet was placed inside the calorimetric bomb, and the electric electrodes were connected to the power source to produce the spark and the corresponding combustion.

The isothermal jacket was filled with water, and the mixer was activated to even the temperatures.

The bomb was placed in the isothermal jacket, and the thermometer that will measure the temperature increase in the water was connected.

The calorimetric bomb was filled with oxygen, at a pressure of 20 bars, and the excess was eliminated.

The electrodes were electrically connected to the corresponding combustion and periodical measurements of temperatures, which were recorded.

The electrodes were disconnected, the oxygen remains were purged, the electrodes were disassembled, and the calorimetric bomb was cleaned.

3. Results and discussion

3.1. Results

Four subsamples were collected, two from Chiclayo, one from José Leonardo Ortiz and another from La Victoria. Five calorimetric tests were conducted per sample. Table 2 shows the arithmetic mean and standard deviation of the results obtained for each of the tests conducted, at normal conditions (temperature: 20 ºC, pressure: 1 atm).

Table 2. Descriptive statistics of the lower heating values – KJ/Kg

Placer	N.° of Sample – Dry Lower calorific value					Mean	Standard
	1	2	3	4	5		
Chiclayo 1	7,150	6,970	7,210	7,145	7,110	7,117	0,090
Chiclayo 2	7,230	7,150	7,190	7,230	7,240	7,208	0,038
JLO 1	6,970	6,890	7,050	7,040	7,050	7,000	0,070
Victoria 1	7,070	7,030	7,050	6,950	6,940	7,008	0,059

The question here is if the composition and, hence, the calorific value of the samples is the same. Then, it is formulated the hypothesis that the USW populations of the different centers have the same calorific value; for this purpose, it is considered the hypothesis $\mu_x = \mu_y$, with five degrees of freedom (n = 5), which according to the tables and a confidence margin of 95% determines a significance level $\alpha = 1,8595$ (equation (**??**)).

$$t = \frac{\left(\overline{X} - \overline{Y}\right) - (\mu_X - \mu_Y)}{\sqrt{\frac{S_X^2 + S_Y^2}{n}}} \tag{1}$$

Was used, which yields 0.9315 < 1.8595 after substituting the values; thus, the hypothesis is rejected. Hence, it is determined that the different USW populations have different calorific value.

Regarding the technical feasibility of experimentally carbonizing moist biomass and make combustion with mineral coal to produce energy, according to the results verified in the literature it has been obtained energetically densified biomass, specifically biochar (homogeneous black powder), having as raw material biomass from urban solid wastes, with energy performance above 40%. The biochar obtained has a calorific value larger than the calorific value of the original biomass (> 15%), and a moisture of 3% after filtering. The hygroscopicity decrease is visible (a reduction of up to 50%), which agrees with what was stated by Peng [18].

It should be added that the combustion tests with mineral coal that were carried out in the laboratory, evidenced interesting reductions of 10% and 30% in the emissions of NO_x and SO_2, respectively. The results obtained are described in Table 3.

Table 3. Conversion factors of moist USW by stages of the process

Stage/Sample	1 (kg)	2 (kg)	3 (kg)	4 (kg)	5 (kg)
Initial weight	8	8	8	8	8
Weight after autoclave and pressing	0,6	0,62	0,59	0,6	0,61
Weight after drying in the furnace	0,56	0,57	0,56	0,57	0,57

Average calorific value of the material dried in the furnace:

The lower heating value (LHV) of biochar is 29,200 KJ/kg, from which the energy potential of the city of metropolitan Chiclayo may be estimated using the following equation (2). This is summarized in Table 4.

$$PC\ Biochar\ (TJ/dia) = P\ RSU\ (Tm/Dia) \cdot PCIBiochar \tag{2}$$

Table 4. Biochar production per zone of metropolitan Chiclayo

Item	City	Production of RSU Tm/Día	Calorific potential of the Biochar TJ/Día
1	Chiclayo	211,40	6172,88
2	José Leonardo Ortiz	91,72	2678,22
3	La Victoria	37,08	1082,74
4	Pimentel	11,72	342,23
5	Reque	6,84	199,73
6	Pomalca	13,84	404,13
7	Monsefú y Eten	27,40	800,08
	Total	400,00	11 688,01

By means of a Rankine thermodynamic cycle with an average efficiency of 40% (a combustion efficiency of about 30% was obtained previously), this biochar enables to obtain the averages of usable energy and power specified below.

Energy: 16,23 Gwhr, for a plant factor 0,90
Power: 591 Mw base
1,000 Mw peak

Since this is the power delivered to the electric generation system, totally scalable, it is prioritized the delivery of power at peak hours because they have a greater selling price both as energy and as power, in order to maximize the income and profitability of the entrepreneurships to be carried out.

This energy is produced with minimum emission of greenhouse gases, sulfur and dangerous and toxic compounds, such as furans, etc., and helps to eliminate practices that are dangerous from the environmental point of view, such as the burning of urban solid wastes outdoors, in the current municipal dump, where the existing hills known as seven roofs save the city of Chiclayo from environmental pollution; the purpose is to eliminate such municipal outdoor dump existing in the Reque pampas, in the southern area of the city of metropolitan Chiclayo.

Table 5 shows the projections in time of energy production due to biochar, which implicitly includes the variations of vegetal growth and USW composition in the different areas of the metropolitan Chiclayo.

Table 5. Projection of biochar production at the different places of metropolitan Chiclayo

	Production of Biochar in the medium term TJ/day						
Year	**Chiclayo**	**JL Ortiz**	**LA Victoria**	**Pimentel**	**Reque**	**Pomalca**	**Monsefu**
2023	6172,88	2678,22	1082,74	342,23	199,73	404,13	800,08
2024	6271,65	2671,52	1100,06	347,71	202,93	410,60	812,88
2025	6371,99	2664,85	1117,66	353,27	206,17	417,17	825,89
2026	6473,94	2658,18	1135,55	358,92	209,47	423,84	839,10
2027	6577,53	2651,54	1153,72	364,66	212,82	430,62	852,53
2028	6682,77	2644,91	1172,18	370,50	216,23	437,51	866,17
2029	6789,69	2638,30	1190,93	376,43	219,69	444,51	880,03
2030	6898,33	2631,70	1209,99	382,45	223,20	451,62	894,11
2031	7008,70	2625,12	1229,35	388,57	226,77	458,85	908,41
2032	7120,84	2618,56	1249,01	394,79	230,40	466,19	922,95

It should be noted the continuous growth of the projection in the Chiclayo district, the reduction in the José Leonardo Ortiz district and the plateau in La Victoria district. These trends may be also visualized in Figure 5.

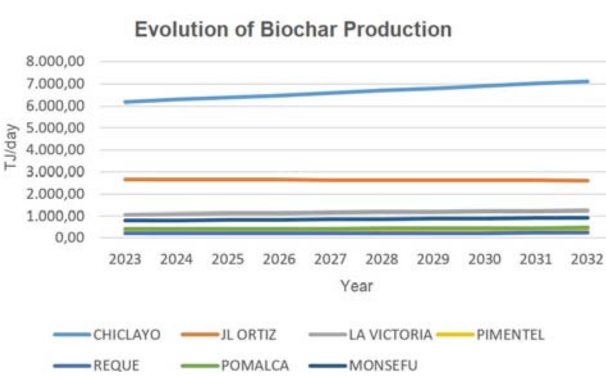

Figure 5. Evolution of Biochar production along time

The biochar production in the carbonization process depends on a series of factors, among which it can be mentioned the average temperature of the drying furnace during the different drying phases (see Figure 6).

There is also an increasing academic interest on hydrothermal processes, which is expressed in the growth in the number of works published about the topic. It is perceived that the interest on HTC has increased with the purpose of creating last generation carbonaceous materials, over the purpose of producing solid biofuels [19].

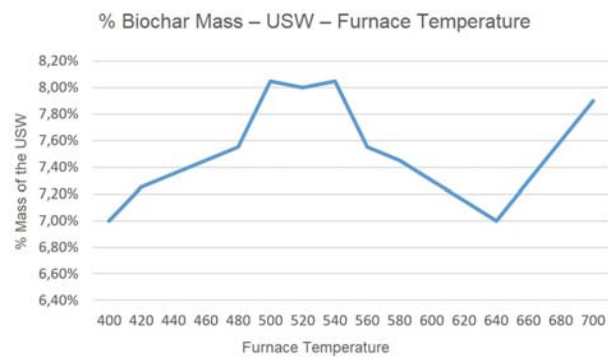

Figure 6. Biochar production from USW, as a function of the furnace temperature

3.2. Discussion

This research work enabled to determine the importance of USW in the metropolitan city of Chiclayo, as well as its energy potential. For this purpose, the urban solid wastes were thermally characterized through samples, and their lower heating value was determined as well. It was also reviewed the production of coal through the hydrothermal carbonization process, with production ranges of 0.56 kg of biochar for every 8 kg of USW, concentrating its calorific value from 7100 KJ/kg to 29 200 KJ/kg, preventing the emission of greenhouse gases, and furans and other poisonous gases, as well as generating job opportunities directly and indirectly, coinciding with what was expressed by DosSantos [20].

Also based on experiences in other areas [21] with similar results regarding the biochar production from USW through the hydrothermal carbonization method, it was observed that it depends on factors such as the furnace temperature (with variables results of increasing and decreasing production), retention time, heating velocity, solution-biomass ratio, working pressure, use of homogeneous or nonhomogeneous catalysts, velocity of combustion gases, among others. Only the first criterion, i.e., the furnace temperature, is analyzed, and it was observed that the biochar production varies with temperature, reaching its maximum production at temperatures of 520 °C and 600 °C [22].

It is important to analyze the thermal efficiency of these products and analyze residual ashes, compared to the results obtained by Trujillo [23] which indicate that the performance of poultry biochar is constant with respect to temperature. Last but not least is the energy availability, which can be summarized in approximately 16.23 Gwh per working day of the solid wastes collection system in the metropolitan area of the city of Chiclayo.

4. Conclusions

It is confirmed the need to leverage the energy capacity of USW and other residues from agricultural production for the generation of electric power, to achieve a sustainable energy matrix and a reliable and stable Peruvian electric system.

The lower heating value of moist urban solid wastes in metropolitan Chiclayo (in the districts of Chiclayo, Leonardo Ortiz, La Victoria, Pimentel, Pomalca, Reque, Monsefú and Eten ciudad y Puerto) , and it is possible to produce biochar with the assistance of a calorimetric bomb through the thermochemical process of hydrothermal carbonization; this biochar has a thermal and electricity generation potential of 16.23 GWh per day and a power between 591 and 1000 MWh, and has also different uses in the biochemical industry.

The optimal temperature to achieve the highest performance in biochar production is in the range from 520 to 700 ºC, obtaining also the entire energy potential.

The energy potential is not the same for the urban solid wastes coming from different places.

On the other hand, it is recommended to continue with the analyses, now focused on the analysis of the environmental quality of the ashes (less presence of sulfur and heavy metals), as well as to implement the design and construction of a biomass hydrothermal carbonization plant at an industrial scale.

References

[1] G. Garrote, H. Domínguez, and J. C. Parajó, “Hydrothermal processing of lignocellulosic materials,” *Holz als Roh- und Werkstoff*, vol. 57, no. 3, pp. 191–202, 1999. [Online]. Available: https://doi.org/10.1007/s001070050039

[2] BBC. (2018) Los 10 países que más y menos basura generan en América Latina (y cómo se sitúan a nivel mundial). [Online]. Available: https://bbc.in/2NyglZo

[3] M. J. Antal and M. Gronli, “The art, science, and technology of charcoal production,” *Industrial & Engineering Chemistry Research*, vol. 42, no. 8, pp. 1619–1640, 2003. [Online]. Available: https://doi.org/10.1021/ie0207919

[4] Y. Pastor Férez, M. M. Martinez Segado, and R. Valdez Illán, *Construcción de una planta de producción de biochar*. Departamento de Ingeniería de Alimentos y del Equipamiento Agrícola, Área de Ingeniería Agroforestal. Universidad Politécnica de Cartagena, 2019.

[5] WBA, *Global Bioenergy Statistics 2019*. World Bioenergy Association, 2019. [Online]. Available: https://bit.ly/3VnXILC

[6] F. Bedussi, “Valutazione delle potenzialitá del biochar come componente dei substrati di coltivazione,” Ph.D. dissertation, 2015. [Online]. Available: https://bit.ly/3irUnwk

[7] D. Mohan, C. U. J. Pittman, and P. H. Steele, “Pyrolysis of wood/biomass for bio oil: A critical review,” *Energy & Fuels*, vol. 20, no. 3, pp. 848–889, 2006. [Online]. Available: https://doi.org/10.1021/ef0502397

[8] A. Brown, *Bioenergy roadmap 2017*. Agencia Internacional de la Energía, 2018. [Online]. Available: https://bit.ly/3FePrUu

[9] M. C. Cueva Díaz, J. L. Rosaldo Santiago, and J. López Luna, “Evaluación de la toxicidad de los suelos mediante bioensayos con semillas,” *INECC*, pp. 87–105, 2018. [Online]. Available: https://bit.ly/3gLD9K7

[10] Y. Matsumura, “Chapter 9 - hydrothermal gasification of biomass,” in *Recent Advances in Thermo-Chemical Conversion of Biomass*. Elsevier, pp. 251–267. [Online]. Available: https://doi.org/10.1016/B978-0-444-63289-0.00009-0

[11] L. Yang, C. Lu, Y. Gao, Y. Lin, J. Xu, H. Xu, X. Zhang, M. Wang, Y. Zhao, C. Yu, and Y. Si, “Hydrogen-rich gas production from the gasification of biomass and hydrothermal carbonization (HTC) aqueous phase.” [Online]. Available: https://doi.org/10.1007/s13399-020-01197-9

[12] E. P. Stambaugh, “Hydrothermal processing – an emerging technology,” *Materials & Design*, vol. 10, no. 4, pp. 175–185, 1989. [Online]. Available: https://doi.org/10.1016/S0261-3069(89)80003-2

[13] D. Shoemaker, *Bomba calorimétrica de mediciones*. Wiley, 1996.

[14] J. Rodríguez, *Caracterización de los residuos sólidos de la ciudad de Chiclayo*. Limusa, 2010.

[15] N. Baccile, M. Antonietti, and M.-M. Titirici, “One-step hydrothermal synthesis of nitrogen doped nanocarbons: Albumine directing the carbonization of glucose,” *ChemSusChem*, vol. 3, no. 2, pp. 246–253, 2010. [Online]. Available: https://doi.org/10.1002/cssc.200900124

[16] T. Wang, Y. Zhai, Y. Zhu, C. Li, and G. Zeng, “A review of the hydrothermal carbonization of biomass waste for hydrochar formation: Process conditions, fundamentals, and physicochemical properties,” *Renewable and Sustainable Energy Reviews*, vol. 90, pp. 223–247, 2018. [Online]. Available: https://doi.org/10.1016/j.rser.2018.03.071

[17] C. W. Garland, J. W. Nibler, and D. P. Shoemaker, *Experiments in Physical Chemistry*. McGraw-Hill Higher Education, 2016. [Online]. Available: https://bit.ly/3irVOen

[18] C. Peng, Y. Zhai, Y. Zhu, B. Xu, T. Wang, C. Li, and G. Zeng, "Production of char from sewage sludge employing hydrothermal carbonization: Char properties, combustion behavior and thermal characteristics," *Fuel*, vol. 176, pp. 110–118, 2016. [Online]. Available: https://doi.org/10.1016/j.fuel.2016.02.068

[19] R. Conti, "Sintesi e caratterizzazione di carboni ottenuti dalla pirolisis di biomasse," 2012. [Online]. Available: https://bit.ly/3GWKJMD

[20] J. V. dos Santos, L. G. Fregolente, M. J. Laranja, A. B. Moreira, O. P. Ferreira, and M. C. Bisinoti, "Hydrothermal carbonization of sugarcane industry by-products and process water reuse: structural, morphological, and fuel properties of hydrochars," *Biomass Conversion and Biorefinery*, vol. 12, no. 1, pp. 153–161, 2022. [Online]. Available: https://doi.org/10.1007/s13399-021-01476-z

[21] S. Mazumder, P. Saha, K. McGaughy, A. Saba, and M. T. Reza, "Technoeconomic analysis of co-hydrothermal carbonization of coal waste and food waste," *Biomass Conversion and Biorefinery*, vol. 12, no. 1, pp. 39–49, 2022. [Online]. Available: https://doi.org/10.1007/s13399-020-00817-8

[22] Z. Liu and R. Balasubramanian, "Hydrothermal carbonization of waste biomass for energy generation," *Procedia Environmental Sciences*, vol. 16, pp. 159–166, 2012. [Online]. Available: https://doi.org/10.1016/j.proenv.2012.10.022

[23] E. Trujillo, C. E. Valencia A., M. C. Alegría-A, Alejandrina, and M. F. Césare-C., "Producción y caracterización química de biochar a partir de residuos orgánicos avícolas," *Revista de la Sociedad Química del Perú*, vol. 85, pp. 489–504, 2019. [Online]. Available: http://dx.doi.org/10.37761/rsqp.v85i4.262

Scientific Paper / Artículo Científico

UNIVERSIDAD POLITÉCNICA SALESIANA ECUADOR
INGENIUS
Revista de Ciencia y Tecnología
https://doi.org/10.17163/ings.n29.2023.06
pISSN: 1390-650X / eISSN: 1390-860X

Scheduled gains control applied to a DC-DC converter for light intensity dimming an LED lamp

Control por ganancias programadas aplicado a un convertidor DC-DC para la regulación de la intensidad luminosa de una lámpara LED

Gregorio Saúl Olivar-Castellanos[1,*], Luis Gerardo Vela-Valdés[1], Jesús Aguayo-Alquicira[1]

Received: 12-11-2022, Received after review: 01-12-2022, Accepted: 09-12-2022, Published: 01-01-2023

Abstract

Nowadays there are several applications of LED lighting, but some of them require to precisely regulate lighting in a wide range of operation, mainly in tracking tasks. In these cases, it is necessary to consider the nonlinearity of the LED for the design of control schemes; moreover, an efficient power source is needed to supply the voltage and current variations required by the lamp. This paper presents the design of a DC-DC converter capable of implementing these variations, as well as the design, simulation and comparison of classical PI, fuzzy PI and gain-scheduling control schemes for these applications. In order to validate the described control schemes and to comply with the recommendations of the World Health Organization, the control of the illuminance produced by an eye protection lamp is taken as a case study, where the controller varies the duty cycle of the converter to adjust the voltage of the lamp, and consequently regulate the luminous intensity. Comparing the control schemes, the gain-scheduling control has a better performance for the case study described above, presenting a steady state error of 0% and lower overshoot.

Keywords: control, converter, dimming, Gain-scheduling, LED, nonlinear

Resumen

En la actualidad existen diversas aplicaciones de la iluminación LED, sin embargo, algunas de estas requieren regular la iluminación con precisión y en un amplio rango de operación, principalmente en tareas de seguimiento. Es en estos casos en donde es necesario considerar la no linealidad del LED para el diseño de esquemas de control, además, se necesita de una fuente de alimentación eficiente ante los cambios de tensión y corriente requeridos por la lámpara. En este trabajo se presenta el diseño de un convertidor DC-DC capaz de realizar y soportar estas variaciones, así como el diseño, simulación y comparación de esquemas de control PI clásico, PI difuso y ganancias programadas para estas aplicaciones. Con el fin de validar los esquemas de control descritos, y con el propósito de cumplir las recomendaciones de la Organización Mundial de la Salud, se toma el control de la iluminancia producida por una lámpara de protección ocular como caso de estudio, en donde el controlador varía el ciclo de trabajo del convertidor, ajustando de esta manera la tensión de la lámpara, y en consecuencia regulando la intensidad luminosa. Comparando los esquemas de control, el desempeño del sistema con el control por ganancias programadas tiene mejores características para el caso de estudio descrito con anterioridad, presentándose un error en estado estable de 0 % y menor sobretiro en comparación con los otros esquemas de control desarrollados.

Palabras clave: control, convertidor, ganancias programadas, LED, no lineal, regulación

[1,*]Centro Nacional de Investigación y Desarrollo Tecnológico, Tecnológico Nacional de México, Cuernavaca, México. Corresponding author ✉: m21ce085@cenidet.tecnm.mx.

Suggested citation: Olivar-Castellanos, G. S.; Vela-Valdés, L. G. and Aguayo-Alquicira, J.“Scheduled gains control applied to a DC-DC converter for light intensity dimming an LED lamp”. *Ingenius, Revista de Ciencia y Tecnología*. N.° 29, (january-june). pp. 66-78. 2023. DOI: https://doi.org/10.17163/ings.n29.2023.06.

1. Introduction

Over time, lightning has experienced various technological advances, such as the incorporation of the LED (light emitting diode) in different applications. This is mainly because LEDs have low consumption, high reliability and a larger useful life compared to other technologies, which make them a sustainable, practical and functional alternative to save energy [1].

In this technology, some applications are so simple that an On-Off control of the LED lamp is enough, but many others often require to regulate light intensity between 0% and 100% with a fine resolution [2].

There are different architectures for LED controllers, whose objective is to address the requirements and limitations posed by different lightning applications, such as indoor/outdoor lightning, greenhouse lamps, traffic signals, etc. LED controllers are often developed and adapted from basic topologies of AC-DC and/or DC-DC converters, to integrate functionalities such as precise power control or regulation of light intensity [3].

Regardless of their complexity, all power conversion systems have at least one DC-DC converter stage. The topologies of DC-DC converters most commonly used in the development of LED drivers include buck, boost, flyback, sepic and/or half-bridge converters [3].

However, there are applications in which it is essential to incorporate control schemes with the aim of improving the precision and response of the system. For this purpose, classical control schemes have been commonly used in [4–7] for regulation applications, i.e., where there is a single operating point of the LED, since they are enough to guarantee the desired dynamics around such point.

On the other hand, there are more complex applications that require stability along the entire operating range of the LED, giving rise to tracking control. Since the LED is a nonlinear device, it is required a nonlinear control strategy to have it work with precision in its entire operating range.

To address this issue, some authors have incorporated schemes based on neural networks [8], fuzzy logic [9–11], or even a combination of control schemes such as the fuzzy PID [12]. Nevertheless, most of these works focus on guaranteeing a low steady-state error, and for these cases it is enough to implement a unique nonlinear control, such as the work presented in [2]. However, there are applications where it is required to watch the maximum overshoot, besides guaranteeing a low error percentage. For this reason, another alternative has been presented in the literature to address the LED nonlinearities, such as the gain-scheduling technique together with a Flyback converter proposed in [13] for light intensity control in a LED arrangement; however, there is no specific application, and the controller is tuned empirically.

The gain-scheduling technique uses linear tools that approximate the nonlinear dynamics of the system, enabling to adjust a controller for every different operating point in advance, and subsequently update the parameters from such designs and according to the operating point of the process [14, 15].

The objective of this work is to design a supply source that regulates the light intensity of a LED lamp in a wide operating range, with low steady-state error and taking care not to damage the lamp with large overshoots. The eye protection lamps are used a case study.

The rest of the paper is organized as follows. Section 2 presents the methodology for developing the system, which comprises from lamp characterization to tuning the control schemes. Section 3 analyzes the results obtained, and finally section 4 addresses conclusions and future works.

1.1. Case study: Eye protection lamp

According to the World Health Organization (WHO), at least 2200 million people have vision impairment or blindness, and more than 1000 million could have prevented it [16]. Some studies demonstrate that for 2050, 50% of the world population will suffer myopia, and human vision will face an increasingly severe test [17].

One of the main causes of visual impairment is myopia, which may be prevented having the appropriate lighting levels. For this reason, the WHO recommends to maintain an illuminance level of 500 lx in the study and working areas, preferably with white light sources, in order to prevent this condition [18].

This is not a simple task, since external light sources, such as natural lighting, or even other sources of artificial lightning, disturb lighting in the desired area, causing that the recommended levels are not reached.

Based on this, it is necessary a system capable of regulating the light intensity provided by an eye protection lamp, such that it complements the external lighting, maintaining the illuminance level at the 500 lx recommended by the WHO.

Taking this into account, a DC-DC converter is designed with control schemes such as classical PI, fuzzy PI and gain-scheduling, with the purpose of selecting the control scheme suitable for this case study, and thus demonstrate that a linear control scheme is not appropriate for tracking tasks in LED lighting.

2. Materials and methods

A LED is a device whose light intensity depends on the current that circulates through it [13]. Nevertheless, this current depends on the voltage across its terminals. Therefore, for varying the light intensity of a LED it is practical to vary the voltage. For this purpose, it is necessary a supply source capable of performing and withstanding these variations.

Because of this, it is proposed to implement a DC-DC converter that fulfills these requirements. In addition, a control scheme should be incorporated to guarantee the levels recommended by the WHO. This is represented by the block diagram shown in Figure 1.

The required illuminance level is assured if it is guaranteed that the lamp voltage is the desired one. Therefore, in order to simplify the system, the different controllers are tuned considering the voltage value as reference.

The entire process is described in subsequent sections, using Simulink/Matlab to simulate the system under the action of the controllers.

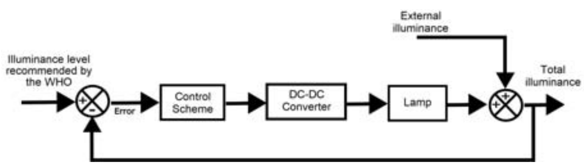

Figure 1. Block diagram of the system proposed

2.1. Lamp characterization

In order to have the eye protection lamp supplementing natural light, it is necessary to design a supply source with a controller that enables to regulate the illuminance depending on the varying conditions of natural light.

The first step is to characterize the lamp. The schematic diagram shown in Figure 2 is used for this purpose. It is known that the lamp requires an input voltage of 12 VDC; hence, such voltage is applied and then progressively reduced, measuring the changes in voltage, current and illuminance.

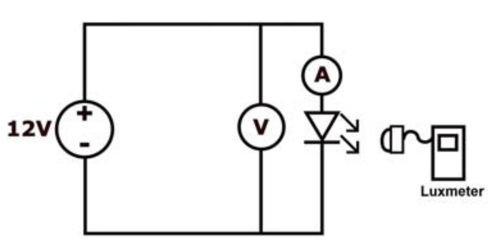

Figure 2. Circuit for characterizing the lamp

Figure 3 shows the V-I (voltage-current) curve and Figure 4 shows the V-E (voltage-illuminance) curve, both obtained plotting the measured data.

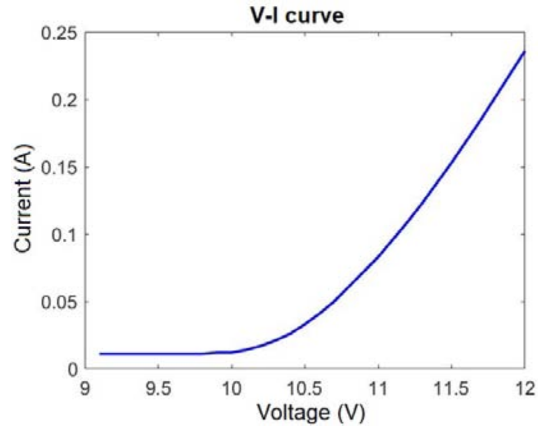

Figure 3. V-I curve of the eye protection lamp

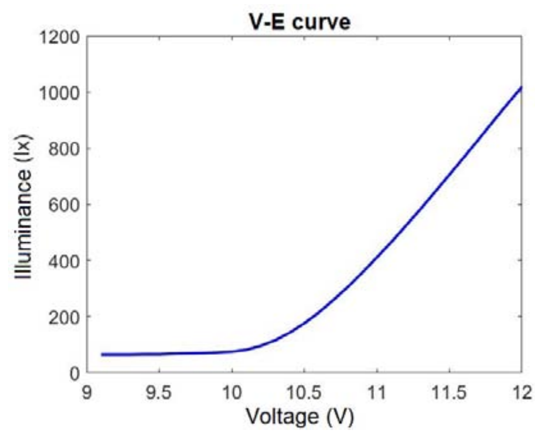

Figure 4. V-E curve of the eye protection lamp

2.2. Design of the DC-DC converter

The Buck converter is used in applications where the load requires voltages lower than the input voltage of the converter. Its implementation is simple due to the few components; in addition, its control is simple because the relationship between the output and input voltages is proportional to the duty cycle of the control signal [13].

For this reason, the Buck converter is chosen as the supply source for the lamp. The specifications shown in Table 1, which are proposed from the characterization of the lamp, are defined for the design of the converter. Figure 5 shows the topology of this converter.

Table 1. Design specifications of the converter

Parameter	Symbol	Value
Input voltage	V_{in}	24 V
Minimum output voltage	$V_{omín}$	9 V
Maximum output voltage	$V_{omáx}$	12 V
Maximum output power	$P_{omáx}$	3.5 W
Switching frequency	f_s	66.67 KHz
Current ripple in the inductor	Δ_{iL}	0.3 $\%I_{omáz}$
Voltage ripple in the capacitor	Δ_{vc}	0.1 $\%V_{omín}$

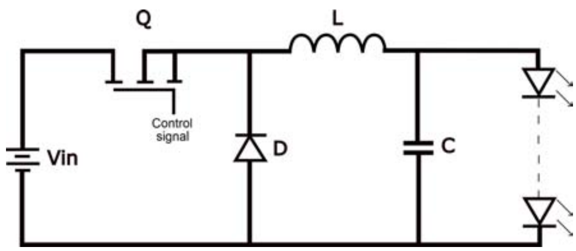

Figure 5. Topology of the Buck converter

From the analysis and the equations showed by Gamboa [19], it is made the calculation and selection of the components. Their values are shown in Table 2.

Table 2. Calculation of the components and variables of the converter

Parameter	Symbol	Value
Minimum duty cycle	$D_{mín}$	0.375
Maximum duty cycle	$D_{máx}$	0.5
Inductor	L	102.85 mH
Capacitor	C	182.29 nF
Average current through the switch	I_Q	0.146 A
Voltage across the switch	V_{DS}	24 V
Average current through the diode	I_D	0.243 A
Voltage across the diode	V_D	24 V

2.3. Transfer functions

To obtain the transfer functions (TF) it should be considered that the converter load is variable, because the LED works at different operating points according to the requirements. Therefore, it is not possible to obtain a unique linear TF that represents the entire dynamics of the system.

Based on the above and to facilitate the design of the controllers, the V-E curve is divided into five ranges approximately linear, as shown in Figure 6. After the curve is divided, it is possible to obtain five TFs that approximate the dynamics in each of those ranges.

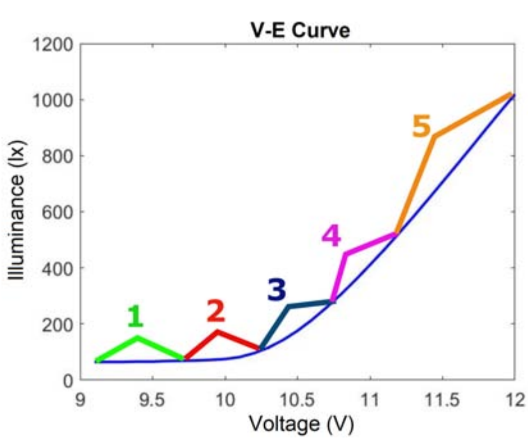

Figure 6. V-E curve divided into five ranges

Afterwards, since the operating points are defined, it is possible to obtain the TF from the control-output characteristic function of a Buck converter, shown in Equation (1).

$$G_{vd} = \frac{y(s)}{\hat{d}(s)} = \frac{V_{in}\left(\frac{1}{LC}\right)}{s^2 + \frac{1}{RC}s + \frac{1}{LC}} \tag{1}$$

Since the controller performs in the entire operating range of the lamp, the value of R in Equation (1) is variable. Therefore, an average R is calculated in each of the ranges defined, thus obtaining a different TF for each operating range. The parameters for these TFs are shown in Table 3, whereas the transfer functions are shown in Equations (2) - (6).

$$\frac{24(53337524.95)}{s^2 + 6385.48s + 53337524.95} \tag{2}$$

$$\frac{24(53337524.95)}{s^2 + 6925.77s + 53337524.95} \tag{3}$$

$$\frac{24(53337524.95)}{s^2 + 14428.63s + 53337524.95} \tag{4}$$

$$\frac{24(53337524.95)}{s^2 + 38978s + 53337524.95} \tag{5}$$

$$\frac{24(53337524.95)}{s^2 + 80507.26s + 53337524.95} \tag{6}$$

Table 3. Parameters of the transfer functions

Range	Vin	L	C	R	T. F.
9.2 V – 9.7 V				859.10 Ω	(2)
9.7 V – 10.2 V				792.08 Ω	(3)
10.2 V – 10.7 V	24 V	102.85 mH	182.29 nF	380.2 Ω	(4)
10.7 V – 11.3 V				140.74 Ω	(5)
11.3 V – 12 V				68.14 Ω	(6)

It is important to remark that having a different transfer function for each operating range implies that different dynamics are achieved in each of them. This is due to the fact that there is a different damping ratio (ζ) in each range, despite the natural frequency is the same (ω_n). This is detailed in Table 4.

Table 4. Damping ratio and natural frequency in the operating ranges

Range	T. F.	ζ	$\boldsymbol{\omega_n}$
9.2 V–9.7 V	(2)	0.437	7304.32 rad/s
9.7 V-10.2 V	(3)	0.474	7304.32 rad/s
10.2 V-10.7 V	(4)	0.988	7304.32 rad/s
10.7 V-11.3 V	(5)	2.66	7304.32 rad/s
11.3 V–12 V	(6)	5.51	7304.32 rad/s

2.4. Tuning of a PI controller

Since the PI control scheme is one of the most widely used in applications with DC-DC converters, such control scheme is tuned to validate and compare its performance in the regulation of the illuminance of an eye protection lamp.

The controller is tuned for the intermediate operating range, corresponding to the TF of Equation (4).

The pole assignment methodology is used for the tuning, considering that the characteristic equation of a second order TF may be simplified as shown in Equation (7).

$$G(s) = \frac{k}{s^2 + as + b} \tag{7}$$

In addition, it is known that the TF of a PI controller is of the form shown in Equation (8).

$$C(s) = \frac{K_c s + K_i}{s} \tag{8}$$

Then, closing the loop of the plant with the controller results in the TF shown in Equation (9).

$$H(s) = \frac{k(K_c s + K_i)}{s^3 + as^2 + (b + kK_c)s + kK_i} \tag{9}$$

Therefore, a pole assignment should be implemented based on a characteristic equation of the form shown in Equation (10), corresponding to a third order system with two complex conjugate poles and a real pole, where β represents a factor of proportionality that relates the distance of the real pole with respect to the complex conjugate poles.

$$P_d = (s + \beta\zeta\omega_n)(s^2 + 2\zeta\omega_n + \omega_n^2) \tag{10}$$

Then, setting (10) equal to the denominator of the closed-loop TF of Equation (9) and solving for the unknowns, results in three equations useful to calculate the gains of the PI controller. is calculated using Equation (11), whereas Equations (12) and (13) are used to calculate the proportional gain (K_c) and the integral gain (K_i), respectively.

$$\beta = \frac{\alpha}{\zeta\omega_n} - 2 \tag{11}$$

$$K_c = (\frac{2\beta\zeta^2 + 1)\omega_n^2 - b}{k} \tag{12}$$

$$K_i = \frac{\beta\zeta\omega_n^3}{k} \tag{13}$$

In this manner, the gains of the PI controller may be calculated from the desired damping ratio (ζ) and natural frequency (ω_n). It is important to mention that it is possible to calculate ζ and ω_n from Equations (14) and (15), defining a maximum overshoot (M_p) and a settling time (t_{ss}). In this case, it is proposed an M_p not larger than 5 % and to search for a t_{ss} of 1 ms.

$$\zeta = \sqrt{\frac{ln\left(\frac{\%M_p}{100}\right)^2}{\pi^2 + ln\left(\frac{\%M}{100}\right)^2}} \tag{14}$$

$$\omega_n = \frac{4}{\zeta t_{ss}} \tag{15}$$

Therefore, it is obtained that $\beta = 1.608$, $K_c = 0.247$ and $K_i = 168.7537$. This is implemented as shown in Figure 7.

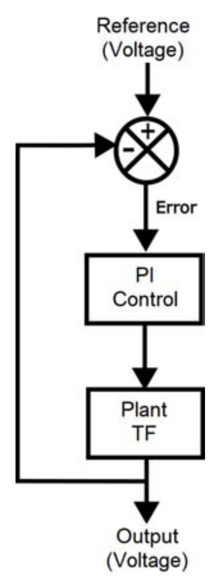

Figure 7. Block diagram of the implementation of the PI control

2.5. Tuning of a fuzzy PI controller

It is common that fuzzy logic control has a level of uncertainty, since it is better expressed as a control through words that interpret common sense, instead of numbers, or sentences instead of equations [20]. However, the process variables are not measured in common sense, but in numbers.

To overcome this issue, it is convenient to incorporate the gains of a PI controller to numerically correct the weaknesses of the fuzzy interpretation. The block diagram that represents this control scheme is shown in Figure 8.

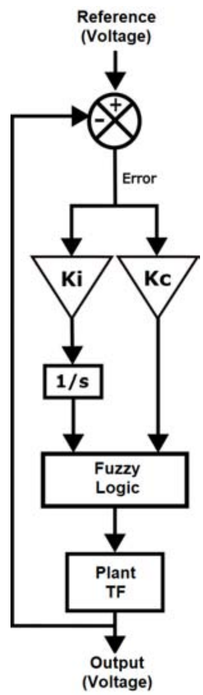

Figure 8. Block diagram of the implementation of the fuzzy PI control

The design of the fuzzy controller requires to clearly know the input and output variables. In this case, the input variables are the error and the integral of the error, and the output is the duty cycle, since this is the variable required by the plant.

Since the error is obtained through the comparison of the output of the converter, which corresponds to a maximum voltage of 12 V, it is defined a universe of discourse between {−12, 12} for both inputs. It is important to mention that the universe defined contains negative numbers, because it is possible to obtain a positive or a negative difference between the output and the reference.

The linguistic variables defined for the error signal are:

- NE: Negative Error
- ZE: Zero Error
- PE: Positive Error

On the other hand, the linguistic variables defined for the integral of the error are:

- NIE: Negative Integral of the Error
- ZIE: Zero Integral of the Error
- PIE: Positive Integral of the Error

Once the different linguistic variables for the inputs have been established, as well as the associated universes of discourse, the corresponding fuzzy sets are defined, as shown in Figure 9 and Figure Figura 10, respectively.

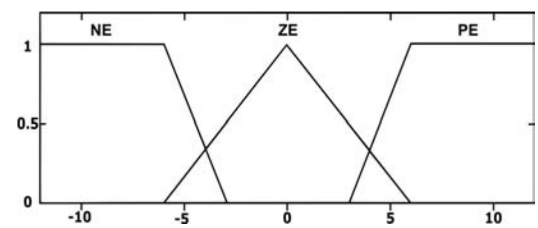

Figure 9. Fuzzy sets for the error

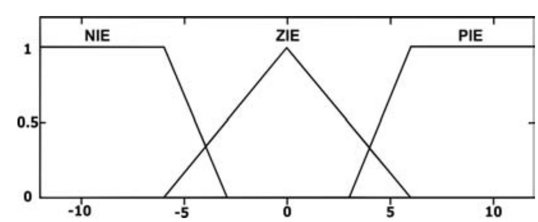

Figure 10. Fuzzy sets for the integral of the error

On the other hand, the output of the fuzzy block is the duty cycle, whose universe of discourse is defined between {0, 1} because this is its interval of operation.

The linguistic variables defined for the duty cycle are:

- S: Small
- I: Ideal
- L: Large

The fuzzy sets of the duty cycle are shown in Figure 11.

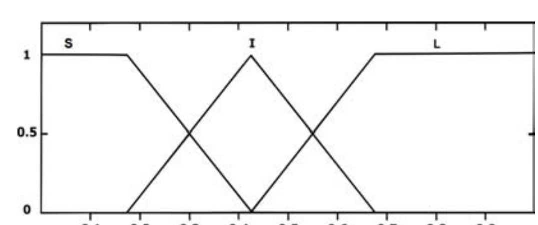

Figure 11. Fuzzy sets for the duty cycle

Once the different fuzzy sets have been defined, the control rules are assigned. For each output it is assigned an appropriate linguistic variable, based on the possible combinations of the inputs. The set of rules is shown in Table 5.

Table 5. Fuzzy rules for the output variable of the controller

		Integral of the error		
		NIE	**ZIE**	**PIE**
Error	**NE**	D: S	D: S	D: S
	ZE	D: I	D: I	D: I
	PE	D: L	D: L	D: L

In order to verify the performance of the fuzzy PI controller, the fuzzy sets and rules defined are uploaded in the fuzzyLogicDesigner tool.

2.6. Gain-scheduling control

Gain-scheduling control consists of designing a controller for every different operating point in advance, and further selecting the controller to be implemented from such designs according to the operating point of the process [14, 15].

One of the most widely used methods for selecting the gains is fuzzy logic, which gives rise to a control strategy known as fuzzy gain scheduling [13].

In this strategy fuzzy logic is responsible for varying the gains in real-time, with the added benefit of enabling a smooth transition between the controllers determining intermediate values of the gains, and thus reducing drastic changes that may affect the controller and the plant.

Based on the above, the block diagram of Figure 12 shows the system to be implemented. The gain-scheduling control designed is constituted by a fuzzy logic block, which is responsible of choosing the gains of the PI controller depending on the operating point.

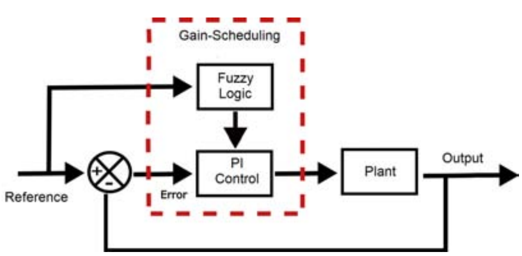

Figure 12. Block diagram of a gain-scheduling control

Since the operating range of the LED lamp has been divided into five intervals, there are 5 different TFs for a which a different PI controller should be designed.

Considering that each operating range has different dynamics, distinct design specifications are proposed for each of those ranges.

An important point to be taken into account is that the overshoot should not be very large in the operating range from 11.3 V to 12 V, because the LED lamp could be damaged. Based on this, Table 6 shows the design specification for each controller.

Table 6. Design specifications for the PI controllers

Range	T. F.	% M_p	t_{ss}
9.2 V-9.7 V	(2)	10%	1.5 ms
9.7 V-10.2 V	(3)	8%	1.5 ms
10.2 V-10.7 V	(4)	5%	1.5 ms
10.7 V-11.3 V	(5)	2%	5 ms
11.3 V-12 V	(6)	1%	8 ms

The pole assignment methodology described in section 2.4 is used for tuning the controllers, which gives the gains shown in Table 7.

Table 7. Gains of the PI controllers

Range	K_c	K_i
9.2 V – 9.7 V	0.0203	16.725
9.7 V – 10.2 V	0.0208	225.323
10.2 V – 10.7 V	0.0079	1.060.908
10.7 V – 11.3 V	0.0059	307.392
11.3 V – 12 V	0.0207	227.538

On the other hand, a fuzzy logic control is designed for selecting the gains of the PI controller.

For this case, it is convenient to have the reference signal as input variable, since it defines the working operating range. Similarly, the Kc and Ki gains are defined as output variables, since these variables vary depending on the operating range.

Taking into account the operating range, the universe of discourse of the input variable is defined as {9, 12}. On the other hand, the linguistic variables for the operating ranges are defined as:

- R1: {9.2 – 9.7}
- R2: {9.7 – 10.2}
- R3: {10.2 – 10.7}
- R4: {10.7 – 11.3}
- R5: {11.3 – 12}

Once the linguistic variables of the input have been established, the fuzzy sets shown in Figure 13 are defined.

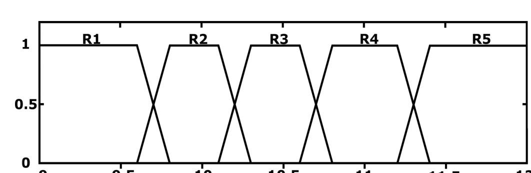

Figure 13. Fuzzy sets of the operating ranges

Regarding the fuzzy sets of the output, the universe of discourse for K_c is {0.004, 0.022} and for K_i is {10, 110}.

Meanwhile, it is observed for linguistic variables that there are two ranges where the gains are very similar; consequently, these two were averaged and defined as a single one, and thus the linguistic variables for K_c are defined as:

- Very small - MP: 0.0059
- Small - S: 0.0079
- Medium - M: 0.0203
- Large - L: 0.02075

On the other hand, the linguistic variables for K_i are defined as:

- Small – S: 16.725
- Medium – M: 22.6430
- Large – L: 30.7392
- Very Large – VL: 106.0908

Then, the fuzzy sets for the Kc gain are defined as shown in Figure 14, whereas the fuzzy sets for the Ki gain is shown in Figure 15.

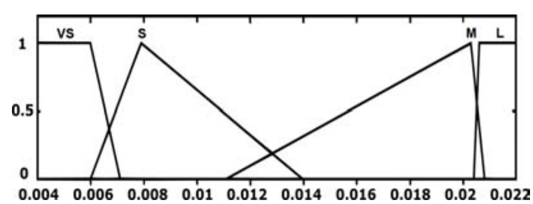

Figure 14. Fuzzy sets for the proportional gain K_c

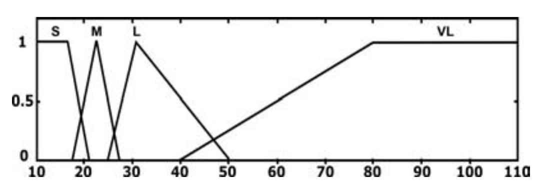

Figure 15. Fuzzy sets for the integral gain K_i

For the set of rules, a linguistic variable is assigned based on the input for each output, as shown in Table 8.

Table 8. Set of rules for selecting the gains

Reference	Gains	
R1	$K_c = M$	$K_i = S$
R2	$K_c = L$	$K_i = M$
R3	$K_c = S$	$K_i = VL$
R4	$K_c = VS$	$K_i = L$
R5	$K_c = L$	$K_i = M$

It should be recalled that it is desired to control the illuminance level in a study or working area, to maintain the 500 lx recommended by WHO. Voltage levels were used to facilitate the design of these controllers, and thus it is required to convert from voltage to illuminance. This may be carried out based on lamp characterization, modifying the block diagram of the system as shown in Figure 16.

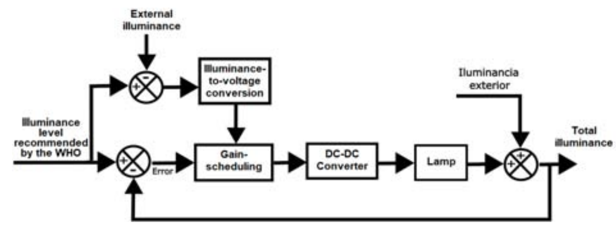

Figure 16. Block diagram of the system including the lamp

3. Results and discussion

For validating the control schemes designed, they are simulated with three different transfer functions: the intermediate transfer function, given by equation (4), and the transfer functions at the ends of the operating range of the lamp, given by equations (2) and (6).

Figure 17 shows the response obtained when simulating the intermediate transfer function with the PI controller. It is observed that there is a steady-state error of 0%, a maximum overshoot of 4.6% and a settling time of approximately 1.8 ms.

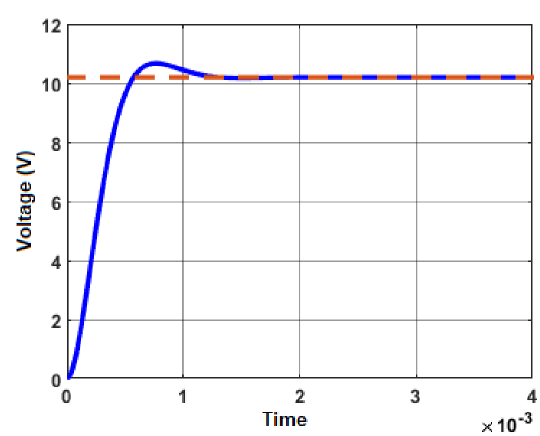

Figure 17. Response of the transfer function corresponding to the intermediate operating range with a PI control scheme

Nevertheless, some undesired dynamics appear when the same control scheme is simulated with the same gains in the operating ranges at the ends; in particular, the maximum overshoot exceeds the 12 V corresponding to the supply voltage of the lamp. The responses of these TFs under the action of the control scheme are shown in Figures 18 and 19 respectively.

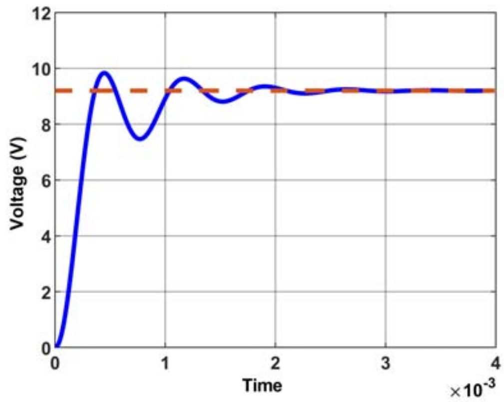

Figure 18. Response of the transfer function corresponding to the lower operating range with a PI control scheme

Although in these three cases a steady-state error of 0% is reached, an overshoot above 12 V may damage the lamp, and thus a unique PI control is not very suitable for the application.

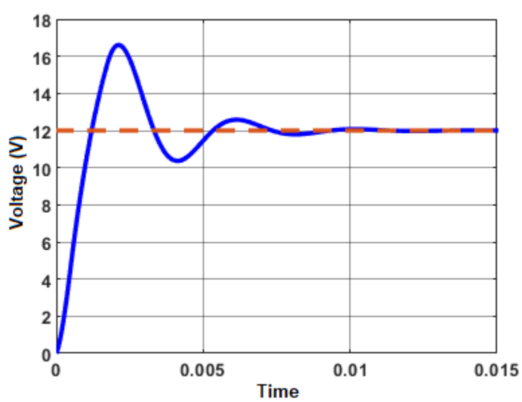

Figure 19. Response of the transfer function corresponding to the upper operating range with a PI control scheme

On the other hand, an improvement in the response within the tuning range is obtained when simulating the fuzzy PI control scheme, since the maximum overshoot is significantly reduced, as shown in Figure 20. In addition, a steady-state error of 0% is guaranteed and a settling time of 1.2 ms is achieved.

Nevertheless, undesired responses are obtained when the same controller is applied in the operating ranges at the ends, since even though there is no overshoot, the steady-state error is greater than 2%, as shown in Figures 21 and 22.

On the other hand, the desired response is obtained for each of the ranges when using the gain-scheduling control scheme. Figure 23 shows the response for the intermediate operating range, whereas the responses for the lower and upper operating ranges are shown in Figures 24 and 25, respectively.

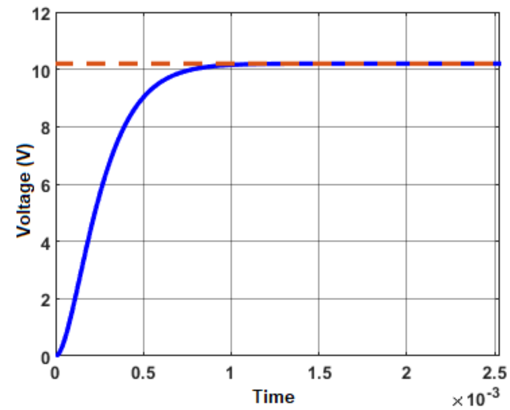

Figure 20. Response of the transfer function corresponding to the intermediate operating range with a fuzzy PI control scheme

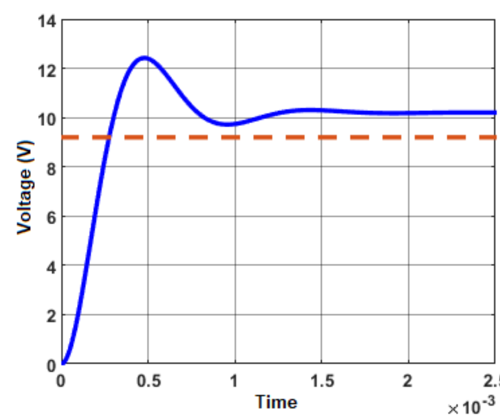

Figure 21. Response of the transfer function corresponding to the lower operating range with a fuzzy PI control scheme

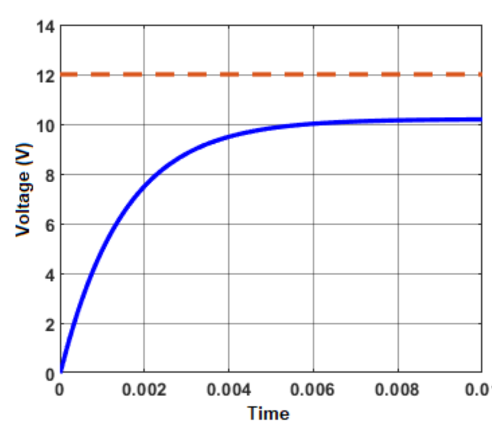

Figure 22. Response of the transfer function corresponding to the upper operating range with a fuzzy PI control scheme

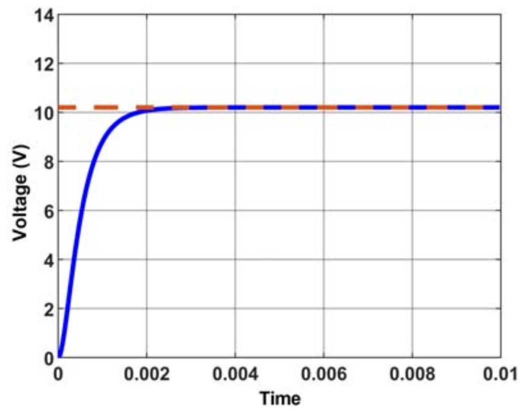

Figure 23. Response of the transfer function corresponding to the intermediate operating range with a gain-scheduling control schem

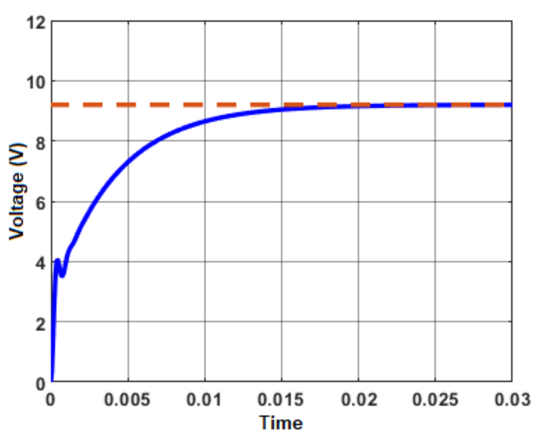

Figure 24. Response of the transfer function corresponding to the lower operating range with a gain-scheduling control scheme

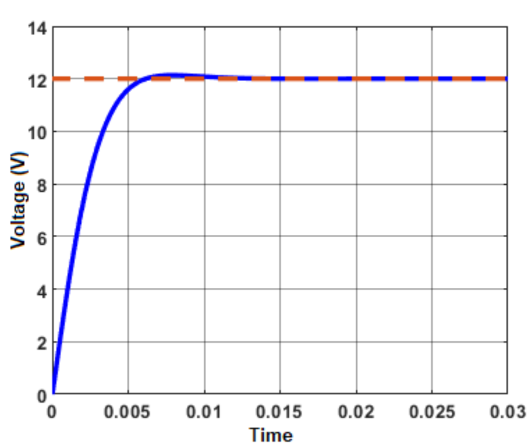

Figure 25. Response of the transfer function corresponding to the upper operating range with a gain-scheduling control scheme

It is seen that all responses have a steady-state error of 0%, and maximum overshoots smaller than 2%. However, the settling time increases.

A comparison of the responses obtained with the three control schemes is shown in Table 9.

Table 9. Comparison of the responses obtained with the PI, fuzzy PI and gain-scheduling control schemes

Parameter	Control scheme	Range: 9.2 V - 9.7 V	Range: 10.2 V - 10.7 V	Range: 11.3 V - 12 V
Setting time	*PI Control*	3.95 ms	1.8 ms	13 ms
	Fuzzy PI Control	2.2 ms	1.2 ms	9 ms
	Gain scheduling	24 ms	3 ms	12 ms
Maximum overshoot	*PI Control*	6.78 %	4.6 %	38.42 %
	Fuzzy PI Control	35%	0%	0%
	Gain scheduling	0%	0%	1.08 %
Steady-estate error	*PI Control*	0%	0%	0%
	Fuzzy PI Control	10.86 %	0%	15%
	Gain scheduling	0%	0%	0%

It is important to mention that the maximum overshoot and the settling time for which the gain-scheduling control was tuned are different from the design specifications. This is mainly due to the effects of the real pole and the zero that appears when the loop is closed.

However, these effects do not harm the desired dynamics but benefit it, achieving very small overshoots. The effect of the real pole and the zero is mostly noted in the settling time; however, this time is in the order of milliseconds, which for the case of lighting and of the converter is not relevant.

Based on the above, the gain-scheduling control shows a better response in the entire operating range of the lamp, and thus the simulations incorporate the model of the lamp. The external illuminance pattern is taken from the levels of solar irradiance during a spring day, in the city of Cuernavaca, Morelos, Mexico, collected from the database of the Instituto Nacional de Ecología y Cambio Climático [21]. This pattern is shown in Figure 26.

The eye protection lamp should supplement the lighting in the case of changes in the external illuminance, in order to maintain the 500 lx recommended by the WHO. The response of the system in the presence of variations in the external illuminance is shown in Figure 27.

It is seen that despite the changes in the external lighting, the level of total illuminance is maintained at the 500 lx recommended by the WHO. However, it is observed a higher ripple when the external lighting is minimum. This ripple is shown in Figure 28, and it appears because at this point the converter should supply a higher voltage to the lamp, and consequently there is a higher voltage ripple due to the effects of the converter output capacitor. However, this ripple is around 1 %, which is within the margins that are acceptable from the point of view of control theory.

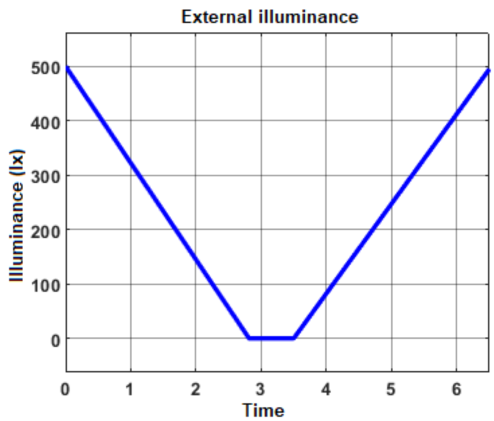

Figure 26. Pattern of external illuminance

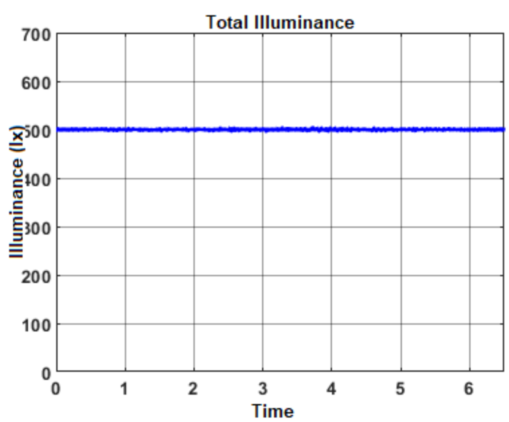

Figure 27. Total illuminance of the system

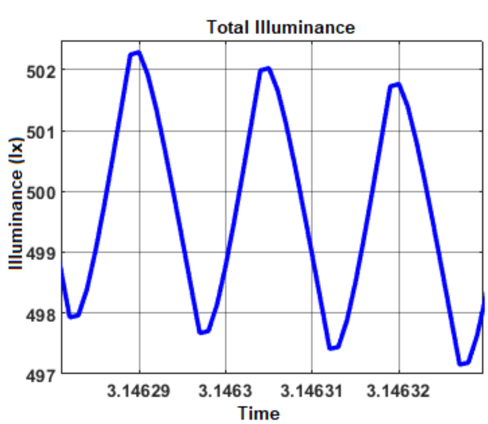

Figure 28. Effects of the voltage ripple on the illuminance

On the other hand, Figure 29 shows the voltage supplied by the designed converter. It is seen that the voltage remains within the operating ranges, which guarantees not damaging the lamp. In addition, it is shown that the lamp does not work in a single operating point, but it demands different voltage levels to the converter according to the changes in the level of external illuminance.

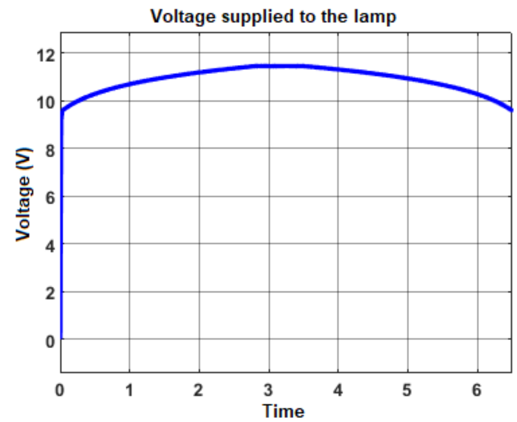

Figure 29. Voltage supplied to the lamp by the DC-DC converter

4. Conclusions

At present, there are different applications of LED lamps. Some of them require precision when varying the light intensity, such as eye protection lamps.

For that reason, this work presented the simulation of a DC-DC converter with three control schemes, which vary the illuminance of an eye protection lamp to maintain the 500 lx recommended by the WHO to prevent eye diseases, and considering that external light sources disturb the lighting provided by the lamp.

A classical PI control scheme is capable of guaranteeing a steady-state error of 0 % in the entire operating range of the lamp, but it does not guarantee appropriate levels of maximum overshoot.

On the other hand, the designed fuzzy PI control scheme is capable of guaranteeing that the voltage levels supported by the lamp are not exceeded; however, if the operating point changes the steady-state error increases.

Conversely, the designed gain-scheduling control scheme is a combination of the PI and fuzzy logic controllers, where the latter is used as gain selector to enable the adjustment of the controller gain depending on the operating point of the system. In this manner, it is guaranteed to have a steady-state error of 0 % and to reduce as much as possible the maximum overshoot.

In the simulation of the gain-scheduling control scheme including the model of the lamp, it was possible to maintain the illuminance level at 500 lx, and thus the lamp supplements external lighting to fulfill the recommendation by the WHO. In addition, it is guaranteed that the DC-DC converter does not supply voltage levels that exceed the operating range of the lamp, and thus it is verified that the light intensity of the LED lamp is regulated precisely and guaranteed not to damage it, as opposed to other works that focus on the control at only one operating point using a linear controller.

As a future work, it is worth mentioning that it is possible to improve the ripple present in the total illuminance, by increasing the capacitance value of the converter output capacitor; however, this modifies the TFs, and thus the dynamics obtained.

On the other hand, gain-scheduling control may be incorporated in different applications, and it is thus recommended its validation with other case studies related to lighting applications.

References

[1] M. C. Gutiérrez Hernández, "Iluminación LED. ahorro, eficiencia e innovación. Proyecto de mejora de la iluminación de un hotel," Universidad de la Laguna, España, 2015. [Online]. Available: https://bit.ly/3uM3vie

[2] N. Pai and S. G. Kini, "Design and prototyping of dimmable LED driver for general lighting application," in *2018 Second International Conference on Electronics, Communication and Aerospace Technology (ICECA)*, 2018, pp. 1–6. [Online]. Available: https://doi.org/10.1109/ICECA.2018.8474548

[3] F. Bento and A. J. M. Cardoso, "Comprehensive survey and critical evaluation of the performance of state-of-the-art LED drivers for lighting systems," *Chinese Journal of Electrical Engineering*, vol. 7, no. 2, pp. 21–36, 2021. [Online]. Available: https://doi.org/10.23919/CJEE.2021.000013

[4] S. Iturriaga-Medina, P. Martínez-Rodrgúez, M. Juárez-Balderas, J. Sosa, and C. Limones, "A buck converter controller design in an electronic drive for LED lighting applications," in *2015 IEEE International Autumn Meeting on Power, Electronics and Computing (ROPEC)*, 2015, pp. 1–5. [Online]. Available: https://doi.org/10.1109/ROPEC.2015.7395105

[5] M. Juárez, P. Martínez, G. Vázquez, J. Sosa, X. Prieto, and R. Martínez, "Analysis of buck converter control for automobile LED headlights application," in *2014 IEEE International Autumn Meeting on Power, Electronics and Computing (ROPEC)*, 2014, pp. 1–4. [Online]. Available: https://doi.org/10.1109/ROPEC.2014.7036298

[6] M. D. Vijay, K. Shah, G. Bhuvaneswari, and B. Singh, "LED based street lighting with automatic intensity control using solar PV," in *2015 IEEE IAS Joint Industrial and Commercial Power Systems / Petroleum and Chemical Industry Conference (ICPSP-CIC)*, 2015, pp. 197–202. [Online]. Available: https://doi.org/10.1109/CICPS.2015.7974074

[7] X. He, H. Wang, J. Cao, and D. Lei, "Design of high-power LED automatic dimming system for light source of on-line detection system," in *2020 IEEE 5th Information Technology and Mechatronics Engineering Conference (ITOEC)*, 2020, pp. 1487–1491. [Online]. Available: https://doi.org/10.1109/ITOEC49072.2020.9141898

[8] N. K. Kandasamy, G. Karunagaran, C. Spanos, K. J. Tseng, and B.-H. Soong, "Smart lighting system using ANN-IMC for personalized lighting control and daylight harvesting," *Building and Environment*, vol. 139, pp. 170–180, 2018. [Online]. Available: https://doi.org/10.1016/j.buildenv.2018.05.005

[9] R. B. Caldo, J. T. Seranilla, D. J. Castillo, K. S. Diocales, W. D. Gulle, B. L. Núñez, and C. T. Parreño, "Design and development of fuzzy logic controlled dimming lighting system using arduino microcontroller," in *2015 International Conference on Humanoid, Nanotechnology, Information Technology,Communication and Control, Environment and Management (HNICEM)*, 2015, pp. 1–6. [Online]. Available: https://doi.org/10.1109/HNICEM.2015.7393161

[10] M. G. Shafer, E. Saputra, K. A. Bakar, and F. Ramadhani, "Modeling of fuzzy logic control system for controlling homogeneity of light intensity from light emitting diode," in *2012 Third International Conference on Intelligent Systems Modelling and Simulation*, 2012, pp. 71–75. [Online]. Available: https://doi.org/10.1109/ISMS.2012.90

[11] D. T. Phan, N. T. Bui, T. H. Vo, S. Park, J. Choi, S. Mondal, B.-G. Kim, and J. Oh, "Development of a LED light therapy device with power density control using a fuzzy logic controller," *Medical Engineering & Physics*, vol. 86, pp. 71–77, 2020. [Online]. Available: https://doi.org/10.1016/j.medengphy.2020.09.008

[12] X. He, C. Huang, Y. Li, H. Wang, D. Lei, and M. Yao, "An adaptive dimming system of high-power led based on fuzzy pid control algorithm for machine vision lighting," in *2020 IEEE 4th Information Technology, Networking, Electronic and Automation Control Conference (ITNEC)*, vol. 1, 2020, pp. 2198–2202. [Online]. Available: https://doi.org/10.1109/ITNEC48623.2020.9084741

[13] R. Gil Bernal and D. F. Díaz Caro, "Driver de potencia dimerizable para un arreglo de LED," 2017. [Online]. Available: https://bit.ly/3WhnzVs

[14] M. Lara Ortiz, J. Garrido Jurado, M. L. Ruz Ruiz, and F. Vázquez Serrano, "Control PI adaptativo por ganancia programada del nivel de un tanque de sección trapezoidal," in *XXXIX Jornadas de Automática*. XXXIX Jornadas de Automática, 2018, pp. 444–451. [Online]. Available: https://doi.org/10.17979/spudc.9788497497565

[15] J. A. Brizuela-Mendoza, A. Zavala-Río, and C. M. Astorga-Zaragoza, "Controlador de ganancias programadas aplicado a la estabilización de una bicicleta sin conductor," in *Congreso Nacional de Control Automático*, 2013, pp. 36–41. [Online]. Available: https://bit.ly/3BxfofX

[16] OMS. (2019) La OMS presenta el primer informe mundial sobre la visión. [Online]. Available: https://bit.ly/3YwQneO

[17] B. A. Holden, T. R. Fricke, D. A. Wilson, M. Jong, K. S. Naidoo, P. Sankaridurg, T. Y. Wong, T. J. Naduvilath, and S. Resnikoff, "Global prevalence of myopia and high myopia and temporal trends from 2000 through 2050," *Ophthalmology*, vol. 123, no. 5, pp. 1036–1042, Feb. 2016. [Online]. Available: https://doi.org/10.1016/j.ophtha.2016.01.006

[18] Y. Xiaogang, W. Wang, and L. Fenna, "Design and simulation of intelligent dimmer based on fuzzy PID," in *2020 International Conference on Intelligent Design (ICID)*, 2020, pp. 86–89. [Online]. Available: https://doi.org/10.1109/ICID52250.2020.00025

[19] R. A. Gamboa López, "Asistente para el diseño y simulación de convertidores CD-CD en lazo cerrado," Master's thesis, 2018. [Online]. Available: https://bit.ly/3iVLSKl

[20] S. González de León, "Control PID con sintonización difusa y control difuso," Master's thesis, 2013. [Online]. Available: https://bit.ly/3Fpn3hC

[21] INECC. (2019) Datos Estación Cuernavaca. Instituto Nacional de Ecología y Cambio Climático. [Online]. Available: https://bit.ly/2wGUPvC

Scientific Paper / Artículo Científico

UNIVERSIDAD POLITÉCNICA SALESIANA ECUADOR
INGENIUS
Revista de Ciencia y Tecnología
https://doi.org/10.17163/ings.n29.2023.07
pISSN: 1390-650X / eISSN: 1390-860X

Prediction of Arrhythmias and Acute Myocardial Infarctions using Machine Learning

Predicción de arritmias e infartos agudos de miocardio usando aprendizaje automático

Darwin Patiño[1,*], Jorge Medina[1], Ricardo Silva[2], Alfonso Guijarro[1], José Rodríguez[1]

Received: 16-11-2022, Received after review: 06-12-2022, Accepted: 12-12-2022, Published: 01-01-2023

Abstract

Cardiovascular diseases such as Acute Myocardial Infarction is one of the 3 leading causes of death in the world according to WHO data, in the same way cardiac arrhythmias are very common diseases today, such as atrial fibrillation. The ECG electrocardiogram is the means of cardiac diagnosis that is used in a standardized way throughout the world. Machine learning models are very helpful in classification and prediction problems. Applied to the field of health, ANN, and CNN artificial and neural networks, added to tree-based models such as XGBoost, are of vital help in the prevention and control of heart disease. The present study aims to compare and evaluate learning based on ANN, CNN and XGBoost algorithms by using the Physionet MIT-BIH and PTB ECG databases, which provide ECGs classified with Arrhythmias and Acute Myocardial Infarctions respectively. The learning times and the percentage of Accuracy of the 3 algorithms in the 2 databases are compared separately, and finally the data are crossed to compare the validity and safety of the learning prediction.

Keywords: arrhythmias, acute myocardial, infarction, machine learning, artificial neural network, convolutional neural network, extreme gradient boosting

Resumen

Las enfermedades cardiovasculares, como el infarto agudo de miocardio, son una de las tres principales causas de muerte en el mundo según datos de la OMS. De forma similar, las arritmias cardíacas¸ como la fibrilación auricular, son enfermedades muy comunes en la actualidad. El electrocardiograma (ECG) es el medio de diagnóstico cardíaco que se utiliza de forma estandarizada en todo el mundo. Los modelos de aprendizaje automático son muy útiles en problemas de clasificación y predicción. Aplicadas al campo de la salud, las redes neuronales artificiales (ANN) y las redes neuronales convolucionales (CNN) en conjunto con modelos basados en árboles como XGBoost, son de vital ayuda en la prevención y control de enfermedades del corazón. El presente estudio tiene como objetivo comparar y evaluar el aprendizaje basado en los algoritmos ANN, CNN y XGBoost mediante el uso de las bases de datos de ECG Physionet MIT-BIH y PTB, que proporcionan ECG clasificados con arritmias e infartos agudos de miocardio, respectivamente. Se comparan por separado los tiempos de aprendizaje y el porcentaje de exactitud de los tres algoritmos en las dos bases de datos, finalmente, se cruzan los datos para comparar la validez y seguridad de la predicción.

Palabras clave: arritmias, infarto agudo miocardio, aprendizaje automático, red neuronal artificial, red neuronal convolucional, impulso del gradiente extremo

[1,*]Universidad de Guayaquil, Ecuador. Corresponding author ✉: darwin.patinop@ug.edu.ec.
[2]University of Villanova, Pensilvania, Estados Unidos.

Suggested citation: Patiño, D.; Medina, J.; Silva, R.; Guijarro, A. and Rodríguez, J. “Prediction of Arrhythmias and Acute Myocardial Infarctions using Machine Learning,” *Ingenius, Revista de Ciencia y Tecnología*, N.° 29, pp. 79-89, 2023, DOI: https://doi.org/10.17163/ings.n29.2023.07.

1. Introduction

A multiplicity of devices (personal computers, smartphones, tablets, cell phones, etc.) are used today to accumulate and process bigdata about human behavior. This bigdata is available for a multiplicity of purpose including medicine [1,2]. Mobile Health (mHealth) and smart devices enable early detection and prompt intervention for patients with Atrial Fibrillation (AF). Single- and multi-lead ECG, photoplethysmography (PPG), and oscillometric, with validated diagnostic capability, can be integrated within the clinical practice to detect AF. Existing clinical practice guidelines suggest that pulse assessment with ECG screening for the high-risk population, for patients >65 years of age, is appropriate to reduce complications. However, easy-to-use, and affordable consumer health and smart devices may be a good alternative screening tool not only for the elderly population with comorbidities, but also for the general low-risk population with frequent monitoring [2–7].

mHealth devices that are capable of monitoring heart rate and/or heart rhythm come in multiple forms such as, smartphone apps, smart watches, rings, necklaces, wearable sensors, and patches [8–10]. Companies have created products capable of producing a point-of-care ECG registries, such as the AliveCor Kardia Monitor series of devices [8]. In a large cohort study conducted in Hong Kong, research on the Kardia single-lead ECG device found that a review cardiologist confirmed that 65% of AFs detected by the device were accurate. In this study of more than 10000 patients with a mean age of 78 years, the number needed to make an accurate new diagnosis of AF was 145 participants [8].36 The sensitivity and specificity of the Kardia monitor were found to be 99, 6% and 97.8%, respectively [11].

The term Ubiquitous Health (u-Health) defined by Weiser as the integration of computing into human actions and behaviors at "anytime" and "anywhere" has been gaining prominence [1,2]. The main attribute of u-Health is the capacity for interaction between individuals and devices in such a way that the technology is transparent to the user [12]. It is not clear what is the best algorithm to detect cardiovascular diseases by means of u-Health devices. The technology needs to be robust, reliable and with low computational cost so that it can be run directly in the devices even when offline. The goal of this paper is to evaluate the best alternative for arrhythmia detection with u-Health Devices.

This work is the product of an ongoing collaboration between the University of Guayaquil and the University of Villanova where multiple artificial intelligence strategies are being developed for real time detection of arrhythmias. The current work uses existing arrhythmia databases to validate the strategies, future work intends to process real time data from wearable devices. Results from this research are highly encouraging and will be further discussed throughout the article.

2. Materials and Methods

2.1. Methodology

Two Physionet databases of ECG MIT electrocardiograms (arrhythmias) with 109444 records (normal 21891 and abnormal 87553) and PTDB (infarcts) with 14550 records (normal 4045 and abnormal 10505) were used. MIT database has 4 categories Normal "N" 0, Supraventricular "S" 1, Ventricular "V" 2, Ventricular Fibrillation "F" 3, Other unclassified "Q" 4. PTDB database has 2 categories "N" 0 and with cardiac problems "A" 1. The SMOTE was used to regularize the categories and avoid Overfitting and Underfitting.

The 80% of the records are used for training and 20% for tests, 20% of the 80% of training is taken again to evaluate the data prediction. This process was carried out separately for both the MIT and PTDB databases, using in both cases ANN artificial neural networks and CNN convolutional neural networks in addition to the decision tree-based algorithm called XGBoost or extreme gradient boosting, the 3 algorithms were evaluated with the 2 databases.

2.2. Cardiovascular Diseases and Artificial Intelligence

Cardiovascular diseases (CVD) are the leading cause of mortality worldwide, accounting for 31% of all deaths [13]. One of the main causes is acute myocardial infarction (AMI). There is an emerging need to study a wide range of cutting-edge techniques for its analysis and diagnosis of heart diseases. To judge the specific situation of the patient, doctors often look at the ECG (electrocardiograph) signal to get enough information to help them diagnose. Many researchers have applied Machine Learning algorithms to study the arrhythmia [14] classification problem. Advances in data processing, storage capacity and Machine Learning ML methods have been transforming the field of medicine, including cardiology [15].

AF is one of the most common types of arrhythmias which is characterized by a rapid and irregular heartbeat [**?**]. Ischemic heart disease (IHD) is a condition in which there is an inadequate supply of blood and oxygen to a part of the heart muscle [16]. This condition usually occurs when there is an imbalance between oxygen supply and demand to the heart muscle (myocardium), usually due to atherosclerotic heart disease [17]. Patients usually do not show typical signs and symptoms (asymptomatic) until ischemic heart disease manifests as angina, myocardial infarction, or sudden cardiac death [18].

Heartbeat classification, in ECG analysis, is the most common way to automate arrhythmia [19] diagnoses. The common machine learning-based ECG learning flow includes signal noise analysis, heartbeat recognition, feature extraction, and heartbeat classification. For deep learning, feature extraction can be replaced by storing fragments of beats from a complete ECG sequence [20]. Existing ECG signal identification algorithms in the literature incorporate three important points: preprocessing, classification, and imbalance of the data set. To analyze characteristics that can be directly related to physiological factors on the development of diseases, three Deep Learning algorithms were considered: CNN convolutional neural network, ANN artificial neural network, and the reinforced tree eXtreme Gradient Boost o XGBoost.

Artificial Neural Networks are learning algorithms that can identify complex relationships in data. ANNs are designed to mimic human nervous system. Typical ANN's are comprised of 3 layers: input, output, and hidden layers. Each layer is made up of neurons [21]. Convolutional neural networks (CNN), recurrent neural networks (RNN), and naïve Bayes (NB) are used as classifiers. There are techniques that use different combinations such as Discrete Wavelet Transform (DWT) and ANN combination were obtained for ECG arrhythmia classification [22]. When the number of features is greater than the number of samples, ANNs can handle multiple classes, there is no effect of large data sets on ANNs, and extensive memory is not required [23].

ANN-based study classifies IHD using heart rate variability (HRV) parameters along with a clinical data such as left ventricular ejection fraction (LVEF), age, and gender. A series of networks with different number of input nodes (varying between 7 and 15), hidden nodes (between 2 and 10) and two output nodes were tested. The training and test ranges were respectively 75% and 25% of the total amount of data [24]. Various investigators have also used artificial neutral network (ANN)-based approaches for diagnostic classification of ECG signals [16].

Modern Deep Neural Network DNN techniques are used to solve the problem of manual feature selection and extraction in conventional automatic systems for MI Image diagnostics [25]. The Neural Network backpropagation algorithms are used to train deep learning [26]. CNN is most applied to analyze visual images. Myocardial infarction is predicted using the characteristic images before and after the attack obtained as input image of a CNN [27]. Commonly used layers in CNN are convolution (Conv), rectified linear unit (ReLU), pooling, batch normalization, and fully connected layer [28]. An input matrix is fed into a detection model that is composed of CNNs and a bidirectional Long short-term memory network (bi-LSTM) with 5-fold cross-stratified validation [29].

DNN have shown success in several domains, including images, audio, and text [30]. In real-world applications, the most common data type is tabular data, which comprises sample (rows) with the same set of features (columns). Tabular data is used in many fields, including medicine, finance, manufacturing, climate science, and many others [31].

Traditional machine learning methods, such as gradient-powered decision trees (GBDT) [32], dominate tabular data modeling and show superior performance to deep learning. Despite their theoretical advantages [33–35], DNNs pose many challenges when applied to tabular data, such as lack of locality, sparseness of data (missing values), mixed feature types (numerical, ordinal, and categorical) and lack of prior knowledge about the structure of the data set (as opposed to text or images). Ensemble-of-trees algorithms, such as XGBoost, are considered the recommended choice for real-life tabular data problems [32], [36].

XGBoost has been used to classify Atrial Fibrillation [37]. One study proposes ECG signals classifier based on XGBoost and ensemble empirical mode decomposition (EEMD) that takes advantage of functions based on time, frequency, and morphological characteristics [38]. Another study proposes to create a set of five-dimensional morphological features regarding QRS complexes and RR intervals, as well as some wavelet coefficient features, to build the feature vector for highly efficient heartbeat classification [21]. Performance measures are trained to find features that are correctly classified and those that are not well classified, then their relationship is used to find the efficiency of the classifier. We can get a high ratio even if all the important classes are misclassified. To overcome this, the data must be properly balanced [39]. SMOTE, "Synthetic Minority Oversampling Technique" can overcome some classification disadvantages [40]. This method has been shown to be better than other mixtures of under-sampling and oversampling.

A study conducted in the year 2021 compared the performance of XGBoost and the DNN using the Adamax optimizer and binary cross-entropy loss function with four hidden layers. The results showed that the XGboost outperformed the DNN by achieving a learning accuracy of 100%, while its prediction accuracy was 95.60% and 93.08%, for the same phases [41]. The overall learning performance of the DNN model was 89.42% and 81.23%, while the prediction accuracy was 80.50% and 77.36%, respectively, for the same variables [41]. The goal of our study was to compare the algorithms to determine the most cost-effective solution for real-time arrhythmia detection.

Single-lead ECG monitors are frequently used because of their highly productive nature, short run time, and low cost [42]. However, single-lead ECG cannot capture all the information due to the great diversity of CVD features that can cause misdiagnosis [43].

2.3. Artificial Intelligence

The object of the work is to select an algorithm for the classification of cardiac alterations that can be executed in real time, while the electrocardiographic signal is being acquired. Given that the evaluated algorithms are based on the identification and classification of a single cardiac cycle, the ideal would be to have an algorithm capable of capturing and classifying the signals during the period between waves, better known as the T-P segment or interval, as shown in Figure 1.

To execute the algorithm in real time, the execution time should be less than the T-P interval or, in other words, less than 200 ms. We analyzed files, from the Physionet databases regarding spread and available for research of electrocardiograms ECG. Physionet was developed by the Beth Israel Hospital in Boston (now the Beth Israel Deaconess Medical Center) in conjunction with the Massachusetts Institute of Technology: (MIT-BIH) [44] and the Physikalisch - Technische Bundesanstalt, the National Metrology Institute of Germany: (PTB). The MIT-BIH Base has 109444 ECGs and the PTB Base has 14550 ECGs [45].

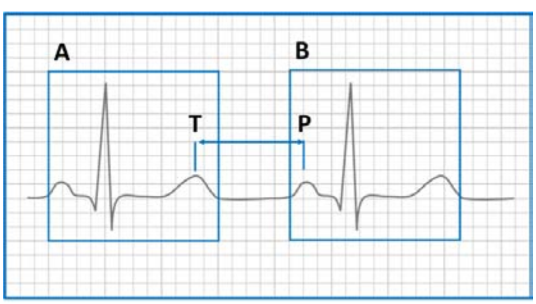

Figure 1. Two Independent Cardiac Cycles A and B within their respective detection window with the T-P interval identified

MIT-BIH is an arrhythmia database, so it has a classification labeled "N": 0, "S": 1, "V": 2, "F": 3, "Q": 4, where 0 is NORMAL and from 1 to 4 are arrhythmias which are classified as Bradyarrhythmia's and Tachyarrhythmias; subclassified as Supraventricular Tachyarrhythmias and Ventricular Tachyarrhythmias. In the PTB database, the classification is 0 NORMAL and 1 ABNORMAL, where severe heart disease such as myocardial infarction (mostly), heart failure and bundle branch block are considered. The csv files available in Kaggle have 187 columns that represent the ECG bio-signal and an additional 188 column that classifies the ECG. This field is available in both databases and allows the applicability of machine learning.

Three algorithms were considered: CNN convolutional neural network, ANN artificial neural network, and the reinforced tree eXtreme Gradient Boost o XGBoost. For the neural network algorithms, the works published by Premanand S, available at Analytics Vidhya, were taken as reference.

To avoid underfitting and overfitting problems in machine learning, the SMOTE function was applied to both databases separately, which creates new ECGs based on the original data and balances the categories.

A division by 80 is performed, -20-20 to both databases obtaining: 289878-72470-90587 ECGs and for PTB 13446-3362-4202 in Training, Test and Validation ECG data for MIT and PTB respectively. ECG samples from both databases and in the different categories of normal and abnormal have been plotted in Figures 2 and 3.

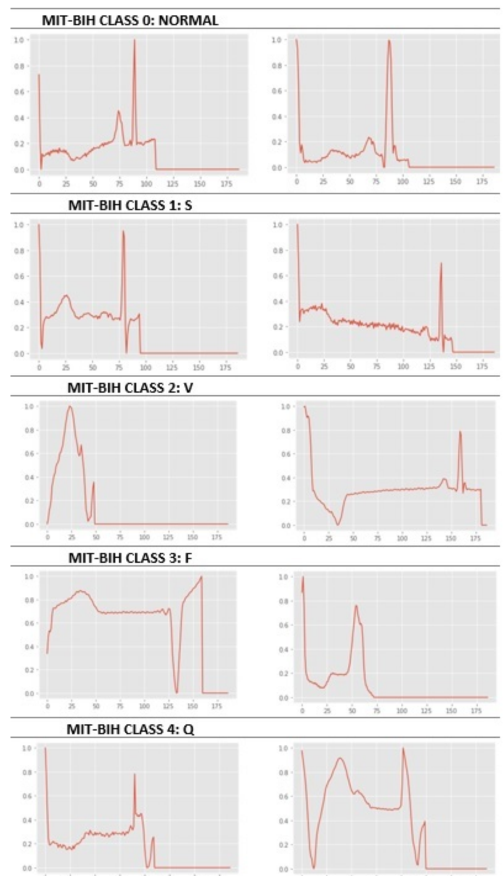

Figure 2. MIT-BIH classified signals

We have proceeded to train with ANN, CNN and XGBoost both the MIT Database and the PTB separately to make a comparison in terms of training times, and levels of precision in the prediction: accuracy, precision, recall, generating the required confusion matrices.

The training results were first validated using the test and validation data from both MIT and PTB separately. And then the prediction level is validated by crossing data between both databases. A CNN architecture proposes to select an optimal group of individual layers and the size of the filters. The following values were the chosen: 2 dense layers, layer size 128, number of 2D convolutional layers and MaxPooling 2D [12N] [46].

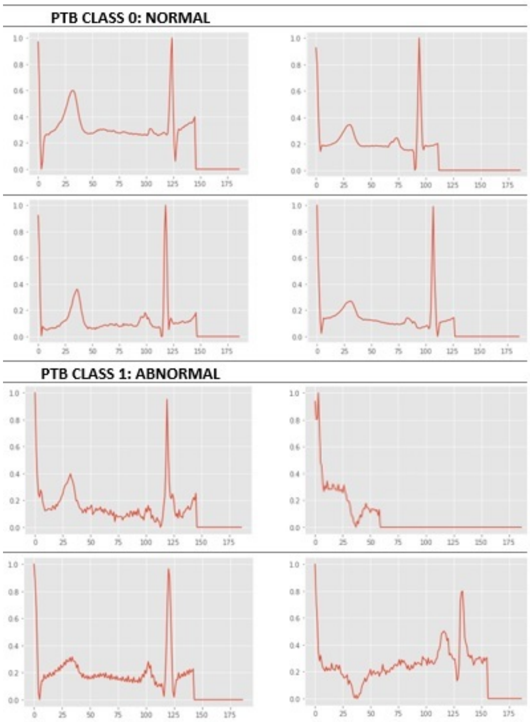

Figure 3. MIT-BIH classified signals

3. Results and discussion

We proceeded to train with ANN, CNN and XGBoost both the MIT Database and the PTB separately to make a comparison in terms of Training times, and levels of precision in the prediction: Accuracy, Precision, Recall, are presented in the required confusion matrices, Figures 4 and 5.

XGBOOST

	precision	recall	f1-score	support
0,0	0,90	0,97	0,93	2091
0,1	0,97	0,89	0,93	2111
accuracy			0,93	4202
macro avg	0,93	0,93	0,93	4202
weighted avg	0,93	0,93	0,93	4202
[[2026 65]				
[236 1875]]				

ANN

	precision	recall	f1-score	support
0,0	0,95	0,99	0,97	2091
0,1	0,99	0,95	0,97	2111
accuracy			0,97	4202
macro avg	0,97	0,97	0,97	4202
weighted av	0,97	0,97	0,97	4202
[[2061 30]				
[104 2007]]				

CNN

	precision	recall	f1-score	support
0,0	0,99	1,00	0,99	2076
0,1	1,00	0,99	0,99	2126
accuracy			0,99	4202
macro avg	0,99	0,99	0,99	4202
weighted avg	0,99	0,99	0,99	4202
[[2074 2]				
[29 2097]]				

Figure 4. PTB classified results

XGBOOST

	precision	recall	f1-score	support
0,00	0,81	0,85	0,83	18109
1,00	0,92	0,87	0,89	17952
2,00	0,93	0,91	0,92	18228
3,00	0,90	0,94	0,92	18037
4,00	0,97	0,97	0,97	18261
accuracy			0,91	90587
macro avg	0,91	0,91	0,91	90587
weighted avg	0,91	0,91	0,91	90587
[[15396 1016 545 859 293]				
[2004 15539 132 233 44]				
[735 117 16534 659 183]				
[503 112 468 16927 27]				
[354 52 150 27 17678]]				

ANN

	precision	recall	f1-score	support
0,00	0,92	0,96	0,94	18109
1,00	0,97	0,95	0,96	17952
2,00	0,99	0,96	0,98	18228
3,00	0,98	0,99	0,99	18037
4,00	0,99	0,99	0,99	18261
accuracy			0,97	90587
macro avg	0,97	0,97	0,97	90587
weighted av	0,97	0,97	0,97	90587
[[17433 393 132 102 49]				
[906 16971 28 19 20]				
[416 28 17563 204 17]				
[75 16 25 17920 1]				
[101 13 18 6 18123]]				

CNN

	precision	recall	f1-score	support
0,00	1,00	0,98	0,99	18026
1,00	0,99	1,00	0,99	17939
2,00	1,00	0,99	0,99	18271
3,00	0,99	1,00	0,99	18032
4,00	1,00	1,00	1,00	18319
accuracy			0,99	90587
macro avg	0,99	0,99	0,99	90587
weighted avg	0,99	0,99	0,99	90587
[[17742 151 43 60 30]				
[42 17893 3 1 0]				
[19 8 18150 90 4]				
[19 0 24 17989 0]				
[2 4 10 2 18301]]				

Figure 5. Resultados de clasificación sobre la MIT-BIH

Accuracy *vs.* Loss for each of the algorithms for the PTB and MIT databases are presented in Figures 6 and 7.

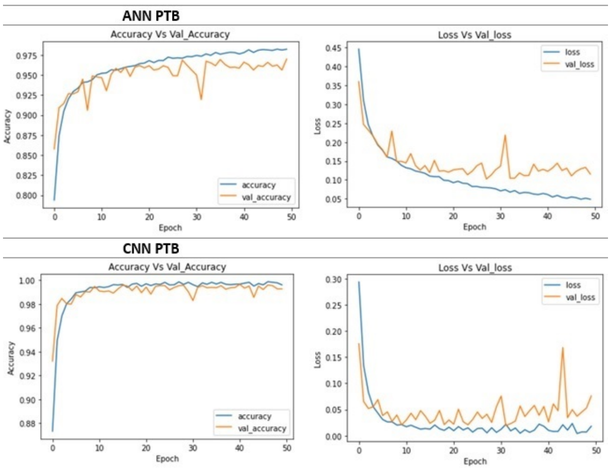

Figure 6. Accuracy *vs.* Loss for each of the algorithms using PTB dataset

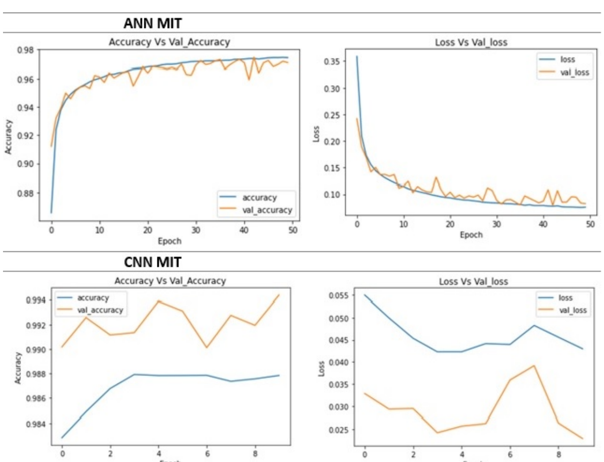

Figure 7. Accuracy *vs.* Loss for each of the algorithms using MIT dataset

FIT Times and Accuracy obtained for each of the databases is presented in Figure 8.

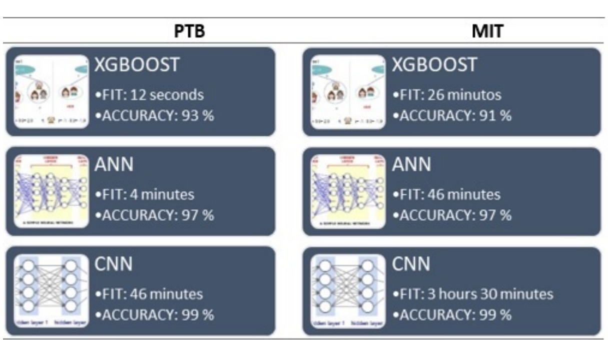

Figure 8. Fit and Accuracy for PTB and MIT datasets

After evaluating the training results separately prediction algorithms level was cross validated by exchanging data between both databases, as shown in Figure 9. For validation purposes, the PTB database was categorized as 0 = normal and 1 = abnormal and processed by the learning models based on XGBoost and ANN.

ANN Normal ECGs (0)

	precision	recall	f1-score	support
0,00	1,00	0,86	0,93	4045
1,00	0,00	0,00	0,00	0
2,00	0,00	0,00	0,00	0
3,00	0,00	0,00	0,00	0
4,00	0,00	0,00	0,00	0
accuracy			0,86	4045
macro avg	0,20	0,17	0,19	4045
weighted av	1,00	0,86	0,93	4045
[[3484 370 163 20 8]				
[0 0 0 0 0]				
[0 0 0 0 0]				
[0 0 0 0 0]				
[0 0 0 0 0]]				

ANN Abnormal ECGs (1)

	precision	recall	f1-score	support
0,00	0,00	0,00	0,00	0
1,00	1,00	0,15	0,27	10505
2,00	0,00	0,00	0,00	0
3,00	0,00	0,00	0,00	0
4,00	0,00	0,00	0,00	0
accuracy			0,15	10505
macro avg	0,20	0,03	0,05	10505
weighted av	1,00	0,15	0,27	10505
[0 0 0 0 0]				
[7247 1616 856 180 606]				
[0 0 0 0 0]				
[0 0 0 0 0]				
[0 0 0 0 0]]				

XBOOST Normal ECGs (0)

	precision	recall	f1-score	support
0,00	1,00	0,85	0,92	4045
1,00	0,00	0,00	0,00	0
2,00	0,00	0,00	0,00	0
3,00	0,00	0,00	0,00	0
4,00	0,00	0,00	0,00	0
accuracy			0,85	4045
macro avg	0,20	0,17	0,18	4045
weighted av	1,00	0,85	0,92	4045
[3439 545 49 6 6]				
[0 0 0 0 0]				
[0 0 0 0 0]				
[0 0 0 0 0]				
[0 0 0 0 0]]				

XBOOST Abnormal ECGs (1)

	precision	recall	f1-score	support
0,00	0,00	0,00	0,00	0
1,00	1,00	0,11	0,20	10505
2,00	0,00	0,00	0,00	0
3,00	0,00	0,00	0,00	0
4,00	0,00	0,00	0,00	0
accuracy			0,11	10505
macro avg	0,20	0,02	0,04	10505
weighted av	1,00	0,11	0,2	10505
[[0 0 0 0 0]				
[7292 1176 641 302 1094]				
[0 0 0 0 0]				
[0 0 0 0 0]				
[0 0 0 0 0]]				

Figure 9. PTB data Cross Validated on MIT dataset using ANN and XGBoost

The training phase was completed through trial-and-error definitions, the hyperparameters were properly configured according to Table 1 so that they reach the expected level of accuracy.

ECGs from the PTB database were validated for prediction to machine learning models based on ECGs from the MIT-BIH database, obtaining Accuracy levels of 85% and 86% for normal ECGs. Regarding the validation of abnormalities, XGBoost had an Accuracy of 11% and ANN 15%. This is because they handle different heart diseases MIT-BIH arrhythmias and PTB acute myocardial infarctions.

Table 1. Hyper-Parameter

Classifier Type	Hyper-Parameter	MIT	PTDB
XGBoost	Max deph	6	6
	Learning rate	0,1	0,1
	Optimum number - estimators	100	100
	Random state	42	42
ANN	Activation function - hidden layers	ReLU	ReLU
	Activation function - output layers	Softmax	Softmax
	Number of epochs	50 epochs	50 epochs
	Batch_size	10	10
	Optimization method	adam	adam
	Layer hidden	3	3
	Learning rate	0,0001	0,0001
CNN	Activation function - hidden layers	ReLU	ReLU
	Activation function - output layers	Softmax	Softmax
	Number of epochs	10 epochs	10 epochs
	Batch_size	10	10
	Optimization method	adam	adam
	Layer hidden	7	7
	Learning rate	0,0001	0,0001

This proves that normal signals can be recognized cross platform, but abnormal ECG data is not interoperable between one database and another.

Finally, using supervised learning, the 2 artificial neural network models and the XGBoost algorithm for prediction by classification, were compared using a weight matrix, considering criteria such as prediction accuracy, sensitivity of medical data (false positive/-false negative), the learning time, the prediction time, as shown in Table 2.

Table 2. PTB data Cross Validated on MIT dataset using ANN and XGBoost

Criterio	ANN	Value	CNN	Valor	XgBoost	Value	Weight	ANN	CNN	XgBoost
Training time	46 min	4	3 h, 30 min	2	26 min	5	3	12	6	15
Resources required for training	Mid	4	High	2	Low	5	3	12	6	15
Resources required for operation	Mid	5	Mid	5	Mid	5	3	15	15	15
Predictive capacuty	Hgh	4	Low	2	High	5	3	12	6	15
Sensitivity	2631	3	504	5	8477	2	5	15	25	10
Mean prediction time	0:00:04.14 2830	3	0:01:22.14 2794	2	0:00:02,02 8421	4	5	15	10	20
Prediction accuracy	97%	3	99 %	5	91 %	2	5	15	25	10
Total							110	96	93	100
							100	87,3	84,5	90,9

As previously defined, the object of the work is to select an algorithm for the classification of cardiac alterations that can be executed in real time, while the electrocardiographic signal is being acquired. Given that the results from Table 2 a point comparison can be obtained to determine what is the best algorithm for a u-health solution (Figure 10).

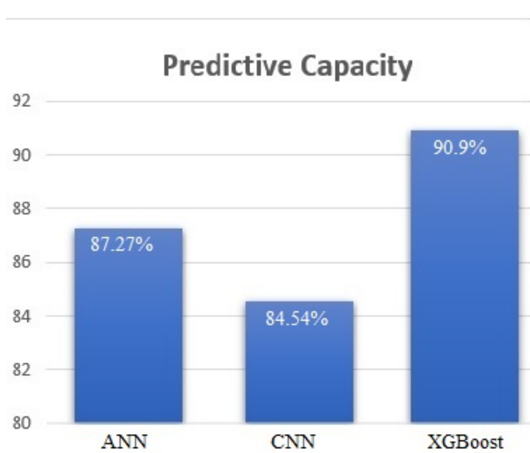

Figure 10. Point comparison between the three algorithms

For the learning phase of the models, the 123994 electrocardiographic records were used, among the predictive values obtained, the model that provides the highest prediction accuracy was determined; Since artificial intelligence has managed to learn how to properly classify conditions with cardiac pathologies, the most suitable and applicable model for the diagnosis of people or population groups was selected. In matters of prevention, the prediction of risk for the general population is of vital importance since it can reduce the impact of deaths due to cardiac pathologies, as well as reduce the costs related to these cases.

4. Conclusions

From the discussion, a weight matrix was used to compare the quality of the 3 prediction algorithms. Based on such results we conclude that CNN (convolutional neural networks) are much more accurate than other algorithms (99%), however, training time is high (in terms of hours), when compared to the XGBoost training that is obtained within minutes. Since we are dealing with Human Health, precision and accuracy in prediction have more weight than speed in training. As an intermediate we have the artificial neural network ANN that with 97% accuracy is very acceptable. XGBoost, given the tabular nature of the data, is the best choice as seen from Figure 10.

Prior conclusion indicates that it is possible to obtain information about arrhythmia within the RR interval. Since the goal of the project was to process data real time, the results are highly encouraging. For future work we intend to use ECG data from smart watches that are being generated as part of a doctoral research. Arrhythmia detection from smart watches would be a great tool for early detection of potential life-threatening events such as fibrillation. False positives however need to be reduced and since we could process data in real time, the joint probability distribution can be used in future work to increase the predictive nature of the algorithm. All in all, this is a significant contribution to the field of real-time arrhythmia detection.

References

[1] K.-Y. Chin, K.-F. Lee, and Y.-L. Chen, "Using an interactive ubiquitous learning system to enhance authentic learning experiences in a cultural heritage course," *Interactive Learning Environments*, vol. 26, no. 4, pp. 444–459, 2018. [Online]. Available: https://doi.org/10.1080/10494820.2017.1341939

[2] F. P. Mota, F. P. d eTôledo, V. Kwecko, S. Devincenzi, P. Núñez, and S. S. da C. Botelho, "Ubiquitous learning: Asystematic review," in *2019 IEEE Frontiers in Education Conference (FIE)*, 2019, pp. 1–9. [Online]. Available: https://doi.org/10.1109/FIE43999.2019.9028361

[3] Y. Guo and G. Y. H. Lip, "Beyond atrial fibrillation detection: how digital tools impact the care of patients with atrial fibrillation," *European Journal of Internal Medicine*, vol. 93, pp. 117–118, 2021. [Online]. Available: https://doi.org/10.1016/j.ejim.2021.08.026

[4] Y. Guo, H. Wang, H. Zhang, T. Liu, Z. Liang, Y. Xia, L. Yan, Y. Xing, H. Shi, S. Li, Y. Liu, F. Liu, M. Feng, Y. Chen, G. Y. H. Lip, and M.A.F.A. II Investigators, "Mobile photoplethysmographic technology to detect atrial fibrillation," *Journal of the American College of Cardiology*, vol. 74, no. 19, pp. 2365–2375, Sep. 2019. [Online]. Available: https://doi.org/10.1016/j.jacc.2019.08.019

[5] M. V. Pérez, K. W. Mahaffey, H. Hedlin, J. S. Rumsfeld, A. García, T. Ferris, V. Balasubramanian, A. M. Russo, A. Rajmane, L. Cheung, G. Hung, J. Lee, P. Kowey, N. Talati, D. Nag, S. E. Gummidipundi, A. Beatty, M. T. Hills, S. Desai, C. B. Granger, M. Desai, and M. P. Turakhia, "Large-scale assessment of a smartwatch to identify atrial fibrillation," *New England Journal of Medicine*, vol. 381, no. 20, pp. 1909–1917, 2019, pMID: 31722151. [Online]. Available: https://doi.org/10.1056/NEJMoa1901183

[6] G. Boriani, R. B. Schnabel, J. S. Healey, R. D. Lopes, N. Verbiest-van Gurp, T. Lobban, J. A. Camm, and B. Freedman, "Consumer-led screening for atrial fibrillation using consumer-facing wearables, devices and apps: A survey of health care professionals by af-screen international collaboration," *European Journal of Internal Medicine*, vol. 82, pp. 97–104, 2020. [Online]. Available: https://doi.org/10.1016/j.ejim.2020.09.005

[7] G. H. Mairesse and H. Heidbüchel, "Consumer-led screening for atrial fibrillation: What is the next step?" *European Journal of Internal Medicine*, vol. 90, pp. 16–18, 2021. [Online]. Available: https://doi.org/10.1016/j.ejim.2021.05.030

[8] J. R. Baman, D. T. Mathew, M. Jiang, and . Passman, R, "Mobile health for arrhythmia diagnosis and management," *Journal of General Internal Medicine*, no. 37, pp. 188–197, 2022. [Online]. Available: https://doi.org/10.1007/s11606-021-07007-w

[9] B. Freedman, J. Camm, H. Calkins, J. S. Healey, M. Rosenqvist, J. Wang, C. M. Albert, C. S. Anderson, S. Antoniou, E. J. Benjamin, G. Boriani, J. Brachmann, A. Brandes, T.-F. Chao, D. Conen, J. Engdahl, L. Fauchier, D. A. Fitzmaurice, L. Friberg, B. J. Gersh, D. J. Gladstone, T. V. Glotzer, K. Gwynne, G. J. Hankey, J. Harbison, G. S. Hillis, M. T. Hills, H. Kamel, P. Kirchhof, P. R. Kowey, D. Krieger, V. W. Y. Lee, L.-A. Levin, G. Y. H. Lip, T. Lobban, N. Lowres, G. H. Mairesse, C. Martínez, L. Neubeck, J. Orchard, J. P. Piccini, K. Poppe, T. S. Potpara, H. Puererfellner, M. Rienstra, R. K. Sandhu, R. B. Schnabel, C.-W. Siu, S. Steinhubl, J. H. Svendsen, E. Svennberg, S. Themistoclakis, R. G. Tieleman, M. P. Turakhia, A. Tveit, S. B. Uittenbogaart, I. C. V. Gelder, A. Verma, R. Wachter, B. P. Yan, A. A. Awwad, F. Al-Kalili, T. Berge, G. Breithardt, G. Bury, W. Caorsi, N. Chan, S. Chen, I. Christophersen, S. Connolly, H. Crijns, S. Davis, U. Dixen, R. Doughty, X. Du, M. Ezekowitz, M. Fay, V. Frykman, M. Geanta, H. Gray, N. Grubb, A. Guerra, J. Halcox, R. Hatala, H. Heidbuchel, R. Jackson, L. Johnson, S. Kaab, K. Keane, Y. Kim, G. Kollios, M. Lochen, C. Ma, J. Mant, M. Martinek, I. Marzona, K. Matsumoto, D. McManus, P. Moran, N. Naik, T. Ngarmukos, D. Prabhakaran, D. Reidpath, A. Ribeiro, A. Rudd, I. Savalieva, R. Schilling, M. Sinner, S. Stewart, N. Suwanwela, N. Takahashi, E. Topol, S. Ushiyama, N. V. van Gurp, N. Walker, and T. Wijeratne, "Screening for atrial fibrillation," *Circulation*, vol. 135, no. 19, pp. 1851–1867, 2017. [Online]. Available: https://doi.org/10.1161/CIRCULATIONAHA.116.026693

[10] M. V. McConnell, M. P. Turakhia, R. A. Harrington, A. C. King, and E. A. Ashley, "Mobile

health advances in physical activity, fitness, and atrial fibrillation: Moving hearts," *Journal of the American College of Cardiology*, vol. 71, no. 23, pp. 2691–2701, 2018. [Online]. Available: https://doi.org/10.1016/j.jacc.2018.04.030

[11] N. Brasier, C. J. Raichle, M. Dörr, A. Becke, V. Nohturfft, S. Weber, F. Bulacher, L. Salomon, T. Noah, R. Birkemeyer, and J. Eckstein, "Detection of atrial fibrillation with a smartphone camera: first prospective, international, two-centre, clinical validation study (DETECT AF PRO)," *EP Europace*, vol. 21, no. 1, pp. 41–47, 2018. [Online]. Available: https://doi.org/10.1093/europace/euy176

[12] M. Weiser, "The computer for the 21st century," *ScientificAmericanUbicompPaperafterSciAmediting*, vol. 265, no. 3, pp. 94–104, 2011. [Online]. Available: https://bit.ly/3uYsmiU

[13] X. Ye, Y. Huang, and Q. Lu, "Explainable prediction of cardiac arrhythmia using machine learning," in *2021 14th International Congress on Image and Signal Processing, BioMedical Engineering and Informatics (CISP-BMEI)*, 2021, pp. 1–5. [Online]. Available: https://doi.org/10.1109/CISP-BMEI53629.2021.9624213

[14] K. Mc Namara, H. Alzubaidi, and J. K. Jackson, "Cardiovascular disease as a leading cause of death: how are pharmacists getting involved?" *Integrated pharmacy research & practice*, vol. 8, pp. 1–11, Feb. 2019. [Online]. Available: https://doi.org/10.2147/iprp.s133088

[15] J. Bao, "Multi-features based arrhythmia diagnosis algorithm using xgboost," in *2020 International Conference on Computing and Data Science (CDS)*, 2020, pp. 454–457. [Online]. Available: https://doi.org/10.1109/CDS49703.2020.00095

[16] G. Silveri, M. Merlo, L. Restivo, B. De Paola, A. Miladinović, M. Ajčević, G. Sinagra, and A. Accardo, "Identification of ischemic heart disease by using machine learning technique based on parameters measuring heart rate variability," in *2020 28th European Signal Processing Conference (EUSIPCO)*, 2021, pp. 1309–1312. [Online]. Available: https://doi.org/10.23919/Eusipco47968.2020.9287800

[17] X. Wu, Y. Zheng, C.-H. Chu, and Z. He, "Extracting deep features from short ecg signals for early atrial fibrillation detection," *Artificial Intelligence in Medicine*, vol. 109, p. 101896, 2020. [Online]. Available: https://doi.org/10.1016/j.artmed.2020.101896

[18] D. Kasper, A. Fauci, S. Hauser, D. Longo, J. Jameson, and J. Loscalzo, *Harrison's principles of internal medicine, 19th ed.* Mc Graw Hill, 2014. [Online]. Available: https://bit.ly/3hqHin8

[19] I. Goldenberg, R. Goldkorn, N. Shlomo, M. Einhorn, J. Levitan, R. Kuperstein, R. Klempfner, and B. Johnson, "Heart rate variability for risk assessment of myocardial ischemia in patients without known coronary artery disease: The HRV-DETECT (heart rate variability for the detection of myocardial ischemia) study," *Journal of the American Heart Association*, vol. 8, no. 24, p. e014540, Dec. 2019. [Online]. Available: https://doi.org/10.1161/jaha.119.014540

[20] E. J. da S. Luz, W. R. Schwartz, G. Cámara-Chávez, and D. Menotti, "Ecg-based heartbeat classification for arrhythmia detection: A survey," *Computer Methods and Programs in Biomedicine*, vol. 127, pp. 144–164, 2016. [Online]. Available: https://doi.org/10.1016/j.cmpb.2015.12.008

[21] H. Zhu, Y. Zhao, Y. Pan, H. Xie, F. Wu, and R. Huan, "Robust heartbeat classification for wearable Single-Lead ECG via extreme gradient boosting," *Sensors (Basel)*, vol. 21, no. 16, Aug. 2021. [Online]. Available: https://doi.org/10.3390/s21165290

[22] S. Bhalerao, I. A. Ansari, and A. Kumar, "Reversible ecg data hiding: Analysis and comparison of ann, regression svm and random forest regression," in *2020 International Conference on Communication and Signal Processing (ICCSP)*, 2020, pp. 0667–0671. [Online]. Available: https://doi.org/10.1109/ICCSP48568.2020.9182219

[23] M. Manjula and A. Sarma, "Comparison of empirical mode decomposition and wavelet based classification of power quality events," *Energy Procedia*, vol. 14, pp. 1156–1162, 2012. [Online]. Available: https://doi.org/10.1016/j.egypro.2011.12.1069

[24] S. Murawwat, H. M. Asif, S. Ijaz, M. Imran Malik, and K. Raahemifar, "Denoising and classification of arrhythmia using MEMD and ANN," *Alexandria Engineering Journal*, vol. 61, no. 4, pp. 2807–2823, 2022. [Online]. Available: https://doi.org/10.1016/j.aej.2021.08.014

[25] M. Chandra Gaddam and S. Pattnaik, "An ANN ensemble based ECG signal classification approach for accurate arrhythmia detection," *International Journal of Emerging Technology and Advanced Engineering*, vol. 10, pp. 57–61, 2020. [Online]. Available: http://dx.doi.org/10.46338/IJETAE0820_08

[26] Y. LeCun, Y. Bengio, and G. Hinton, "Deep learning," *Nature*, vol. 521, no. 7553, pp. 436–444, 2015. [Online]. Available: https://doi.org/10.1038/nature14539

[27] T. Kanai, N. Tanabe, Y. Miyagi, and J. Aoyama, "CNN-type myocardial infarction prediction based on cardiac cycle determination," in *2021 International Symposium on Intelligent Signal Processing and Communication Systems (ISPACS)*, 2021, pp. 1–2. [Online]. Available: https://doi.org/10.1109/ISPACS51563.2021.9651000

[28] A. Escontrela. (2020) Convolutional neural networks from the ground up. [Online]. Available: https://bit.ly/2EXtsnf

[29] M. Dey, N. Omar, and M. A. Ullah, "Temporal feature-based classification into myocardial infarction and other CVDs merging CNN and Bi-LSTM from ECG signal," *IEEE Sensors Journal*, vol. 21, no. 19, pp. 21 688–21 695, 2021. [Online]. Available: https://doi.org/10.1109/JSEN.2021.3079241

[30] J. Devlin, M. Chang, K. Lee, and K. Toutanova, "BERT: pre-training of deep bidirectional transformers for language understanding," *NAACL*, vol. abs/1810.04805, 2018. [Online]. Available: https://doi.org/10.48550/arXiv.1810.04805

[31] R. Shwartz-Ziv and A. Armon, "Tabular data: Deep learning is not all you need," *CoRR*, vol. abs/2106.03253, 2021. [Online]. Available: https://doi.org/10.48550/arXiv.2106.03253

[32] T. Chen and C. Guestrin, "Xgboost: A scalable tree boosting system," *KDD '16: Proceedings of the 22nd ACM SIGKDD International Conference on Knowledge Discovery and Data Mining*, vol. abs/1603.02754, 2016. [Online]. Available: https://doi.org/10.1145/2939672.2939785

[33] R. Shwartz-Ziv, A. Painsky, and N. Tishby, "Representation compression and generalization in deep neural networks," in *ICLR 2019 Conference Blind Submission*, 2018. [Online]. Available: https://bit.ly/3YjzJz0

[34] T. Poggio, A. Banburski, and Q. Liao, "Theoretical issues in deep networks," *Proceedings of the National Academy of Sciences*, vol. 117, no. 48, pp. 30 039–30 045, 2020. [Online]. Available: https://www.pnas.org/doi/abs/10.1073/pnas.1907369117

[35] Z. Piran, R. Shwartz-Ziv, and N. Tishby, "The dual information bottleneck," *CoRR*, vol. abs/2006.04641, 2020. [Online]. Available: https://doi.org/10.48550/arXiv.2006.04641

[36] A. V. Dorogush, A. Gulin, G. Gusev, N. Kazeev, L. O. Prokhorenkova, and A. Vorobev, "Fighting biases with dynamic boosting," *CoRR*, vol. abs/1706.09516, 2017. [Online]. Available: https://doi.org/10.48550/arXiv.1706.09516

[37] H. Shi, H. Wang, Y. Huang, L. Zhao, C. Qin, and C. Liu, "A hierarchical method based on weighted extreme gradient boosting in ECG heartbeat classification," *Computer Methods and Programs in Biomedicine*, vol. 171, pp. 1–10, 2019. [Online]. Available: https://doi.org/10.1016/j.cmpb.2019.02.005

[38] Z. Yue and Z. Jinjing, "Atrial fibrillation detection based on EEMD and XGBoost," *Journal of Physics: Conference Series*, vol. 1229, no. 1, p. 012074, 2019. [Online]. Available: https://dx.doi.org/10.1088/1742-6596/1229/1/012074

[39] B. R. Manju and A. R. Nair, "Classification of cardiac arrhythmia of 12 lead ECG using combination of SMOTEENN, XGBoost and machine learning algorithms," in *2019 9th International Symposium on Embedded Computing and System Design (ISED)*, 2019, pp. 1–7. [Online]. Available: https://doi.org/10.1109/ISED48680.2019.9096244

[40] N. V. Chawla, K. W. Bowyer, L. O.Hall, and W. P. Kegelmeyer, "Smote: synthetic minority oversampling technique," *Journal of Artificial Intelligence Research*, vol. 16, pp. 321–357, 2002. [Online]. Available: https://doi.org/10.1613/jair.953

[41] F. Giannakas, C. Troussas, A. Krouska, C. Sgouropoulou, and I. Voyiatzis, "XGBoost and deep neural network comparison: The case of teams' performance," in *Intelligent Tutoring Systems*, A. I. Cristea and C. Troussas, Eds. Springer International Publishing, 2021, pp. 343–349. [Online]. Available: https://doi.org/10.1007/978-3-030-80421-3_37

[42] P. D. Arini and E. R. Valverde, "Beat-to-beat electrocardiographic analysis of ventricular repolarization variability in patients after myocardial infarction," *Journal of electrocardiology*, vol. 49, no. 2, pp. 206–213, Dec. 2015. [Online]. Available: https://doi.org/10.1016/j.jelectrocard.2015.12.003

[43] W. Liu, F. Wang, Q. Huang, S. Chang, H. Wang, and J. He, "MFB-CBRNN: A hybrid network for MI detection using 12-lead ECGs," *IEEE journal of biomedical and health informatics*, vol. 24, no. 2, pp. 503–514, Apr. 2019. [Online]. Available: https://doi.org/10.1109/jbhi.2019.2910082

[44] M. R. Rajeshwari and K. S. Kavitha, "Arrhythmia ventricular fibrillation classification on ECG signal using ensemble feature selection and deep

neural network," *Cluster Computing*, vol. 25, no. 5, pp. 3085–3102, 2022. [Online]. Available: https://doi.org/10.1007/s10586-022-03547-w

[45] H. M. Rai and K. Chatterjee, "Hybrid CNN-LSTM deep learning model and ensemble technique for automatic detection of myocardial infarction using big ECG data," *Applied Intelligence*, vol. 52, no. 5, pp. 5366–5384, 2022. [Online]. Available: https://doi.org/10.1007/s10489-021-02696-6

[46] B. Król-Józaga, "Atrial fibrillation detection using convolutional neural networks on 2-dimensional representation of ECG signal," *Biomedical Signal Processing and Control*, vol. 74, p. 103470, 2022. [Online]. Available: https://doi.org/10.1016/j.bspc.2021.103470

Scientific Paper / Artículo Científico

UNIVERSIDAD POLITÉCNICA SALESIANA ECUADOR
INGENIUS
Revista de Ciencia y Tecnología
https://doi.org/10.17163/ings.n29.2023.08
pISSN: 1390-650X / eISSN: 1390-860X

Performance for interoperability between Raspberry pi and ESP8266 with a PLC in a Node-RED server for IIoT

Rendimiento para la interoperabilidad entre Raspberry pi, ESP8266 y PLC con Node-RED para el IIoT

J. Torres Ventura[1,*], A. H. Ruelas Puente[2], J. R. Herrera García[1]

Received: 21-06-2022, Received after review: 06-12-2022, Accepted: 13-12-2022, Published: 01-01-2023

Abstract

This work evaluates the feasibility of integrating low-cost Raspberry pi boards and ESP8266 microcontrollers with industrial Programmable Logic Controllers (PLC) in a decentralized network. These devices will be the nodes that participate in the exchange of data between the manufacturing floor and the business services in a simple, reliable and economical way. The network nodes produce and consume data that is exchanged by an open-source protocol manager node called Node-RED. The protocol manager is a server with a Linux kernel on a RISC (Reduced instruction set computing) microprocessor. The sensors in the manufacturing nodes use SoC (System On Chip) microcontrollers, and through the concept of Edge computing they acquire, process and send their data to the protocol manager. Thus, the performance of the communication link and the status of the participating nodes in their data production/consumption processes will be measured using the Iperf3, Wireshark and MTR tools.

Keywords: IoT, interoperability, production/consumption, microservices, link, distributed.

Resumen

Este trabajo evalúa la viabilidad de integrar en una red descentralizada las placas de bajo costo Raspberry pi, microcontroladores ESP8266 con equipos industriales de controladores lógicos programables (PLC). Estos dispositivos serán los nodos que participan en el intercambio de datos entre el piso de manufactura y los servicios empresariales de manera simple, fiable y económica. Los nodos de la red producen y consumen datos que son intercambiados por un nodo gestor de protocolos open source llamado Node-RED. El gestor de protocolos es un servidor con núcleo de Linux sobre un microprocesador RISC (*Reduced Instruction Set Computing*). Los sensores en los nodos de manufactura utilizan microcontroladores SoC (*System On Chip*) y mediante el concepto de Edge computing adquieren, procesan y envían sus datos al gestor de protocolos. Así, mediante la herramienta Iperf3, Wireshark y MTR, mediremos el rendimiento del enlace de comunicaciones y el estado que guardan los nodos participantes en sus procesos producción/consumo de datos.

Palabras clave: IoT, interoperabilidad, producción/consumo, microservicios, enlace, distribuida

[1,*]Laboratorio de Mecatrónica, Universidad Autónoma de Baja California, México. Corresponding author ✉: jose.torres.ventura@uabc.edu.mx.
[2]Laboratorio de Ingeniero en Computación, Universidad Autónoma de Baja California, México.

Suggested citation: Torres Ventura, J.; Ruelas Puente, A. H. and Herrera García, J. R. "Performance for interoperability between Raspberry pi and ESP8266 with a PLC in a Node-RED server for IIoT," *Ingenius, Revista de Ciencia y Tecnología*, N.° 29, pp. 90-97, 2023, doi: https://doi.org/10.17163/ings.n29.2023.08.

1. Introduction

The concept of IoT has triggered the fourth industrial revolution [1]; however, the history started at 1960 with the need to share data of manufacturing and production processes with the business administrative services. At an industrial level, Modular Digital Controller (MODICON), a manufacturer of Programmable Logic Controllers (PLC), patented in 1979 [2] the protocol for data exchange known as Modbus. Contemporary personal computers also required to be part of this information for managing the operation of the industrial process. In 1983, Microsoft, the main distributor of personal computers, introduced the Distributed Component Object Model (DCOM) protocol [3], which has evolved to become the Object Linking and Embedding Process Control (OPC) [4].

The production process uses Manufacturing Execution Systems (MES) platforms [5], which are complex modular computing systems that manage the flow control of raw material, inventory in the process, purchase orders, list of materials, defects and finished products among others. The monitoring and control of the performance of the machinery and equipment in the manufacturing floor is carried out through specialized hardware and software systems known as Supervisory Control and Data Acquisition (SCADA) [6]. They execute models such as Key Production Index (KPI) and Overall Equipment Effectiveness (OEE). The MES and SCADA systems are grouped in a platform known as Computer Integrated Manufacturing (CIM) [7].

On the other hand, the interoperability between the different administrative departments of the business is carried out with the technique known as Enterprise Service Bus (ESB) [8], whose function is to control the process of data flow between the different nodes of the corporate network, supported on data structures with multiple types of Application Programming Interface (API). Similarly, these business systems are integrated in a platform known as Enterprise Resource Planning (ERP) [9]. This work has the following structure: section II describes the methodology to measure the performance and status of the data exchange in a distributed network, oriented to production/consumption microservices between the nodes of the local network. Section III presents the results of network analysis and diagnosis, measuring parameters associated to the transfer and latency of the data flow between the nodes.

Section IV presents the conclusion of the research work and some areas of opportunity. The objective of this work is to evaluate, in a descriptive manner, the reliability of the integration of the Raspberry Pi and ESP8266 development boards to traditional industrial technologies regarding data exchange. Thus, it will be possible to provide an interoperability alternative which is reliable, low-cost and a with a relatively shallow learning curve. This will enable the CIM and ERP platforms to carry out their processes oriented to microservices. Historically, the need of data exchange between the different administrative departments of the business and the manufacturing floor, has been a topic delegated to the great gurus of computer systems such as SAP [10], Oracle ERP [11], Microsoft Dynamics 365 [12], among others.

The objective of these powerful computer systems is oriented to address services that grow in such a way that they demand many resources, code increase, and, above all high investment, operation and maintenance costs. The strategy proposed in this research is based on the nature of the operations of industrial nodes, oriented to microservices due to its application only for specific functionalities, which enables a scalability that depends on the hardware and not on the software. For this reason, a search is started about how the issue of data exchange between the production floor and the business has been addressed.

1.1. Data exchange between business departments

Data exchange protocols independent of the technological platform or type of service are used in computer systems for corporate business services. In this manner, the Simple Object Access Protocol (SOAP) was developed, which uses the eXtensible Markup Language (XML) [13]. This protocol generates Web Services Description Language (WSDL) text documents [14], to offer a service contract to the participants. Afterwards, improvements are achieved with the Representational State Transfer (RESTful), which seek to safely obtain a virtual address without the need of contracts.

1.2. Data exchange between manufacturing systems

In 1994, the Object Linking and Embedding for Process Control Foundation (OPC foundation) [15], presented internationally the OPC Server and OPC Client as a model to regulate the interoperability in the industrial sector. OPCs are software libraries nested in automation equipment and personal computers. Their cost varies according to each product and the number of labels, although some demonstration versions are available with limited labels and service time. At present, some technology developers, such as IBM and Eclipse, have promoted Open-Source ecosystems based on this model; this is how OPC Unification Automation (OPC UA) [16] and Node-RED [17] emerged; the latter is multiplatform, and also has support from Open-Source communities.

An administrator of industrial protocols is a server that manages in a centralized manner the flow of data packets through the nodes of the network, taking advantage of libraries released by manufacturers of industrial automation equipment. The Node-RED computer system is perfectly embedded in the Industrial Internet of Things (IIoT), because it is multiplatform and multiparadigm, consumes few resources, provides a shallow learning curve, and above all, provides a high processing power and administration of communications. The literature reviewed shows the continuous search for flexible solutions to address, on one hand, the unsynchronized nature of the production floor with the business times and, on the other hand, the no compatibility of the data formats between their applications; moreover, the communication protocols between their distributed network buses are atypical. This complexity justifies the involvement of a multidisciplinary group to attempt to address these setbacks, which result in high costs, a steep learning curve and a relatively low scalability level, challenges that prevail until today.

2. Materials and methods

The contribution of this work is to become a reference, based on real production system, for researchers and technology developers in the area of Information and Communication Technologies (ICT), as an alternative to carry out the exchange of the data produced and consumed between the nodes of a distributed network, oriented to deploy CIM and ERP systems in a reliable and low-cost manner, and also with a relatively shallow learning curve. The descriptive method will be used to validate the data exchange between the nodes of the network, based on the measurement of the network performance using the latency and the transfer. Thus, it was proceeded as follows:

- Select the interface that enables the interoperability between the data produced/consumed by all nodes of the distributed network
- Build a distributed network with nodes from different industrial platforms and development boards, for process automation
- Create a map of variables to be packaged and measured
- Transfer packages between participating nodes (maximum load)

2.1. Node-RED as an administrator of data exchange

Node-RED is a project developed mainly by IBM in 2013 and released in 2016 [18]. It is multiplatform, which implies that it runs on Windows, Macintosh, and Linux and Solaris cores. Since it is a visual flow programming tool, it may be used by non-specialized staff, even enthusiastic and creative people. It was developed to consume few computer resources, and enables to create a network server to manage the connection with IIoT devices with Advanced RISC Machine (ARM) architectures and RISC platforms.

2.2. Deployment of the distributed network

Figure 1 shows the nodes participating in the distributed network that was installed to carry out the data exchange. At the physical layer level, the link between the Node-RED server uses the IEEE.802.11 standard, as well as the ESP-8266 MQTT Relay. All other use the IEEE.802.3 standard with UTP Cat 5 structured cabling. The Netis Wi-Fi router communicates all link on a TCP/IP socket, at a frequency of 2.4 GHz.

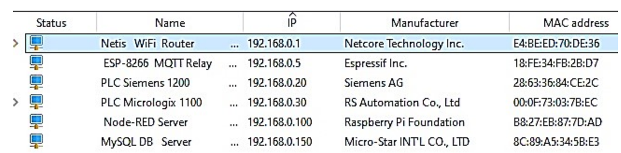

Status	Name	IP	Manufacturer	MAC address
	Netis WiFi Router ...	192.168.0.1	Netcore Technology Inc.	E4:BE:ED:70:DE:36
	ESP-8266 MQTT Relay ...	192.168.0.5	Espressif Inc.	18:FE:34:FB:2B:D7
	PLC Siemens 1200 ...	192.168.0.20	Siemens AG	28:63:36:84:CE:2C
	PLC Micrologix 1100 ...	192.168.0.30	RS Automation Co., Ltd	00:0F:73:03:7B:EC
	Node-RED Server ...	192.168.0.100	Raspberry Pi Foundation	B8:27:EB:87:7D:AD
	MySQL DB Server ...	192.168.0.150	Micro-Star INT'L CO., LTD	8C:89:A5:34:5B:E3

Figure 1. Nodes participating in the decentralized network

At the application layer level, Node-RED concentrates and manages flow traffic by means of MySQL DB María connectors, with the node labeled MySQL DB Server. The labeled node ESP-8266 MQTT Relay interacts through the MQTT (Message Query Telemetric Transport) protocol, whereas it uses the S7 protocol for the PLC Siemens 1200 node, and relies on the PCCC protocol for the PLC Micrologix 1100 node.

2.2.1. Construction of a gateway using a Raspberry Pi board

The flow administrator labeled as Node-RED server uses an ARM-v7 single core processor of 1 GHz, with 512 MB of RAM, Wireless 2.4 GHz and IEEE802.11. It uses the Debian Linux distribution as operating system, and a Node-RED server application that is deployed on Node JS. The technological platform of ARM processors uses very few instructions for its operation, which releases resources for client applications; they also have a low energy consumption, are reliable, low-cost, with a shallow learning curve, and also have a large support from open-source communities.

2.2.2. Functionality of the node with ESP8266

The hardware for the node that starts the operation of the manufacturing cell in the production floor is an IoT device, which receives the command labeled as start/stop. It consists of a microcontroller with an ESP8266 integrated circuit manufactured by Espressif, based on a 32-bit Xtensa LX106 RISC CPU, with an 80 MHz clock, 64 KB of RAM, and a QSPI 512 KB flash memory. It has a radiofrequency connection under the IEEE 802.11 b/g/n standard, and communication interface SPI (Serial Peripherical Interface) and I^2 C (Inter-Integrated Circuit).

2.2.3. Functionality of industrial nodes

The industrial nodes have been labeled as explained below. A Siemens 1200 PLC that measures the temperature of the process in a variable range from 0 to 40 °C. It was also installed an AB 1100 PLC with a process that deploys a production cycle, once it receives in a consumption label the value "true" / "false". On the other hand, an ESP8266 microcontroller device was installed to give the start/stop, whose variable takes values of "1" / "0". Finally, a server of relational MySQL databases is installed in a PC with the Win10 operating system, to record (consume) the history of the process cycle produced in the AB 1100 PLC, in a variable executed in a range of decimal integers from 0 to 5.

2.3. Map of variables

Table 1 shows the physical nodes and their identification at the level of layer 3 of the OSI model. The value column indicates the type of data transferred as useful load (payload), which will be packaged to be further transferred between the microservices. Similarly, the production and consumption columns are oriented to the microservices that have its source and destination IP address as reference.

Table 1. Map of the variables used in the data transfer flow

N.º	Produce	Consume	Valor
1	192.168.0.100	192.168.0.5	"1" / "0"
2	192.168.0.20	192.168.0.100	0-40 °C
3	192.168.0.100	192.168.0.20	True/False
4	192.168.0.30	192.168.0.150	0-5 segundos

2.4. Measure the process

The performance indices will be the transfer rate, the network latency and the data exchange status. It is considered relevant to monitor the initial reference without a total load between the participating nodes, to see the status stored by the network that relies on a link under the IEEE 802.11 and IEEE 802.3 standards, with TCP (Transmission Control Protocol) transport protocol.

2.4.1. Transfer in the distributed network

The analytical calculation of the transfer rate is defined as the speed at which information may be transferred in a network transmission medium. This may be modeled by equation (1).

$$v_t = \frac{i_t}{t} \tag{1}$$

Where:

v_t = transfer rate (MB/s)
i_t = amount of information (MB)
t = transmission time (s)

The method used to measure the performance of the network is descriptive. The Iperf ver. 3 software is used to analyze the network transfer. In the case of the latency, a diagnosis of the network was performed using the Internet Control Message Protocol (ICMP), through the Echo Requests and Echo Replay methods. In addition, the Wireshark tool is used to monitor the status of the data. Finally, MTR is used to analyze the router jumps.

2.4.2. Latency of the distributed network

The latency considers the time that a bit takes to travel through a network, from source to destination. Analytically, it would be modelled as shown by equation (2).

$$Latency = TP + TT + TC \tag{2}$$

Where:

TP = propagation time (s)
TT = transmission time (s)
TC = queue time (s)

The propagation time is the time taken by a bit to travel from source to destination through a specific transmission medium, measured in milliseconds (ms). The transmission time is the time necessary to put all the bits of a package in the transmission medium, measured in milliseconds (ms). Finally, the queue time is the time required by a communication equipment during the transmission, to manage the flow of data packets from the input to the output of the transmission medium, measured in milliseconds (ms).

2.4.3. Initial monitoring of network performance

For developing experiment, it is obtained a reference of the status stored by the link of the network used. Figure 2 shows the data flow between the MySQL server and the Node-RED server with TCP protocol. It is seen that the transmission velocity between them is acceptable, considering that the transmission medium is between UTP Cat 5 cable and Wi-Fi at 2.4 GHz. It is also observed that the Node-RED server has a utilization of 4.4%, i.e., with initial load. The diagnosis tool was Iperf3, with a client and a server.

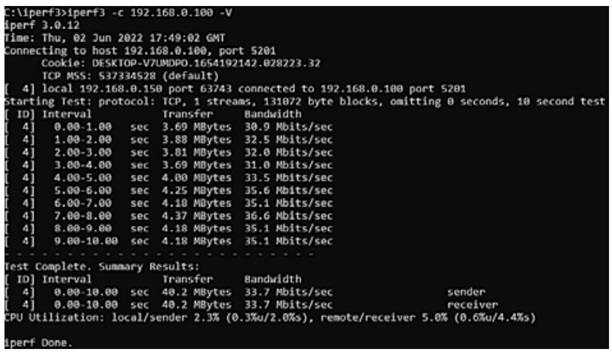

Figure 2. Monitoring the transmission between the MySQL server and the Node-RED server

Figure 3 shows the variation of the latency between the same nodes. In this case the User Datagram Protocol (UDP) will be used, considering that it is most transparent since it does not have a window, and thus it is necessary to wait for the confirmation from the destination.

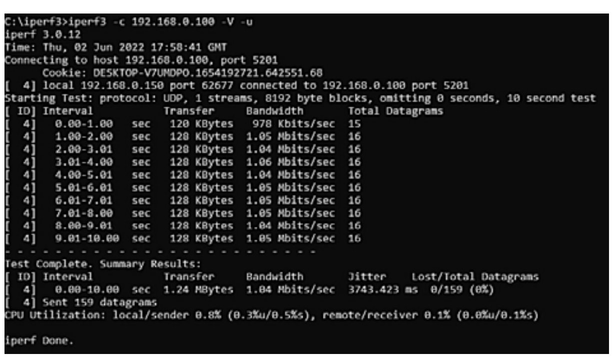

Figure 3. Variability of the latency, also known as jitter

It can be seen that the loss of packages is 0%, for a packet of 8192 bytes with a bandwidth of 1.05 Mbits/s before the beginning of operations. It may be confirmed that it is an acceptable behavior for the transfer as initial reference conditions.

3. Results and discussion

First, the latency of the network will be measured considering all participating nodes, demanded at full load. Figure 4 shows a plot of the trend of the latency round-trip solved by the ICMP protocol.

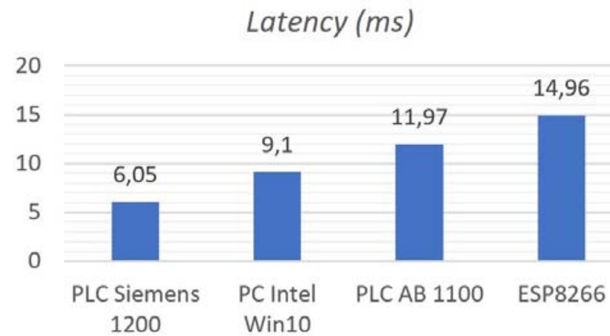

Figure 4. Diagnosis of the round-trip latency using ICMP packages

Specifically, the ping command was used from the command screen (Shell) of the Node-RED server node, to each of the nodes participating in the network. It was resolved for ten packets that were sent, and entirely received in all cases. Nevertheless, due to the latency increase at the link of each node, it was also prudent to report its standard deviation, which is shown in Figure 5.

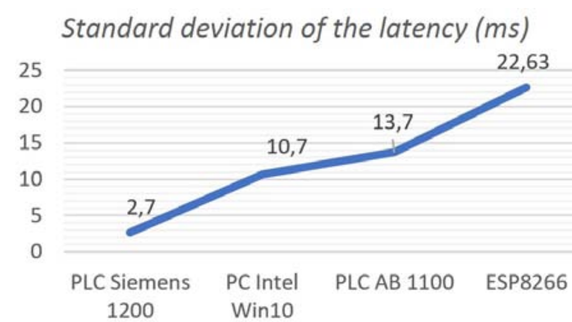

Figure 5. Standard deviation as a function of the network routing

It is sought to find a relationship of the increase of up to 50% in the latency between the Node-RED server and the ESP-8266 node, compared to the rest of the nodes. An analysis was performed with the MTR diagnosis tool to discard that this is due to the jumps between packets of the network; this is shown in Figure 6.

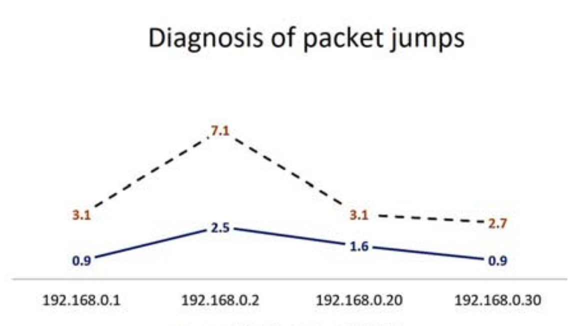

Figure 6. Diagnosis of packet jumps in each node participating in the network

It can be observed that ten packets were sent from the Node-RED server, and it is found that there is a jitter (Javg) up to 2.5 ms larger in average. In addition, the standard deviation once again increases significantly to more than twice of the remaining participating nodes with 7.1 ms. For this reason, it was also necessary to verify the transfer of the Node-RED server, flooding the network with ten packages in a UDP protocol, for a maximum demand of 54 MB on the Wi-Fi link, which is shown in Figure 7.

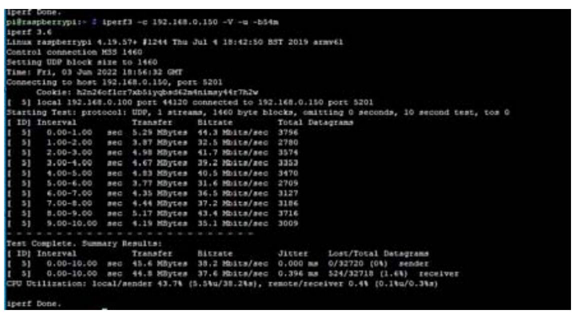

Figure 7. Saturation of the Wi-Fi link with 54 MB using the UDP protocol

It can be seen that the variability of the round-trip latency is around 0.396 ms, with 1.6% of packet loss, considering a utilization of 43.7% of the processor at the side of the Node-RED server. Finally, an analysis of the data flow was performed with the Wireshark software tool to validate the status of the data exchange transmitted through the network, and this is shown in Figure 8. The update of the label produced at the Siemens 1200 PLC is recorded in the Node-RED server with the consumption field «value».

Regarding the transfer of the data produced by the AB 1100 PLC and consumed by the server of the MySQL relational database, Figure 9 shows the label value in the field «VALUES» by means of the report of TCP flow made with Wireshark.

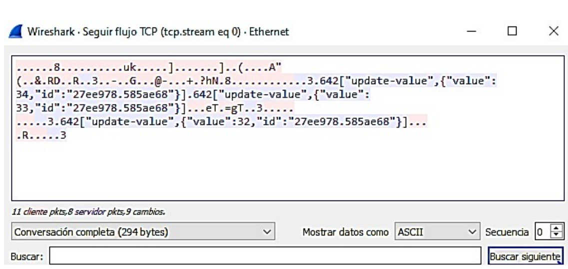

Figure 8. Transfer of the label value produced at the Siemens 1200 PLC node and consumed in the Node-RED server

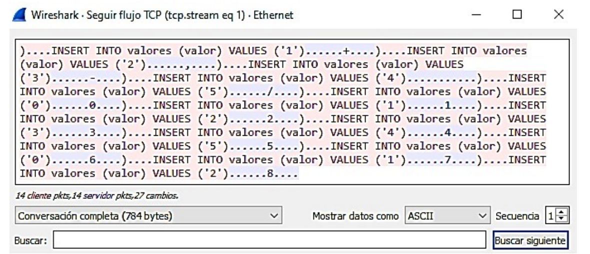

Figure 9. Transfer of the data produced at the AB 1100 PLC node and consumed at the MySQL Server node

It was found that the exchange of data between the nodes and the Node-RED server, which manages the protocols, operates with a high reliability. Based on the results shown in the transfer diagnosis, it can be stated that there is no evidence that demonstrates loss of the packets sent through the link suggested between the nodes managed with Node-RED; a 0% of packet loss is achieved in all cases. On the other hand, the low-cost Raspberry Pi board used to execute the Node-RED flow administrator maintains utilization levels between 4.4% and 43.7%, which is not negligible considering that it is in charge of the total administration of the flow of packets. Similarly, it is relevant to mention that the latency of the network is clearly altered in the flow of packets routed on the 2.4 GHz radiofrequency links, such as the ESP8266 and the Raspberry Pi. It is observed that the jitter fluctuates in up to 50% of the remaining links with equipment, using a UTP Cat 5 twisted pair cable as transmission medium.

Finally, it was demonstrated that the data exchange between the different microservices for production/-consumption of the nodes, and the Node-RED protocol administrator server is 100% reliable.

4. Conclusions

It may be confirmed that the reduced and low-cost boards such as the Raspberry Pi and the ESP8266 microcontroller, are reliable devices for data exchange at an industrial level. The flow control of packets in a distributed network by means of a protocol administrator such as Node-RED is totally reliable, and it has a high degree of availability to operate with multiple platforms of industrial protocols; in addition, it is very intuitive and friendly with the technical and operational staff. The following step would be to work in radiofrequency links oriented to industry which enable to improve the latency. At this moment, it is suggested to employ networks wired using UTP Cat 6 twisted pair, among all the nodes participating in the industrial network.

References

[1] R. Huo, S. Zeng, Z. Wang, J. Shang, W. Chen, T. Huang, S. Wang, F. R. Yu, and Y. Liu, "A comprehensive survey on blockchain in industrial internet of things: Motivations, research progresses, and future challenges," *IEEE Communications Surveys & Tutorials*, vol. 24, no. 1, pp. 88–122, 2022. [Online]. Available: https://doi.org/10.1109/COMST.2022.3141490

[2] R. Sandusky, "PLC and PC system documentation concepts," in *Forty-First Annual Conference of Electrical Engineering Problems in the Rubber and Plastics Industries*, 1989, pp. 38–47. [Online]. Available: https://doi.org/10.1109/RAPCON.1989.47714

[3] D. Thompson and D. Watkins, "Comparisons between CORBA and DCOM: architectures for distributed computing," in *Proceedings. Technology of Object-Oriented Languages. TOOLS 24 (Cat. No.97TB100240)*, 1997, pp. 278–283. [Online]. Available: https://doi.org/10.1109/TOOLS.1997.713554

[4] H. Bauer, S. Höppner, C. Iatrou, Z. Charania, S. Hartmann, S. U. Rehman, A. Dixius, G. Ellguth, D. Walter, J. Uhlig, F. Neumärker, M. Berthel, M. Stolba, F. Kelber, L. Urbas, and C. Mayr, "Hardware implementation of an OPC UA server for industrial field devices," *IEEE Transactions on Very Large Scale Integration (VLSI) Systems*, vol. 29, no. 11, pp. 1998–2002, 2021. [Online]. Available: https://doi.org/10.1109/TVLSI.2021.3117401

[5] P. Helo, M. Suorsa, Y. Hao, and P. Anussornnitisarn, "Toward a cloud-based manufacturing execution system for distributed manufacturing," *Computers in Industry*, vol. 65, no. 4, pp. 646–656, 2014. [Online]. Available: https://doi.org/10.1016/j.compind.2014.01.015

[6] F. A. Osman, M. Y. M. Hashem, and M. A. R. Eltokhy, "Secured cloud SCADA system implementation for industrial applications," *Multimedia Tools and Applications*, vol. 81, no. 7, pp. 9989–10 005, Mar. 2022. [Online]. Available: https://doi.org/10.1007/s11042-022-12130-9

[7] C. Liu, Z. Su, X. Xu, and Y. Lu, "Service-oriented industrial internet of things gateway for cloud manufacturing," *Robotics and Computer-Integrated Manufacturing*, vol. 73, p. 102217, 2022. [Online]. Available: https://doi.org/10.1016/j.rcim.2021.102217

[8] L. P. Manik, "Performance factors effect on the performance metrics of the enterprise service bus," *International Journal of Computing and Digital Systems*, no. 1, pp. 107–115, 2022. [Online]. Available: https://dx.doi.org/10.12785/ijcds/110108

[9] H. ElMadany, M. Alfonse, and M. Aref, "Forecasting in enterprise resource planning (ERP) systems: A survey," in *Digital Transformation Technology*, D. A. Magdi, Y. K. Helmy, M. Mamdouh, and A. Joshi, Eds. Singapore: Springer Singapore, 2022, pp. 395–406. [Online]. Available: https://doi.org/10.1007/978-981-16-2275-5_24

[10] J. A. Nina Chani, *El marketing B2B para optimizar el sistema interconectado de proveedores SAP y mejorar el posicionamiento industrial de la empresa METSO*. Universidad Autónoma San Francisco, Perú, 2021. [Online]. Available: https://bit.ly/3hzSxtu

[11] M. Archana, D. V. Varadarajan, and S. S. Medicherla, "Study on the ERP implementation methodologies on SAP, Oracle NetSuite, and microsoft dynamics 365: A review," 2022. [Online]. Available: https://doi.org/10.48550/arXiv.2205.02584

[12] A. Luszczak, *What is Microsoft Dynamics 365/AX?* Wiesbaden: Springer Fachmedien Wiesbaden, 2019, pp. 1–4. [Online]. Available: https://doi.org/10.1007/978-3-658-24107-0_1

[13] J. Müller, M. Lorenz, F. Geller, A. Zeier, and H. Plattner, "Assessment of communication protocols in the EPC network - replacing textual SOAP and XML with binary google protocol buffers encoding," in *2010 IEEE 17th International Conference on Industrial Engineering and Engineering Management*, 2010, pp. 404–409. [Online]. Available: https://doi.org/10.1109/ICIEEM.2010.5646586

[14] A. Abdelli, W. Serrai, and L. Mokdad, "A novel and efficient index based web service discovery approach," *Computer Standards & Interfaces*, vol. 80, p. 103586, 2022. [Online]. Available: https://doi.org/10.1016/j.csi.2021.103586

[15] J. P. Sousa, Jand Mendoną and J. Machado, "A generic interface and a framework designed for industrial metrology integration for the internet of things," *Computers in Industry*, vol. 138, p. 103632, 2022. [Online]. Available: https://doi.org/10.1016/j.compind.2022.103632

[16] Q.-D. Nguyen, S. Dhouib, J.-P. Chanet, and P. Bellot, "Towards a web-of-things approach for OPC UA field device discovery in the industrial IoT," in *2022 IEEE 18th International Conference on Factory Communication Systems (WFCS)*, 2022, pp. 1–4. [Online]. Available: https://doi.org/10.1109/WFCS53837.2022.9779181

[17] A. Rajalakshmi and H. Shahnasser, “Internet of things using node-red and Alexa,” in *2017 17th International Symposium on Communications and Information Technologies (ISCIT)*, 2017, pp. 1–4. [Online]. Available: https://doi.org/10.1109/ISCIT.2017.8261194

[18] C. Ashhwath, V. Rohitram, and G. Sumathi, “Smart parking system using MQTT communication protocol and IBM cloud,” *Journal of Physics: Conference Series*, vol. 2115, no. 1, p. 012013, nov 2021. [Online]. Available: https://dx.doi.org/10.1088/1742-6596/2115/1/012013

Scientific Paper / Artículo Científico

UNIVERSIDAD POLITÉCNICA SALESIANA ECUADOR
INGENIUS
Revista de Ciencia y Tecnología
https://doi.org/10.17163/ings.n23.2023.09
pISSN: 1390-650X / eISSN: 1390-860X

Design of a micro-hydraulic generation system based on an Archimedes screw

Diseño de un sistema de generación microhidráulica basado en un tornillo de Arquímedes

Alan Cuenca Sánchez[1,*], Willian Farinango Galeano[1], Joan Murillo Zambrano[1]

Received: 20-10-2022, Received after review: 08-12-2022, Accepted: 14-12-2022, Published: 01-01-2023

Abstract

In this work, it is applied the principle of hydroelectric generation which is used on a large scale in Ecuador. The system built represents a didactic laboratory tool for teaching courses on renewable energies. The objective of this article is to construct a didactic hydraulic micro generator, that enables to take advantage of the kinetic energy of water to produce electrical power. In addition, to have such system available in an educational institution becomes an aid to teach concepts of renewable energies such as microhydraulics, and promote its applications in rural areas through projects related to the society. Important design aspects such as power generation, use of the Archimedes screw model, supply of water resources, cost of materials, installation of the generator, among others, have been considered. This proposal offers a low-cost educational solution that is easy to replicate, which generates a maximum power of 8(W) with a flow rate of 10(l/s), thus being able to fulfill a particular electric power demand, mainly for lighting. Through a model validated in the laboratory by means of the removable system that must be used in a real environment, tests were carried out using a water storage tank and a pump. The results enable to conclude that the system built takes advantage of a reduced water flow rate to produce clean and renewable energy.

Keywords: flow, renewables energies, microgeneration, microhydraulic, Archimedes screw

Resumen

En este trabajo se aplica el principio de generación hidroeléctrica, utilizado a gran escala en nuestro país. El sistema construido representa una herramienta didáctica de laboratorio en los cursos de docencia sobre energías renovables. El objetivo de este artículo es la construcción de un microgenerador hidráulico de carácter didáctico que permita aprovechar la energía cinética del agua para la producción de energía eléctrica. Además, disponer de dicho sistema en una institución educativa ayuda a enseñar conceptos de energías renovables como la microhidráulica y potenciar sus aplicaciones en zonas rurales a través de proyectos de vinculación con la sociedad. Se han considerado aspectos de diseño importantes como potencia de generación, uso del modelo tornillo de Arquímedes, suministro del recurso hídrico, costo de materiales para la elaboración, instalación del generador, entre otros. Esta propuesta ofrece una solución didáctica de bajo costo fácil de reproducir, que genera una potencia máxima de 8 (W) con un caudal de 10 (l/s), lo que permite abastecer una determinada demanda eléctrica, principalmente de iluminación. A través de un modelo validado en laboratorio gracias al sistema desmontable que posee para ser utilizado en un entorno real, se realizaron pruebas, utilizando un tanque de almacenamiento de agua y una bomba. Con estos resultados se concluye que el sistema construido aprovecha un caudal de agua reducido para producir energía limpia y renovable.

Palabras clave: caudal, energías renovables, microgeneración, microhidráulica, tornillo de Arquímedes

[1,*]Escuela de Formación de Tecnólogos, Escuela Politécnica Nacional, Ecuador.
Corresponding author ✉: alan.cuenca@epn.edu.ec.

Suggested citation: Cuenca Sánchez, A.; Farinango Galeano, W. and Murillo Zambrano, J. “Design of a micro-hydraulic generation system based on an Archimedes screw,” *Ingenius, Revista de Ciencia y Tecnología*, N.° 29, pp. 98-107, 2023, doi: https://doi.org/10.17163/ings.n29.2023.09.

1. Introduction

The development of clean technologies for electric power generation in Ecuador has enabled to fulfill a large part of the power demand; hydroelectric generation is one of the most important nationwide, since it represents 92% of the energy matrix. However, there are certain remote places that lack a connection to the domestic electric network due to their remote location or isolation from urbanization.

The inhabitants of such rural areas do not have this basic service, and thus other types of energy, such as microhydraulics, have been used as a feasible strategy to supply the electric service. In Ecuador, this technology is within 1% together with other technologies such as biomass, biogas, geothermal, as shown in [1], which has enabled to leverage water resources at a low scale, such as streams, irrigation water or small water falls [2].

Within the field of microhydraulics, it is known that Archimedes screw is used as one of the strategies to take advantage of the flows of rivers and waterfalls. In such application it is known as hydrodynamic screw, and it consists in applying inverse engineering to the Archimedes screw, i.e., it will not operate as a rudimentary pump but more as a turbine. This system is applied at low scale to capture small water drops in rivers, waterfalls or small dams. From the technical point of view, this strategy is feasible provided that it is operated with minimum waterfalls; as opposed to those that require conventional turbines to operate, the hydrodynamic screws are high-efficiency elements regarding production of electricity for larger operating ranges, reaching a 90% with small disturbances due to changes in the flow rate. In addition, its efficiency increases according to the design volume [3].

This is the reason why, based on the available flow of water, the use of this technology facilitates the execution of this project regarding efficiency and cost, as opposed to the case that it is executed with another type of turbine, which would the efficiency and versatility of the system.

At present, hydroelectric and micro hydroelectric power generation are generally focused on the use of three turbine models, namely, Kaplan, Francis and Pelton, which, based on their structure, place of installation and efficiency [4] are among the most frequently used and studied.

The system built is based on the model developed by Archimedes, which has been used from the III century B.C., and was initially employed to raise water and other materials, i.e., as a pump [5]. Afterwards, a further change in the direction of the helixes of the screw enabled this system to be used as a turbine for power generation, as it was previously stated, taking advantage of low water jumps and flow rates, such as the one put into operation in 2012 in the Tess river dam located in England [2].

The Japanese company Sumino Co., located in the city of Ena [6], is one of the pioneers in microhydraulic systems. It has developed modules of different specifications according to the features of the installation site, which have been able to supply lighting systems in rice production places, taking advantage of the water that circulates through the irrigation channels [7].

The implementation of modules based on particular features such as the turbine structure, lengths and main elements used such as an electric generator and the water resource [8], has enabled to demonstrate various concepts such as energy transformation and the use of the hydraulic potential in places where it is difficult to access to electric power, which poses a challenge regarding technological innovation to address this type of problems.

Based on the above, the main objective is the implementation of a microhydraulic generation didactic system based on a hydrodynamic screw, to supply one or more lighting loads using a reduced flow of a water resource.

Despite the advantages offered by the use of this technology with hydrodynamic screws, if it is chosen as an economically feasible alternative to be used in the long term in rural areas, it is compulsory, due to environmental care issues, to measure the impact on the incorporation rate of oxygen to the river, which should be preserved. Therefore, it is a topic of study to add a corrective or preventive strategy when using this technology; indeed, there is very little said and researched about assessing if there is a significant impact on rivers and lagoons, as well as on marine fauna [9].

2. State of the art

Santa Cruz [10] carried the study and design of a micro hydroelectric system to supply electric power to a household in Cuenca. This study stated that Archimedes screw is the best alternative for small water jumps and low flow rates; however, a Kaplan turbine was used because this locality had high flows.

Ramírez and Ramón [11] conducted a preliminary study for the implementation of a hydroelectric microgeneration system for self-supply of a hostel in the Ecuadorian Amazon. They found that it was feasible to install a 7.5 (kW) turbogenerator that takes advantage of the water of various internal waterfalls that exist due to the Reventador river crossing; a group of Pelton-type turbines were chosen because the water resource is abundant in the area. Nevertheless, they point out that for powers below 300 (W) and flow rates below 50 (l/s), it is recommended to use hydrodynamic screws.

Arias [12] conducted a feasibility study of a hydroelectric microgeneration system using Kaplan turbines, pointing out the initial investment and the benefits for communities that do not have a high population growth and are at distances smaller than 500 meters from the power supply point. In addition, this study states the importance of implementing low-cost microhydraulic systems to supply the power demand of particular lighting loads, and shows that hydrodynamic screws are an excellent alternative.

Lucio [13] carried out the construction of an Archimedes screw mini turbine, where it is shown the optimal operation of the system in an irrigation channel, obtaining power and torque levels that are appropriate to generate mechanical power (it does not supply electric loads).

All the studies described above show the importance of microhydraulics in Ecuador and its applications; nevertheless, none of them presents the design and implementation of a cost-effective electric microgeneration system based on hydrodynamic screws for self-supply at places that have small water jumps and low flow rates, and are isolated from the electric network. Although the system built has academic purposes, it is intended to formulate projects related to the society to repower it for its use at isolated places. In addition, this work contains all the technical information for the implementation of the microturbine and its application, showing the contribution of this paper in the area of renewable energies.

Table 1 gathers some papers that analyze the parameters, operation, modelling, etc. of microhydraulic systems that use Archimedes screw generators. These papers remark the efficiency of these turbines to generate hydroelectricity at places with little height and moderate flow rate.

Table 1. Similar papers about Archimedes screw generators

Paper	Feature analyzed
[14]	Performance
[15]	Slope and number of blades
[16]	Power
[17]	Size
[18]	Types of fluids

Simmons *et al.* [19] analyzed Archimedes screw generators for sustainable energy development, generating hydroelectric energy in plants of up to 200 (kW). In addition, they state that this type of technology can be used for rural electrification in developing regions with reliable little water resources. Raza *et al..*. [20] remark that the electricity generated using hydraulic energy is cheaper and environmentally friendly; in addition, they state that microgeneration systems not connected to the network may use waste water, and that Archimedes turbine is the most appropriate one for a hydroelectric plant with a low waterfall.

The objective of this research is to develop a cost-effective and easy to replicate didactic system, to disseminate the knowledge in the area of microhydraulics, generating clean and renewable energy. Low-cot materials were used for the construction of the microturbine. The energy generated enabled to supply lighting loads using low water flow rates, thus validating the operation of the system developed. The system put into operation in this research work may be repowered to supplement and lower costs in projects [10–13]. In addition, it may be used in a didactic manner in university labs to motivate students to study and become experts in the area of renewable energies, to contribute to the change of the energy matrix in Ecuador.

3. Materials and methods

This section presents the development stages of the project, describing the materials and methods employed. The system proposed may be divided into two parts:

1. Mechanical design
2. Electric-electronic system

3.1. Mechanical design

3.1.1. Power of an Archimedes screw turbine

In the case of a hydraulic turbine, the power is governed by variables defined by the place where it will be installed, such as the inlet flow rate, the height, and also aspects such as water density and gravity. Equation (1) establishes the parameters to be included to obtain the hydraulic power of a turbine [21].

$$P_H = \rho \times g \times Q \times H \qquad (1)$$

Where P_H is the hydraulic power in (W), ρ corresponds to the water density in (kg/m^3), g is the gravity on earth in (m/s^2), Q is the flow rate that enters the turbine in (m^3/s), and H is the height of the waterfall in (m).

3.1.2. Inertia and area of the helix

Table 2 considers the inertia of the turbine as a function of the contact area. A minimum area is contemplated for this design; specifically, a 10 % is considered since the inlet area of the recirculation water is smaller than one inch.

Considering the equations for such 10 %, it is obtained that A is the area of contact of the water with the helixes of the turbine in (m^2), R is the external radius of the turbine in (m) and Y_c is the inertia of the blade in (m) depending on the area of contact to be chosen [21].

Table 2. Inertia of the turbine as a function of the percentage of the contact area [21]

Area of contact	Area (A)	Percentage	Inertia (Yc)
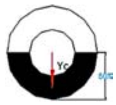	$\frac{3}{8}\times\pi\times R^2$	50%	$0.4951\times R$
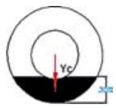	$\frac{9}{40}\times\pi\times R^2$	30%	$0.6907\times R$
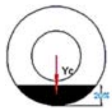	$\frac{3}{20}\times\pi\times R^2$	20%	$0.7544\times R$
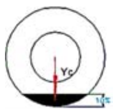	$\frac{3}{40}\times\pi\times R^2$	10%	$0.8471\times R$

3.1.3. Theoretical torque and power

Figure 1 shows the horizontal thrust force exerted by the water (F_X), the tangential force exerted by the water (F_Z), the thrust force in the direction of the X plane (F_R), the force exerted by the water on the housing (F_y), the vertical force (W) and (α) the angle external to the helix [21].

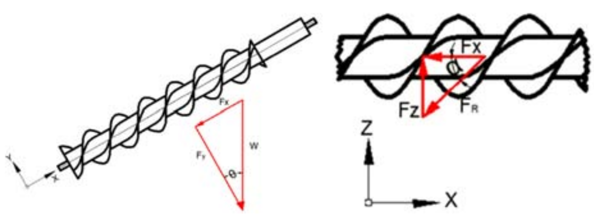

Figure 1. Forces that act on an Archimedes screw [21]

If the relationship between the XZ plane is considered, the relationship given by equation (2) may be obtained.

$$tan\alpha = \frac{F_Z}{F_X} \tag{2}$$

Where the tangential force (F_z) together with the inertia of the blade (Y_C), describe the torque generated at the moment of contact of the water with the screw, thus obtaining equation (3).

$$T = F_Z \times Y_C \tag{3}$$

Equation (4) may be obtained analyzing the tangential force (F_Z); this equation describes the torque of the screw considering the effects of the water, the height, the contact area and the angles.

$$T = \rho \times g \times LT \times A \times sen\ (\Theta) \times tan\ (\alpha) \times Y_C \tag{4}$$

Where T is the torque of the turbine in (Nm), ρ is the water density in (kg/m^3), LT is the total length of the turbine in (m), whose value is assumed based on technical criteria of design, materials, manufacturing feasibility and versatility, Θ is the inclination angle of the turbine in (°) and h is the height of the hydraulic head; LT, Θ and h are shown in Figure 2.

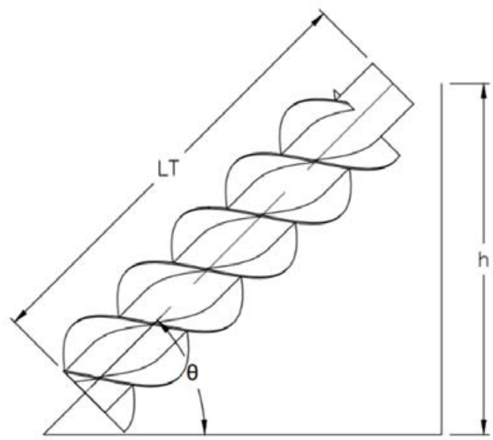

Figure 2. Dimensions considered for the turbine

On the other hand, the theoretical mechanical power of an Archimedes screw may be also expressed as shown in equation (5).

$$P_{theoretical} = T \times \omega \tag{5}$$

Where T is the torque obtained from equation (4), and ω is the angular speed in (rad/s) given by equation (6).

$$\omega_{angular} = \frac{Q \times tan(\alpha)}{A \times Y_h} \tag{6}$$

Substitution of equations (4) and (6) in equation (5) yields equation (7), which describes not only standard variables as in equation (1), but is also makes emphasis on the contact area, inertia, angles and lengths.

$$P_{theoretical} = \rho \times g \times LT \times A \times Q \times sen(\Theta)\tan^2(\Theta) \tag{7}$$

In order to obtain the angle α, it is considered that the efficiency should be assumed in this case due to various factors such as friction, weight of the turbine, the environment, etc. Hence, equation (8) gives the efficiency of a turbine.

$$\eta = \frac{P_{theoretical}}{P_{theoretical\_max}} \times 100\% \tag{8}$$

Where η is the efficiency of a turbine and $P_{theoretical\_max}$ is the maximum mechanical power that can be reached by the turbine in (W). Simplifying equation (7) and substituting the result in both variables of equation (8) yields equation (9), where it can be observed that $\tan^2(\alpha)$ is 1 in the numerator because the maximum angle α should be 45°.

$$\eta = \frac{\rho \times g \times LT \times A \times Q \times sin(\Theta)\tan^2(\alpha)}{\rho \times g \times h \times Q} \times 100\% \tag{9}$$

From Figure 2 it is determined that the height is given by equation (10):

$$H = LT \times sin(\Theta) \tag{10}$$

Considering equation (10) and substituting and simplifying equation (9) results in equation (11), which can be used to determine the value of the external angle (α):

$$\eta = \tan^{\alpha} \times 100\ \% \tag{11}$$

The theoretical torque and power that may be obtained from an Archimedes screw turbine can be found using equations (4) and (7).

3.1.4. Dimensions and modeling

It was adapted an Archimedes screw with three threads and two revolutions along a plastic shaft with a length of 0.76 (m), according to the base design taken as reference. This piece was divided into two sections that may be coupled. Figure 3 shows the Archimedes screw; it does not have a solid filling and has a thickness of 0.003 (m) in its shaft and a thickness of 0.002 (m) in its helixes. In the lateral end it has a hole to attach the turbine with respect to a metallic shaft.

Figure 3. Archimedes screw hydraulic microturbine

A prototype of the existing microgeneration turbine was taken into account for the design of the microturbine. The corresponding geometrical specifications were adapted to the proposed design, and such features are specified in Table 3.

Table 3. Features of the hydraulic microturbine

Property	Value
Material	Ácido poliláctico
Length	0.760 (m)
External diameter of the helix	0.198 (m)
Diameter of the helix shaft	0.109 (m)
Thickness	0.003 (m)

Measures to prevent friction in rotating parts include maintaining the bearings lubricated and protecting the metallic parts from rust, since in Archimedes screws it is of vital importance to avoid friction, especially in the helical helixes, because of efficiency issues [22].

A metallic structure, with the dimensions shown in Table 4, was designed to fix the bearings that bear the microturbine. This structure is the support of the water stream channel and the microturbine, and also holds the generator and the electronic circuit. Such structure is associated to auxiliary mounts that define the inclination and equilibrium of the surface on which the entire turbine-generator system will be deployed.

Table 4. Features of the hydraulic microturbine

Property	Valor
Width	0,81 (m)
Length	0,281 (m)
Height	0,221 (m)

Once the purpose of the base metallic structure has been defined, the plane of its final design is obtained (Figure 4).

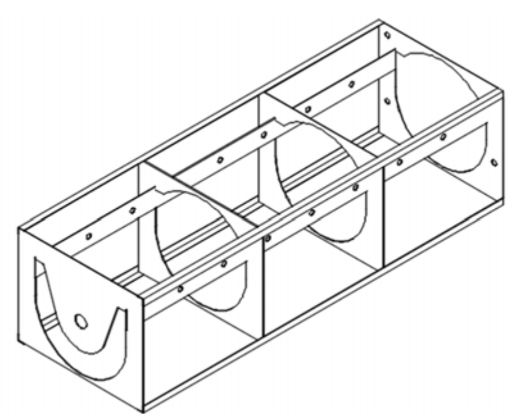

Figure 4. Support base of the hydraulic screw

Figure 5 shows the 3D model of the microturbine. An insulated container is placed in the back of the metallic structure to hold the generator and the electronic circuit. In addition, it can be observed the auxiliary metallic structures to set the inclination of the hydraulic turbine, and even fix the hydraulic pump and the water storage tank for laboratory tests. Such structures may be removed for operation in a stream or creek.

Figure 5. Rendered design of the microgeneration system

3.2. Electric-electronic system

A water recirculation system was used for the laboratory tests, and thus a storage tank was arranged to receive and discharge the fluid by means of a 372.85 (W) hydraulic pump.

A brushless DC motor (BLDC), whose main parts are shown in Figure 6, was used to produce electricity. This BLDC is operated as a generator without velocity multipliers, and is coupled to the back of Archimedes screw. This element adapts to the revolutions by means of a direct mechanical coupling provided by the turbine; in addition, the inclination of Archimedes screw and the flow rate that enters the turbine through the helixes have influence on the conversion from mechanical energy to electrical energy.

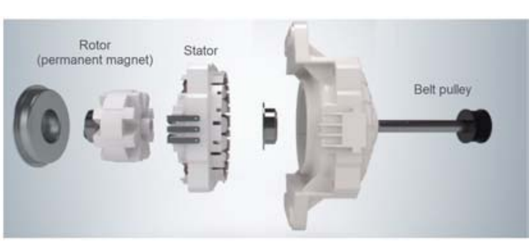

Figure 6. Permanent magnet synchronous motor [23]

It was designed the electronic circuit for the voltage rectifier circuit that will supply the loads. This circuit has stages for rectifying, filtering and linearizing the alternate voltage wave at the output of the generator. In addition, a step-up DC–DC booster converter (MT3608) was incorporated to regulate and amplify the filtered DC voltage waves. The electronic scheme is shown in Figure 7.

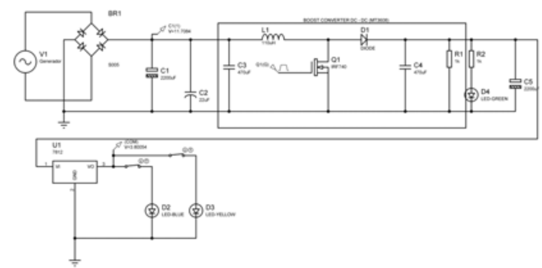

Figure 7. Electronic scheme of the full-wave AC-DC voltage rectifier

4. Results and discussion

Taking into account all the parameters, features and requirements of the hydraulic microgeneration technology, a cost-effective and easy to replicate didactic system was built capable of using a water resource to generate up to 8 (W), supplying the demand of 6 (V) LED lighting loads. The system may be easily disassembled for its transportation from one place to another when it is required to observe its operation, either in the laboratory or outdoors. In addition, the system designed and built represents an innovative and efficient solution that may be improved for generating electricity from unconventional renewable sources.

The hydraulic screw was made through 3D printing (Figure 8) in fused deposition modeling (MDF), using polylactic acid filament in the entire structure of the hydraulic microturbine.

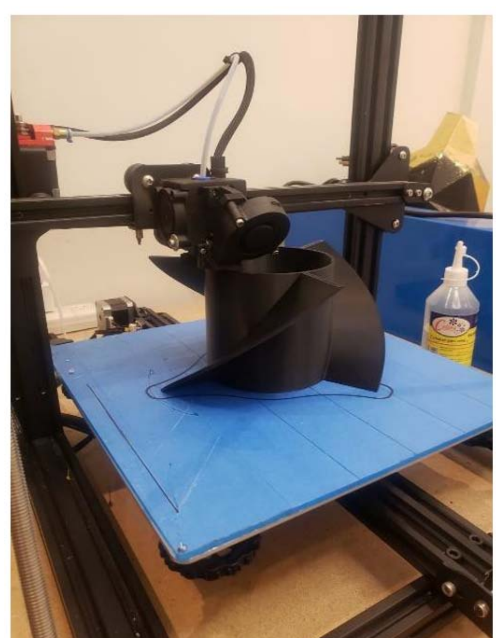

Figure 8. Metallic structure that supports the microgeneration system

Figure 9shows the system built and operating in the laboratory, the demand (6V LED lights) is satisfactorily supplied using to the inlet flow of water that is recirculating through the system.

Figure 9. Metallic structure that supports the microgeneration system

En la Figura 10 se observa el sistema construido y funcionando en laboratorio, la demanda establecida (luces LED de 6 V) es abastecida correctamente gracias al flujo de agua de entrada que se encuentra recirculando por el sistema.

Si bien el sistema de microgeneración cuenta con una bomba de agua para un circuito hidráulico que recircula el agua, esto sirve para emular el medio físico donde se instalaría dicho sistema y realizar las respectivas pruebas de funcionamiento en laboratorio. Para la adaptación y utilización del sistema en lugares externos al laboratorio no son necesarios estos componentes por lo cual se pueden desmontar fácilmente, ya que lo único que se necesita es la presencia de un riachuelo y la colocación del generador para el paso de agua (Figura 11).

Figure 10. Hydraulic microgeneration system

As a constant flow rate (minimum) of 0.583 (l/s) enters the turbine, it rotates at a speed in the range from 18.85 to 20.94 (rad/s) with the corresponding coupling to the generator. As a flow rate (maximum) of 10 (l/s) enters the turbine, it rotates at a speed of approximately 220 (rad/s).

Figure 11. Microhydraulic generation system installed in a stream

Tests were carried out for different inlet flow rates, measuring the power generated to supply a particular load. Table 5 and Figure 12 show the power generated by the microturbine built in this work, as a function of the inlet flow rate.

The power generated was established through operation tests, which show that as the inlet flow rate increases so does the power. With the minimum flow rate of 0.583 (l/s), a current of 0.4 (A) and a voltage of 6 (V) were obtained, which can be used to supply a LED light with these specifications, whereas the maximum flow rate enables supplying up to 3 LED lights. Although there are various systems to supply the power demand without connecting to the electric network, even obtaining higher levels of power, the microturbine built represents a very attractive alternative for school students to get involved in the area of microhydraulics. This type of technology is capable of recovering the energy from a great variety of small water jumps, and its installation and maintenance costs are very low compared to other renewable energies.

The system presented in this work is feasible because it uses low-cost materials; in addition, the technical information presented in this paper constitutes a basis to build, replicate and repower a system, that can also adapt to different environments, indoors or outdoors.

These results evidence that the objective of the microgeneration didactic system was fulfilled, which is to contribute to the development of students' knowledge about renewable energies, by means of the supply of the demand of lighting loads from the kinetic energy of water. Figure 13 shows the training of students from the Escuela de Formación de Tecnólogos (ESFOT) of the Escuela Politécnica Nacional, in the operation of the system.

Table 5. Values of power generated as a function of the inlet flow rate

Inlet flow rate (l/s)	Power generated (W)
0.583	0.57
1.243	0.93
1.846	1.24
2.394	1.38
2.749	1.47
3.198	1.78
3.639	2.16
4.957	2.78
5.293	3.11
5.384	3.21
6.393	4.09
7.475	5.28
8.273	6.14
9.583	7.32
10	7.95

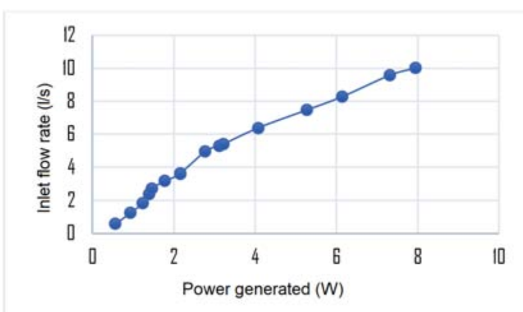

Figure 12. Power generated by the microturbine vs. inlet flow rate

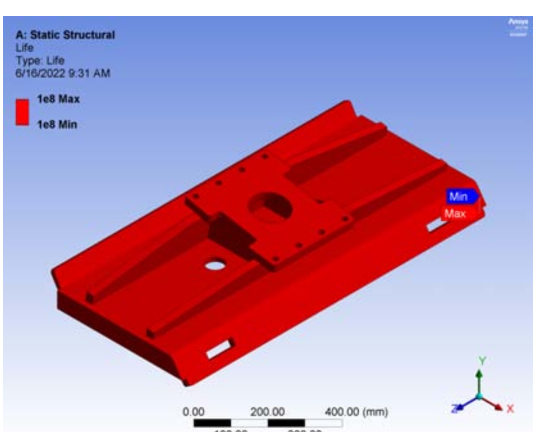

Figure 13. Students observing the operation of the microgeneration system in the laboratory

The installation of a rectifier was considered to supply the lighting load, in order to avoid the intermittency in the lamp used and to stabilize the power delivered by the generator.

Consequently, based on the microturbine design specifications, there are losses due to different factors, such as the friction, resistance of the generator, weight, etc., which cause losses in the stage of transformation from mechanical to electrical energy. Nevertheless, hydrodynamic screws exhibit high efficiency regarding generation of electricity for larger operating ranges, reaching 90% with little disturbances in the flow rate; in addition, its efficiency increases according to the design volume.

The system built is a contribution to the development of knowledge about microhydraulics, since the results obtained enable to verify that the module operates correctly and that it may be used for teaching activities in laboratory practices. In addition, it should be pointed out that the operation tests have been carried out with the system to recirculate the water (pumps, pipes and storage tank) in the ESFOT laboratory and in a stream in the locality of Guayllabamba, being able to satisfactorily supply lighting loads. Therefore, it is stated that the didactic microturbine implemented in this work may serve as a base to extend the system to real applications in areas isolated from the electric network, taking into account the demand that should be fulfilled.

An aspect that should be considered is the energy storage system that would be used by the lighting load during dry seasons; however, a continuous and stable presence of the water resource has been considered for the present project, i.e., it is used the energy produced when the system is operated.

5. Conclusions

Based on the values obtained and on the implementation of the microgeneration system, it is emphasized that the water flow is the resource used to produce movement, as it was verified in the tests carried out with a water flow rate of 0.583 (l/s), in which the screw moved at a considerable speed. However, a higher efficiency is obtained when the flow rate is increased, generating better torque and a power of up to 8 (W) to supply a larger number of loads connected.

The microgeneration system based on an Archimedes screw enables to supply up to three LED lights of 6 (V) and 0.4 (A). Although it is a didactic system, it could be improved and its performance extended to supply a larger demand.

The turbine was thoroughly calibrated and adjusted, so that there is no direct contact of the turbine with the metallic structure and also to guarantee that it is as centered as possible at the moment of starting operation. The dimensions of the general system were defined and mechanical design planes were made for the corresponding description.

Taking into account the electric demand to be supplied and the technical information of the present paper, the system built may be repowered to increase the generation levels through a generator of higher power. This will enable to use the microturbine in lighting systems, in passages and streets without a public lighting system, for electrifying fences to protect crops and cattle, and even in irrigation systems in rural areas of Ecuador.

In the present work, a system based on clean and renewable energy was designed and built. Low-cost materials were used to obtain a cost-effective and easy to replicate system, and also easy to repower compared to other types of technologies.

The system built is a contribution for the microhydraulic technology and its socialization in educational institutions, so that students and other people interested may know and learn about this type of technology. In the case of the ESFOT, the microturbine can be used for didactic applications in the laboratory, where students may extend, strengthen and supplement their knowledge related to renewable energies. In addition, this work is framed within the area of Applied Technology projects at the ESFOT, which have enabled to state technical solutions in different projects that involve a relationship with the society.

References

[1] Ministerio de Energía y Minas, *Ecuador consolida la producción eléctrica a partir de fuentes renovables*. Ministerio de Energía y Minas. República del Ecuador, 2022. [Online]. Available: https://bit.ly/3jbARot

[2] J. E. Santa Cruz Herrera, "Análisis energético de un tornillo de Arquímedes para canales de regadío con una caída de 2 m y caudal de 2 m^3/s," 2018. [Online]. Available: https://bit.ly/3BHjzG4

[3] M. E. Madrid Wolff and J. M. Toro Bedoya, "Viabilidad técnica y económica de tornillos hidrodinámicos para generación eléctrica," 2013. [Online]. Available: https://bit.ly/3v1axzK

[4] Enel. (2022) Turbina hidroeléctrica. [Online]. Available: https://bit.ly/3Pzvmf7

[5] E. Martínez Rull. (2019) Lista la primera central de tornillo de Arquímedes. [Online]. Available: https://bit.ly/3FsebaI

[6] J-GoodTech. (2022) Corporate profile. [Online]. Available: https://bit.ly/3WnNb3b

[7] M. Sumino. (2022) Generador móvil de energía hidráulica ultrapequeño, tienes agua tienes energía. [Online]. Available: https://bit.ly/3PuN4k9

[8] Sumino. (2022) Spiral pico hydropower generation device picopica®10. [Online]. Available: https://bit.ly/3V58xkX

[9] FAO. (2022) Mejora de la calidad de agua en los estanques. [Online]. Available: https://bit.ly/3BEGhyo

[10] V. R. Vásquez Huiracocha, "Estudio y diseño de un sistema microhidroeléctrico para la generación y abastecimiento de energía eléctrica mediante energía renovable para una vivienda típica del sector de Sinincay perteneciente al cantón Cuenca," 2015.

[11] R. A. Ramírez-Coronel and G. M. Ramón-Poma, "Estudio preliminar para la implementación de un sistema de microgeneración hidroeléctrico, para autoconsumo, en la Hostería El Reventador," *Revista Científica FIPCAEC (Fomento de la investigación y publicación científico-técnica multidisciplinaria)*, vol. 7, no. 1, pp. 275–311, 2022. [Online]. Available: https://bit.ly/3BGscjY

[12] M. D. Arias Venegas, "Estudio de factibilidad y análisis de sistema de microgeneración hidroeléctrica," 2019. [Online]. Available: https://bit.ly/3UXyF0Y

[13] L. E. Escobar Luna and D. M. Lucio Yugsi, "Diseño y construcción de una miniturbina tipo tornillo de Arquímedes para ser instalada en canales primarios abiertos y generar energía mecánica," 2019. [Online]. Available: https://bit.ly/3FB0s1o

[14] S. C. Simmons, C. Elliott, M. Ford, A. Clayton, and W. D. Lubitz, "Archimedes screw generator powerplant assessment and field measurement campaign," *Energy for Sustainable Development*, vol. 65, pp. 144–161, 2021. [Online]. Available: https://doi.org/10.1016/j.esd.2021.09.007

[15] G. Dellinger, S. Simmons, W. D. Lubitz, P.-A. Garambois, and N. Dellinger, "Effect of slope and number of blades on Archimedes screw generator power output," *Renewable Energy*, vol. 136, pp. 896–908, 2019. [Online]. Available: https://doi.org/10.1016/j.renene.2019.01.060

[16] A. Kozyn and W. D. Lubitz, "A power loss model for Archimedes screw generators," *Renewable Energy*, vol. 108, pp. 260–273, 2017. [Online]. Available: https://doi.org/10.1016/j.renene.2017.02.062

[17] H. Lavriç, A. Rihar, and R. Fišer, "Influence of equipment size and installation height on electricity production in an Archimedes screw-based ultra-low head small hydropower plant

and its economic feasibility," *Renewable Energy*, vol. 142, pp. 468–477, 2019. [Online]. Available: https://doi.org/10.1016/j.renene.2019.04.095

[18] K. Shahverdi, R. Loni, B. Ghobadian, M. Monem, S. Gohari, S. Marofi, and G. Najafi, "Energy harvesting using solar ORC system and Archimedes screw turbine (AST) combination with different refrigerant working fluids," *Energy Conversion and Management*, vol. 187, pp. 205–220, 2019. [Online]. Available: https://doi.org/10.1016/j.enconman.2019.01.057

[19] S. Simmons and W. Lubitz, "Archimedes screw generators for sustainable energy development," in *2017 IEEE Canada International Humanitarian Technology Conference (IHTC)*, 2017, pp. 144–148. [Online]. Available: https://doi.org/10.1109/IHTC.2017.8058176

[20] A. Raza, D. Xu, M. S. Mian, and J. Ahmed, "A micro hydro power plant for distributed generation using municipal water waste with Archimedes screw," in *INMIC*, 2013, pp. 66–71. [Online]. Available: https://doi.org/10.1109/INMIC.2013.6731326

[21] J. Alberto, "Diseño de una turbina hidráulica basada en el tornillo de Arquímedes," Ph.D. dissertation, 2012. [Online]. Available: https://bit.ly/3YvJYk0

[22] Hidrometálica. (2022) Tornillo de Arquímedes. [Online]. Available: https://bit.ly/3WrAcxx

[23] LG Chile. (2022) ¿Por qué te conviene una lavadora de carga superior LG con motor smart inverter? [Online]. Available: https://bit.ly/2svHe8D

Scientific Paper / Artículo Científico

UNIVERSIDAD POLITÉCNICA SALESIANA ECUADOR
INGENIUS
Revista de Ciencia y Tecnología
https://doi.org/10.17163/ings.n29.2023.10
pISSN: 1390-650X / eISSN: 1390-860X

Sentimental analysis of COVID-19 Twitter data using deep learning and machine learning models

Análisis de sentimiento de los datos de Twitter sobre COVID-19 utilizando modelos de aprendizaje profundo y aprendizaje máquina

Simran Darad[1,*], Sridhar Krishnan[2]

Received: 15-10-2021, Received after review: 01-12-2022, Accepted: 16-12-2022, Published: 01-01-2023

Abstract

The novel coronavirus disease (COVID-19) is an ongoing pandemic with large global attention. However, spreading fake news on social media sites like Twitter is creating unnecessary anxiety and panic among people towards this disease. In this paper, we applied machine learning (ML) techniques to predict the sentiment of the people using social media such as Twitter during the COVID-19 peak in April 2021. The data contains tweets collected on the dates between 16 April 2021 and 26 April 2021 where the text of the tweets has been labelled by training the models with an already labelled dataset of corona virus tweets as positive, negative, and neutral. Sentiment analysis was conducted by a deep learning model known as Bidirectional Encoder Representations from Transformers (BERT) and various ML models for text analysis and performance which were then compared among each other. ML models used were Naïve Bayes, Logistic Regression, Random Forest, Support Vector Machines, Stochastic Gradient Descent and Extreme Gradient Boosting. Accuracy for every sentiment was separately calculated. The classification accuracies of all the ML models produced were 66.4%, 77.7%, 74.5%, 74.7%, 78.6%, and 75.5%, respectively and BERT model produced 84.2%. Each sentiment-classified model has accuracy around or above 75%, which is a quite significant value in text mining algorithms. We could infer that most people tweeting are taking positive and neutral approaches.

Keywords: COVID-19, coronavirus, Twitter, tweets, sentiment analysis, tweepy, text classification

Resumen

En este artículo, se aplicaron técnicas de aprendizaje automático para predecir el sentimiento de las personas que usan las redes sociales como Twitter durante el pico de COVID-19 en abril de 2021. Los datos contienen tuits recopilados en las fechas entre el 16 de abril de 2021 y el 26 de abril de 2021, donde el texto de los tuits se ha etiquetado mediante la formación de los modelos con un conjunto de datos ya etiquetado de tuits de virus de corona como positivo, negativo y neutro. El análisis del sentimiento se llevó a cabo mediante un modelo de aprendizaje profundo conocido como Representaciones de Codificadores Bidireccionales de Transformers (BERT) y varios modelos de aprendizaje automático para el análisis de texto y el rendimiento, que luego se compararon entre sí. Los modelos ML utilizados son Bayes ingenuas, regresión logística, bosque aleatorio, máquinas vectoriales de soporte, descenso de gradiente estocástico y aumento de gradiente extremo. La precisión de cada sentimiento se calculó por separado. La precisión de clasificación de todos los modelos de ML producidos fue de 66.4 %, 77.7 %, 74.5 %, 74.7 %, 78.6 % y 75.5 %, respectivamente y el modelo BERT produjo 84.2 %. Cada modelo clasificado de sentimiento tiene una precisión de alrededor o superior al 75 %, que es un valor bastante significativo en los algoritmos de minería de texto. Vemos que la mayoría de las personas que tuitean están adoptando un enfoque positivo y neutral.

Palabras clave: COVID-19, corona virus, twitter, tuits, análisis de los sentimientos, *tweepy*, clasificación de texto

[1,*]Data Science and Analytics, Toronto Metropolitan University, Canada. Corresponding author ✉: sdarad@ryerson.ca.
[2]Department of Electrical, Computer, and Biomedical Engineering, Toronto Metropolitan University, Canada.

Suggested citation: Darad, S. and Krishnan, S. "Sentimental analysis of COVID-19 Twitter data using deep learning and machine learning models," *Ingenius, Revista de Ciencia y Tecnología*, N.° 29, pp. 108-117, 2023, doi: https://doi.org/10.17163/ings.n29.2023.10.

1. Introduction

There are various kinds of social media platforms that are used by users for many reasons. In recent times, the most used social media platforms for informal communications have been Facebook, Twitter, Reddit, etc. Amongst these, Twitter, the microblogging platform, has a well-documented Application Programming Interface (API) for accessing the data (tweets) available on its platform. Therefore, it has become a primary source of information for researchers working on the Social Computing domain [1]. Social Media platforms such as Twitter are a great resource to capture human emotions and thoughts. During these trying times, people have taken to social media to discuss their fears, opinions, and insights on the global pandemic [2]. For this research, we focused on a dataset that belonged to the Twitter tweets and accessed tweets related to "COVID-19 Pandemic".

Coronavirus disease 2019 (COVID-19) was first detected in Wuhan, China, in December 2019 and has spread worldwide in more than 198 countries [3]. The outbreak of COVID-19 has a socio-economic impact. The World Health Organization declared it an epidemic on 30 January 2020. Since then, it has spread exponentially, inflicting serious health issues including painful deaths [4]. Large-scale datasets are required to train machine learning models or perform any kind of analysis. The knowledge extracted from small datasets and region-specific datasets cannot be generalized because of limitations in the number of tweets and geographical coverage. Therefore, this paper introduces a large-scale COVID-19-specific English language tweets dataset [5].

The main objective of this work is to predict people's sentiments during the peak of the pandemic in April 2021. How can we classify coronavirus tweets as positive, negative, and neutral; which tells us about how people are feeling? So, there are two ways to label the tweets that were extracted using the Twitter API with tweepy. The first way is training already labelled data with BERT and various machine learning models, evaluating which model classifier could correctly label the tweets and then using it to label the text of the tweets extracted. The second way is to find the sentiment comes by using an open-source sentiment analyzer pre-built library known as VADER. It automatically predicts the sentiment score of the tweets classifying the tweets with the power of machine learning and using it to make inferences about the extracted tweets. Based on the classification of different tweets, the effort was to be able to provide more insights about the pandemic affecting mental health and people's reaction about how well they are handling this situation.

1.1. Literature Review

The main aim of this work is to analyze people's reactions on the global pandemic COVID-19 via tweets and classify them as positive, negative, or neutral. This is done by performing sentiment analysis on the data obtained from Twitter. Several Machine Learning techniques have been used to obtain the results. In this section, we will provide an overview of the papers used as references for this work.

There have been many studies on this in a short span of time. To begin with, the trends of positive, negative, and neutral tweets state-wise and month-wise in India are captured and presented in this paper. Firstly, state-wise analysis is done and then the frequency of Positive, Negative, and Neutral tweets are calculated. From the analysis in this paper, it is observed that people in India were mostly expressing their thoughts with positive sentiments [1]. In another paper, a very large dataset of almost over 310 million tweets is taken into consideration. This study specifies the sentiment scores of the tweets in English language only. And it was observed that a common hashtag was being used in most of the tweets [5]. In another research work, country-wise sentiment analysis of the tweets has been done. This research work has taken into account the tweets from twelve countries gathered from 11th March 2020 to 31st March 2020. The tweets have been collected, pre-processed, and then used for text mining and sentiment analysis. The result of the study concludes that while the majority of the people throughout the world took a positive and hopeful approach, there are instances of fear, sadness and disgust exhibited worldwide [6]. Another research paper in which the BERT model was used to analyze the sentiments behind tweets made by netizens of India. There were several common words that came out in the analysis and based on that the tweets are classified into four sentiments such as fear, sad, anger, and joy. This model was 89% accurate as compared to other models like LR, SVM, LSTM [7]. A short research aimed at analyzing the sentiments and emotions of people during COVID-19 was conducted based on the tweets from March 11th to March 31st, 2020, which gave us the results that the mindsets of people was almost at the same level all around the world [8].

There have been few papers in which the exploratory analysis of the data is performed to obtain the results. For instance, in a research paper, exploratory data analysis was performed for a dataset providing information about the number of confirmed cases on a per-day basis in a few of the worst-hit countries to provide a comparison between the change in sentiment with the change in cases since the start of this pandemic till June 2020 [2]. In this paper, the authors have tried to understand and analyze the tweets around COVID-19 in India and have tried to analyze these data using NVIVO processors and word cloud. The study involves the words, hashtag being used and the sentiments involved around these words. The conclusion gives an understanding of high-impact and low-impact words [9]. In this research paper, data is collected from the users who shared their location as 'Nepal' between 21st May 2020 and 31st May 2020. The result of the study concluded that while majority of the people of Nepal took a positive and hopeful approach, there are instances of fear, sadness and disgust exhibited too [10].

Since Twitter is a place where individuals can express their views without revealing their identity, this is used as an advantage by many of them to present their opinions either positive negativelyive based on their sentiments. By using various Machine Learning techniques and knowledge from social media, sentiment analysis on COVID Twitter data was performed, which gave us the results as positive or negative. Logistic Regression Algorithm was used to perform the analysis which gave an accuracy up to 78.5% [11].

Data mining was conducted on Twitter to collect a total of 107,990 tweets related to COVID-19 between December 13, 2019, and March 9, 2020. A Natural Language Processing (NLP) approach and the latent Dirichlet allocation algorithm were used to identify the most common tweet topics as well as to categorize clusters and identify themes based on the keyword analysis. The results indicate the main aspects of public awareness and concern regarding the COVID-19 pandemic. First, the trend of the spread and symptoms of COVID-19 can be divided into three stages. Second, the results of the sentiment analysis showed that people have a negative outlook toward COVID-19 [12]. In this paper, our aim is to perform a sentimental analysis of tweets during the COVID-19 pandemic and classify them as positive, negative, or neutral.

After learning about the dataset, the next step was to solve the classification problem. The classification problem in this paper is sentiment analysis. Many of the papers already mentioned earlier [1, 5] performed sentiment analysis on tweets to classify them in three different categories. These research papers provided vital information about how sentiment analysis can be performed for the classification of tweets in the dataset. Creating a classifier was the next step. "The impact of preprocessing on text classification" is a resourceful paper that provided details and leads on how to conduct preprocessing on data and which classifier would be optimal. It mentions that SVM is state-of-the-art pattern classifier and is recommended to be used as the classification algorithm [13]. The papers use Random Forest, Naïve Bayes, SVM, and Random Forest for classification and tells us that Linear SVM provided the best results. Almost 95% accuracy was achieved using this technique. Based on this research, we have decided to use Naïve Bayes, Logistic Regression, Random Forest, SVM, SGD, XGB and BERT.

Before moving further to the dataset, it is important to know about the dataset and learn as much about it as possible. A detailed exploratory analysis of the dataset was conducted using reference from various papers.

2. Materials and Methods

2.1. Material

Data for this work is acquired from Twitter using its API and tweepy. Tweepy is an open-source and easy-to-use Python package for accessing the functionalities provided by the Twitter API. Tweepy includes a set of classes and methods that represent Twitter's models and API endpoints, and it transparently handles various implementation details, such as: Data encoding and decoding. Data extraction of tweets from Twitter API is done from date 16th April 2021 to 26th April 2021 containing 2,00,000 tweets to get a bigger dataset and better results.

The other dataset is open-sourced and collected from a blog [14] which contains coronavirus tweets with labelled sentiments. The dataset that has been collected for tweets by the blog was a labelled sentiment analysis dataset. This dataset was split into two subsets for training and testing of the various classifiers. The dataset we gathered and fetched from Twitter is unlabelled.

2.1.1. Descriptive Analytics

The dataset contains text fields, so text analysis of the tweets was performed as outlined below. But before that analysis was conducted to learn more about the dataset. Firstly, even before the cleaning process, one should get familiar with the kind of data they'll be dealing with. This just helps in providing more context and background information to the data scientist. So, after loading the csv file, a few functions were run on the data just to familiarize with it. We get to know the size of the data, the data types of each column, the number of null entries, the distribution of different classes, etc. Next is dropping duplicate rows if any. We then realize that we won't be needing a few columns in further analysis, so we drop it.

After those preprocessing techniques were applied to the data to clean the tweets. It includes converting the text to lowercase, tokenization, and removal of username tags, retweet symbol, hashtags, white spaces, punctuations, numbers, emoji, and URLs to clean the text. Using this clean text, further text analysis was conducted as outlined below. The analysis was conducted on the dataset we collected from Twitter API with 200,000 tweets (Figure 1).

```
print('There are {} rows and {} columns in the dataset.'.format(df.shape[0],df.shape[1]))
There are 200000 rows and 13 columns in the dataset.
```

Figure 1. Dataset size

We look at the information of the dataset. It tells us about the type of field it is and about how many non-null values are present in the dataset, which helps us understand our dataset better (Figure 2).

```
df.info()

<class 'pandas.core.frame.DataFrame'>
RangeIndex: 200000 entries, 0 to 199999
Data columns (total 13 columns):
 #   Column            Non-Null Count   Dtype
---  ------            --------------   -----
 0   user_name         199990 non-null  object
 1   user_location     142121 non-null  object
 2   user_description  180498 non-null  object
 3   user_created      200000 non-null  object
 4   user_followers    200000 non-null  int64
 5   user_friends      200000 non-null  int64
 6   user_favourites   200000 non-null  int64
 7   user_verified     200000 non-null  bool
 8   date              200000 non-null  object
 9   text              200000 non-null  object
 10  hashtags          55136 non-null   object
 11  source            200000 non-null  object
 12  is_retweet        200000 non-null  bool
dtypes: bool(2), int64(3), object(8)
memory usage: 17.2+ MB
```

Figure 2. Dataset information

With social media, one can never retrieve all the data. There are always some missing values in the dataset. People like to keep few things discreet such as their location and description in case of twitter. Also, some people as we can see are not comfortable of using hashtags see Figure 3.

```
df.isna().sum()

user_name              10
user_location       57879
user_description    19502
user_created            0
user_followers          0
user_friends            0
user_favourites         0
user_verified           0
date                    0
text                    0
hashtags           144864
source                  0
is_retweet              0
dtype: int64
```

Figure 3. Total null values

Then finding out what is term frequency of the words showing the most frequently used words by their count. We see that "COVID-19" is the most used word (Figure 4).

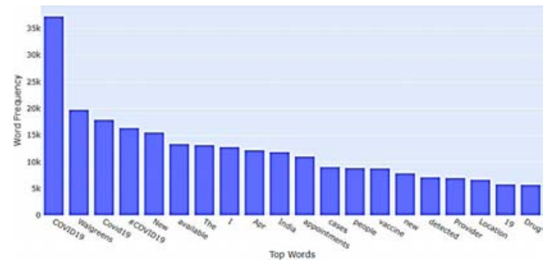

Figure 4. Top words used in tweets

To get a closer look at the text contained in the dataset, a visualization of the word cloud was created (Figure 5).

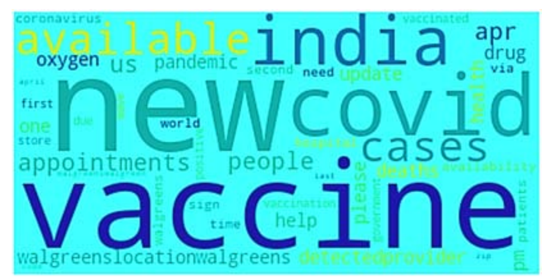

Figure 5. Word Cloud for top 50 most used words

The word cloud above lists all words with the top 50 most used words. Word clouds are useful in understanding what the users are posting about. Most of the words are related to COVID, and new cases, and it seems like most people posted about vaccines as well (Figure 6).

After looking at an overview of the tweet text in our corpus, let's move on to hashtags looking for the most trending ones.

Figure 6. Word Cloud for Hashtags

The word cloud above lists all words with extremely used hashtags. Word clouds are useful in understanding what the users are posting about. Most of the words are related to COVID, new cases, and it seems like most people posted about vaccines as well.

Figure 7 shows the location of the people from where most of them are tweeting. We can see a large number of people are tweeting from India and USA, as the time period selected for extracting the tweets was during the third wave and the number of cases was higher in those countries.

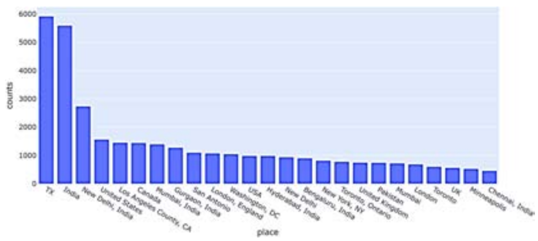

Figure 7. Top 25 locations where tweets originate from

Figure 8 shows which verified users tweeted the most about COVID. We can see that almost all of them are news channels tweeting about the latest updates about COVID and the number of cases in their respective countries.

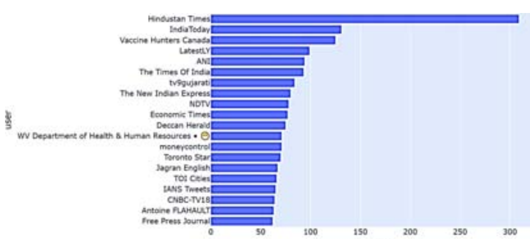

Figure 8. Top 20 user-verified tweets

After looking at an overview of the data, we clean and preprocess the text of the tweets in our corpus, moving on to do some n-gram analysis. N-grams provide a better context of what the users are posting about as we move to bi and trigrams because these provide the most frequent phrases instead of just words. Figure 9 shows that most frequent unigrams are based on new cases, vaccines, health, pandemic, people, availability and appointments.

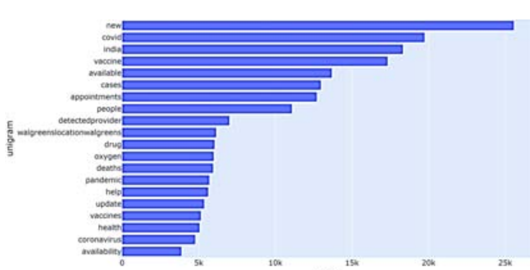

Figure 9. Top 20 Unigrams

A bigram (Figure 10) analysis provides further details trending during that time giving details about availability of vaccine appointments, new cases and second wave.

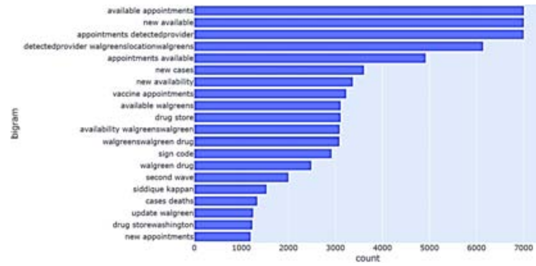

Figure 10. Top 20 Bigrams

A trigram (Figure 11) analysis provides further details on where the COVID new vaccine appointments are available. It seems like most of them are in Walgreens which is an American company that operates as the second-largest pharmacy store chain in the United States behind CVS Health.

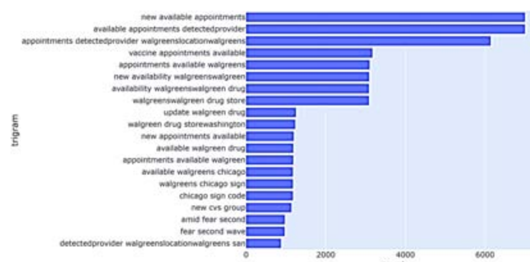

Figure 11. Top 20 Trigrams

2.2. Methods

The aim of this study is to train text from the labelled tweets that could automatically assess if the unlabelled tweet gathered is positive, negative, or neutral. After training the models on labelled twitter data, models were applied to data extracted to label the sentiments and compare the results of different algorithms. The second method of tweets labelling is done by using NLTK VADER inbuilt python package based on lexicons.

In this work, the response is labelling the tweets as positive, negative or neutral. The dataset gathered contains a lot of information on the user such as name, description, followers, friends and many more but only the text of the tweet was used to label the data from training the existing labelled data.

2.2.1. Experimental Design 1

It is very difficult to label the sentiments for COVID-19 data because of the words used to represent the situation. For example, if there are new cases, there is a tweet saying "I am tested Corona positive" which ML technically would label as positive. So, there is a huge uncertainty in predicting the sentiments of the pandemic. Therefore, we apply two different techniques to understand the sentiments.

a) Text Processing

The dataset called "coronavirustweets" contained labelled data of tweets showing the sentiment as extremely positive, positive, neutral, negative and extremely negative. Narrowing down the categorical labels to only three-class classifications, there is neutral, negative combined with extremely negative, and positive combined with extremely positive to achieve greater accuracy. The text from the original tweet needs to be pre-processed to train and test the data by removing punctuations, stop words, spaces, emoticons and stemming the data.

The preprocessing of the text data is an essential step as it makes the raw text ready for mining. The objective of this step is to clean text irrelevant to search the sentiment of tweets such as punctuation(.,?,"etc.), special characters (,%,&,$, etc.), numbers (1,2,3, etc.), Twitter handle, links(HTTPS: / HTTP:) and stop words which don't mean anything in context to the text.

Stop words are those words in natural language that have very little meaning, such as "is", "an", "the", etc. To remove stop words from a sentence, the text can be divided into words and then remove the word if it exists in the list of stop words provided by NLTK.

b) Randomization

The dataset was randomly divided into two sets stratifying with sentiment values of the dataset, one for training with 80% data and another for testing with 20% data.

c) Vectorizing the tweets

Before we implement different ML text classifiers, we need to convert the text data into vectors. It is crucial as the algorithms expect data in some mathematical for rather than textual form. Count Vectorizer counts the number of times a word appears in the document (in each tweet). This process helps in converting the text data as we understand it, to numerical data, that is easier for the computer to understand.

d) Classifiers

After vectorizing the tweets, we are all set to implement classification algorithms. There are three types of sentiments so we must train our models so that they can give us the correct label for the test dataset. We have built different machine learning models such as Naive Bayes, Logistic Regression, Random Forest, Support Vector Machine, Stochastic Gradient Descent and Extreme Gradient Boosting along with BERT, a deep learning model. Ensemble Classifier such as bagging and boosting are applied on the dataset as well to minimize any over-fitting by the classifiers.

We use the accuracy score to measure the performance of the model (precision score, recall and confusion matrix are also calculated). Precision score, recall and confusion matrix let us know how correctly labelled the actual values are. BERT(bi-directional Encoder Representation of Transformers) is a technique developed by Google based on the Transformers mechanism. In our sentiment analysis application, our model is trained on a pre-trained BERT model. BERT models have replaced the conventional RNN based LSTM networks which suffered from information loss in large sequential text [15]. The results from paper explained that a language model that is bi-directionally prepared can have a more profound feeling of language setting and stream than single directional models. In contrast to directional models that enable sequential reading of text input (right to left or left to right), the transformer encoder recognizes the total sequence of words at once. Thus, it is considered bidirectional, but it is a non-directional model with higher accuracy than other established models [7].

e) Labelling new tweets

Since our collected data is not labelled, we save and load our trained models with pickle. This allows us to save our model to a file and load it later in order to make predictions. We can then apply them to label the data we extracted and preprocessed.

f) Comparing algorithms

Obtaining the sentiments of the tweets from different models and saving the csv files of different models, we compare the results of the labelled data.

2.2.2. Experimental Design 2

VADER stands for Valence Aware Dictionary and Sentiment Reasoner. VADER belongs to a type of sentiment analysis that is based on lexicons of sentiment-related words. It is a rule-based model for general sentiment analysis, and its effectiveness was compared to 11 typical benchmarks, including Word Count (LIWC), Affective Norms for English Words (ANEW), the General Inquirer, Linguistic Inquiry, Senti WordNet, and machine learning techniques that rely on Support Vector Machine (SVM) algorithms, Naive Bayes, and Maximum Entropy. In this approach, each of the words in the lexicon is rated as to whether it is positive or negative, and in many cases, how positive or negative.

VADER performs well in the analysis of sentiments expressed in social media. These sentiments must be present in the form of comments, tweets, retweets, or post descriptions, and it works well on texts from other domains also. We design our VADER sentiment model, which extracts features from Twitter data, formulates the sentiment scores, and classifies them into positive, negative, neutral classes.

a) Data Cleaning

The dataset extracted from the tweet needs the text to be pre-processed by removing punctuations, stop words, spaces, emoticons and stemming the data.

b) Finding Polarity

The compound score (polarity) is computed by summing the valence scores for each word in the lexicon, adjusted according to the rules, and then normalized to be between -1 (most extreme negative) and +1 (most extreme positive).

c) Finding Sentiments

After getting the compound scores, the polarity of the tweets is used to categorize them into 3 classes: Positive, Negative and Neutral. Positive Sentiments are those with a score above 0. Negative sentiments from less than 0, and neutral sentiments are having 0.0 polarity. These 3 classes were stored along with the tweets in the dataset called “Sentiments”.

3. Results and discussion

3.1. Results

3.1.1. Experimental Result 1

Multi-class classification on different models was applied to train data to find the accuracy of the correct label for the test dataset. I have built different ML models like Naive Bayes, Logistic Regression, Random Forest, Support Vector Machine, Stochastic Gradient Descent and Extreme Gradient Boosting (Figure 12).

We have observed that the Stochastic Gradient Descent classifier gives the best result with accuracy reaching 78.64%. The accuracy is pretty much close to the accuracy of Logistic Regression, and both models can be used to predict the sentiment of unlabelled data. The least accuracy is shown by Naïve Bayes Classifier. It works well with large data. Naïve Bayes works on n-grams, I have tried using different n-grams, but accuracy stays around 65%.

	Model	Test accuracy
4	Stochastic Gradient Decent	0.786460
1	Logistic Regression	0.777095
5	XGBoost	0.755143
3	Support Vector Machines	0.747467
2	Random Forest	0.745011
0	Naive Bayes	0.664569

Figure 12. Comparison of model accuracies

The BERT model performs extremely well in comparison to other ML models. It gives an accuracy score of 84.2%, which is the highest accuracy we got by training and testing the models. BERT is an excellent and different technique, which provides the best accuracy because it is designed to read in both directions at once. This capability, enabled by the introduction of Transformers, is known as bi-directionality. BERT, however, was pre-trained using only an unlabeled, plain text corpus (namely the entirety of the English Wikipedia, and the Brown Corpus). It continues to learn unsupervised from the unlabeled text and improve even as its being used in practical applications (ie Google search). Its pre-training serves as a base layer of "knowledge" to build from. From there, BERT can adapt to the ever-growing body of searchable content and queries and be fine-tuned to a user’s specifications. This process is known as transfer learning [16].

Next using this trained model on our dataset, we see the following results based on the test accuracy (Figure 13).

SGD Classifier gives:
Neutral: 65462
Positive: 48785
Negative: 35741

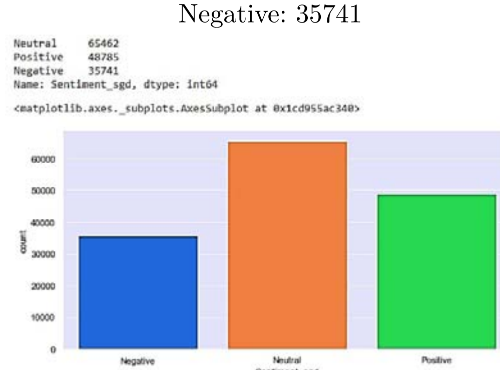

Figure 13. SGD Classifier results

Stochastic Gradient Descent is a simple yet very efficient approach to fitting linear classifiers and regressors under convex loss functions. SGD has been successfully applied to large-scale and sparse machine learning problems often encountered in text classification and natural language processing, which is why it performs better than all other models (Figure 14).

LG Classifier gives:
Neutral: 62263
Positive: 49022
Negative: 38703

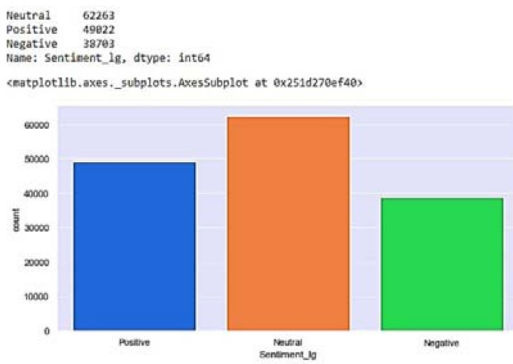

Figure 14. LG Classifier results

Seeing the results, we observe Logistic Regression gives more Positive and Negative labelled tweets whereas Stochastic Gradient Boosting predicts some of them as Neutral. Even though the accuracy for these both is almost the same, there is different labelling of approximately 3,000 tweets as neutral. Multinomial logistic regression is an extension of logistic regression that adds native support for multi-class classification problems. Logistic regression, by default, is limited to two-class classification problems, which is why SGD is better in accuracy for predicting sentiments.

Ensemble Classifier such as bagging and boosting are applied on the dataset to minimize any over-fitting by the classifiers. But there isn't any over-fitting of the data because the accuracy obtained by bagging is 72.1% which is around the same whereas accuracy of boosting is 51.4% which is pretty much lower.

A similar analysis has been presented in [17] for the understanding of pandemic anxiety among Twitter users based on keywords. About 900,000 tweets were extracted from Twitter Application programming interface (API) and analysed using Naïve Bayes and logistic regression models. The model accuracy that appeared in short tweets is 91% and 74%, respectively. However, the main limitation of this study is all sentiments depend on the single word "fear" of only USA citizens and they are short tweets [7].

3.1.2. Experimental Result 2

VADER sentiment model is an automatic labelling technique in which we formulated the sentiment score by classifying the tweets as positive, negative and neutral. The main difference we observe here is, it gives fewer (around 5000 fewer) neutral tweets and classifies them as positive and negative. We can see that it almost matches our trained labelled models accuracy by showing us the results as follows (Figure 15):

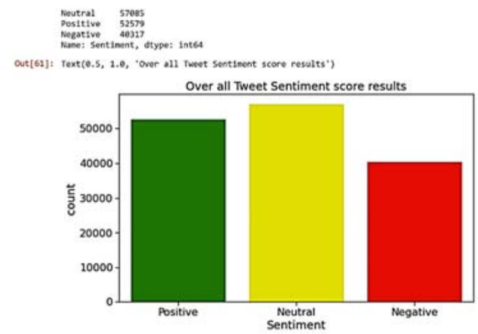

Figure 15. VADER results

3.2. Discussion

This study can be used to analyze the changing sentiments of people from all over the world and check whether there are major shifts in them over the period of time along with the increased supply of vaccinations. It is expected that as the spread of this pandemic will increase for unvaccinated people, the sentiments in the tweets to positive almost entirely as things get back to normal.

A similar analysis was conducted using TextBlob as we did in Experiment 2 but we used VADER. But according to the TextBlob documentation, TextBlob takes advantage of Naïve Bayes (NB) model for classification. NB classifier has been trained on NLTK (Natural Language Tool Kit) to detect the valence of aggregated tweets [10]. As we saw Naïve Bayes gives the least accuracy so Textblob is not accurate for labelling sentiments. Classical ML methods provided an accuracy of high 70%, whereas the deep learning model that uses BERT provided an impressive accuracy rate of 84.2%.

4. Conclusions

The results of the study conclude that majority of the people throughout the world took a positive and hopeful approach. However, countries such as India and United States of America have shown signs of bigger-scale tweeting due to the third wave as compared to remaining countries.

We used two techniques for our dataset to get the labels, but as we show, there is always some margin of error in text classification. We also show that BERT requires high computational power, GPU and a large time to train on a model. The prediction of any social media text is nearly impossible to give a perfect accuracy score. Through this, we can learn the main issue to help the healthcare providers to identify some kind of mental illness before it's too late.

Support and Acknowledgements

The authors would like to thank Ryerson University for supporting this project.

References

[1] T. Vijay, A. Chawla, B. Dhanka, and P. Karmakar, "Sentiment analysis on COVID-19 Twitter Data," in *2020 5th IEEE International Conference on Recent Advances and Innovations in Engineering (ICRAIE)*, 2020, pp. 1–7. [Online]. Available: https://doi.org/10.1109/ICRAIE51050.2020.9358301

[2] M. Mansoor, K. Gurumurthy, A. R. U, and V. R. B. Prasad, "Global sentiment analysis of COVID-19 Tweets over time," *CoRR*, vol. abs/2010.14234, 2020. [Online]. Available: https://doi.org/10.48550/arXiv.2010.14234

[3] H. Drias and Y. Drias, "Mining Twitter Data on COVID-19 for sentiment analysis and frequent patterns discovery," *medRxiv*, 2020. [Online]. Available: https://doi.org/10.1101/2020.05.08.20090464

[4] F. Rustam, M. Khalid, W. Aslam, V. Rupapara, A. Mehmood, and G. S. Choi, "A performance comparison of supervised machine learning models for COVID-19 Tweets sentiment analysis," *PLOS ONE*, vol. 16, no. 2, pp. 1–23, 02 2021. [Online]. Available: https://doi.org/10.1371/journal.pone.0245909

[5] R. Lamsal, "Design and analysis of a large-scale COVID-19 Tweets dataset," *Applied Intelligence*, vol. 51, no. 5, pp. 2790–2804, May 2021. [Online]. Available: https://doi.org/10.1007/s10489-020-02029-z

[6] A. D. Dubey, "Twitter sentiment analysis during COVID-19 Outbreak," *SSRN*, 2021. [Online]. Available: https://dx.doi.org/10.2139/ssrn.3572023

[7] N. Chintalapudi, G. Battineni, and F. Amenta, "Sentimental analysis of COVID-19 Tweets using deep learning models," *Infect Dis Rep*, vol. 13, no. 2, pp. 329–339, Apr. 2021. [Online]. Available: https://doi.org/10.3390/idr13020032

[8] M. A. Kausar, A. Soosaimanickam, and M. Nasar, "Public sentiment analysis on Twitter Data during COVID-19 Outbreak," *International Journal of Advanced Computer Science and Applications*, vol. 12, no. 2, 2021. [Online]. Available: http://dx.doi.org/10.14569/IJACSA.2021.0120252

[9] A. Mitra and S. Bose, "Decoding Twitter-verse: An analytical sentiment analysis on Twitter on COVID-19 in india," *Impact of Covid 19 on Media and Entertainment*, 2020. [Online]. Available: https://bit.ly/3YMj1c3

[10] B. P. Pokharel, "Twitter sentiment analysis during COVID-19 Outbreak in Nepal," *SSRN*, 2020. [Online]. Available: https://dx.doi.org/10.2139/ssrn.3624719

[11] C. R. Machuca, C. Gallardo, and R. M. Toasa, "Twitter sentiment analysis on coronavirus: Machine learning approach," *Journal of Physics: Conference Series*, vol. 1828, no. 1, p. 012104, feb 2021. [Online]. Available: https://dx.doi.org/10.1088/1742-6596/1828/1/012104

[12] S. Boon-Itt and Y. Skunkan, "Public perception of the COVID-19 pandemic on Twitter: Sentiment analysis and topic modeling study," *JMIR Public Health Surveill*, vol. 6, no. 4, p. e21978, Nov. 2020. [Online]. Available: https://doi.org/10.2196/21978

[13] A. K. Uysal and S. Gunal, "The impact of preprocessing on text classification," *Information Processing & Management*, vol. 50, no. 1, pp. 104–112, 2014. [Online]. Available: https://doi.org/10.1016/j.ipm.2013.08.006

[14] S. Gujral, "Sentiment analysis: Predicting sentiment of COVID-19 Tweets," *Analytics Vidhya*, 2021. [Online]. Available: https://bit.ly/3j9tMVj

[15] ——, "Amazon product review sentiment analysis using BERT," *Analytics Vidhya*, 2021. [Online]. Available: https://bit.ly/3Vad9WE

[16] B. Lutkevich. (2022) BERT language model. TechTarget Enterprise Al. [Online]. Available: https://bit.ly/3Wo5Pb4

[17] J. Samuel, G. G. M. N. Ali, M. M. Rahman, E. Esawi, and Y. Samuel, "COVID-19 public sentiment insights and machine learning for Tweets classification," *Information*, vol. 11, no. 6, 2020. [Online]. Available: https://doi.org/10.3390/info11060314

UNIVERSIDAD POLITÉCNICA SALESIANA ECUADOR
INGENIUS
Revista de Ciencia y Tecnología
pISSN: 1390-650X / eISSN: 1390-860X

Guidelines for publication in Ingenius Journal

1. General Information

Ingenius is a scientific publication of the *Universidad Politécnica Salesiana* of Ecuador, published since January 2007, with a fixed biannual periodicity, specialized in Mechanical Engineering, Electrical Engineering, Electronics, Computer Science and its integration in what is now known as Mechatronics; these lines of action strengthen areas such as automation, control, robotics, among others..

It is a scientific journal, which uses the peer-review system, under double-blind review methodology, according to the publication standards of the Institute of Electrical and Electronics Engineers (IEEE). Compliance with this system allows authors to guarantee an objective, impartial and transparent review process, which facilitates the publication of their inclusion in reference databases, repositories and international indexing.

Ingenius is indexed in the directory and selective catalog of the Regional Online Information System for Scientific Journals of Latin America, the Caribbean, Spain and Portugal (Latindex), in the Directory of Journals of Open Access DOAJ, In the Information Matrix for the Analysis of Journals, MIAR, In the Ibero-American Network of Innovation and Scientific Knowledge, REDIB and in repositories, libraries and specialized catalogs of Latin America.

The journal is published in a double version: printed (ISSN: 1390-650X) and digital (e-ISSN: 1390-860X), in Spanish, each work being identified with a DOI (Digital Object Identifier System. The articles sent to Ingenius magazine must comply with the following criteria:

2. Scope and policy

2.1. Theme

Original contributions in Mechanical Engineering, Electrical and Electronic Engineering, Computer Science and its integration in what is now known as Mechatronics, as well as related areas: Automation, Control, Domotics, Robotics in their different fields of action and all those related disciplines with the same central theme.

All the work carried out by national or foreign researchers may be published once they meet the required scientific quality criteria.

2.2. Contributions

Ingenius Journal preferably publishes articles related to empirical research, and also reports of technological development, proposals for models and innovations, products for the elaboration of graduate and postgraduate thesis that contribute to the field of science and technology, as well as select revisions of literature. (state-of-the-art).

- **Research:** 5,000 to 6,500 words of text, including title, abstracts, descriptors, charts and references.
- **Reports:** 5,000 to 6,500 words of text, including title, abstracts, charts and references.
- **Reviews:** 6,000 to 7,000 words of text, including charts and references. Current, selective and justified references, would be specially valued from among 40 works

The Ingenius Journal publishes original and unpublished works written in Spanish and English, they may not have been published through any printed or electronic media, nor be in the process of arbitration or publication.

Every article will be subjected to a rigorous arbitration process; the evaluation of the article will be made according to criteria of originality, relevance, relevance, contributions, scientific rigor and compliance with established editorial guidelines.

Being an arbitrated publication, the Editorial Board approves its publication based on the concept of specialized pairs. The reception of a document does not imply commitment of publication.

It is essential to present a letter of presentation and grant of rights which can be downloaded from: <
urlhttps://goo.gl/ZNkMRD>.

Contributions must be exclusively sent and through the OJS (Open Journal System) <`https://goo.gl/JF7dWT`>. In which all authors must previously register as a user. For any consultation of the procedure you should contact:

<revistaingenius@ups.edu.ec>,
<jcalle@ups.edu.ec> ó
<mquinde@ups.edu.ec>.

3. Presentation and structure of the manuscripts

For those works that are empirical investigations, the manuscripts will follow the IMRDC structure (Introduction, Materials and Methods, Results and Discussion and Conclusions), being optional the Notes and Supports. Those papers that, on the contrary, deal with reports, studies, proposals and reviews may be more flexible in their epigraphs, particularly in material and methods, analysis, results, discussion and conclusions. In all typologies of works, references are mandatory.

Articles may be written on Microsoft Word (.doc or .docx) or LaTeX(.tex). The template to be used can be downloaded from the journal's website, a, <`https://goo.gl/gtCg6m`>, while for LaTeX in <`https://goo.gl/hrHzzQ`>, it is necessary that the file be anonymised in Properties of File, so that the author(s) ID is not displayed.

Figures, Graphs and/or Illustrations, as well as Charts shall be numbered sequentially including an explanatory description for each. The equations included in the article must also be numbered; the figures, charts and equations must be cited in the text.

Use space after point, commas and question marks.

Use "enter" at the end of each paragraph and title heading. Do not use .enter.anywhere else, let the word processor program automatically break the lines.

Do not center headings or subheadings as they should be aligned to the left.

Charts must be created in the same program used for the document body, but must be stored in a separate file. Use tabs, not spaces, to create columns. Remember that the final size of printed pages will be 21 x 28 cm, so the tables must be designed to fit the final print space.

3.1. Structure of the manuscripts

3.1.1. Presentation and cover letter

1. **Título (español) / Title (inglés):** Concise but informative, in Spanish on the front line and in English on the second, when the article is written in Spanish and vice versa if it is written in English.
2. **Authors and affiliations:** Full name and surname of each author, organized by order of priority and their institutional affiliation with reference to the end of the first sheet, where it must include: Dependency to which belongs within the

institution, Institution to which he/she belongs, country, ORCID. A maximum of 5 authors will be accepted, although there may be exceptions justified by the complexity and extent of the topic.

3. **Abstract (Spanish) / Abstract (English):** It will have a maximum extension of 230 words, first in Spanish and then in English. : 1) Justification of the topic; 2) Objectives; 3) Methodology and sample; 4) Main results; 5) Main conclusions.
4. **Keywords (Spanish) / Keywords (English):** 6 descriptors must be presented for each language version directly related to the subject of the work. The use of the key words set out in UNESCO's Thesaurus will be positively valued.
5. **Presentation (Cover Letter):** A statement that the manuscript is an original contribution, not submission or evaluation process in another journal, with the confirmation of the signatory authors, acceptance (if applicable) of formal changes in the manuscript according to the guidelines and partial assignment of rights to the publisher, according to the format established in: <`https://goo.gl/ZNkMRD`>

3.1.2. Manuscript

1. **Título (español) / Title (inglés):** Concise but informative, in Spanish on the front line and in English on the second, when the article is written in Spanish and vice versa if it is written in English.
2. **Authors and affiliations:** Full name and surname of each author, organized by order of priority and their institutional affiliation with reference to the end of the first sheet, where it must include: Dependency to which belongs within the institution, Institution to which he/she belongs, country, ORCID. A maximum of 5 authors will be accepted, although there may be exceptions justified by the complexity and extent of the topic.
3. **Abstract (Spanish) / Abstract (English):** It will have a maximum extension of 230 words, first in Spanish and then in English. : 1) Justification of the topic; 2) Objectives; 3) Methodology and sample; 4) Main results; 5) Main conclusions.
4. **Keywords (Spanish) / Keywords (English):** 6 descriptors must be presented for each language version directly related to the subject of the work. The use of the key words set out in UNESCO's Thesaurus will be positively valued.
5. **Introduction:** It should include the problem statement, context of the problem, justification, rationale and purpose of the study, using bibliographical citations, as well as the most significant and current literature on the topic at national and international level.
6. **Material and methods:** It must be written so that the reader can easily understand the development of the research. If applicable, it will describe the methodology, the sample and the form of sampling, as well as the type of statistical analysis used. If it is an original methodology, it is necessary to explain the reasons that led to its use and to describe its possible limitations.
7. **Analysis and results:** It will try to highlight the most important observations, describing, without making value judgments, the material and methods used. They will appear in a logical sequence in the text and the essential charts and figures avoiding the duplication of data.
8. **Discussion and Conclusions:** It will summarize the most important findings, relating the observations themselves to relevant studies, indicating contributions

and limitations, without adding data already mentioned in other sections. It should also include deductions and lines for future research.

9. **Supports and acknowledgments (optional):** The Council Science Editors recommends the author (s) to specify the source of funding for the research. Priority will be given to projects supported by national and international competitive projects.
10. **The notes (optional):** will go, only if necessary, at the end of the article (before the references). They must be manually annotated, since the system of footnotes or the end of Word is not recognized by the layout systems. The numbers of notes are placed in superscript, both in the text and in the final note. The numbers of notes are placed in superscript, both in the text and in the final note. No notes are allowed that collect simple bibliographic citations (without comments), as these should go in the references.
11. **References:** Bibliographical citations should be reviewed in the form of references to the text. Under no circumstances should references mentioned in the text not be included. Their number should be sufficient to contextualize the theoretical framework with current and important criteria. They will be presented sequentially in order of appearance, as appropriate following the format of the IEEE.

3.2. Guidelines for Bibliographical references

Journal articles:

[1] J. Riess, J. J. Abbas, "Adaptive control of cyclic movements as muscles fatigue using functional neuromuscular stimulation". IEEE Trans. Neural Syst. Rehabil. Eng vol. 9, pp.326–330, 2001. [Onine]. Available: https://doi.org/10.1109/7333.948462

Books:

[1] G. O. Young, "Synthetic structure of industrial plastics" in Plastics, 2nd ed., vol. 3, J. Peters, Ed. New York: McGraw–Hill, 1964, pp. 15–64.

Technical reports:

[1] M. A. Brusberg and E. N. Clark, "Installation, operation, and data evaluation of an oblique–incidence ionosphere sounder system," in "Radio Propagation Characteristics of the Washington–Honolulu Path," Stanford Res. Inst., Stanford, CA, Contract NOBSR–87615, Final Rep., Feb. 1995, vol. 1

Articles presented in confeences (unpubished):

[1] Vázquez, Rolando, Presentación curso "Realidad Virtual". National Instruments. Colombia, 2009.

Articles of memories of Conferences (Published):

[1] L. I. Ruiz, A. García, J. García, G. Taboada. "Criterios para la optimización de sistemas eléctricos en refinerías de la industria petrolera: influencia y análisis en el equipo eléctrico," IEEE CONCAPAN XXVIII, Guatemala 2008.

Thesis:

[1] L.M. Moreno, "Computación paralela y entornos heterogéneos," Tesis doctoral, Dep. Estadística, Investigación Operativa y Computación, Universidad de La Laguna, La Laguna, 2005.

Guidelines:

[1] IEEE Guide for Application of Power Apparatus Bushings, IEEE Standard C57.19.100–1995, Aug. 1995.

Patents:

[1] J. P. Wilkinson, "Nonlinear resonant circuit devices," U.S. Patent 3 624 125, July 16, 1990.

Manuals:

[1] Motorola Semiconductor Data Manual, Motorola Semiconductor Products Inc., Phoenix, AZ, 1989.

Internet resources:

[1] E. H. Miller, “A note on reflector arrays” [Online]. Available. https://goo.gl/4cJkCF

3.3. Epigraphs, Figures and Charts

The epigraphs of the body of the article will be numbered in Arabic. They should go without a full box of capital letters, neither underlined nor bold. The numbering must be a maximum of three levels: 1. / 1.1. / 1.1.1. At the end of each numbered epigraph will be given an enter to continue with the corresponding paragraph.

The charts must be included in the text according to order of appearance, numbered in Arabic and subtitled with the description of the content, the subtitle should go at the top of the table justified to the left.

Figures can be linear drawings, maps or black and white halftone or color photographs in 300 dpi resolution. Do not combine photographs and line drawings in the same figure.

Design the figures so that they fit eventually to the final size of the journal 21 x 28 cm. Make sure inscriptions or details, as well as lines, are of appropriate size and thickness so that they are not illegible when they are reduced to their final size (numbers, letters and symbols must be reduced to at least 2.5 mm in height After the illustrations have been reduced to fit the printed page). Ideally, the linear illustrations should be prepared at about a quarter of their final publication size.

Different elements in the same figure should be spelled a, b, c, etc.

Photographs should be recorded with high contrast and high resolution. Remember that photographs frequently lose contrast in the printing process. Line drawings and maps should be prepared in black.

The text of the figures and maps must be written in easily legible letters.

If the figures have been previously used, it is the responsibility of the author to obtain the corresponding permission to avoid subsequent problems related to copyright.

Each figure must be submitted in a separate file, either as bitmap (.jpg, .bmp, .gif, or .png) or as vector graphics (.ps, .eps, .pdf).

4. Submission process

The manuscript must be sent through the OJS system of the journal, <`https://goo.gl/JF7dWT`>,the manuscript should be uploaded as an original file in .pdf without author data and anonymized according to the above; In complementary files the complete manuscript must be loaded in .doc or .docx (Word file), that is to say with the data of the author (s) and its institutional ascription; Also the numbered figures should be uploaded in independent files according to the corresponding in the manuscript (as bitmap .jpg, .bmp, .gif, or .png or as vector graphics .ps, .eps, .pdf). It is also obligatory to upload the cover letter and grant of rights as an additional file.

All authors must enter the required information on the OJS platform and only one of the authors will be responsible for correspondence.

Once the contribution has been sent the system will automatically send the author for correspondence a confirmation email of receipt of the contribution.

5. Editorial process

Once the manuscript has been received in OJS, a first check by the editorial team of the following points:

- The topic is in accordance with the criteria of the journal.
- Must have the IMRDC structure.
- Must be in the INGENIUS format.
- Must use the IEEE citation format.
- All references should be cited in the text of the manuscript as well as charts, figures and equations.
- The manuscript is original; for this, software is used to determine plagiarism.

The assessment described above can take up to 4 weeks.

If any of the above is not complete or there is inconsistency, an email will be sent to the author to make the requested corrections.

The author will make the corrections and resend the contribution through an email in response to the notification and will also upload the corrected manuscript into OJS supplementary files.

The editorial team will verify that the requested corrections have been incorporated, if it complies, the manuscript will start the second part of the process that may be followed by the author through OJS, otherwise the author will be notified and the manuscript will be archived.

The second phase of the process consists of the evaluation under the methodology of double-blind review, which includes national and foreign experts considering the following steps:

- The editor assigns two or more reviewers for the article.
- After reviewing the article, the reviewers will submit the evaluation report with one of the following results.
  - Publishable
  - Publishable with suggested changes
  - Publishable with mandatory changes
  - Non publishable
- The editor once received the evaluation by the reviewers will analyze the results and determine if the article is accepted or denied.
- If the article is accepted, the author will be notified to make corrections if required and the corresponding editorial process will be continued.
- If the article is denied, the author will be notified and the manuscript will be archived.
- In the two previous cases the result of the evaluation of the reviewers and their respective recommendations will be sent.

The second phase of the process lasts at least 4 weeks, after which they will be notified to the author giving instructions to continue with the process.

6. Publication

The INGENIUS Journal publishes two issues per year, on January 1st and July 1st, so it is important to consider the dates for sending the articles and their corresponding publication. Articles received until October will be considered for the January publication and those received until April for the July publication.

UNIVERSIDAD POLITÉCNICA SALESIANA DEL ECUADOR
Juan Cárdenas Tapia, sdb,
Rector

Turuhuayco 3-69 y Calle Vieja
Postal code 2074
Cuenca, Ecuador
Teléfono: (+593 7) 205 00 00
Fax: (+593 7) 408 89 58
Email: srector@ups.edu.ec

Exchange

Exchange with other periodicals is accepted.

Address:
Secretaría Técnica de Comunicación
Universidad Politécnica Salesiana
Turuhuayco 3-69 y Calle Vieja
Postal code 2074
Cuenca, Ecuador
Phone: (+593 7) 205 00 00 Ext. 1182
Fax: (+593 7) 408 89 58
Email: rpublicas@ups.edu.ec
www.ups.edu.ec
Cuenca – Ecuador

INGENIUS, Journal Science of Technology,
Issue 29
january/june 2023
John Calle Sigüencia, Editor in chief
revistaingenius@ups.edu.ec

Printed
Centro Gráfico Salesiano: Antonio Vega Muñoz 10-68 y General Torres.
Phone: (+593 7) 283 17 45
Cuenca – Ecuador
Email: centrograficosalesiano@lns.com.ec

OTHER PERIODIC PUBLICATIONS OF THE UNIVERSITY

UNIVERSITAS, Journal of Social and Human Sciences.

LA GRANJA, Journal of the Sciences.

ALTERIDAD, Journal of Education.

RETOS Journal of Administration Sciences and Economics.

UTOPÍA, University Youth Ministry Magazine.

SOPHIA, Collection of Philosophy of Education.

ABYA YALA | UNIVERSIDAD POLITÉCNICA SALESIANA

ECUADOR SALESIANOS DON BOSCO